

Investigation of Semiconductor and Metal-Metal Oxide Surface Nanostructures by Scanning
Tunneling Microscopy/Spectroscopy

A Dissertation

Presented to
the faculty of the School of Engineering and Applied Science
University of Virginia

in partial fulfillment
of the requirements for the degree

Doctor of Philosophy

by

Gopalakrishnan Ramalingam

December

2016

APPROVAL SHEET

The dissertation
is submitted in partial fulfillment of the requirements
for the degree of
Doctor of Philosophy



AUTHOR

The dissertation has been read and approved by the examining committee:

Petra Reinke

Advisor

John R. Scully

Jerrold A. Floro

Ian Harrison

Hendrik Heinz

Accepted for the School of Engineering and Applied Science:



Craig H. Benson, Dean, School of Engineering and Applied Science

December
2016

ABSTRACT

“God made the bulk, but surfaces were the work of the devil” – Wolfgang Pauli

A surface is where all physical and chemical interaction between the material and environment takes place. The interactions between a surface and its environment are complex and often hard to predict. Scanning tunneling microscopy and spectroscopy (STM/STS) is a powerful tool that provides information on the atomic and electronic structure of surfaces and has been used in this work to study the adsorption of atoms or molecules, the structure of thin films and structural changes during controlled reactions. In this dissertation, growth of surface nanostructures and changes in the surface structure during controlled chemical reactions are studied using STM/STS. The dissertation is divided into two parts: in the first part, the evolution of the atomic and electronic structure of Ni-Cr alloys during oxidation is presented while the second part deals with the growth of 1D and 2D nanostructures on silicon surfaces.

NiCr-based superalloys are ubiquitous in high temperature applications such as turbine blades and steam reactors that require a combination of high oxidation resistance and good mechanical strength. The initial stages of oxidation of alloys are studied to understand the changes in the nucleation and growth of the oxides that are induced by Cr and other minor alloying elements and to determine the factors that control the formation of a passive oxide layer on the surface. In order to systematically vary the composition of the alloy while retaining the same starting surface structure, strategies for the growth of smooth Ni-Cr and Ni-Cr-Mo alloy thin films on MgO(001) are successfully developed. The

alloy thin films (5-35 wt.% Cr) are oxidized at 300 °C in incremental steps and the evolution of atomic and electronic structure of the surface is captured. No oxides are formed on pure Ni surfaces in ultrahigh vacuum at 300 °C and the addition of just 5 wt.% Cr results in the nucleation and growth of oxides on the surface. The oxides grow to a certain critical height beyond which the growth mode is altered and the oxides begin to grow laterally to cover the metal surface. Our results show that increasing Cr content in the alloy decreases the oxygen exposure necessary to form a continuous oxide. Extensive statistics on the oxide height, area and volume are used to discuss the nucleation and growth of oxides as a function of alloy composition. The nucleation and growth of the oxides is dependent on the supply of Cr from the bulk to the surface and an atomic-scale reaction model is proposed to explain the initial stages of oxidation. The current experimental approach also allows us to measure the local density of states of the surface during oxidation. The evolution of bandgap of the oxide is measured and correlated with the oxide dimensions. The current work serves as input for phase field, DFT and molecular dynamics simulations to describe the initial stages of oxidation of Ni-Cr alloys. The experimental framework used in this dissertation can be extended to study the interaction of ternary Ni-Cr-X alloys to determine the effect of minor alloying elements such as W or Mo on the initial stage of oxidation as well as to other A-B alloys where the alloying element (B) is either more or less reactive than the host metal (A).

In the second part of the dissertation, the adsorption of Co and Mn on a Si(100) surface and the response of elastically strained Ge wetting layers on Si(100) to thermal energy is discussed. The incorporation of Co atoms on a clean Si(100)-2×1 surface and a Mn wire-decorated Si surface is studied to understand the initial stages of adsorption of

magnetic dopants and their bonding structure with the ultimate goal of achieving magnetic semiconductors for spintronics applications. The interactions between Co-Si, Co-Mn, and Mn-Mn are discussed through sequential and co-deposition of Mn and Co. Subsequently, annealing-induced formation of novel three-dimensional structures on the elastically strained Ge/Si(100) wetting layers is presented. The role of the stored misfit strain energy in determining the type of structure formed is discussed.

To my beloved wife, parents and brother

ACKNOWLEDGEMENTS

First and foremost, I would like to acknowledge the valuable mentorship I received from my advisor, Prof. Petra Reinke. Petra is an inspirational mentor and has a dizzying passion for research. I owe her a debt of gratitude for molding my research skills over the years and the stimulating research discussions we have shared have made me a better researcher. The time I have spent in Petra's research group has been a wonderful chapter in my life.

I would like to thank my dissertation committee members for their valuable suggestions and discussions during my proposal. I would also like to acknowledge my past and current group members for being a source of support and encouragement. The Materials Science department at UVA is a close-knit community and the relationships that have been fostered here will stay for life. Special shout-out goes to Ehsan, Cameron, Jay, Bernard and Balaji for the enjoyable times we have shared at work and outside. A special note of thanks goes to Kim for our engaging conversations on a motley mix of topics and for her efforts to develop a cooperative and collaborative environment in MSE!

My wife and parents have been a constant source of support and encouragement. I would not be here without their presence and my gratitude cannot be adequately expressed in words. My wife, Indu, has always heard me out and helped with my problems in research to the point that she might as well be a co-author! She has been a beacon of positivity in my lowest moments and I am truly blessed to have her in my life.

PUBLICATION LIST

1. Ramalingam, G. & Reinke, P. Towards a Mn–Co surface alloy: Scanning Tunneling Microscopy (STM) study of Co adsorption on Si(100) and its interaction with Mn wires. *Surface Science* **620**, 1–8 (2014).
2. Ramalingam, G., Floro, J. A. & Reinke, P. Three-dimensional nanostructures on Ge/Si(100) wetting layers: Hillocks and pre-quantum dots. *Journal of Applied Physics* **119**, 205305 (2016).
3. Ramalingam, G. & Reinke, P. Growth of Ni and Ni-Cr Alloy Thin Films on MgO(001): Effect of Alloy Composition on Surface Morphology. *Accepted, Journal of Applied Physics* **120** (2016).
4. Volders, C., Monazami, E., Ramalingam, G. & Reinke, P. Alternative Route to Silicene Synthesis via Surface Reconstruction on h-MoSi₂ Crystallites. *Under review – Nano Letters* (2017)
5. Monazami, E., Ramalingam, G. & Reinke, P. Alternative Visualization Strategies for Tunneling Spectroscopy Images: Use of Bandgap Maps – *in preparation*
6. Ramalingam, G., Monazami, E. & Reinke, P. Evolution of Atomic and Electronic Structure of Ni(001) Surface during Oxidation. – *in preparation*
7. Ramalingam, G. & Reinke, P. Nano-scale Insights into the Evolution of Atomic and Electronic Structure during Oxidation of Ni-Cr Alloys. – *in preparation*
8. Gusieva, K., Lutton, K., Ramalingam, G., Berkowitz, K., Blades, W., Reinke, P. & Scully, J.R. Structural Characterization of Passive Oxides on Ni-Cr and Ni-Cr-Mo Alloys. – *in preparation*

Future Publications

9. Reinke & Voorhees group – Phase field modeling and STM data. (*mid-2017*)
10. Blades, W., Ramalingam, G. & Reinke, P. High temperature oxidation of Ni-Cr Alloys. (*mid-2017*)
11. Ramalingam, G., Avincola, V., Blades, W., Zeitchick, E., Perepezko, J., Opila, E.J. & Reinke, P. Ambient Pressure XPS during Ni-Cr and Ni-Cr-Mo Alloy Oxidation. (*late-2017*)
12. Blades, W., Ramalingam, G. & Reinke, P. Ni-Cr-Mo Alloy Oxidation by STM/STS. (*late-2017*)

TABLE OF CONTENTS

ABSTRACT	i
ACKNOWLEDGEMENTS.....	v
PUBLICATION LIST	vi
LIST OF FIGURES	xi
LIST OF TABLES	xviii
Overview	19
1. Opportunities and Challenges	23
References	28
2. Background	29
2.1. Chemical Reactions at Solid Surfaces.....	30
2.1.1. Physical Adsorption (Physisorption)	31
2.1.2. Chemical Adsorption (Chemisorption).....	32
2.1.3. Compound Formation – Nucleation and Growth.....	35
2.2. Oxide Film Growth.....	39
2.2.1. Thin Oxide Films – Cabrera-Mott Theory	40
2.2.2. Thicker Oxides – Wagner and Extended Cabrera-Mott Theories	41
2.3. Physical Properties of Oxides in Ni-Cr-Mo System.....	43
2.4. Thin Film Growth	43
2.4.1. Thermodynamics of Film Growth	44
2.4.2. Kinetics of Film Growth.....	46
References	48
3. Experimental Approach	52
3.1. Thin Film Deposition Techniques.....	53
3.1.1. Electron Beam Evaporation.....	54
3.1.2. Effusion Cell	55
3.2. Characterization Techniques.....	55
3.2.1. Scanning Tunneling Microscopy.....	55
3.2.2. Atomic Force Microscopy (ex-situ)	59
3.2.3. Ambient Pressure Photoelectron Spectroscopy	60

3.2.4. Scanning Electron Microscopy (SEM)	63
3.2.5. Other Techniques.....	64
3.3. Use of Thin Films to Study Chemical Reactions	64
3.4. Substrate Preparation	65
3.4.1. MgO(001)	65
3.4.2. Si(100).....	68
3.5. STM/STS Data Analysis Rubric.....	69
3.5.1. Topography Images	70
3.5.2. Spectroscopy Data	75
References	79
4. Growth of Ni and Ni-Cr Alloy Thin Films on MgO(001).....	81
4.1. Introduction.....	81
4.2. Experimental Details.....	83
4.3. Results.....	85
4.3.1. Effect of MgO Pre-Treatment	85
4.3.2. Effect of Growth Temperature	87
4.3.3. Effect of Cr Alloying.....	91
4.4. Discussion.....	96
4.5. Conclusions.....	99
References	100
5. Atomic and Electronic Structure Changes during Oxidation of Ni(001).....	103
5.1. Introduction.....	103
5.2. Methods.....	105
5.3. Results and Discussion.....	108
5.3.1. Ni Oxidation at 300 °C.....	108
5.3.2. Effect of Temperature on Ni Oxidation	115
5.4. Summary.....	120
5.5. Future Work	121
References	123
6. Nano- and Meso-scale Insights into the Evolution of Atomic and Electronic Structure during Oxidation of Ni-Cr Alloys	125
6.1. Introduction.....	125
6.2. Methods.....	128

6.3. Results.....	129
6.3.1. Oxidation of Low-Cr Alloy: Ni5Cr.....	130
6.3.2. Oxidation of a Nominal NiCr alloy – Ni-14Cr.....	136
6.3.3. Oxidation of High-Cr Alloys.....	142
6.4. Discussion.....	144
6.5. Future Directions	148
References	150
7. Oxidation of Ni-Cr-Mo Alloys: Probing the Effect of Mo Addition	153
7.1. Introduction.....	153
7.2. Methods.....	154
7.3. Results and Discussion.....	154
7.3.1. Topography Evolution (0-130 L Oxidation).....	154
7.3.2. Evolution of Electronic Structure.....	158
7.4. Summary.....	164
7.5. Future Work.....	166
References	167
8. Ambient Pressure Photoelectron Spectroscopy Study of Oxidation of NiCr Alloys	168
8.1. Motivation	168
8.2. Merits of our Approach.....	169
8.3. Methods.....	169
8.4. Results.....	170
8.4.1. Sample Cleaning Strategies.....	170
8.4.2. Ni-5Cr Oxidation.....	171
8.5. Summary and Future Work.....	174
References	176
9. AFM Characterization of Electrochemically Oxidized Ni-Cr and Ni-Cr-Mo Alloys.....	177
9.2. Methods.....	178
9.3. Results.....	179
9.3.1. Chloride versus Sulfate Oxidation.....	179
9.4. Future Work	180
10. Concluding Remarks.....	182
11. Co Adsorption on Si(100) and its Interaction with Mn Wires.....	188
11.1. Introduction.....	188

11.2. Experimental Section	191
11.3. Results and Discussion	192
11.3.1. Co on Si(100)-2×1	192
11.3.2. Sequential deposition of Mn and Co	202
11.3.3. Co-deposition of Co and Mn:	207
11.4. Conclusions	209
References	211
12. 3D Nanostructures on Ge/Si(100) Wetting Layers: Hillocks and Pre-Quantum Dots	213
12.1. Introduction	213
12.2. Experimental section	214
12.3. Results	215
12.4. Discussion	228
12.5. Conclusion	231
References	233

LIST OF FIGURES

Figure 2-1. Potential energy diagram for physisorption and chemisorption. ²¹	31
Figure 2-2. Adsorbate overlayer structures on an FCC (001) surface ²⁵ : p(2×2) and c(2×2) structure with adsorption on four-fold hollow site.....	34
Figure 2-3. Ni(001) surface after 100 L oxygen exposure at 370 K showing the reorganization of step edges after c(2×2) structure is formed. ³¹ Oxide structures are visible at the step edges along with spherical sub-oxide particles nucleating on the flat terrace region.....	35
Figure 2-4. Processes that occur during the initial stages of oxidation of Ni(001) as developed by Holloway et al. ^{28,29} This model applied to a majority of other metal oxidation reactions. ^{21,42,45}	38
Figure 2-5. Possible reaction paths for oxidation after the establishment of a continuous barrier oxide layer between metal and gaseous atmosphere. ²¹	40
Figure 2-6. Oxide growth rate of hypothetical p-type NiO as a function of film thickness calculated using Cabrera and Mott ($X < X_1$) and Wagner equations ($X > X_1$). ⁴⁷	42
Figure 2-7. Ball and stick models of crystal structures of Cr ₂ O ₃ , NiCr ₂ O ₄ and NiO.....	43
Figure 2-8. The three equilibrium film growth modes classified by Bauer: (a) Frank-van der Merwe or layer-by-layer growth, (b) Volmer-Weber growth, and (c) Stranski-Krastanov growth mode. ⁶⁸ ..	45
Figure 3-1. Schematic of the UHV system used: (1) VT-STM, (2) MULTIPROBE analysis chamber, (3) Manipulator containing the sample heating assembly, (4) pockets for deposition sources, and (5) leak valve for introduction of gases.....	53
Figure 3-2. Principle of Electron Tunneling through a potential barrier between sample and tip separated by distance 's' and biased by voltage V lower than work functions, Φ_1 and Φ_2 . ³	56
Figure 3-3. Schematic STS spectra illustrating the two approaches used to calculate bandgap in the MATLAB code. In method-I, a cut-off is defined corresponding to zero (or very low) density of states while method-II is based on the valence and conductance band edge (HOMO-LUMO gap).	58
Figure 3-4. Three step model to explain a typical photoelectron spectroscopy experiment. ¹²	61
Figure 3-5. Universal curve for inelastic electron mean free path (λ) of an electron in a solid. ¹²	62
Figure 3-6. AFM images during different stages of MgO pre-treatment: (a) as-received, (b) after H ₃ PO ₄ etch, (c) post-1200 °C annealing in air, and (d) after second acid etch and 1100 °C anneal. The inset in (c) is a 10×10 μm^2 area showing the distribution of Ca spires throughout the surface. Scale bar in all images is 1 μm	66
Figure 3-7. Atomic force microscopy (AFM) images of MgO substrate after (a) T1 and (b) T2 pre-treatments. Scale bar is 500 nm.	68
Figure 3-8. Filled states STM image of Si(100)-2x1 surface: (a) high quality surface with low defect concentration, and (b) highly defective surface unsuitable for experiment. The images are recorded at -1.5 V, 0.03 nA and scale bar is 15 nm.	69
Figure 3-9. STM image of Ni-10Cr-6Mo surface after 30 L oxidation: (a) raw image, (b) plane level, (c) linear background subtraction only and (d) plane level and linear background. Scale bar is 20	

nm. The black arrows in (b-d) indicate incorrect background subtraction due to height variations. (e) Height profiles across oxide marked by green line in (d) after the above background subtraction.	72
Figure 3-10. STM image of Ni-14Cr alloy after 30 L oxidation: (a) leveled, (b) islands marked by threshold, (c) binary mask extracted from the image.	74
Figure 3-11. Comparison of oxide island masking on 30 L oxidized Ni-14Cr surface: (a) STM image, (b) mask obtained with segmentation code implemented in MATLAB, (c) mask extracted using thresholding and manual correction in Gwyddion. (d) Oxide area distribution from both the methods shows that the automated route is somewhat better at counting small islands. However, the error for $<5 \text{ nm}^2$ is still significant due to challenges in island separation.	75
Figure 3-12. Representative STS curve of oxide-like, metal-like and intermediate species sorted using the cut-offs described in section 3.5.2.2 on an oxidized NiCrAl alloy surface.	77
Figure 3-13. Snapshot of the GUI-enabled implementation of the MATLAB code for the analysis of grid spectroscopy data. An oxide that is selected for subsequent analysis in the bandgap map is marked by red crosses.	78
Figure 4-1. AFM images of MgO substrates after (a) T1 and (b) T2 pre-treatments (scale bar is 500 nm). STM images of Ni thin film grown on (c) T1 and (d) T2 substrates using the G1 growth recipe (scale bar is 50 nm). False color scale in AFM images is in nm.	86
Figure 4-2. STM and AFM images show the effect of growth temperature on the Ni thin film morphology. STM images after (a) deposition at 100 °C (step 1 of the G1) and (b) post-deposition annealing at 300 °C for 2 hours (step 2 of G1) – same deposition as shown in Figure 1(d); scale bar is 50 nm. Ex-situ AFM images of Ni film grown using (c) G1 and (d) G2 growth conditions; scale bar is 1 μm . Color scale is in nm.	89
Figure 4-3. STM image of Ni13Cr alloy thin film showing the effect of growth temperature on surface morphology: (a) (G1,T1) conditions and (b) (G2,T2) conditions. Scale bar is 50 nm. (c) Terrace width distribution of Ni-13Cr thin film grown using G1 and G2 conditions.	90
Figure 4-4. STM and AFM images of alloy thin films showing the effect of Cr addition on surface morphology: (a,d) Ni-5Cr, (b,e) Ni-14Cr and (c,f) Ni-33Cr films grown on T2 substrates using G2 growth recipe. Scale in STM and AFM images is 50 nm and 1 μm respectively. The derivative STM image (current image) is shown in (a) due to large height variations in the image; the inset shows the topographic image.	92
Figure 4-5. Large-area STM images of the Cr thin film grown on MgO(001): (a) as-deposited at room temperature, and (b) post-deposition anneal at 550 °C for 2 hours. Scale bar is 100 nm. High resolution images of the surface after 550 °C anneal showing (a) the atomic rows of the Cr film along $<110>$, and (b) small pockets of trace adsorbate-induced reconstruction on an otherwise clean surface. Scale bar is 10 nm in (c) and (d).	93
Figure 4-6. ToF-SIMS data of the Ni13Cr sample grown on T2-MgO indicating uniform film composition and no segregation at the film-substrate interface.	94

Figure 4-7. Variation of island heights in alloy thin films as a function of Cr concentration. The island heights are measured from AFM images except for the Ni-33Cr sample where STM images are used as the individual islands are not distinguished in AFM images.....	96
Figure 5-1. Variation of tip character during grid spectroscopy: the region when nanoscale features are imaged corresponds to good quality spectra (pink curve) while the featureless region in the upper portion of the image corresponds to noisy spectra (black curve).....	107
Figure 5-2. Contrast changes in the conductance maps due to changes in tip termination: (a,b) W-terminated tip when regions near the step edge appear more conductive, (c,d) likely O-termination at the tip resulting in contrast reversal.....	108
Figure 5-3. Sequence of STM images of the Ni surface showing the changes on the surface during oxidation at 300 °C: (a) as-deposited film, (b) 2 L, (c) 7 L, (d) 30 L, and (e) 80 L. The arrows indicate the <100> direction. Scale bar is 50 nm in all images.	110
Figure 5-4. High resolution images of the stacked pyramid structures observed on the Ni(001) surfaces after (a) 30 L and (b,c) 80 L oxidation. Derivative image of (b) is shown in (c) for better contrast. Scale bar is 50 nm in (a) and 20 nm in (b,c). Blue arrows are pointers marking the orientation of the step edges.	112
Figure 5-5. (a) Scanning tunneling spectroscopy curves after 0, 2, 7, 30 and 180 L oxidation at 300 °C, (b) STM image section of c(2×2)-O/Ni surface (scale is 10 nm), (c) corresponding (dI/dV)/(I/V) map showing the difference in electronic structure on terrace and at step edge. The map is sliced at -0.1 V where contrast between terrace and step edge is maximum. Single and double steps are marked with solid and dotted arrows respectively. (d) Averaged STS curves from the surface and from the step edges after 30 L oxidation. Pink arrows point to the distinct signature of c(2×2) layer.	114
Figure 5-6. STM and STS data of a Ni surface after 200 L oxidation (in 1×10^{-7} mbar of O ₂) at room temperature: (a) STM image of the surface showing the presence of small oxide particles; the imaging conditions are 2 V, 0.1 nA and scale bar is 50 nm, (b) bandgap map measured in the area marked by the pink square in (a); the ellipse and arrow in the image correspond to the same regions in the bandgap map; the color scale is from 0 to 2 eV, (c) distribution of bandgap on the surface populated from the bandgap map.	116
Figure 5-7. Scanning tunneling microscopy images of the Ni(001) surface after 200 L oxidation at room temperature and 450 °C anneal recorded at (a) 4 V, 0.1 nA, (b) 3 V, 0.1 nA, and (c) 2V, 0.1 nA; scale bar is 50 nm in all images. (d) Height profiles of oxide islands as a function of bias voltage. The arrows in (a) and (b) point to the same oxide islands and the 2V image in (c) is from a different region on the sample.....	118
Figure 5-8. (a) STM image of the Ni(001) surface after 200 L oxidation at room temperature and 450 °C anneal; scale bar is 25 nm, (b) bandgap map of the image shown in (a); color scale is 0 to 2 eV, and (c) STS curves recorded from the chemisorbed surface and nickel oxide structures.	120
Figure 6-1. Current status of the literature on the initial stages of oxidation of Ni-Cr alloys. The plot does not include the partial pressure of oxygen used in the study which is another parameter that affects the oxidation products.....	127

Figure 6-2. Plot of alloy composition and oxygen exposures used in this study. The minimum amount of oxygen required for >75% oxide coverage during oxidation at 300 °C is marked. Pure Cr was oxidized at 200 °C to avoid formation of a thick oxide layer that cannot be measured with STM.

..... 130

Figure 6-3. STM images of Ni-5Cr surface with different amounts of oxygen exposure: (a) 7 L, (b) 30 L, (c) 80 L, and (d) 130 L. Scale bar in (a-c) is 25 nm and is 50 nm in (d). The derivative image is shown in (d) due to large height variations. All images are recorded at 2 V and 0.1 nA. (e) Oxide coverage evolution during oxidation. 131

Figure 6-4. Evolution of (a) oxide height, (b) oxide area and (c) number density (per 100 nm²) during oxidation of Ni-5Cr alloy at 300 °C. 134

Figure 6-5. Scanning tunneling spectroscopy data during Ni-5Cr oxidation: (a) topography image after 30 L, (b) corresponding bandgap map; color scale is 0 eV (blue) to 1 eV (red), and (c) Bandgap distribution as a function of oxidation progression..... 136

Figure 6-6. STM images of Ni-14Cr alloy after (a,b) 30 L and (c,d) 80 L oxidation at 300 °C. Scale bar is 25 nm. White arrows point to opposing oxide growth interfaces that have coalesced. Large oxides having a different surface structure compared to the flatter oxides are seen in (c)..... 138

Figure 6-7. STS data recorded on Ni-14Cr alloy after 30 L oxidation at 300 °C showing (a) the STM topography image with the corresponding (b) bandgap map. The scale bar in STM image is 25 nm and the color scale in the bandgap map is 0 eV (blue) to 2 eV (red). (c) The variation of oxide gap as a function of oxide dimensions is shown on the oxides after 30 and 80 L. The arrows in (b) indicate oxides of different height exhibiting different bandgap..... 140

Figure 6-8. Bandgap distribution of Ni-14Cr surface after 7, 30 and 80 L oxidation at 300 °C. 142

Figure 6-9. (a) STM image of Ni-33Cr thin film after 11.5 L oxidation at 300 °C with over 75% oxide coverage, (b) corresponding bandgap map indicating an average gap of 0.6 eV, and (c) Cr thin film after 10 L oxidation at 200 °C presenting a near-continuous oxide layer. 143

Figure 6-10. The variation of oxide surface coverage is shown as a function of oxygen exposure for the three Ni-Cr alloys that are studied in this work..... 145

Figure 6-11. Schematic reaction model during the very initial stages of oxidation of Ni-Cr alloys. 147

Figure 7-1. STM images of Ni-10Cr-6Mo surface after (a) 0 L, (b) 7 L, (c) 30 L, (d) 80 L, and (e) 130 L oxidation recorded at 2 V, 0.1 nA. Inset in (e) shows a large oxide structure observed after 50 nm. Scale bar is 50 nm in all images. Black and white arrows in (b) point to oxide islands that assemble into 1D chains and lattices respectively(f) Plot of oxide coverage as a function of oxygen exposure captures the surface evolution and shows a parabolic trend. 156

Figure 7-2. (a) Oxide height distributions after 7-80 L oxidation, (b) Correlated area versus height indicating the existence of a critical height above which vertical growth does not occur. The oxide dimensions are obtained from images recorded at 2.0 V. 157

Figure 7-3. STM images of Ni-10Cr-6Mo surface after 7 L oxidation at 300 C recorded at different bias voltages: (a) 0.15 V, (b) 2.0 V, (c) 0.15 V, (d) 1.0 V and (e) 2.0 V. Feedback current is constant at 0.1 nA. Scale bar is 50 nm in (a,b) and 5 nm in (c-e). 159

Figure 7-4. Oxide height distribution as a function of bias voltage. Feedback current is 0.1 nA.	160
Figure 7-5. STM image of 30 L oxidized Ni-10Cr-6Mo surface recorded at (a) 0.15 V and (b) 2.0 V illustrating the different contrast mechanisms; scale bar is 50 nm. Oxides in (a) which completely disappear, appear as streaks or appear as flatter islands are marked by black, white and blue arrows respectively. (c) Representative height profile across the oxide marked with pink and red lines in both images quantifies the contrast variation observed as a function of bias voltage.....	161
Figure 7-6. Scanning tunneling spectroscopy data from Ni-10Cr-6Mo surface: (a,b) topography image after 30 L oxidation with corresponding bandgap map; color scale of map is 0-1 eV, (c) STS spectra obtained from oxide and metal region marked in (a), (d) Bandgap distribution on the surface after 30, 80 and 130 L oxidation of alloy.....	163
Figure 7-7. Variation of oxide bandgap as a function of height for Ni-10Cr-6Mo and Ni-14Cr alloys.	164
Figure 7-8. Variation of oxide coverage on Ni-Cr and Ni-Cr-Mo alloys during oxidation at 300 °C.	165
Figure 8-1. Experimental protocol followed in the PES-oxidation experiments on the Ni-5Cr alloy. The base pressure of the chamber is $<1.5 \times 10^{-8}$ torr.....	171
Figure 8-2. High resolution Ni 2p spectra at various stages of Ni-5Cr oxidation recorded using a photon energy of 1120 eV. The purple and orange dotted lines correspond to the Ni-metal and NiO positions respectively.2,3.....	172
Figure 8-3. High resolution Cr2p spectra on a thermally oxidized Ni-5Cr alloy as a function of incident photon energy for the 473 K oxidation step. The purple and orange dotted lines correspond to the Cr-metal and Cr ₂ O ₃ positions respectively. ^{4,5,13,14}	174
Figure 9-1. The evolution of the Ni ₂₂ Cr surface during oxidation in chloride and sulfate solution is shown along with the variation of oxide film thickness measured by impedance spectroscopy.	180
Figure 9-2. AFM images of Ni ₂₂ Cr sample after electrochemical corrosion at pH=4 for (a) 100 s in Cl ⁻ , (b) 10 ⁴ s in Cl ⁻ , and (c) 5000 s in SO ₄ ²⁻	180
Figure 9-3. AFM images of {514} grain on Ni ₁₁ Cr alloy (a) before and (b) after electrochemical oxidation in chloride solution.	181
Figure 11-1. STM images (-1.5 V, 0.03 nA) of (a) pristine Si(100)-2×1 surface, and (b) Si surface after deposition of 0.054 ML of Co. The circle and square in (b) mark an A-type defect (single missing dimer) and a B-type defect (two adjacent dimers missing). (C) summarizes the overall defect concentration in % of surface occupied by defects as a function of Co-concentration.	194
Figure 11-2. (a) Line scans across an A-type and a B-type defect on a pristine Si surface are shown. (b) shows the depth distribution of A-type and B-type defects before and after Co deposition.....	195
Figure 11-3. Ball and stick model of the adsorption sites of Co on the Si(100)-2x1 surface reconstruction. The adsorption sites are named as following: Surface site: P – Symmetric Pedestal Site; Subsurface sites: U _D – Under dimer site, U _H – Site under high site of Si-surface dimer, U _L – Site under low site of Si-surface dimer, DV – Dimer vacancy site. The ball and stick model of adsorption sites and the site nomenclature were adapted from Refs. ^{19,20}	197

Figure 11-4. Higher resolution STM image (-1.5 V, 0.03 nA) of an individual Si terrace after Co deposition. The circles in the image indicate Co occupying the asymmetric UH/UL site and the square indicates Co adsorbed at symmetric UD site.....	199
Figure 11-5. Percentage of Co in UD and UH/UL sites as a function of Co coverage.....	200
Figure 11-6. STM images after (a) deposition of 0.23 ML of Mn, and (b) deposition of 0.06 ML of Co on the same surface; (i) and (ii) in part-(b) are empty and filled states image of the same area. Part (c) shows image segments illustrating a kink (i) and protrusion (ii) along a Mn wire with corresponding line scans. The inset in (a) shows a representative wire-structure (scale bar is 3 nm). Empty and filled states images are recorded at +1.5 V and -1.5 V at feedback current of 0.03 nA..	203
Figure 11-7. Wire length distribution before and after Co deposition which indicates a greater number of Mn dimers and ultrashort wires after the deposition of Co.	205
Figure 11-8. STM images of the Si surface after co-deposition of 0.3 ML of Mn and 0.06 ML of Co - the blue squares marks identical image segments offset by a slight drift between the images: (a) empty states image recorded at +1.5 V, 0.03 nA, (b) filled states image recorded at -1.5 V, 0.03 nA; (c) shows the wire length distribution for the same experiment.....	208
Figure 12-1. (a) 3D parameter space map of all the samples prepared in the current work. The parameters that yield hillocks and p-QDs (pre-quantum dots) are color coded as green and violet respectively. The red circle in (a) is the reference QD sample. Each symbol in the map represents a sequential annealing experiment and is summarized in Table I.	216
Figure 12-2. Evolution of S[1.2] when annealed at (a) 405 °C for 1 hour and the inset shows the as deposited surface (at 360 °C) with the same magnification, (b) 460 °C for 45 minutes, (c) 540 °C for 1 hour, and (d) 540 °C for 7.5 hours. Scale bar is 15 nm. Black arrows in (b), (c) and (d) point to DVLS on the surface.	218
Figure 12-3. Evolution of 3.3 ML thick Ge wetting layer: (a) as deposited at 570 °C and after annealing at 540 °C for (b) 1 hour and (c) 7 hours. Partially and fully formed {105} facets on p-QDs are seen in (b) and (c).....	220
Figure 12-4. High resolution STM images of pre-quantum dots (p-QDs) and conventional quantum dots: (a) and (b) show images of p-QD from S[3.5], filled states, and S[3.3], empty states. (c) and (d) show empty and filled states images of conventional QDs from S _{ref} . The reconstructed {105} surface is clearly visible and consistent with literature. ⁴⁻⁶ Empty states images were recorded at +2.0 V, 0.1 nA and the filled states images were recorded at -2.0 V, 0.1 nA.....	221
Figure 12-5. (a) Distribution of facet angles as a function of WL thickness with representative STM images of the structures obtained from S[1.2] (inset-1), S[2.1] (inset-2) and S[3.3] (inset-3). (b) WL thickness-annealing temperature map showing the minimum WL thickness and temperature required to nucleate hillocks and p-QDs. The error in our measurements is indicated for the data point corresponding to S[1.2].	223
Figure 12-6. (a) Island volume and number density of hillocks and p-QDs as a function of Ge WL thickness. (b) Scatter plot of lateral dimensions of all hillocks, p-QDs, and the reference QD sample. The number in parenthesis refers to the wetting layer thickness.	225

Figure 12-7. The evolution of (a) hillocks (from sample S[1.6]) and (b) p-QDs (from sample S[3.3]) with sequential annealing steps after Ge wetting layer deposition. The hillocks are, on average, larger than the corresponding p-QDs and also show increasing lateral dimension with multiple annealing steps. The size and shape distribution for all QDs are included in Figure 12-6..... 227

LIST OF TABLES

Table 1-I. Important NiCrMo Alloys currently used in various applications.....	25
Table 2-I. Physical properties of the oxides expected to form in the Ni-Cr system during oxidation.	43
Table 4-I. Sample Index showing the composition of thin films grown and the corresponding substrate pre-treatment and growth conditions.....	85
Table 5-I. Various structures observed after each oxidation step on Ni(001).....	121
Table 11-I. Summary of Mn and Co coverage for sequential deposition experiments, capture zone area as percent of total surface area [definition of capture zone CZ is given in Figure 3], and density of Co-atoms in the CZ and on the free surface - not touching any Mn wire. The last column gives the ratio of Co-atoms in the CZ compared to the FS.	207
Table 12-I. Sample index with corresponding wetting layer growth temperature and annealing temperatures used in this work.	217

Overview

The overarching theme of this dissertation is the study of the nucleation and growth of surface nanostructures primarily using scanning tunneling microscopy and spectroscopy (STM/STS). Scanning probe microscopy is a powerful characterization tool that has been used in this work to characterize the atomic and electronic structure of surfaces during controlled chemical reactions. This dissertation is partitioned into two parts. In Part – I, my work on understanding the initial stages of oxidation of Ni-Cr alloys is presented while Part – II deals with nanostructure growth on Si(001) surfaces.

Part – I:

The motivation of the Ni-Cr alloy oxidation work and the fundamental questions that form the basis for our experimental approach is outlined in Chapter 1. A brief introduction to the various aspects of surface science as it applies to the oxidation studies is presented in Chapter 2 and the working principle of all the instrumentation used in this work is described in Chapter 3. The subsequent chapters discuss the results of my work beginning, in Chapter 4, with optimization experiments to establish a recipe for the growth of smooth alloy thin films that can be used as a substrate for studying oxidation reaction. A prerequisite to understanding the effect of Cr addition on the initial stages of oxidation of Ni-Cr alloys is to probe the oxidation of pure Ni under similar conditions. Results of the oxidation studies on pure Ni are discussed in Chapter 5 and gaps in current literature are addressed along with information on the STS signature of an O-chemisorbed Ni surface. In Chapter 6, STM/STS data that capture the evolution of the atomic and electronic structure of the $\text{Ni}_{1-x}\text{Cr}_x$ alloy ($5 \leq x \leq 35$ wt.%) during oxidation at 300 °C are presented.

Understanding Ni-Cr and Ni-Cr-Mo alloy oxidation is a long-term project and work initiated during the course of this dissertation which will form the basis for future experiments are discussed in Chapters 7-9. Initial results of oxidation experiments performed on ternary Ni-Cr-Mo alloys are presented in Chapter 7 and the differences in initial stages of oxidation between Ni-Cr and Ni-Cr-Mo alloys are addressed. This work is an extension of the binary alloy oxidation and demonstrates that the current experimental framework can be used to evaluate the effect of minor alloying elements on the initial stages of oxidation (atomic and electronic structure).

In addition to the UHV experiments, work has also been initiated to understand the initial stages of oxidation of Ni-Cr and Ni-Cr-Mo alloys as a function of oxygen pressure. Ambient pressure photoelectron spectroscopy experiments are performed during oxidation of bulk Ni-Cr alloys to address the “pressure gap” between the ultrahigh vacuum STM work and ambient operating conditions of NiCr-based components. The goal of these experiments is to identify the oxidation products that are formed at 100-500 °C and compare them to the UHV-XPS experiments that will be performed in the future.

In addition to dry oxidation, the surface structure of bulk Ni-Cr and Ni-Cr-Mo alloys is characterized after electrochemical passivation. The electrochemical response of the Ni-Cr and Ni-Cr-Mo alloys is an important question due to the effect of Mo in improving the resistance to localized corrosion. We aim to understand the changes in oxidation behavior (in solution) with and without the presence of Mo and its effect on the surface morphology of the oxide. The effect of solution chemistry, grain orientation and grain boundaries on the oxide layer morphology will be investigated and initial results are shown in Chapter 9. The

surface structure of the oxides obtained in this work will be combined with transmission electron microscopy and atom probe tomography data to provide a more complete picture of the electrochemically grown oxide structure.

Part – II:

This part pertains to the study of nanostructures growth on silicon surfaces. In Chapter 10, the adsorption of Co on a pristine Si(100)-2×1 surface and a Mn wire-decorated Si surface is presented along with a discussion of surface alloying of Co and Mn. In the next chapter, the annealing-induced formation of hitherto unobserved three-dimensional structures on elastically strained Ge/Si(100) wetting layers is presented. The formation of different 3D structures depends on the stored misfit strain energy in the system and various stability regimes are discussed. Each chapter/project in Part-II is self-sufficient and it consists of, in addition to the results and discussion, an introduction specific to the topic, important conclusions and directions for future work.

PART – I

1. Opportunities and Challenges

Corrosion is the degradation of a material, often accompanied by deterioration in its properties, as a result of chemical reaction with its environment.¹ The effects of corrosion are ubiquitous and range from degradation and damage to personal electronic appliances and automobiles, communal infrastructure such as highway bridges and airplanes to sensitive industries such as defense warships and nuclear reactors. The direct cost of metallic corrosion to the U.S. economy was estimated in 1998 to be \$276 billion annually or 3.1% of the gross domestic product.² This does not include auxiliary costs such as lost productivity, potential litigation costs, health hazards and, in the case of damage to defense equipment, readiness of the military to meet the country's needs. In 2010, the Department of Defense estimated its corrosion cost to be over \$23 billion.³ Therefore, there is a strong financial and societal motivation to better understand corrosion mechanisms and limit the resulting damage through careful material selection and design.

The causes of corrosion and mitigation strategies to slow or prevent corrosion have been pursued for a long time but many questions about the fundamental processes in corrosion remain open. This research into the fundamental processes of corrosion and the underlying mechanisms has the potential to advance the development of new and more effective methods to reduce the impact of corrosion. A strong link between fundamental research at the atomistic level and engineering research is critical to advance new strategies for corrosion control.⁴ For example, it is known that surface and the near-surface region (selvedge region) of an alloy play a critical role in the oxidation (corrosion) behavior of the component but the effect of atomistic processes during the initial stages of corrosion

and the macroscopic corrosion resistance is not well understood. Similarly, the effects of minor alloying elements in improving the corrosion resistance of high performance, multi-component alloys are known but not well understood at a mechanistic level. A small concentration of an alloying element can result in a drastic improvement in corrosion resistance but the exact amount of alloying was achieved usually by trial and error. A classic example is the effect of Mo addition in Ni-Cr alloys: while Mo addition drastically improves localized corrosion resistance, the changes induced by Mo addition on the atomic and electronic structure of the surface/selvedge region are not fully understood.^{5,6}

Ni-Cr and Ni-Cr-Mo alloys are corrosion-resistant alloys of technical interest to the Department of Defense and is the material system investigated in this dissertation. Ni-Cr alloys exhibit good oxidation resistance due to the presence of Cr ($\approx >13\text{wt.}\%$) which enables the formation of an adherent Cr_2O_3 passive layer to protect the underlying metal from further degradation. In electrochemical corrosion conditions, the formation of passive oxide layer results in low corrosion rates and the passive current density decreases with increasing Cr content of the alloy.^{7,8} These superalloys are used in highly corrosive, aqueous environments in the nuclear fuel industry, petrochemical industry and marine applications due to their excellent corrosion resistance.^{9,10} They are also used in high temperature applications such as turbine blades and as structural components in energy industry due to the combination of good mechanical stability and corrosion resistance. The breadth of corrosion and mechanical properties of these alloys is due to the high solubility of alloying elements in Ni (solid solution regime). Table 1-1 lists the important Ni-Cr-based alloys that are currently used in various applications.

Table 1-I. Important NiCrMo Alloys currently used in various applications.

Alloy	Ni	Cr	Mo	Fe	Other
Alloy 22	56.0	22.0	13.0	3.0	W, C, Si
Alloy 625	≥58	20 – 23	8 – 10	5.0	C, Si, Mn, Ti, Nb
Alloy 825	36 – 46	19.5 – 23.5	2.5 – 3.5	24 – 40	C, Si, Mn, Ti, Cu, Al
Hastelloy C-4	58 – 60	14 – 18	14 – 17	3.0	C, Si, Mn, Co, Ti
Hastelloy C-276	60 – 63	14.5 – 16.5	15 – 17	4 – 7	W, C, Si, Co, Mn, V

While the importance of these alloys and the effect of Cr on the oxidation resistance are well-established, changes caused by Cr addition on the atomic and electronic structure of the alloy as it relates to the oxidation response have not been studied. For example, it is known that a minimum of 10-15 wt.% Cr is necessary for the alloy to be passivating¹¹⁻¹³ but the factors that are responsible for this boundary condition are unknown. Some of the questions that motivate this dissertation work are:

- How does the amount of Cr affect the initial nucleation of oxides?
- Do the Cr atoms in the alloy act solely as a ‘getter’ for oxygen due to its high oxygen affinity or does the presence of Cr promote the reactivity of the neighboring Ni atoms?
- Is the minimum Cr content (10-15 wt.%) required for passivation due to the kinetic limitations of Cr transport to the interface?
- Is the minimum Cr limit a function of the operating pressure? Will lower O₂ pressure (and slower oxidation reaction) reduce the minimum Cr limit?
- How does Cr addition affect the initial stages of oxidation compared to pure Ni? Does the O-chemisorbed phase that is observed on pure Ni still form on an alloy surface?
- What is the effect of Cr content on the electronic structure (bandgap, density of states in the gap, Fermi level position) of the oxide? Does it affect the minimum Cr limit?

A nano- and meso-scale surface science investigation of the initial stages of oxidation will provide answers on the fundamental oxidation mechanism of these alloys. With the advancement of microscopic and spectroscopic techniques that can successfully probe at the atomic level, there is a unique opportunity for the surface science/nanoscale community and the corrosion community to collaborate and bridge the gap in the understanding of the effects of alloying elements at the atomic scale. Besides providing detailed insight on the initial stages of oxidation of an alloy, such collaborations will enable the relation of relevant atomistic processes during initial stages of oxidation to the observed macroscale oxidation/corrosion resistance and ultimately promises new approaches for tailoring materials systems with exceptional resistance to environmental degradation. The overarching goal of this work is to generate a knowledge base and mechanistic understanding of the initial stages of oxidation which can subsequently be extended to other similar alloy systems where the alloying element (Cr) is more reactive with oxygen than the parent metal (Ni).

Scanning tunneling microscopy (STM) is a powerful instrument which has been used in this work to study the surface structure during controlled corrosion reactions with atomic resolution as the ultimate limit.¹⁴⁻¹⁹ Ultrahigh vacuum (UHV) conditions are especially attractive for monitoring the initial stages of oxidation (corrosion) since it provides a clean environment where low doses of oxygen can be introduced to initiate oxidation on the alloy surface. Chemical reactions on alloy surfaces involve a high degree of complexity and a clean UHV environment allows us to decouple critical processes during the reaction and understand the mechanism of oxidation. An atomic scale study of corrosion reactions require the fabrication of well-defined surfaces: this is usually realized

either by use of single crystal materials or the in-situ growth of thin films. Thin films allow for a systematic variation of the alloy composition in a controlled manner and are ideal for the current work. Once a thin film of Ni-Cr alloy is grown, we image the alloy surface before oxidation and after small doses of oxidation to obtain information on the oxygen-chemisorbed structure, the transition from chemisorption to oxide formation, preferred nucleation sites of oxide clusters and growth characteristics of the oxide. In addition, scanning tunneling spectroscopy provides information on local density of states (LDOS) of the surface. This allows for identification of different oxide species on the surface based on differences in their bandgap value or any characteristic features in the LDOS such as the Fermi level position or surface states.

An UHV-STM study will, therefore, provide valuable information that will advance the current understanding of alloy corrosion and the role of minor alloying elements from the viewpoint of atomic structure, defect mediation, and electronic structure. The results of this work directly feed into theoretical work to develop oxidation models for this alloy system as a function of alloy composition, pressure, and temperature. These experiments, in combination with other experimental and theoretical approaches such as photoelectron spectroscopy, atom probe tomography, phase field modeling and molecular dynamics, will capture the mechanistics of the oxidation reaction on Ni-Cr alloys in the nano-, meso-, and micro-scale as a function of alloy composition, temperature and pressure.

References

1. Council, N. R. *Research Opportunities in Corrosion Science and Engineering*. (The National Academies Press, 2011).
2. Koch, G. H., Brongers, M. P. H., Thompson, N. G., Virmani, Y. P. & Payer, J. H. Corrosion cost and preventive strategies in the United States. *FHWA-RD-01-156* (2002).
3. Herzberg, E. F. The Impact of Corrosion on the Availability of DOD Weapon Systems and Infrastructure. (2009).
4. *Research Opportunities in Corrosion Science and Engineering*.
5. Lloyd, A. C., Noël, J. J., McIntyre, S. & Shoesmith, D. W. Cr, Mo and W alloying additions in Ni and their effect on passivity. *Electrochimica Acta* **49**, 3015–3027 (2004).
6. Bocher, F., Huang, R. & Scully, J. R. Prediction of Critical Crevice Potentials for Ni-Cr-Mo Alloys in Simulated Crevice Solutions as a Function of Molybdenum Content. *Corrosion* **66**, 55002–55002–15 (2010).
7. Bond, A. P. & Uhlig, H. H. Corrosion Behavior and Passivity of Nickel-Chromium and Cobalt-Chromium Alloys. *J. Electrochem. Soc.* **107**, 488–493 (1960).
8. Horvath, J. & Uhlig, H. H. Critical Potentials for Pitting Corrosion of Ni, Cr-Ni, Cr-Fe, and Related Stainless Steels. *J. Electrochem. Soc.* **115**, 791–795 (1968).
9. Pollock, T. M. & Tin, S. Nickel-Based Superalloys for Advanced Turbine Engines: Chemistry, Microstructure and Properties. *Journal of Propulsion and Power* **22**, 361–374 (2006).
10. Maurice, V. *et al.* Effects of molybdenum on the composition and nanoscale morphology of passivated austenitic stainless steel surfaces. *Faraday Discuss.* (2015). doi:10.1039/C4FD00231H
11. Wood, G. C. & Hodgkiess, T. Mechanism of Oxidation of Dilute Nickel–Chromium Alloys. *Nature* **211**, 1358–1361 (1966).
12. Wood, G. C. & Chattopadhyay, B. Transient oxidation of Ni-base alloys. *Corrosion Science* **10**, 471–480 (1970).
13. Chattopadhyay, B. & Wood, G. C. The transient oxidation of alloys. *Oxid Met* **2**, 373–399 (1970).
14. Meyer, E., Hug, H. J. & Bennewitz, R. *Scanning Probe Microscopy: The Lab on a Tip*. (Springer, 2004).
15. Kopatzki, E. & Behm, R. J. STM imaging and local order of oxygen adlayers on Ni(100). *Surface Science* **245**, 255–262 (1991).
16. Maurice, V., Cadot, S. & Marcus, P. XPS, LEED and STM study of thin oxide films formed on Cr(110). *Surface Science* **458**, 195–215 (2000).
17. Maurice, V., Yang, W. P. & Marcus, P. XPS and STM Study of Passive Films Formed on Fe-22Cr(110) Single-Crystal Surfaces. *J. Electrochem. Soc.* **143**, 1182–1200 (1996).
18. Sporn, M. *et al.* Anti-corrugation and nitrogen c(2 × 2) on Cr(100): STM on atomic scale and quantitative LEED. *Surface Science* **396**, 78–86 (1998).
19. Picone, A. *et al.* Atomic Scale Insights into the Early Stages of Metal Oxidation: A Scanning Tunneling Microscopy and Spectroscopy Study of Cobalt Oxidation. *J. Phys. Chem. C* **120**, 5233–5241 (2016).

2. Background

A significant amount of work has been done to study the oxidation behavior of NiCr-based alloys in the last 50 years due to its exceptional resistance to corrosion.¹⁻⁹ Historically, the studies were focused on Ni-20Cr alloys (nichrome) due to their use as heating elements.¹⁰⁻¹² The primary motivation was to understand the microstructure of the oxides and to develop strategies to improve the stability of the chromium sesquioxide through various minor alloying additions. Concurrently, NiCr-based alloys were found to be extremely resistant to corrosion in aqueous media which led to a large body of work on understanding the passivation of these alloys in various solutions.^{3,13-16} These alloys are susceptible to pitting corrosion in chloride media^{16,17} and it was found that adding small amounts of Mo and/or W improved the pitting resistance.^{2,14,18}

Despite the abundance of technical knowledge of the Ni-Cr alloy system, a number of fundamental questions on the initiation of oxidation still remain unanswered. Surface science experiments on these alloys systems can provide insight on the initial nucleation of the oxide and also capture the evolution from nucleation stage to the growth of a complete layer in terms of both atomic and electronic structure of the oxide. To the best of our knowledge, such a systematic research undertaking to gain insight on the initial stages of oxidation of Ni-Cr alloys as a function of Cr composition has not been pursued.

This chapter introduces the various stages involved in gas-metal interactions namely physical adsorption, chemisorption, solution (incorporation into metal lattice) and finally, bulk product formation. This background to the surface science aspects of chemical reactions is provided in general terms but the examples are predominantly of the

interaction of oxygen gas with the surface since oxidation of alloys is the main focus of this dissertation. Current literature on interaction of oxygen with Ni and Cr are reviewed in the relevant subsections with initial stages of oxygen interaction with Ni-Cr alloy included wherever available. Subsequently, the oxidation models developed by Cabrera-Mott and Wagner are introduced to link the current nanoscale work to the micro-scale oxide scales that are frequently the focus of existing literature. Since alloy thin films that are grown in ultrahigh vacuum (UHV) are used, the thermodynamic and kinetic considerations in epitaxial thin film growth are discussed. A more rigorous survey of literature on Ni and NiCr thin film growth and oxidation of these materials is tackled in the relevant chapters.

2.1. Chemical Reactions at Solid Surfaces

A solid surface will always exhibit altered reactivity compared to the bulk due to the breakdown in periodicity (fewer nearest neighbor atoms). As a result, when a gas molecule from the ambient atmosphere impinges on the surface of a metal, the surface atoms will interact and react with the molecule (or atom in case of dissociation). A typical gas-metal interaction involves the following stages: (a) physisorption, (b) molecular chemisorption, (c) atomic chemisorption (dissociative adsorption), and (d) formation of reaction product (oxides during oxidation reaction).^{19,20} Appropriate choice of experimental parameters and the measurement technique allows us to observe all or only some of the above stages. One of the advantages of a surface science experiment performed in UHV is that the kinetics of chemical reactions is sufficiently retarded for the observation of various elementary steps. When oxidation of metals/alloys is studied in an UHV system, the partial pressure of oxygen at a given temperature can be controlled so that the progression of oxidation

reaction is observable in real-time and important information on the oxygen-chemisorbed structure, minimum oxygen uptake required for oxide nucleation (incubation period) and preferential nucleation sites for oxides are obtained.

2.1.1. Physical Adsorption (Physisorption)

The physical adsorption of gases on the surface is a long-range interaction dominated by van der Waals forces due to the attraction between mutually induced dipoles of the electron cloud of gas molecule and surface. This process is non-activated and has a low heat of adsorption (ΔH_P). Curve I in Figure 2-1 represents the potential energy of a diatomic gas as it is attracted to the surface by long-range forces. Physisorption is not observed in typical room temperature microscopy and spectroscopy experiments due to the shallowness of the potential well. However, calorimetry experiments have been used to indirectly observe physisorption by tracking the changes in the heat of adsorption during continuous gas exposure.²¹

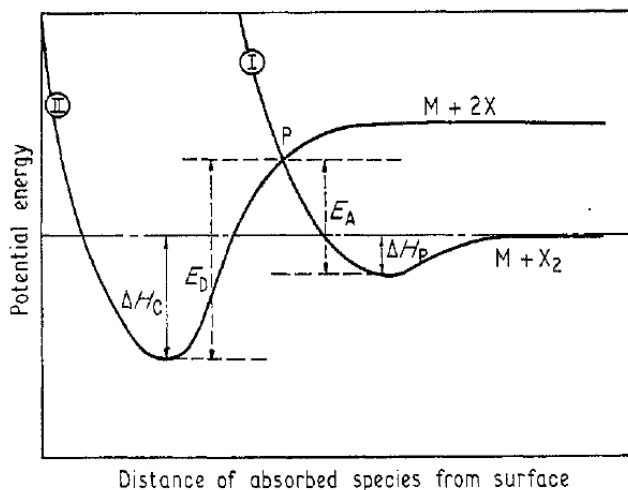


Figure 2-1. Potential energy diagram for physisorption and chemisorption.²¹

2.1.2. Chemical Adsorption (Chemisorption)

Chemisorption is a chemical reaction that involves a rearrangement of valence electrons of the metal and gas to form a chemical bond. When the gas molecule approaches the solid surface, the electron clouds begin to overlap and form a chemical bond. The gas molecule initially forms a bond with the metal surface which is followed by dissociative adsorption. The intersection of the physisorption and chemisorption curves in Figure 2-1 (at $P > 0$) suggests that there is an activation barrier that needs to be overcome for chemisorption. However, this is not always the case and if the intersection point were below zero, chemisorption becomes non-activated.¹⁹ It has been observed that oxygen undergoes dissociative adsorption with zero activation energy on most metal surfaces.²¹ An adsorbed molecule typically undergoes surface diffusion prior to dissociative adsorption. If a favorable crystallographic site is not found during this diffusion lifetime, the gas molecule may desorb from the surface.

The absolute coverage Θ of adsorbates is the ratio of density of adsorbed particles (n_a) to the density of surface atoms on the substrate (n_s), $\Theta = n_a/n_s$. Assuming each surface atom represents an adsorption site, saturation coverage ($\Theta = 1$) is rarely attained. Therefore, a relative coverage, $\delta = \Theta/\Theta_{\text{sat}}$, is introduced which, by definition, reaches 1 at saturation.¹⁹ Every particle that strikes the surface is only rarely adsorbed and in most cases, only a fraction, called the sticking fraction (s), is adsorbed. With increasing coverage, the sticking coefficient decreases i.e., the probability of finding a low energy site for adsorption decreases. A chemisorbed layer may be visualized as adsorbed atoms occupying the potential energy minima on the surface or it can be pictured as a reconstruction where the

surface layer contains both the metal atom and adsorbate. This distinction is not always clear and oxygen adsorption on Ni(001) causes displacement of the surface metal atoms and would strictly be required to be considered as reconstructive adsorption.²²⁻²⁴

Depending on the surface sites occupied, adsorbate overlayer structures such as $p(1\times1)$, $p(2\times2)$ and $c(2\times2)$ can be observed on metal surfaces. Schematic models of (2×2) structures are shown in Figure 2-2.²⁵ The adsorbate structure unit cell does not depend on whether the adsorption site is on the surface atom or on four-fold hollow site as shown in Figure 2-2(a,b) for the $p(2\times2)$ overlayer. Scientific interest in studying the chemisorption of oxygen and other gases on transition metals was primarily motivated by the use of Pt, Pd and Ni in heterogeneous catalysis. Various chemisorbed structures have been reported on most other metals and semiconductors.^{21,26,27} Historically, heats of adsorption were measured to identify physisorption and chemisorption during the initial stages of gas exposure. Other approaches such as work function measurements, ultraviolet photoemission spectroscopy (UPS) and LEED yield structural and electronic information. The capabilities of the STM lend itself to the characterization of the surface structures due to adsorption and a vast amount of work has been performed in this direction. In literature and this dissertation, gas exposures are expressed in units of Langmuir where $1\text{ L}=10^{-6}$ torr-s (a gas pressure of 1×10^{-6} torr for 1 s will completely cover the surface if each particle striking the surface is adsorbed).

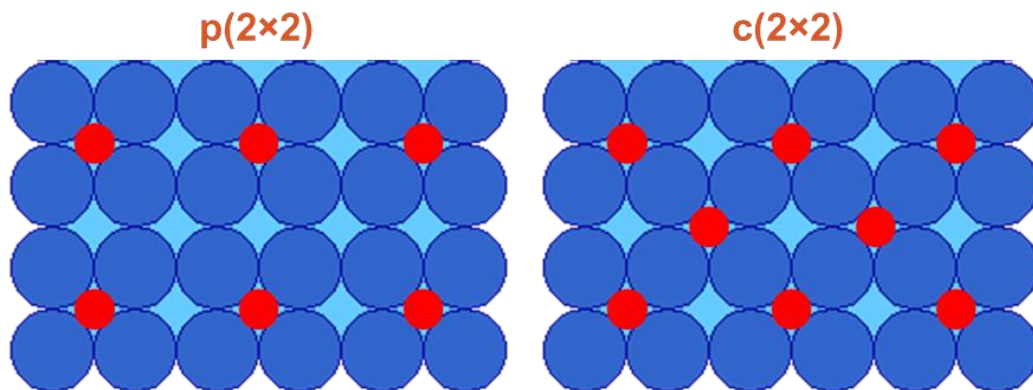


Figure 2-2. Adsorbate overlayer structures on an FCC (001) surface²⁵: p(2×2) and c(2×2) structure with adsorption on four-fold hollow site.

2.1.2.1. Chemisorption of oxygen on Ni(001)

Ni(001) presents p(2×2) and c(2×2) chemisorbed structures and the stability of these phases is dictated by oxygen exposures and temperature.^{22,28-36} The four-fold hollow site on Ni(001) is the most stable site for oxygen adsorption.³⁷⁻³⁹ Oxygen adsorbs on the Ni surface to form a p(2×2) overlayer during the first half monolayer of oxidation and transforms to a c(2×2) structure with prolonged exposure. Both adsorbate structures are found to increase the interlayer Ni-Ni spacing due to the attractive bond between O and Ni in the four-fold hollow site.^{23,24,40,41}

It has been found that the stability of the chemisorbed phases and the oxides on Ni surface strongly depends on the temperature.^{31,32,36} Oxide formation (amorphous) is favored at room temperature after small exposures (<30 L) while the c(2×2)-O/Ni(001) is more stable at 100-400 °C for exposures as high as 200 L. The incubation period before oxide formation on a c(2×2) surface increases with temperature with 100 L required to nucleate oxides at 300 °C and >300 L at 500 °C. The c(2×2) phase results in massive

reorientation of straight step-edges into mutually perpendicular segments at temperatures as low as 100 °C as shown by Koptazi and Behm³¹ in Figure 2-3 and in our results in section 5.3.1. Since the $c(2\times 2)$ -O/Ni(001) is associated with an increase in the interlayer Ni-Ni spacing, it decreases the barrier for penetration of oxygen atoms into the lattice. Oxygen incorporation in the subsurface layer can, therefore, create a configuration where Ni layer is sandwiched between two O-layers. This atomic arrangement is reminiscent of NiO(111) structure and likely represents the initial oxide nuclei that forms on the surface.^{30,32,36}

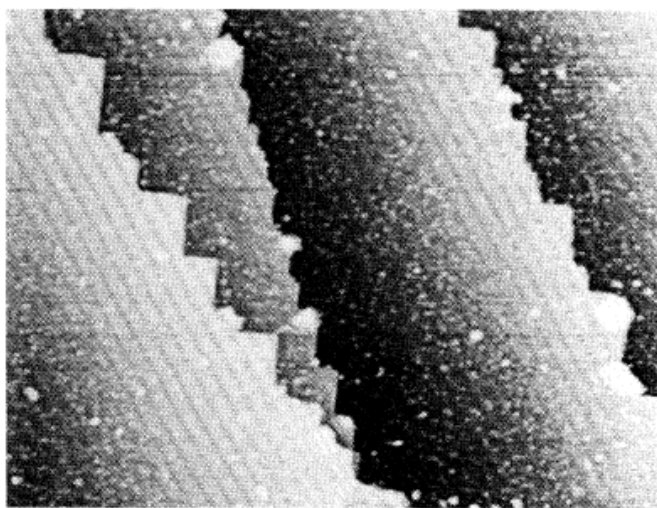


Figure 2-3. Ni(001) surface after 100 L oxygen exposure at 370 K showing the reorganization of step edges after $c(2\times 2)$ structure is formed.³¹ Oxide structures are visible at the step edges along with spherical sub-oxide particles nucleating on the flat terrace region.

2.1.3. Compound Formation – Nucleation and Growth

As discussed earlier, continued gas exposure leads to the adsorbate incorporation in the Ni metal lattice and forms layered or three-dimensional reaction products. Although metal-oxygen bond is formed during chemisorption, the bonds are not yet repeated in three dimensions to form a stable compound. The formation of the compound on the surface occurs by nucleation and growth on the surface. Nucleation is an activated process

and depends sensitively on pressure and temperature. In order to comment on the preferential nucleation sites, size of initial nuclei, and consolidate nucleation models, it is useful to perform experiments at low pressures so that the kinetics is sufficiently retarded. Step edges, which have a high dangling bond density, are frequently preferred nucleation sites if the adatom diffusion length is sufficient to reach the step edge. This nucleation and growth during Ni(001) oxidation was observed by Kopatzi et al.³¹ STM, XPS, LEED, AES and LEEM have been used to determine the preferential nucleation sites during a chemical reaction, the atomic structure and chemical configuration of reaction products, and surface and subsurface composition changes of a number of metals and alloys.

For most metals oxidized at low temperature and pressure, it has been found that the reaction with oxygen can be described by a sequence consisting initially of chemisorption, oxide nucleation at energetic sites followed by lateral growth to cover the surface and vertical growth (or oxide thickening).^{28,29,42} In practice, this sequence is not always distinct and lateral growth of oxide nuclei, agglomeration of oxides (resulting in grain boundaries), Ostwald ripening of nuclei as well as vertical growth may take place while new oxides are being nucleated on the surface. Some of the elemental processes that occur during the initial stages of oxidation are shown in Figure 2-4. In general, oxides will heterogeneously nucleate on the surface at high energy sites such as step edges, point defects or even dislocations that terminate on the surface. Therefore, the oxide growth rate during the initial stages of oxidation of metals and alloys at low temperatures and pressures depends sensitively on the surface morphology which controls the nucleation density. In addition, the crystallographic orientation also affects oxide nucleation and growth. In case of Ni, the sticking coefficient of oxygen depends on the crystallographic orientation with Ni(001)

showing slower oxygen uptake compared to Ni(111).^{29,43,44} Therefore, single crystal surfaces are ideal for oxidation studies where complexities due to the presence of grain orientation and grain boundaries are avoided.

Once the initial oxides are nucleated, continued oxidation will move the oxidation regime from a competing nucleation and growth process to a steady-state growth regime. A capture zone can then be defined around each oxide nucleus based on the diffusion constant (D_s) and activation energy for diffusion. Any oxygen that adsorbs within this capture zone will participate in the lateral growth of the oxide. When a saturation oxide density is reached such that the inter-oxide spacing is less than the capture zone, further nucleation is suppressed and lateral growth takes over. In the treatment by Holloway,²⁹ Orr and Fehlner,⁴² it was shown that the rate is limited by one of the three processes: (a) initial sticking on the surface, (b) diffusion of adsorbate on the surface, or (c) capture of adsorbate at the edges of existing oxide nuclei. Depending on the combination of temperature and oxygen pressure, one or more of the above processes can be rate controlling. At high temperatures and very low oxygen pressures, the sticking of oxygen on the metal surface could be rate limiting and the sticking coefficient of oxygen on the metal must be considered. Under typical experimental conditions when oxidation is performed in a continuous supply of oxygen, oxygen desorption from the surface is expected to be a small fraction of adsorbed molecules. In this case, the temperature-activated process of surface diffusion and incorporation into the oxide (growth of oxide) are the major controlling processes. The model shown in Figure 2-4 is a simplistic picture after oxides have nucleated on the surface and does not take into account the initial terrace and step edge structure that controls the initial nucleation of these oxide islands.

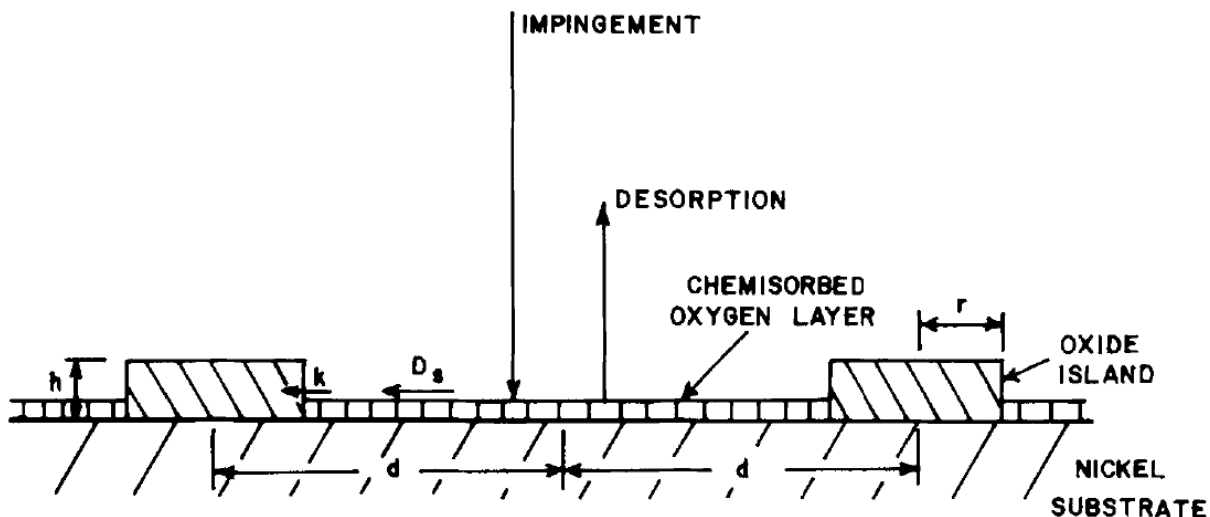


Figure 2-4. Processes that occur during the initial stages of oxidation of Ni(001) as developed by Holloway et al.^{28,29} This model applied to a majority of other metal oxidation reactions.^{21,42,45}

2.1.3.1. Factors Controlling Oxide Formation on Ni(001)

Oxide formation and stability on Ni strongly depends on the temperature.^{31,32,36} Oxide formation (amorphous) is favored at room temperatures after small exposures (<30 L) while more than 200 L is required for oxide formation at 200 °C. In a high resolution LEED-STM study, Bäumer et al.³⁶ discuss the role of surface defects in oxide formation and report preferential nucleation of NiO islands at the step edges of Ni(100) surface after exposures of 10 L of O₂ at room temperature. The behavior changes at higher temperatures and 200 L of oxygen is required³² to initiate oxide at 200 °C and it increases to over 500 L at 300 °C. This is consistent with our observations that NiO does not form after 200 L oxidation at 300 °C and after 1000 L oxidation at 500 °C. In contrast, Luo et al.⁴⁶ show that nickel oxides are formed on a Ni-10Cr alloy at 450 °C when exposed to 300 L at 450 °C. The observed NiO formation at 450 °C diverges, at first glance, from the findings of Wang et al.³² on Ni(001) where NiO formation was not detected at high temperatures for these low oxygen doses.

However, the oxygen pressures used in the two studies are different with higher oxygen pressures used by Luo et al.⁴⁶ possibly driving the formation of NiO at 450 °C at lower exposures than observed by Wang et al.³² This suggests a strong pressure-dependence, in addition to temperature, on the oxidation products formed on Ni and Ni-Cr alloys.

2.2. Oxide Film Growth

Once a thin, continuous oxide layer forms on a metal surface, the metal and gaseous reactants are separated by a physical barrier. Oxidation reaction can, therefore, only proceed if cations and/or anions and electrons can diffuse through the oxide layer. This charge transport builds up a potential between the oxide/gas interface and the oxide/metal interface and further growth of the oxide is described by transport through the film. The rate determining step in the growth of the oxide can be initial chemisorption process on the oxide surface, mass or charge transport through the oxide film or transport across one of the oxide/gas or oxide/metal interfaces. A schematic of the possible reaction paths for oxide film growth is shown in Figure 2-5.⁴⁷ A number of mechanisms such as quantum mechanical tunneling of electrons, cation diffusion in a space charge field, place exchange, and deactivation of surface for oxygen chemisorption with increasing oxide thickness were proposed to explain experimental observations. The growth of oxide films depends on the thickness regime and very thin films (<10 nm) have different processes governing the growth rate compared to films which are a few hundred nanometers thick. The growth of thicker films (>1 μm) are governed by a parabolic rate law postulated by Wagner in 1933 and it predates the theories postulated by Mott and Cabrera to explain oxide film growth in the initial stages (<10 nm).

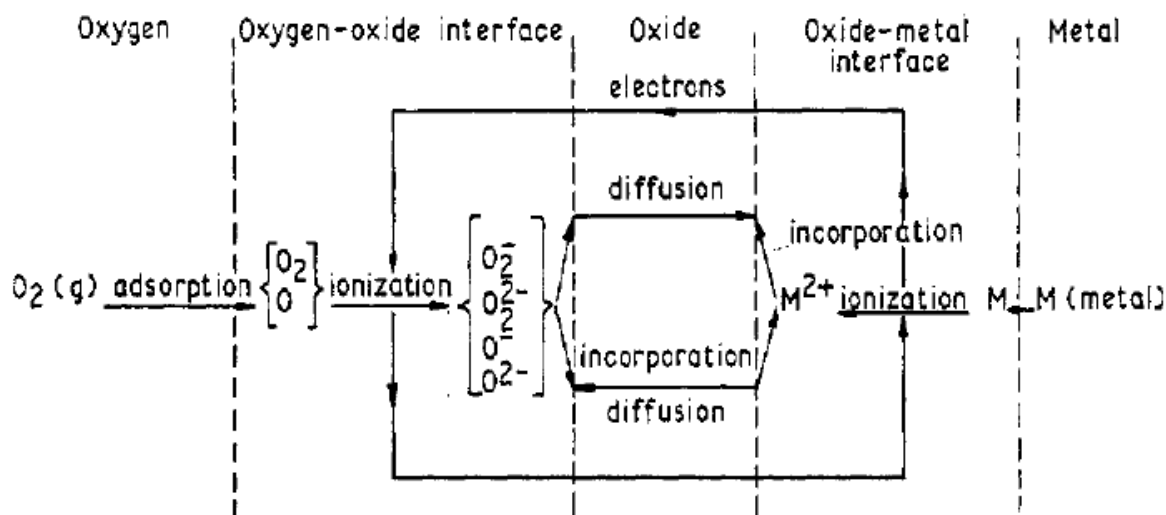


Figure 2-5. Possible reaction paths for oxidation after the establishment of a continuous barrier oxide layer between metal and gaseous atmosphere.²¹

2.2.1. Thin Oxide Films – Cabrera-Mott Theory

A number of theories were developed initially by Mott^{48,49} to explain the growth of ultra-thin protective oxide films based on the assumption of metal ion and electron transport across the oxide film. He suggested that for oxide films less than 50 Å, electrons transport across the oxide occurs by quantum mechanical tunneling. Therefore, the electron tunneling becomes the rate controlling step as the thickness of the oxide increases towards 50 Å and oxide growth can be explained by a logarithmic rate law. Based on tunneling phenomena, he posited that oxide growth is independent of temperature and growth terminates after 50 Å when the tunneling probability becomes zero. However, experimental evidence^{42,50,51} disproved this theory and no clear evidence for oxide growth rates limited by electron tunneling was found. Subsequently, Mott^{52,53} suggested that thermionic emission of electrons can occur which results in the formation of oxygen ions on the oxide surface. This ionic layer sets up an electric field in the oxide and promotes the

transport of metal ions (cations) to move through the oxide. The Mott oxidation model was further developed by Cabrera and Mott⁵⁴ who together derived the well-known Cabrera-Mott (C-M) theory for the growth of thin oxide films. In the C-M model, oxide growth is mediated by cation migration. For thin films, the electric field is very strong and facilitates fast diffusion of metal cations to promote continued growth of oxide. If every cation that is pulled across the oxide and combines with oxygen, then the rate of oxidation is determined by the rate at which ions leave the metal surface. Cabrera and Mott proposed an approximate solution to the oxide growth rate equation to give an inverse logarithmic equation to describe the oxide growth rate. Ample experimental evidence exists for the inverse logarithmic growth law and are discussed in reviews by Lawless²¹ and Wallwork.⁴⁵

A modification to the Cabrera-Mott theory was suggested by Fehlner and Mott for low temperature oxidation of metals where amorphous oxides are formed. In this case, it is insufficient to assume that the reaction is propagated by cation transport to the oxide-gas interface and the anion transport from the surface to the oxide-metal interface should be included. Metals that form amorphous oxides during low temperature oxidation include Al, Ta, and Si while Cu, Fe and Ni form crystalline oxides even at low temperatures.

2.2.2. Thicker Oxides – Wagner and Extended Cabrera-Mott Theories

As the oxide film grows thicker, the field set up across the oxide is not as strong as for very thin films (<50 Å) and the velocity of charge carrier decreases. Cabrera and Mott extended their theory for thicker oxide films using the same assumptions as thin oxide films and the growth rate simplifies to a parabolic growth law. Cabrera suggests that the upper limit for the applicability of the parabolic law is 200 nm.^{21,54} This is not to be

confused with Wagner's parabolic growth law which is governed by a different set of assumptions and is applicable in a different thickness regime (>5000 nm).^{21,55} Wagner based his theory on the linear diffusion equation of charged particles and assumed a neutral oxide that evolved during growth (i.e., number of cations is same as number of anions). Wagner's theory does not elucidate the mechanism of specific oxidation processes; however, it explains the experimental data well and forms the basis for more sophisticated theories such as the Cabrera-Mott,⁵⁴ Uhlig⁵¹ and Fromhold⁵⁶ oxidation models. The oxide growth rate calculated for NiO film growth using the Cabrera-Mott and Wagner theories is shown in Figure 2-6: this shows that the oxide models capture the oxidation reaction only when the film is at least a few nanometers thick; in addition, there is a range ($X_1 < X < X_2$) where oxide film growth is not explained by both the models.

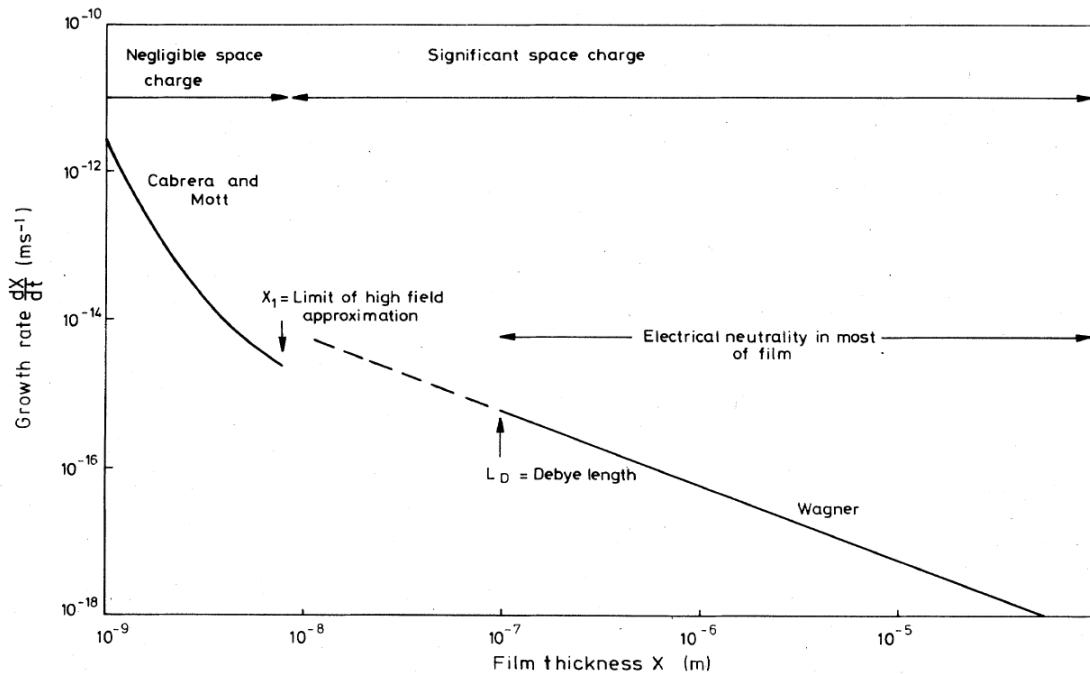


Figure 2-6. Oxide growth rate of hypothetical p-type NiO as a function of film thickness calculated using Cabrera and Mott ($X < X_1$) and Wagner equations ($X > X_1$).⁴⁷

2.3. Physical Properties of Oxides in Ni-Cr-Mo System

The important physical properties of nickel oxide, chromium oxide and mixed nickel-chromium oxide are listed in Table 2-I. The crystal structures of the three oxides are shown in Figure 2-7.⁵⁷

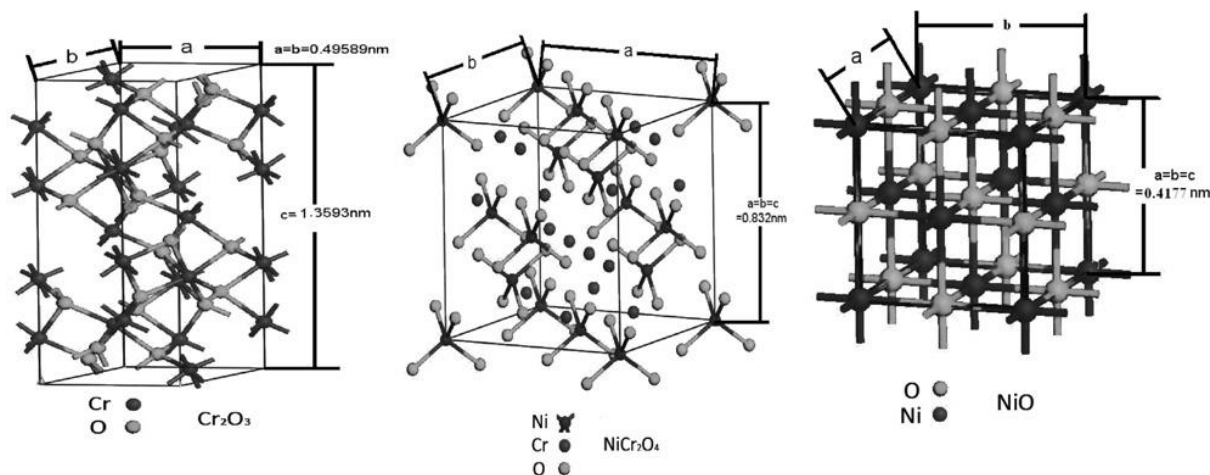


Figure 2-7. Ball and stick models of crystal structures of Cr_2O_3 , NiCr_2O_4 and NiO .

Table 2-I. Physical properties of the oxides expected to form in the Ni-Cr system during oxidation.

	Cr_2O_3	NiCr_2O_4	NiO
Crystal Structure	Corundrum structure $a=0.495 \text{ nm}$, $c=0.1359 \text{ nm}$	Cubic* $A=0.832 \text{ nm}$	NaCl Structure $a=0.4177 \text{ nm}$
Density	5.22 g/cc	-	6.67 g/cc
Melting Point	2435 °C	-	1955 °C
Bandgap	3.7-5.0 eV ^{58,59}	4.1 eV ⁶⁰	3.5-4.3 eV ⁶⁰⁻⁶²

*A tetragonal phase has been reported at low temperatures⁶³

2.4. Thin Film Growth

An atomic scale study of the oxidation reaction requires the fabrication of well-defined surfaces. In this dissertation work, this is realized by in-situ growth of thin films prior to oxidation. The ability to easily tune the composition of the thin film and to obtain

the same starting surface makes thin film surfaces an ideal template for the current work. In ultrahigh vacuum, thin films are grown by the in-situ evaporation of source materials. Physical vapor deposition technology has matured over the years to the point that quaternary alloy thin films (and higher) are frequently grown. The substrates for growth of epitaxial films are chosen so that the lattice mismatch is small and no interfacial products are formed.

2.4.1. Thermodynamics of Film Growth

The thermodynamic classification of thin film growth modes was first addressed by Bauer⁶⁴ when the film morphology was classified based on the balance between interfacial and surface free energy. Bauer's wetting criterion is given by

$$\Delta\gamma = \gamma_f + \gamma_i - \gamma_s$$

where γ_f and γ_s are the surface free energy of film and substrate while γ_i is the interfacial energy between the film and substrate. Depending on the value of $\Delta\gamma$, Bauer postulated the existence of three distinct growth modes which are sketched in Figure 2-7.^{19,64,65}

- **Frank-van der Merwe (FM) or the layer-by-layer mode:** Film growth proceeds by complete wetting of the substrate by the film material (1st layer) before the next layer starts to grow on top of the first layer. In this case, the film surface has a significantly lower surface energy compared to the substrate such that $\Delta\gamma < 0$. Systems with small lattice mismatch where a coherent interface is formed (low γ_i) follow the FM growth mode. A purely layer-by-layer growth is difficult to visualize due to non-equilibrium conditions during growth.

- **Volmer-Weber or Island Mode:** Film growth is dominated by formation of 3D islands. In this case, the substrate has a very low surface energy compared to the film ($\Delta\gamma > 0$) and wetting of substrate is not preferred. This mode is also favored due to large lattice mismatch between the film and substrate resulting in high interfacial energy (incoherent interface). Examples where VW growth has been observed include Ni/MgO(001),⁶⁶ Al/SiO₂ and Ag/SiO₂.⁶⁷

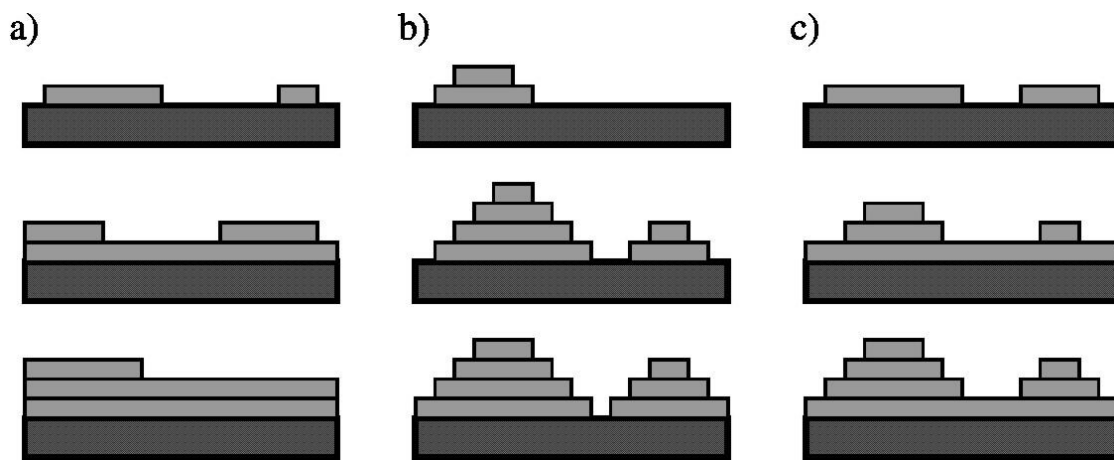


Figure 2-8. The three equilibrium film growth modes classified by Bauer: (a) Frank-van der Merwe or layer-by-layer growth, (b) Volmer-Weber growth, and (c) Stranski-Krastanov growth mode.⁶⁸

- **Stranski-Krastanov Mode:** This is an intermediate mode where characteristics of FM and VW growth modes are observed. The initial growth follows the FM mode to form a wetting layer; subsequently, the growth switches to VW mode and three dimensional islands are formed on top of the wetting layer. This mode is typical observed in heteroepitaxy when the lattice mismatch between film and substrate causes the film to be strained. Initially, the strain is accommodated by lattice distortions in the wetting layer and when a critical thickness is exceeded, 3D islands

are nucleated to accommodate the strain. A well-known system exhibiting SK growth is the Ge/Si(001) system.^{69–72}

2.4.2. Kinetics of Film Growth

While the previous section deals with the near-equilibrium classification of growth modes based on thermodynamics, the final film morphology also depends on kinetic factors due to deviations from equilibrium. The kinetics of film growth is a balance of the various competing atomic processes and is strongly influenced by the experimental conditions such as deposition temperature, flux of atoms and the initial surface structure of the substrate. A classic example is Pt on Pt(111) homoepitaxy where a whole range of surface morphologies are observed as a function of deposition temperature and deposition rate.⁶⁵ While most of the atomic processes on the surface during interaction with gaseous reactants have been introduced in Section 2.1, important processes relevant to film growth are discussed here.

The three main processes that need to be considered with respect to film growth are deposition, surface diffusion, and desorption. In most cases, the desorption rate is usually a small fraction of the deposition rate and can be ignored. Deposited adatoms move on the surface by terrace, interlayer and edge diffusion (thermally activated). On a perfect surface, adatom motion at a given temperature can be predicted based on the diffusion coefficient. However, imperfections on the surface such as missing atoms and dislocations can trap a mobile adatom and serve as a nucleation site for subsequent growth process. While a step edge acts a sink for adatoms due to the high density of dangling bonds, it has also been observed that a descending step can reflect atoms away from the edge due to the additional barrier for hopping down a step. This barrier at the edge is called Ehrlich-Schwoebel

barrier and it has a strong influence on the final morphology of epitaxial films.^{65,73,74} Since the diffusion is a thermally activated process, the interplay between the various surface diffusion processes at a given deposition temperature controls the morphology of the thin film. It is clear that thermodynamic classification of growth modes, while certainly useful, does not predict the film growth process in its entirety and a kinetic description based on the various atomic processes is necessary to explain the surface structure of the thin films.

References

1. de De Micheli, S. M. & Riesgo, O. Electrochemical study of corrosion in NiCr dental alloys. *Biomaterials* **3**, 209–212 (1982).
2. Bocher, F., Huang, R. & Scully, J. R. Prediction of Critical Crevice Potentials for Ni-Cr-Mo Alloys in Simulated Crevice Solutions as a Function of Molybdenum Content. *Corrosion* **66**, 55002–55002–15 (2010).
3. Marchetti, L., Miserque, F., Perrin, S. & Pijolat, M. XPS study of Ni-base alloys oxide films formed in primary conditions of pressurized water reactor. *Surf. Interface Anal.* **47**, 632–642 (2015).
4. Li, M. H. *et al.* Oxidation Behavior of a Single-Crystal Ni-Base Superalloy in Air. I: At 800 and 900°C. *Oxidation of Metals* **59**, 591–605 (2003).
5. Essuman, E. *et al.* Protective and non-protective scale formation of NiCr alloys in water vapour containing high- and low-pO₂ gases. *Corrosion Science* **50**, 1753–1760 (2008).
6. Wood, G. C., Hodgkiess, T. & Whittle, D. P. A comparison of the scaling behaviour of pure iron-chromium and nickel-chromium alloys in oxygen. *Corrosion Science* **6**, 129–147 (1966).
7. Steffen, J. & Hofmann, S. Oxidation of NiCr and NiCrFe alloys at room temperature. *Surf. Interface Anal.* **11**, 617–626 (1988).
8. Pollock, T. M. & Tin, S. Nickel-Based Superalloys for Advanced Turbine Engines: Chemistry, Microstructure and Properties. *Journal of Propulsion and Power* **22**, 361–374 (2006).
9. Viswanathan, R. High Temperature Corrosion of Some Gas Turbine Alloys. *Corrosion* **24**, 359–368 (1968).
10. Hickman, J. W. & Gulbransen, E. A. An electron diffraction study of oxide films formed on nickel-chromium alloys. *Trans. Am. Inst. Min. Metall. Pet. Eng* **180**, 519–546 (1949).
11. Amano, T. & Itoh, A. Surface oxidation of Ni20Cr alloys with small additions of Ce and Si. *Applied Surface Science* **60**, 677–680 (1992).
12. Calvarin, G., Molins, R. & Huntz, A. M. Oxidation Mechanism of Ni—20Cr Foils and Its Relation to the Oxide-Scale Microstructure. *Oxidation of Metals* **53**, 25–48 (2000).
13. Bond, A. P. & Uhlig, H. H. Corrosion Behavior and Passivity of Nickel-Chromium and Cobalt-Chromium Alloys. *J. Electrochem. Soc.* **107**, 488–493 (1960).
14. Mishra, A. k. & Shoesmith, D. w. Effect of Alloying Elements on Crevice Corrosion Inhibition of Nickel-Chromium-Molybdenum-Tungsten Alloys Under Aggressive Conditions: An Electrochemical Study. *Corrosion* **70**, 721–730 (2014).
15. Hayes, J. R., Gray, J. J., Szmodis, A. W. & Orme, C. A. Influence of Chromium and Molybdenum on the Corrosion of Nickel-Based Alloys. *Corrosion* **62**, 491–500 (2006).
16. Horvath, J. & Uhlig, H. H. Critical Potentials for Pitting Corrosion of Ni, Cr-Ni, Cr-Fe, and Related Stainless Steels. *J. Electrochem. Soc.* **115**, 791–795 (1968).
17. Hodge, F. G. & Wilde, B. E. Effect of Chloride Ion on the Anodic Dissolution Kinetics of Chromium-Nickel Binary Alloys in Dilute Sulfuric Acid. *Corrosion* **26**, 246–250 (1970).
18. Lloyd, A. C., Noël, J. J., McIntyre, S. & Shoesmith, D. W. Cr, Mo and W alloying additions in Ni and their effect on passivity. *Electrochimica Acta* **49**, 3015–3027 (2004).
19. Ertl, G. *Reactions at Solid Surfaces*. (John Wiley & Sons, 2010).
20. Norskov, J. K., Studt, F., Abild-Pedersen, F. & Bligaard, T. *Fundamental Concepts in Heterogeneous Catalysis*. (Wiley, 2014).

21. Lawless, K. R. The oxidation of metals. *Rep. Prog. Phys.* **37**, 231 (1974).
22. Roberts, M. W. & Wells, B. R. Chemisorption and incorporation of oxygen by nickel films. *Trans. Faraday Soc.* **62**, 1608–1619 (1966).
23. Stöhr, J., Jaeger, R. & Kendelewicz, T. Structure of p(2×2) and c(2×2) Oxygen on Ni(100): A Surface Extended-X-Ray Absorption Fine-Structure Study. *Phys. Rev. Lett.* **49**, 142–146 (1982).
24. Oed, W. *et al.* Adsorbate induced reconstruction phase p(2 × 2)O/Ni(100). *Surface Science* **225**, 242–248 (1990).
25. Nix, R. M. 6.1 Classification of Overlayer Structures.
http://www.chem.qmul.ac.uk/surfaces/scc/scat6_1.htm - *An Introduction to Surface Chemistry*
Available at: http://www.chem.qmul.ac.uk/surfaces/scc/scat6_1.htm. (Accessed: 24th November 2016)
26. Halachev, T. & Ruckenstein, E. Dissociative chemisorption of O₂ on transition metal clusters in the presence or absence of subsurface oxygen and the effect of cluster size. *Journal of Molecular Catalysis* **16**, 149–165 (1982).
27. Lahtonen, K., Hirsimäki, M., Lampimäki, M. & Valden, M. Oxygen adsorption-induced nanostructures and island formation on Cu{100}: Bridging the gap between the formation of surface confined oxygen chemisorption layer and oxide formation. *The Journal of Chemical Physics* **129**, 124703 (2008).
28. Holloway, P. H. Chemisorption and oxide formation on metals: Oxygen–nickel reaction. *Journal of Vacuum Science & Technology* **18**, 653–659 (1981).
29. Holloway, P. H. & Hudson, J. B. Kinetics of the reaction of oxygen with clean nickel single crystal surfaces. *Surface Science* **43**, 123–140 (1974).
30. Kopatzki, E. & Behm, R. J. STM imaging and local order of oxygen adlayers on Ni(100). *Surface Science* **245**, 255–262 (1991).
31. Kopatzki, E. & Behm, R. J. Step Faceting: Origin of the Temperature Dependent Induction Period in Ni(100) Oxidation. *Phys. Rev. Lett.* **74**, 1399–1402 (1995).
32. Wang, W.-D., Wu, N. J. & Thiel, P. A. Structural steps to oxidation of Ni(100). *The Journal of Chemical Physics* **92**, 2025–2035 (1990).
33. Leak, R. J. & Selwood, P. W. The Chemisorption of Oxygen on Nickel. *J. Phys. Chem.* **64**, 1114–1120 (1960).
34. Partridge, A. *et al.* Scanning-tunneling-microscopy investigation of the p(2×2) and c(2×2) overlayers of S on Ni(100). *Phys. Rev. B* **48**, 8267–8276 (1993).
35. Donati, F. *et al.* Scanning tunneling spectroscopy of the Fe(001)-p(1×1)O surface. *Phys. Rev. B* **79**, 195430 (2009).
36. Bäumer, M. *et al.* The structure of thin NiO(100) films grown on Ni(100) as determined by low-energy-electron diffraction and scanning tunneling microscopy. *Surface Science* **253**, 116–128 (1991).
37. Kalinkin, A. V., Boreskov, G. K., Savchenko, V. I., Dadayan, K. A. & Bulgakov, N. N. Low temperature adsorption of oxygen on Ni(100). *React Kinet Catal Lett* **18**, 55–58 (1982).
38. Richter, H. & Gerhardt, U. Adsorption Sites of Oxygen on Cu(001) and Ni(001) Determined from the Shape of the Low-Energy Electron-Diffraction Spots. *Phys. Rev. Lett.* **51**, 1570–1572 (1983).

39. Xu, C., Burnham, J. S., Goss, S. H., Caffey, K. & Winograd, N. Oxygen-induced near-surface structural rearrangements on Ni{001} studied by shadow-cone-enhanced secondary-ion mass spectrometry. *Phys. Rev. B* **49**, 4842–4849 (1994).
40. Oed, W., Lindner, H., Starke, U., Heinz, K. & Müller, K. Adsorbate-induced relaxation and reconstruction of c(2 × 2)O/Ni(100): A reinvestigation by leed structure analysis. *Surface Science* **224**, 179–194 (1989).
41. Caputi, L. S., Jiang, S. L., Amoddeo, A. & Tucci, R. Oxygen-nickel bond length in Ni(111)-p(2×2)O determined by electron-energy-loss fine-structure spectroscopy. *Phys. Rev. B* **41**, 8513–8515 (1990).
42. Fehlner, F. P. & Mott, N. F. Low-temperature oxidation. *Oxid Met* **2**, 59–99 (1970).
43. Stuckless, J. T. *et al.* Oxygen chemisorption and oxide film growth on Ni{100}, {110}, and {111}: Sticking probabilities and microcalorimetric adsorption heats. *The Journal of Chemical Physics* **106**, 2012–2030 (1997).
44. Muñoz-Márquez, M. A., Tanner, R. E. & Woodruff, D. P. Surface and subsurface oxide formation on Ni(1 0 0) and Ni(1 1 1). *Surface Science* **565**, 1–13 (2004).
45. Wallwork, G. R. The oxidation of alloys. *Rep. Prog. Phys.* **39**, 401 (1976).
46. Luo, L. *et al.* In-situ transmission electron microscopy study of surface oxidation for Ni–10Cr and Ni–20Cr alloys. *Scripta Materialia* **114**, 129–132 (2016).
47. Atkinson, A. Transport processes during the growth of oxide films at elevated temperature. *Rev. Mod. Phys.* **57**, 437–470 (1985).
48. Mott, N. F. A theory of the formation of protective oxide films on metals. *Trans. Faraday Soc.* **35**, 1175–1177 (1939).
49. Mott, N. F. The theory of the formation of protective oxide films on metals, II. *Trans. Faraday Soc.* **35**, 472–483 (1940).
50. Rhodin, T. N. Low Temperature Oxidation of Copper. I. Physical Mechanism1a. *J. Am. Chem. Soc.* **72**, 5102–5106 (1950).
51. Uhlig, H. H. Initial oxidation rate of metals and the logarithmic equation. *Acta Metallurgica* **4**, 541–554 (1956).
52. Mott, N. F. The theory of the formation of protective oxide films on metals.—III. *Trans. Faraday Soc.* **43**, 429–434 (1947).
53. Mott, N. F. Oxidation of Metals and the Formation of Protective Films. *Nature* **145**, 996–1000 (1940).
54. Cabrera, N. & Mott, N. F. Theory of the oxidation of metals. *Rep. Prog. Phys.* **12**, 163 (1949).
55. Wagner, C. Z. *phys. Chem. B* **21**, 25 (1933).
56. Fromhold, A. T. & Cook, E. L. Kinetics of Oxide Film Growth on Metal Crystals: Thermal Electron Emission and Ionic Diffusion. *Phys. Rev.* **163**, 650–664 (1967).
57. Liang, G. Y., Zhu, C., Wu, X. Y. & Wu, Y. The formation model of Ni–Cr oxides on NiCoCrAlY-sprayed coating. *Applied Surface Science* **257**, 6468–6473 (2011).
58. Hong, S., Kim, E., Kim, D.-W., Sung, T.-H. & No, K. On measurement of optical band gap of chromium oxide films containing both amorphous and crystalline phases. *Journal of Non-Crystalline Solids* **221**, 245–254 (1997).
59. Kim, E., Jiang, Z.-T. & No, K. Measurement and Calculation of Optical Band Gap of Chromium Aluminum Oxide Films. *Jpn. J. Appl. Phys.* **39**, 4820 (2000).

60. Marchetti, L., Perrin, S., Wouters, Y., Martin, F. & Pijolat, M. Photoelectrochemical study of nickel base alloys oxide films formed at high temperature and high pressure water. *Electrochimica Acta* **55**, 5384–5392 (2010).
61. Sawatzky, G. A. & Allen, J. W. Magnitude and Origin of the Band Gap in NiO. *Phys. Rev. Lett.* **53**, 2339–2342 (1984).
62. Irwin, M. D., Buchholz, D. B., Hains, A. W., Chang, R. P. H. & Marks, T. J. p-Type semiconducting nickel oxide as an efficiency-enhancing anode interfacial layer in polymer bulk-heterojunction solar cells. *PNAS* **105**, 2783–2787 (2008).
63. Ueno, G., Sato, S. & Kino, Y. The low-temperature tetragonal phase of NiCr₂O₄. *Acta Crystallogr C Cryst Struct Commun* **55**, 1963–1966 (1999).
64. Bauer, E. Phänomenologische Theorie der Kristallabscheidung an Oberflächen. I. *Zeitschrift für Kristallographie* **110**, 372–394 (1958).
65. Michely, T. & Krug, J. *Islands, Mounds and Atoms*. **42**, (Springer Berlin Heidelberg, 2004).
66. Lukaszew, R. A., Zhang, Z., Stoica, V. & Clarke, R. Annealing effects on (001) Ni films grown on MgO. *Applied Surface Science* **219**, 74–79 (2003).
67. Floro, J. A. *et al.* The dynamic competition between stress generation and relaxation mechanisms during coalescence of Volmer–Weber thin films. *Journal of Applied Physics* **89**, 4886–4897 (2001).
68. Hillebrands, A. G. Molecular beam epitaxy - Technische Universität Kaiserslautern. *Molecular beam epitaxy - Technische Universität Kaiserslautern* (2010). Available at: <https://www.physik.uni-kl.de/hillebrands/research/methods/molecular-beam-epitaxy/>. (Accessed: 28th November 2016)
69. Sutter, P. & Lagally, M. G. Nucleationless Three-Dimensional Island Formation in Low-Misfit Heteroepitaxy. *Phys. Rev. Lett.* **84**, 4637–4640 (2000).
70. Mo, Y.-W., Savage, D. E., Swartzentruber, B. S. & Lagally, M. G. Kinetic pathway in Stranski-Krastanov growth of Ge on Si(001). *Phys. Rev. Lett.* **65**, 1020–1023 (1990).
71. Zhang, J. J. *et al.* Monolithic Growth of Ultrathin Ge Nanowires on Si(001). *Phys. Rev. Lett.* **109**, 85502 (2012).
72. Ramalingam, G., Floro, J. A. & Reinke, P. Three-dimensional nanostructures on Ge/Si(100) wetting layers: Hillocks and pre-quantum dots. *Journal of Applied Physics* **119**, 205305 (2016).
73. Kalff, M., Šmilauer, P., Comsa, G. & Michely, T. No coarsening in Pt(111) homoepitaxy. *Surface Science* **426**, L447–L453 (1999).
74. Kyuno, K. & Ehrlich, G. Step-Edge Barriers on Pt(111): An Atomistic View. *Phys. Rev. Lett.* **81**, 5592–5595 (1998).

3. Experimental Approach

All experiments in this dissertation are performed under ultrahigh vacuum (UHV) conditions. A schematic of the UHV system used is shown in Figure 3-1 and the various components are labeled. The UHV system is designed by ScientaOmicron and consists of a MULTIPROBE preparation/analysis chamber (#1 in Figure 3-1) that is coupled to the scanning tunneling microscope (#2). The former consists of a sample manipulator (#3) for sample motion in the chamber and various operations such as sample heating up to 1000 °C, thin film deposition (#4), and the introduction of gases (#5) such as O₂ for oxidation can be performed in the preparation chamber. The variable temperature scanning tunneling microscope (VT-STM) is attached in series to the MULTIPROBE system and permits characterization of the atomic and electronic structure of the sample at various stages of the experiment such as deposition, annealing, and/or oxidation. Substrates are introduced into the UHV chamber through the loadlock system which is pumped independently. During operation, the UHV base pressure ($<3 \times 10^{-10}$ mbar) is maintained by an ion getter pump and a titanium sublimation pump. Since the STM is sensitive to vibrations, the entire system is on an air table which isolates the microscope from building vibrations. The microscope was initially controlled by ScalaPro software (ScientaOmicron) and it was upgraded to the MATRIX user interface system in 2013.

In this chapter, a brief introduction to characterization tools and deposition sources is provided. The reasons for using thin films to study oxidation is outlined and the preparation of MgO(001) and Si(001) substrates is presented. Finally, STM image analysis,

using commercial software packages, and STS data analysis strategies, using the MATLAB code developed in our group, are discussed in detail with related examples.

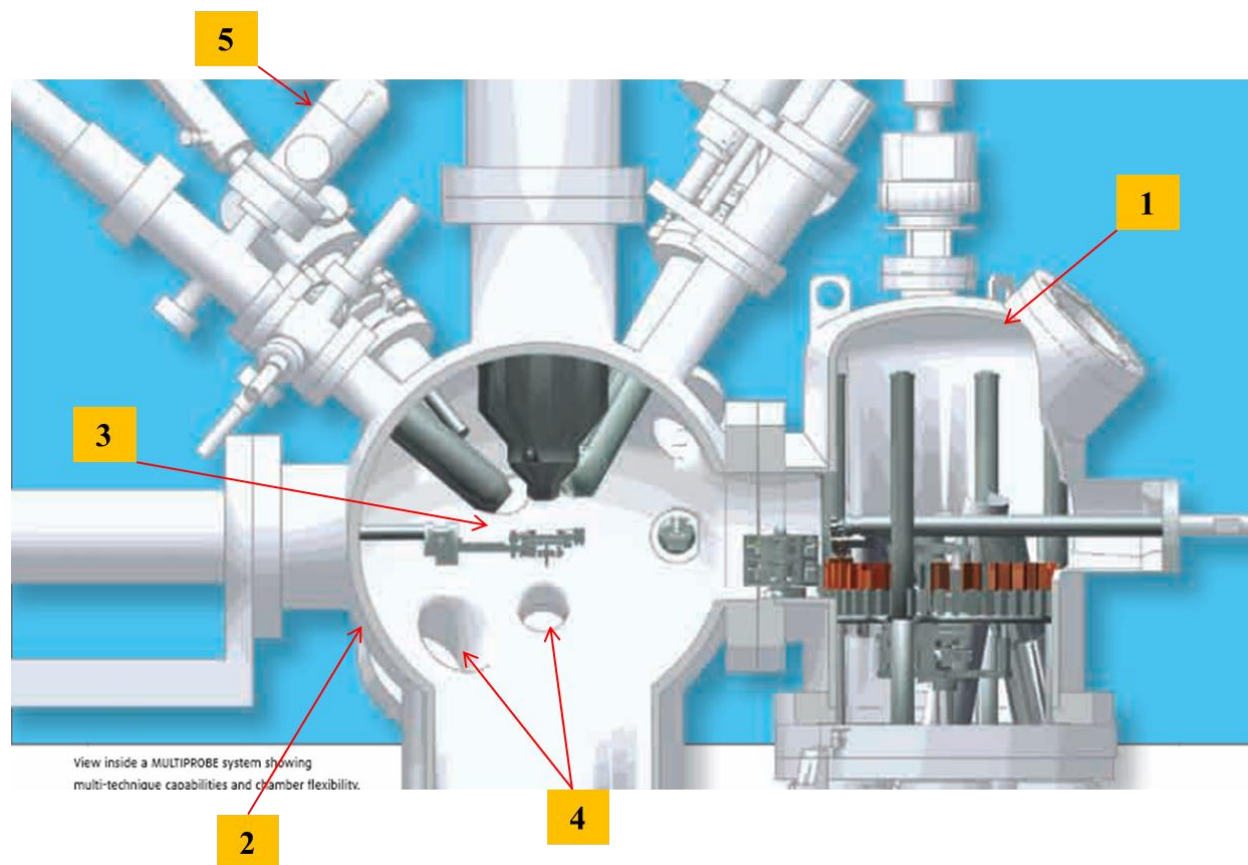


Figure 3-1. Schematic of the UHV system used: (1) VT-STM, (2) MULTIPROBE analysis chamber, (3) Manipulator containing the sample heating assembly, (4) pockets for deposition sources, and (5) leak valve for introduction of gases.

3.1. Thin Film Deposition Techniques

Two different physical vapor deposition sources are used in this research: (1) effusion cell for Ge evaporation and (2) electron beam evaporator for metals (Co, Mn, Ni, Cr, Mo). The deposition flux in case of the latter is measured using a quartz crystal monitor (QCM) while the thermal load during the use of the former adversely impacts the performance of the QCM. In such a situation, the rates are estimated by calculating Ge

surface coverage on Si by STM image analysis and relating to the known critical thickness for QD nucleation at a given deposition temperature.

3.1.1. Electron Beam Evaporation

During e-beam evaporation, the source material maintained a high voltage (up to 2000 V) is heated by electron bombardment of thermionic electrons emitted from a tungsten filament. The point source is either a crucible containing the source material or a rod of the material. The filament current and positive bias voltage are controlled so that the temperature (vapor pressure) to yield the desired particle flux for deposition is reached. The e-beam evaporators require water cooling due to the high temperatures reached during operation. Two commercial e-beam evaporators sold by Mantis are used: (a) quad source (QUAD-EV-C) that allows for simultaneous deposition of different elements (used in this study for depositing Mn, Co, Ni, and Cr), and (b) single mini evaporator fitted with a circular W filament to deposit high- T_m metals such as Mo and W. A specially designed Mantis power source for the quad system is used for simultaneous deposition of two or more elements. A stand-alone high voltage source (Glassman) in combination with a power supply is used for single-material deposition.

The various source materials evaporated using the e-beam evaporator are Co (Goodfellow, 99.99%), Ni (Alfa Aesar, 99.999%), Mn (Kurt Lesker, 99.99%), Cr (American Elements, 99.95%) and Mo (American Elements, 99.99%). 28 mm long cylindrical rods with a diameter of 2 mm are used in all cases except for Mn which is evaporated from a Mo crucible lined with alumina. Evaporating Cr and Ni from a $\text{Al}_2\text{O}_3/\text{Mo}$ crucible was attempted in order to increase the throughput but aluminum contamination was detected

in both cases likely due to a solid state reaction between the native oxide on Ni/Cr and the alumina liner. The use of a graphite liner could be a possible option for the future. The rods are cleaned in an ultrasound bath using acetone and isopropanol to remove all traces of machining residue. Before use in an experiment, the rods/crucibles are degassed by heating to temperatures greater than ones used in the experiment. The various rates used for different materials are specified in the relevant chapters in this dissertation and are measured with a quartz crystal monitor.

3.1.2. Effusion Cell

Effusion cell evaporator supplied by Veeco Ltd. is used for Ge deposition (Goodfellow, 99.999%). In this case, a long alumina crucible (4 cc volume) containing Ge pieces is heated to the required temperature by a tungsten filament. The filament is wound around the entire length of the crucible to ensure uniform heating. A thermocouple junction is attached at the base of the crucible for temperature measurement. The effusion cell requires slow heating and cooling rates (10 °C/min) to prevent cracking of the crucible. Phase changes in the material during heating/cooling need to be taken into account and care should be taken to avoid rapid temperature fluctuations. In order to obtain deposition rates of 0.25 ML/min of Ge in our setup, the crucible is maintained to 1040-1050 °C.

3.2. Characterization Techniques

3.2.1. Scanning Tunneling Microscopy

Scanning tunneling microscopy (STM) is the main characterization tool used in this work to capture the evolution of the atomic and electronic structure of the alloy surface during oxidation. STM was invented by Binnig and Rohrer in 1981 and it revolutionized

the approach to understand the atomic structure of materials, reactions at surfaces and electronic properties at the atomic scale.^{1,2} The basic principle of STM is the tunneling of electrons through a potential barrier between the tip and the surface as shown in Figure 3-2. A sharp metal tip, usually tungsten, is brought in close proximity to the sample surface so that electrons can tunnel through the vacuum gap. The tunneling current decays exponentially with the width of the barrier (separation between tip and surface) and the height of the barrier is governed by the work function difference between the tip and the surface. An applied bias voltage will result in electrons tunneling through this barrier; depending on the polarity of the applied bias, we can image the filled or empty electronic states of the sample.^{1,3} Topography and spectroscopy are the two data acquisition modes in the STM and are discussed in the following sections.

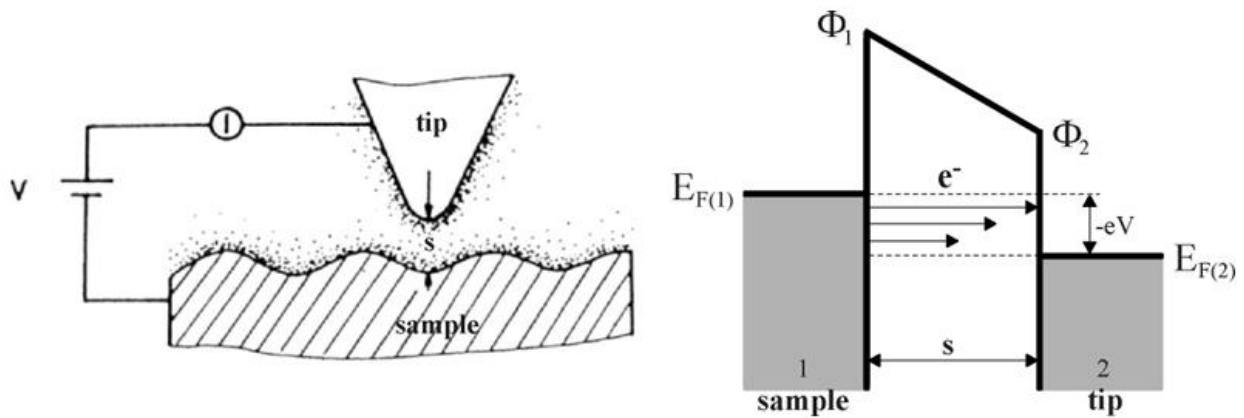


Figure 3-2. Principle of Electron Tunneling through a potential barrier between sample and tip separated by distance 's' and biased by voltage V lower than work functions, Φ_1 and Φ_2 .³

3.2.1.1. Topography Imaging

To record a topography image, the microscope operates by scanning the tip along the lateral X and Y directions on the surface and recording the tunneling current at each

position (pixel). Constant current mode is used to record images shown in this dissertation: in this mode, a feedback loop is used to adjust the vertical position (Z-axis) of the tip in order to maintain the tunneling current at the user-defined set point. The image file consist of an array of apparent height that are linked to the corresponding (X,Y) position. These source image files can be read directly with Gwyddion⁴ or WSxM.⁵

It is worth mentioning that STM is not element specific. However, it is possible to differentiate between different atomic species in an alloy if one of the constituent elements has a unique surface state. This was shown in the case of Fe-Cr alloy by Choi et al.⁶ where imaging was performed at a voltage corresponding to the surface state of Fe in order to differentiate them from Cr atoms. However, no imaging condition was identified that allowed the differentiation of Cr from the Ni atoms on the alloy surface. A detailed description of the STM image analysis is provided in section 3.5.1.

3.2.1.2. Scanning Tunneling Spectroscopy

Spectroscopic measurements can be performed with the same electronics by recording current-voltage characteristics at a given X-Y point on the surface. The normalized derivative, $(dI/dV)/(I/V)$, is proportional to the local density of states (LDOS), and yields information on the local electronic structure.^{1,7-10} Spectroscopic data was measured in two modes: (a) point spectroscopy where I-V curves are measured at a chosen point on the image, and (b) grid spectroscopy where I-V curves are measured on a predefined grid which can be of the same resolution as the image (1×1 grid which gives 512×512 STS curves) or lesser (for example, a 5x5 grid where STS curve is recorded at every 5th point yields 103×103 curves).

I-V curves obtained in STS are numerically differentiated to yield dI/dV curves using a MATLAB code developed by Monazami et al. The code was subsequently modified to meet the needs of this dissertation. The dI/dV curves were subsequently normalized by I/V to remove the exponential dependence on distance and yields a quantity which is only proportional to the local density of states (LDOS). From these normalized dI/dV curves, we calculate the bandgap as that region around $V=0$ where the density of states is zero i.e., $(dI/dV)/(I/V) = 0$. A schematic conductance curve is shown in Figure 3-3 with two approaches to determine the bandgap. The method outlined above underestimates the real gap which is measured from the band edges. The spectroscopy data can be visualized as {1} $(dI/dV)/(I/V)$ maps (or conductance maps) where the normalized dI/dV is mapped on the image area or {2} bandgap maps where the bandgap measured from each curve is mapped onto the image area. Using these approaches, we can differentiate the metallic surface from oxides that form during oxidation. STS data analysis methods are discussed in section 3.5.2.

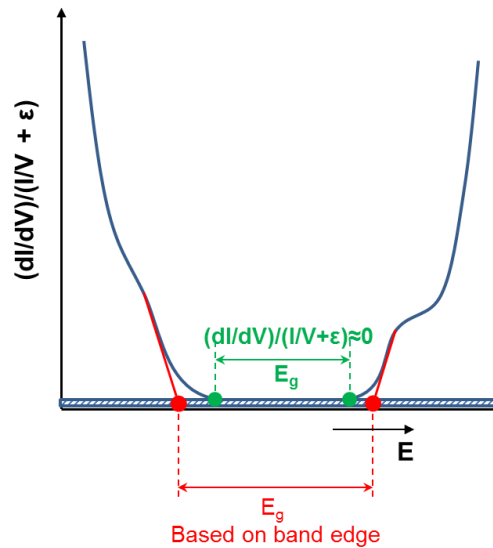


Figure 3-3. Schematic STS spectra illustrating the two approaches used to calculate bandgap in the MATLAB code. In method-I, a cut-off is defined corresponding to zero (or very low) density of states while method-II is based on the valence and conductance band edge (HOMO-LUMO gap).

3.2.1.3. Tip Making

The STM tips for imaging/spectroscopy are prepared by electrochemically etching in 1 M NaOH solution.² A small segment of tungsten wire ($\varphi=0.05$ mm) is cleaned thoroughly with acetone and isopropanol and subsequently spot-welded to Omicron tip holder. A gold wire loop serves as an electrode and the sodium hydroxide solution forms a lamella on this loop. The W wire is introduced into this loop and a DC voltage is applied to start the etching process (redox reaction). At the end of the etching process, the free-standing wire drops off while the atomically sharp tip is attached to the tip holder. In order to remove back etching which blunts the newly-formed tip, care is taken to turn off the power supply immediately after the wire drops off. The success rate of the above tip fabrication recipe, judged based on imaging and spectroscopy quality, is >50%.

3.2.2. Atomic Force Microscopy (ex-situ)

An atomic force microscope uses a cantilever with a sharp tip to scan the sample surface.¹¹ As the surface is approached, the close-range attractive forces cause the cantilever to be deflected towards the surface. When the tip-sample distance crosses the equilibrium separation, repulsive forces dominate and the cantilever is deflected away from the surface. The cantilever deflections are detected by using laser beams where changes in the reflection of the laser beam due to cantilever deflections are detected and converted into topography images. Standard imaging modes with AFM are contact mode, non-contact mode, and tapping modes. In this work, AFM is used in tapping mode to characterize the long-range surface morphology of MgO substrates after during pre-treatment and after thin film growth. In addition, bulk samples are characterized before

and after corrosion in sulfate and chloride solutions to capture the changes in the surface morphology after exposure to corrosive environments. Imaging is performed ex-situ with an NT-MDT Solver Pro instrument (courtesy of the Floro research group) with ETALON HA/NC tips with curvature radius less than 10 nm.

3.2.3. Ambient Pressure Photoelectron Spectroscopy

Photoelectron spectroscopy during oxidation will deliver a detailed view of compositional changes in the alloy, the bonding environment in the oxide layer and at the oxide/alloy interface, and capture the complex gas-solid and solid-solid reaction sequences involved in formation of the passivating oxide layer. Information on the various oxides that form on the surface at various stages of oxidation will shed valuable insight into the atomistic processes during the initial stages of oxidation. Ambient pressure experiments are pursued so that surface reactions can be studied at pressures closer to the actual operating conditions thereby bridging what has been called the “pressure gap” between UHV surface science research and real-world reaction conditions. These experiments are expected to augment the UHV STM/STS research on alloy thin film samples.

Photoelectron spectroscopy (PES) is based on the phenomenon of photoemission which was first detected by Heinrich Hertz in 1887 during experiments with a spark-gap generator.^{12,13} The experimental observations of photoemission were explained in 1905 by Albert Einstein by invoking the particle nature of electrons i.e., incoming radiation should be thought of as quanta of energy. The three step model, where the PES experiment is broken down into three distinct steps, can be used to explain the PES experiment and is shown in Figure 3-4.¹² A typical PES experiment involves (1) optical excitation when a

photon impinges on the sample, (2) transport of the excited electron to the surface with or without inelastic scattering losses, and (3) escape of electron into vacuum. The light source is an X-ray tube or a synchrotron light source and the emitted photoelectrons are analyzed with respect to their kinetic energy (E_K) using a hemispherical energy analyzer. Knowing the energy of light source and the work function, the binding energy, E_B , of the photoelectron is determined using the following equation:

$$E_K = h\nu - \phi - E_B$$

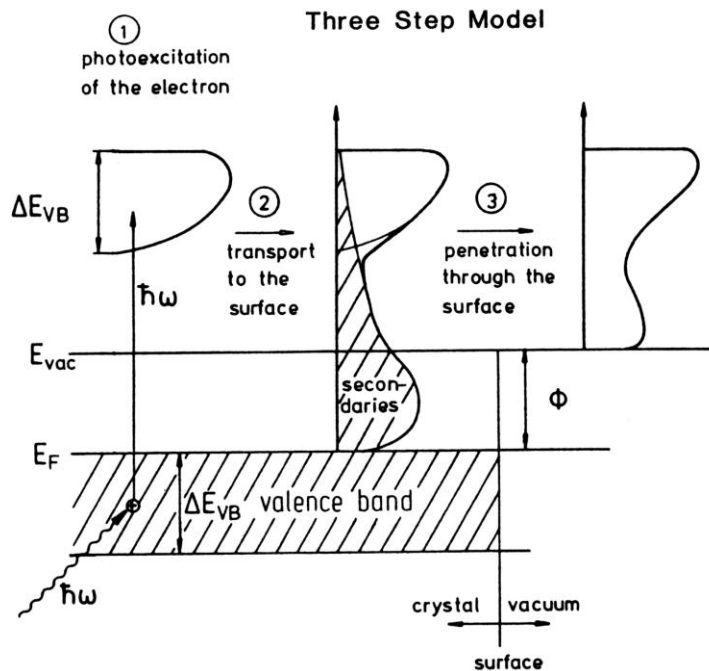


Figure 3-4. Three step model to explain a typical photoelectron spectroscopy experiment.¹²

The chemical elements on the surface and selvedge region are identified based on their binding energy. For a photoelectron to be ejected from the surface, they must escape the surface without interacting with other atoms which could result in a loss of kinetic

energy. The Beer-Lambert law^{14,15} gives the probability of photoelectron reaching the surface without losing its E_K . The intensity of an electron emitted from a depth 'd' is:

$$I_d = I_o e^{-d/\lambda}$$

where λ is the inelastic mean free path (IMPF). From this equation, it is seen that 95% of the electrons detected in a PES experiment would be produced within a depth of 3λ . Typical mean free path for Ni and Cr 2p photoelectrons are 1.5-1.7 nm which translates to an information depth of 4.5-5 nm. Due to the small escape depth, conventional XPS systems operate under UHV conditions in order to minimize losses in photoelectron intensity due to scattering from the ambient atmosphere. However, PES at higher pressures has been made possible due to the advent of synchrotron light sources which emit a constant beam with high photon flux. PES experiments presented in this dissertation are performed at the National Synchrotron Light Source II (NSLS-II) at Brookhaven National Laboratory (BNL).

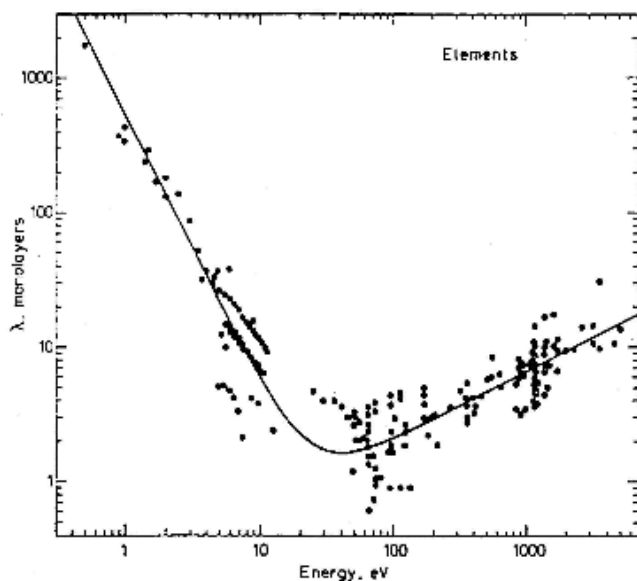


Figure 3-5. Universal curve for inelastic electron mean free path (λ) of an electron in a solid.¹²

A synchrotron is a particle accelerator that can be used to accelerate both electrons and protons. Synchrotron light sources provide a high intensity of monochromatic photons for XPS analysis. The high photon flux, which translates to high flux of photoelectrons, allows for XPS measurements in ambient pressures. NSLS-II is a medium energy (3.0 GeV) electron storage ring designed to deliver photons with high average spectral brightness. The NSLS-II radiation sources span a very wide spectral range from the far-IR (down to 0.1 eV) and to the very hard X-ray region (>300 keV). This is achieved by a combination of bending magnets, three-pole wigglers, and insertion device (ID) sources. The tunable photon energy allows us to nondestructively probe different depths of the sample. The dependence of IMPF on the electron energy is shown in Figure 3-5 and it illustrates the sample depth ($\approx 3\lambda$) from which XPS signals are generated as a function of photon energy.

3.2.4. Scanning Electron Microscopy (SEM)

SEM is primarily used in this work to determine the composition of the alloy thin film by energy dispersive spectroscopy (EDS). It will be shown in Chapter 4 that composition estimates based on deposition rates are accurate. In a scanning electron microscope, an electron beam is scanned across the sample surface. When the electrons strike the sample, numerous signals are generated and the detection of specific signals produces an image. For EDS, we are concerned with the X-ray emissions that result from the interaction of the primary electron beam with atoms in the sample. The emitted X-ray has an energy which is characteristic of the atom from which it was generated. Detection and measurement of the energy permits elemental analysis and this technique is called Energy Dispersive X-ray Spectroscopy (EDS). EDS provides quantitative analysis of elemental composition with a

sampling depth of 1-2 microns. Different modes exist in EDS and besides point EDS analysis, line profiles or 2D maps can be generated showing the distribution of various elements in the sample.

3.2.5. Other Techniques

In addition to the above techniques, X-ray diffraction (XRD), X-ray reflectometry (XRR), and time of flight secondary ion mass spectroscopy (ToF-SIMS) are sparingly used. XRD was used to determine the crystallographic orientation of Ni/NiCr films when sufficiently thick films were specifically grown for crystallographic analysis. The nominal thickness of the thin films grown is 25-30 nm and these films are not sufficiently thick to get a strong signal from the thin film. XRR was employed to calculate the film thickness. The long-range roughness of the acid-treated MgO (see Figure 3-7) affects the use of XRR for determination of film thickness. ToF-SIMS was pursued to determine the distribution of Ni and Cr in the alloys and also to obtain film thickness on two samples: Ni₁₃Cr and Ni₈Cr where the latter is found to be contaminated with Al (section 3.1.1). These measurements were performed at Surface Science Western (University of Western Ontario, Canada) and the results are discussed in Chapter 4.

3.3. Use of Thin Films to Study Chemical Reactions

Oxidation resistance of Ni-Cr alloys depends strongly on the Cr concentration but the initial reaction steps in the oxidation of the alloy are not well understood. A facile route for fabrication of high quality NiCr alloy thin films would open up a path for the atomic scale study of oxidation as a function of Cr composition and prevents the need for cost intensive fabrication and cleaning of single crystals of different compositions. Majority of the work to

investigate oxidation of NiCr alloys presented in the literature has been performed on bulk polycrystalline samples^{16–20} where the effect of Cr concentration cannot be decoupled from other factors such as grain size, residual stresses and crystallographic orientations. In contrast, the use of smooth alloy thin films provides a direct route to study the initial stages of alloy oxidation as a function of Cr content with high spatial resolution.

3.4. Substrate Preparation

3.4.1. MgO(001)

Epi-polished MgO(100) crystals are used as substrates for NiCr thin film growth. MgO preparation is critical for the growth of high quality NiCr thin films. Two different pre-treatments routes^{21–24} are used to prepare a smooth substrate surface suitable for film growth: (T1) annealing at 600 °C in-situ (UHV conditions) for 2 hours immediately following an overnight anneal at 200 °C and (T2) two-step acid etch plus anneal route: the substrate is etched with 85% phosphoric acid for 30 seconds and annealed in air in a box furnace at 1200 °C for 5 hours followed by a second 30 second etch and annealing in air at 1100 °C for 4 hours; this is followed by overnight anneal after introduction into the UHV chamber. The overnight anneal at 200 °C in the UHV chamber is used to remove adventitious hydrocarbons and water.

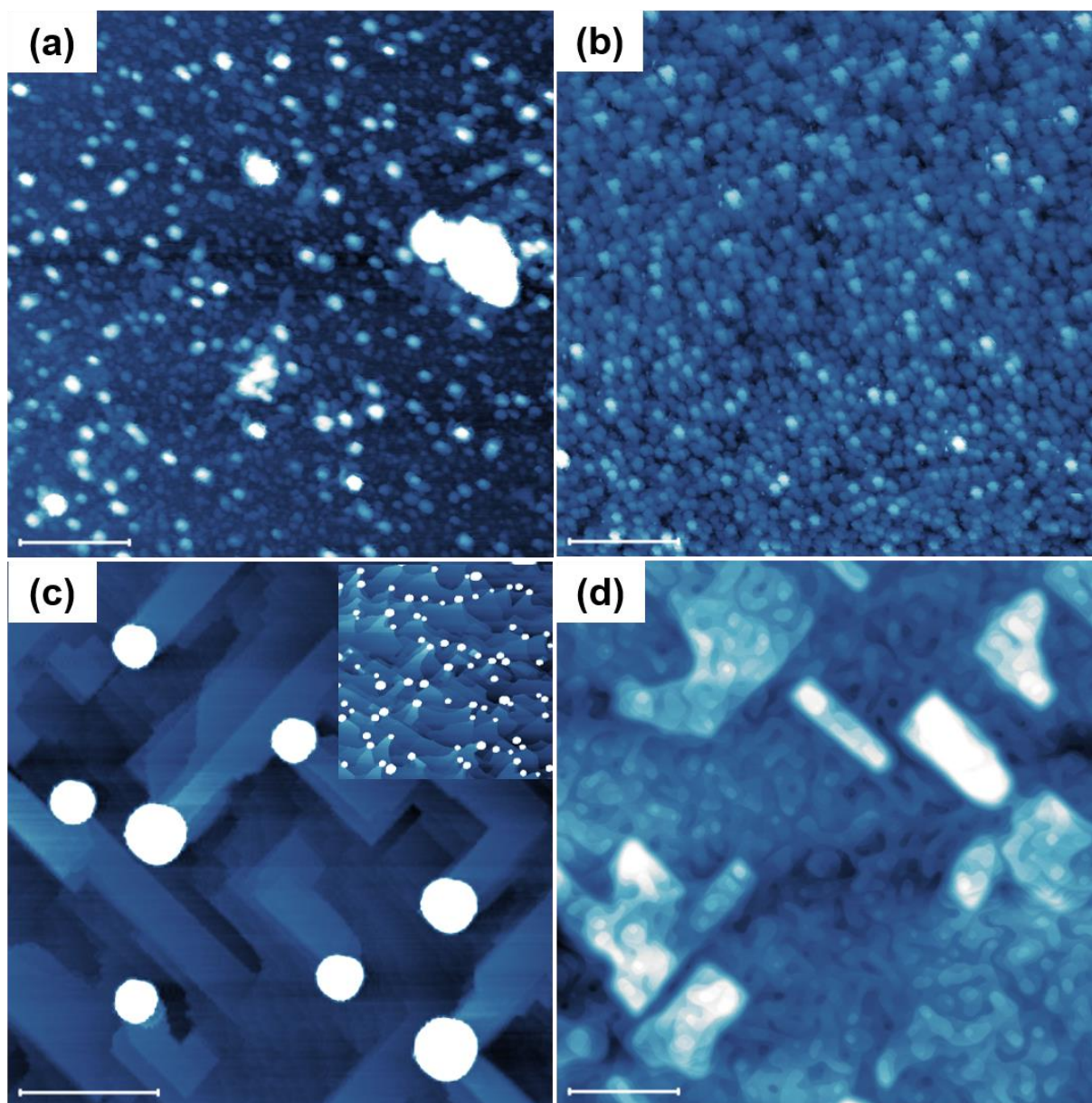


Figure 3-6. AFM images during different stages of MgO pre-treatment: (a) as-received, (b) after H_3PO_4 etch, (c) post-1200 °C annealing in air, and (d) after second acid etch and 1100 °C anneal. The inset in (c) is a $10 \times 10 \mu\text{m}^2$ area showing the distribution of Ca spires throughout the surface. Scale bar in all images is 1 μm .

AFM images of the MgO substrate after various stages of T2 pre-treatment^{22,24} are shown in Figure 3-6. The as-received sample is rough and is contaminated by adsorbates such as water and hydrocarbons from ambient atmosphere; the structures in Figure 3-6(a) are 30-60 nm high while some larger impurity particles are also seen. After the first H_3PO_4

etch, the surface is more homogeneous but is still corrugated as seen in Figure 3-6(b); the surface structures are less than 20 nm high. After annealing in air at 1200 °C, the surface is populated with large CaCO_3 spire structures that are formed due to Ca segregation to the surface.²⁵ The AFM image in Figure 3-6(c) shows the presence of these spires on an otherwise smooth surface. Terraces and step edges are observed after this 1200 °C annealing step. The terraces are at least 100 nm wide with well-defined step-edges; step bunching and pinning due to the CaCO_3 structures are also clearly observed. The inset in Figure 3-6(c) shows the population of Ca spires throughout the surface (inset area is $10 \times 10 \mu\text{m}^2$). The second phosphoric acid etching and subsequent 1100 °C anneal yields a smooth surface as shown in Figure 3-6(d) without any Ca-induced spires: the lower annealing temperature precludes any further Ca segregation and the long-range surface diffusion at these temperatures results in a smooth terrace structure suitable for thin film growth. The AFM images of the MgO surface after T1 and T2 pre-treatment are shown in Figure 3-7. The MgO substrate surface after T1 pre-treatment is smooth with an average RMS roughness of 0.18 ± 0.04 nm but no terrace structure is observed. The T2 pre-treatment yields a terrace structure with well-defined step-edges. The higher temperature annealing used in the T2 pre-treatment results in wide terraces and the step edges are predominantly oriented along the $\langle 110 \rangle$ direction.

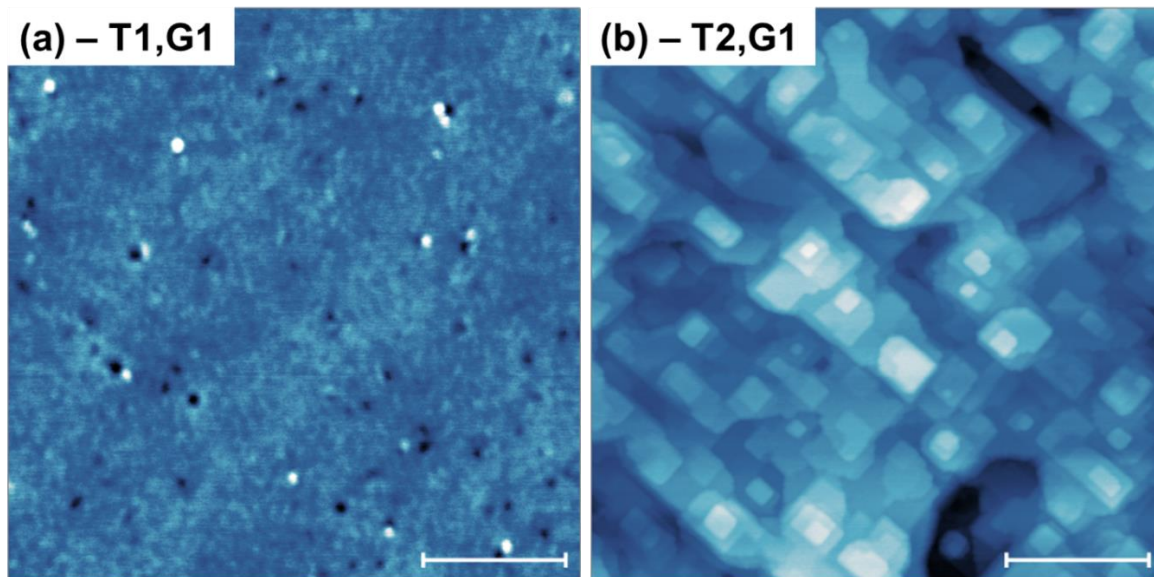


Figure 3-7. Atomic force microscopy (AFM) images of MgO substrate after (a) T1 and (b) T2 pre-treatments. Scale bar is 500 nm.

3.4.2. Si(100)

The sample dimension of the Si(100) wafers used in this work are $10 \times 1 \times 0.5 \text{ mm}^3$ and they are mounted in a sample holder specially designed to allow for direct current heating. The Si(100) samples obtained from Fiber Optic Inc. are B-doped with resistivity between $0.01\text{-}0.02 \text{ } \Omega\cdot\text{cm}$. Every wafer is outgassed by annealing at $550 \text{ } ^\circ\text{C}$ until the chamber pressure recovers back to the base pressure; this is typically achieved by overnight annealing. Thermal cleaning, as outlined in literature,^{26,27} is used to obtain a clean Si(100) surface which presents the typical 2×1 reconstruction. In this procedure, the sample is rapidly heated to increasing temperatures until the final step when a temperature of $1200 \text{ } ^\circ\text{C}$ is reached. The sample is held at a high temperature for short 2-3 s bursts while ensuring that the pressure is below $1 \times 10^{-9} \text{ mbar}$. A rough measure of the temperature can be gleaned by looking at the sample through a viewport during each flash cycle. After the flashed sample cools to room temperature, it is imaged with the STM to ensure a high

quality surface with minimal surface defects is obtained. The defect concentration (missing dimers and missing atoms) on the Si(100)-(2x1) surface is usually 4% or less in order to proceed with the experiment. If the defect concentration is too high, flashing is repeated but a higher final temperature is used to anneal the defects. Figure 3-8 shows STM images of a good quality Si surface with a low defect concentration and is compared with a highly defective surface obtained after the first flashing treatment.

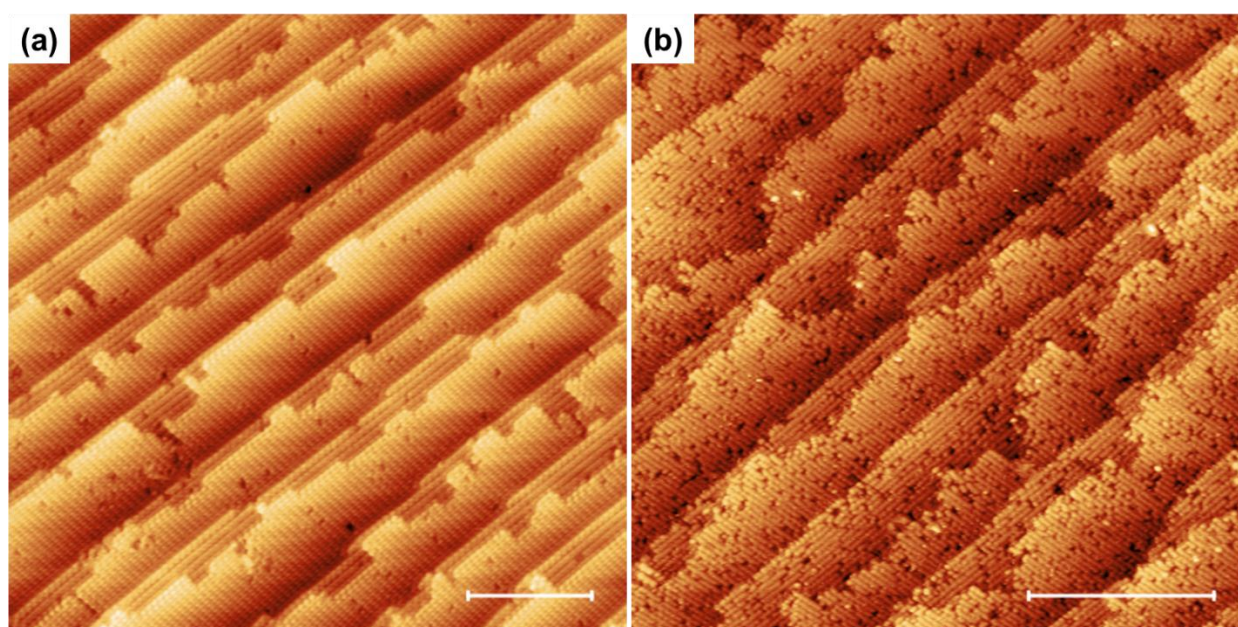


Figure 3-8. Filled states STM image of Si(100)-2x1 surface: (a) high quality surface with low defect concentration, and (b) highly defective surface unsuitable for experiment. The images are recorded at -1.5 V, 0.03 nA and scale bar is 15 nm.

3.5. STM/STS Data Analysis Rubric

Two scanning probe microscopy analysis programs that are frequently used by the surface science community are Gwyddion⁴ and WSxM.⁵ In this work, Gwyddion is the software that is primarily used for topography image analysis. WSxM is used to convert the raw grid STS data in a format that can be read subsequently by the MATLAB code

developed in our group. The MATLAB code expresses the data as either a conductance map or a bandgap map. In addition, various other modules were implemented to obtain information specific to the oxidation work such as Fermi energy position in each oxide and to sort STS curves as metal, oxide and intermediate states.

3.5.1. Topography Images

Data obtained from scanning probe microscopes are not leveled and the image file contains the raw input computed from the piezo-scanner voltage. An unprocessed image of Ni-10Cr-6Mo surface after 30 L oxidation is shown in Figure 3-9(a) with the corresponding height profile in 3-9(e). The need for leveling and/or background subtraction (terminology depends on the software used and the two operations are distinct in Gwyddion) is clear from this image. Plane leveling is done for all images in this work with Gwyddion and the software computes the plane from all the image points and subtracts from the data. The leveled image is shown in Figure 3-9(b) along with the line-scan in (e). The features are clear after the leveling and the height of oxide can be measured from the line-scan without the ambiguity of a sloping background. However, the surface is not entirely flat and a non-zero slope is seen on the metal surface (right side of height profile). An additional background subtraction is necessary to flatten the image and a linear background is chosen in this work (other options include quadratic and cubic). The background is calculated for every line in the image (512 in a 512×512 image) and is subtracted from the data. Figure 3-9(c,d) show the image after linear background subtraction and after both plane leveling and linear background subtraction. There is no difference in image contrast between (c) and (d) but they are different compared to plane leveling. The feature heights themselves

do not change appreciably and the height of the oxide island marked only in Figure 3-9(d) after the three processing steps are 0.249, 0.224 and 0.223 nm. It should be noted that there are small pockets on the metal surface that appear darker in Figure 3-9(c,d). One such instance is marked with a black arrow where the presence of a small metal pocket surrounded by oxides on the terrace and at step edge results from the line-by-line treatment during background subtraction. The image analysis is nontrivial and excessive background subtraction can smear small features and also result in an inaccurate representation of the background surface (artificial depressions on the surface, smearing of step edges et cetera). Therefore, care should be taken and various leveling and background subtractions options should be compared and quantified with height profiles of features to ensure that the user does not amplify desired features or suppress undesired information that is contained in the image.

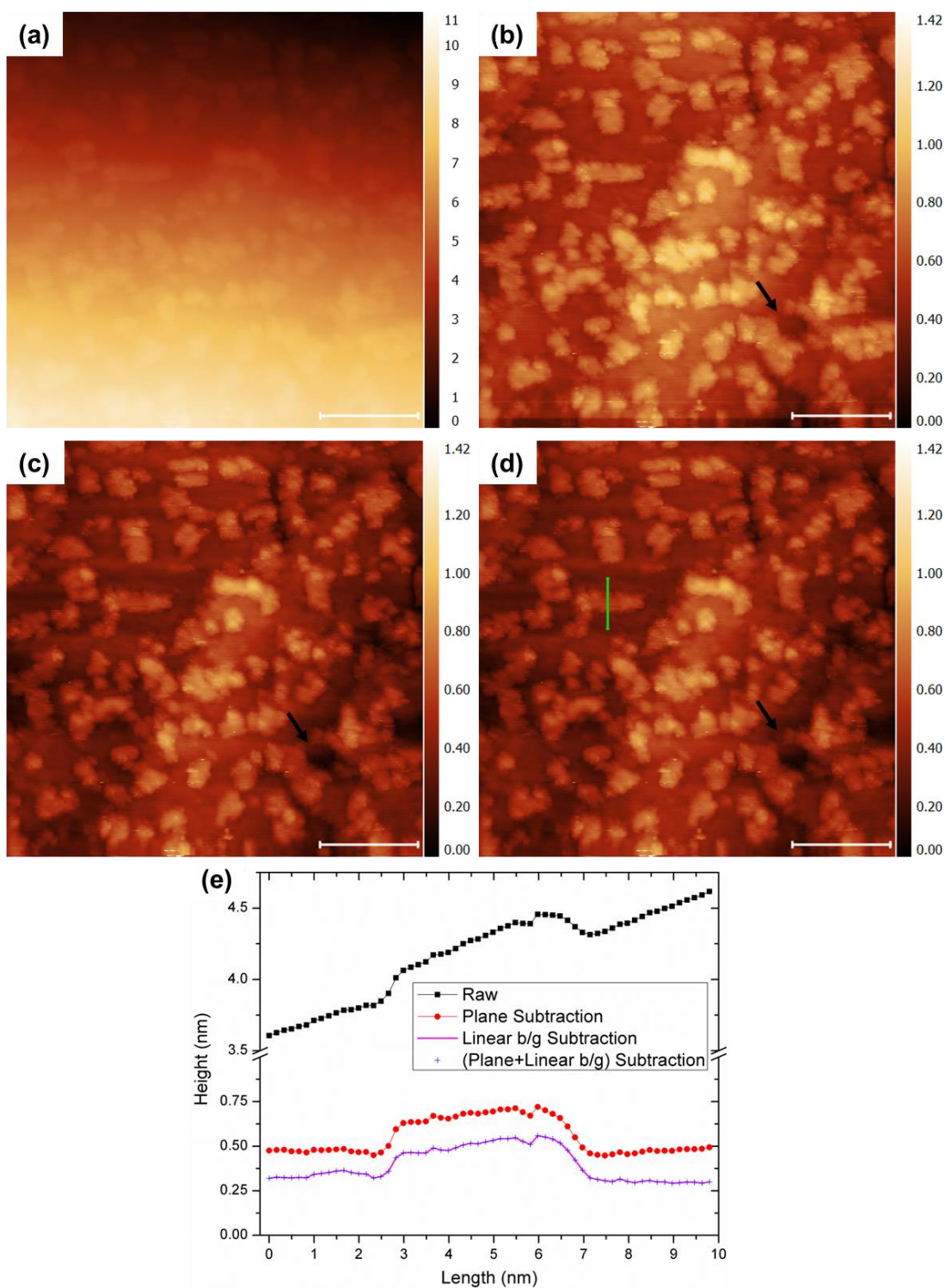


Figure 3-9. STM image of Ni-10Cr-6Mo surface after 30 L oxidation: (a) raw image, (b) plane level, (c) linear background subtraction only and (d) plane level and linear background. Scale bar is 20 nm. The black arrows in (b-d) indicate incorrect background subtraction due to height variations. (e) Height profiles across oxide marked by green line in (d) after the above background subtraction.

In order to determine the defect concentration on the Si surface or the oxide coverage on the surface, a mask is created to mark the feature of interest (referred to as a grain in Gwyddion) as shown in Figure 3-10. Simple thresholding algorithms are implemented in the software and are used to create the mask. A combination of height, slope and curvature thresholding is used to capture all the features in the image. In many cases, the algorithm overestimates the feature size and the masks have to be manually altered. Wherever available, the topography image is compared with bandgap map to ensure all oxides are captured during the thresholding step. Individual oxides that are clustered in a small region may not be separated automatically and have to be partitioned manually (not required if only surface coverage is desired). A high surface coverage makes reliable island separation impossible. A binary mask can be extracted in the end as shown in Figure 3-10(c) which can be input in image processing software products such as ImageJ.²⁸ Gwyddion provides all the quantitative information necessary such as height, volume and area as well as derived quantities such as equivalent side of square, radius and so on. Correlations between various dimensions can be plotted in the software if desired. All correlations and height/area distributions in this dissertation are obtained by saving raw data and computing histograms separately in OriginPro.

Since the masks need to be manually altered, it is possible that this subjectivity leads to different oxide dimensions when the images are analyzed by a different student. To circumvent this problem, we have collaborated with Prof. Peter Voorhees (Northwestern University) for automating this process. A segmentation code was written in MATLAB in the last month so that the oxide islands in the grayscale image (input) are detected and the height, area and/or volume are computed. The masks obtained in Gwyddion and with the

segmentation code are shown in Figure 3-11 and it is clear that the latter does a better job in separating oxides that appear coalesced based on images and cannot be manually separated. The oxide area distribution is shown for both the masking methods and we see that the segmentation code is biased towards smaller islands: this is unsurprising since large oxides which are deemed coalesced in the manual masking are separated into many smaller islands. This segmentation route is useful to eliminate subjectivity from the coverage/area determination and improve the image analysis throughput. In general, islands with an area less than 5 nm^2 ($r < 1 \text{ nm}$) are difficult to measure in a reliable manner. If height and volume distributions are desired, then masking will need to be performed in Gwyddion at this moment. Strategies to implement z-scale (height) determination based on the greyscale intensity can be considered in the future to obtain height distributions.

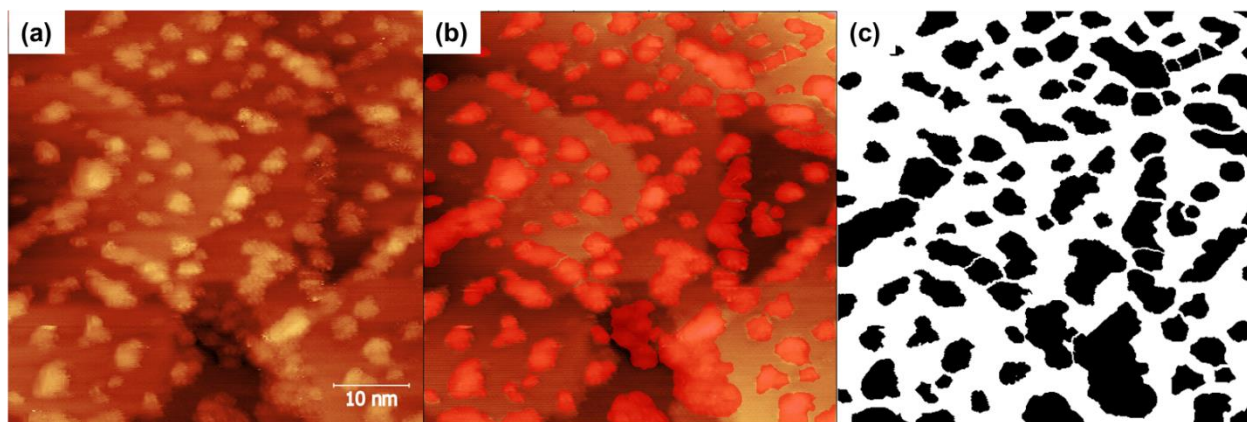


Figure 3-10. STM image of Ni-14Cr alloy after 30 L oxidation: (a) leveled, (b) islands marked by threshold, (c) binary mask extracted from the image.

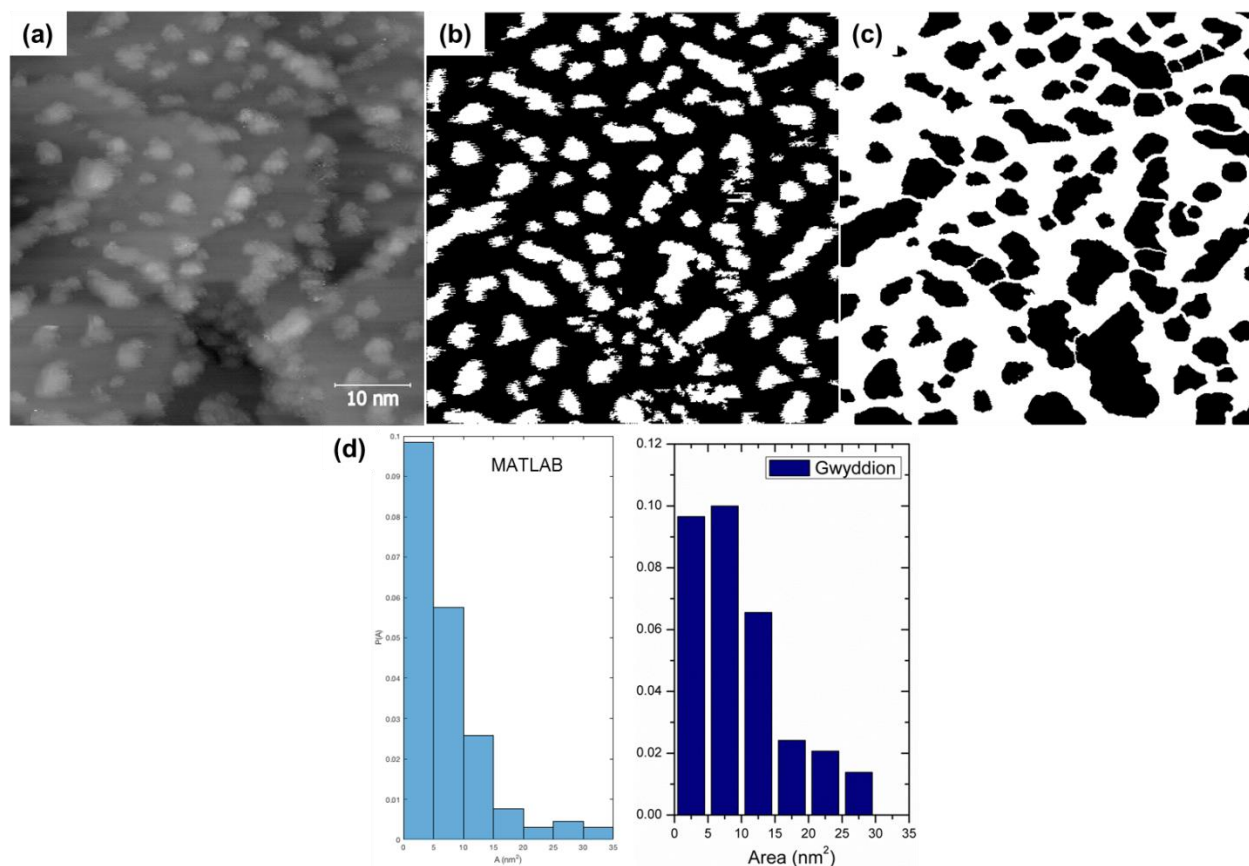


Figure 3-11. Comparison of oxide island masking on 30 L oxidized Ni-14Cr surface: (a) STM image, (b) mask obtained with segmentation code implemented in MATLAB, (c) mask extracted using thresholding and manual correction in Gwyddion. (d) Oxide area distribution from both the methods shows that the automated route is somewhat better at counting small islands. However, the error for $<5 \text{ nm}^2$ is still significant due to challenges in island separation.

3.5.2. Spectroscopy Data

3.5.2.1. Bandgap and Fermi Energy Calculation

Point and grid STS data are analyzed using the MATLAB code developed by Ehsan Monazami in our research group. The input file for grid spectroscopy is a text file that contains four columns for X position, Y position, voltage and current; the source file from Matrix software is converted into a formatted text file in WSxM software. I-V curves are numerically differentiated using a 5-point differential method and are normalized by the tunneling resistance ($I/V+\epsilon$) where $\epsilon=0.2$ is used to avoid singularity when I/V tends to

zero. The cut-off method for determination of bandgap was already discussed in section 3.2.1.2. It is also possible to measure the bandgap region from the STS curves based on the valence and conductance band-edge extrapolation. The two approaches are sketched in Figure 3-3. The second approach has pitfalls due to the inherent noise in room temperature STS spectra. A subroutine to implement the calculation of the gap using band edge extrapolation is included in the code but is not used in this work. The use of the cut-off to define the bandgap has been found to be more robust for comparison between different experiments and yields consistent values even if the gap value from this method is slightly underestimated. In addition to measuring the bandgap, we can also track, for example, the Fermi energy (E_F) of the oxide and relate to the structural changes of the oxides during oxidation. E_F is defined as the voltage (energy) corresponding to the midpoint of the gap – the oxide is therefore p-type if E_F is negative and n-type if $E_F > 0$.

3.5.2.2. Sorting STS Spectra to Identify Oxide and Metals

In order to identify the chemisorbed species, we utilized the observation by Eastman and Cashion that an O-chemisorbed Ni surface exhibits lower density of states compared to a metallic Ni surface.²⁹ However, defective oxide species on the surface could also exhibit a similar reduced conductance value without opening a bandgap. Therefore, we have defined lower and upper cutoffs to identify oxide and metallic regions respectively: any regions where $(dI/dV)/(I/V) < 0.01$ are classified as oxides and while regions with $(dI/dV)/(I/V) > 0.1$ are considered metallic. The intermediate values between these two limits could be attributed to intermediate species that include O-chemisorbed surfaces and defective oxides. Figure 3-12 shows the normalized dI/dV curves from an oxide-like (presence of

bandgap), metal-like (large DOS near Fermi level) and chemisorbed region (suppressed DOS near Fermi level but zero gap) sorted using the abovementioned criteria.

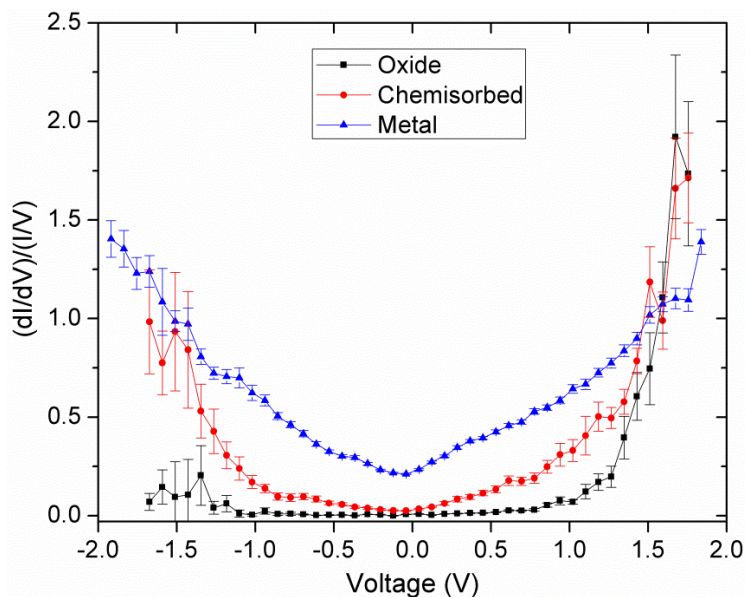


Figure 3-12. Representative STS curve of oxide-like, metal-like and intermediate species sorted using the cut-offs described in section 3.5.2.2 on an oxidized NiCrAl alloy surface.

3.5.2.3. Extracting STS Spectra from Specific Oxides

A GUI-enabled version of the code has been implemented which allows the user to select specific regions of interest on the surface and extract spectroscopy data. This functionality allows for correlation of the oxide height/area, measured in Gwyddion as described earlier, and the electronic structure of the oxide. A snapshot of the GUI is shown in Figure 3-13 along with the corresponding bandgap map. The area selected for analysis is marked with red crosses; the vertices as well as the number of spectral points in the chosen area is fed back to the GUI. Various subroutines can be written to analyze the STS curves that are acquired from any given area and in the oxidation work, the average bandgap and E_F position are usually of interest. This area selection feature allows us to check if $c(2 \times 2)$ -

O/Ni(001) phase is present in the un-oxidized regions. In addition, the GUI shows the other options available: (a) plot dI/dV map without normalization, (b) plot bandgap map using the two approaches discussed in the previous section, and (c) extract individual spectra.

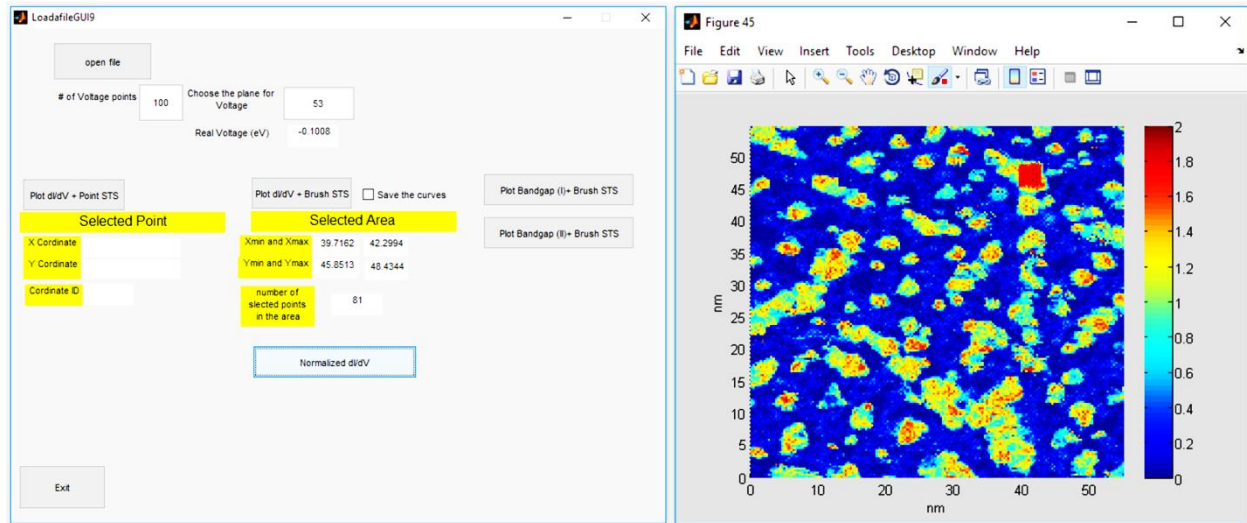


Figure 3-13. Snapshot of the GUI-enabled implementation of the MATLAB code for the analysis of grid spectroscopy data. An oxide that is selected for subsequent analysis in the bandgap map is marked by red crosses.

References

1. Wiesendanger, R. *Scanning Probe Microscopy and Spectroscopy: Methods and Applications*. (Cambridge University Press, 1994).
2. Meyer, E., Hug, H. J. & Bennewitz, R. *Scanning Probe Microscopy: The Lab on a Tip*. (Springer, 2004).
3. Marcus, P., Maurice, V., Costa, D. & Galtayries, A. The contribution of surface analysis to corrosion science: Historical background and current status. in *Proceedings-Electrochemical Society* **13**, 117–137 (2002).
4. Nečas, D. & Klapetek, P. Gwyddion: an open-source software for SPM data analysis. *Central European Journal of Physics* **10**, 181–188 (2012).
5. Horcas, I. *et al.* WSXM: A software for scanning probe microscopy and a tool for nanotechnology. *Review of Scientific Instruments* **78**, 13705 (2007).
6. Choi, Y. J. *et al.* Surface alloy formation of Fe on Cr(100) studied by scanning tunneling microscopy. *Phys. Rev. B* **59**, 10918–10922 (1999).
7. Stroscio, J. A., Feenstra, R. M. & Fein, A. P. Electronic structure of the Si (111)-2×1 surface by scanning-tunneling microscopy. *Physical review letters* **57**, 2579 (1986).
8. Feenstra, R. M. Tunneling spectroscopy of the (110) surface of direct-gap III-V semiconductors. *Phys. Rev. B* **50**, 4561–4570 (1994).
9. Feenstra, R. M. Tunneling spectroscopy of the GaAs(110) surface. *Journal of Vacuum Science & Technology B: Microelectronics and Nanometer Structures* **5**, 923 (1987).
10. Picone, A. *et al.* Atomic Scale Insights into the Early Stages of Metal Oxidation: A Scanning Tunneling Microscopy and Spectroscopy Study of Cobalt Oxidation. *J. Phys. Chem. C* **120**, 5233–5241 (2016).
11. Jalili, N. & Laxminarayana, K. A review of atomic force microscopy imaging systems: application to molecular metrology and biological sciences. *Mechatronics* **14**, 907–945 (2004).
12. Hüfner, S. *Photoelectron Spectroscopy: Principles and Applications*. (Springer Science & Business Media, 2003).
13. Fadley, C. S. X-ray photoelectron spectroscopy: Progress and perspectives. *Journal of Electron Spectroscopy and Related Phenomena* **178–179**, 2–32 (2010).
14. Beer. Bestimmung der Absorption des rothen Lichts in farbigen Flüssigkeiten. *Ann. Phys.* **162**, 78–88 (1852).
15. Lambert, J. H. *J.H. Lambert ... Photometria sive De mensura et gradibus luminis, colorum et umbrae*. (Sumptibus viduae Eberhardi Klett, typis Christophori Petri Detleffsen, 1760).
16. Hoflund, G. B. & Epling, W. S. Oxidation study of a polycrystalline Ni/Cr alloy I: room-temperature exposure to O₂. *Thin Solid Films* **307**, 126–132 (1997).
17. Hoflund, G. B. & Epling, W. S. Oxidation Study of a Polycrystalline Ni/Cr Alloy II. *Chem. Mater.* **10**, 50–58 (1998).
18. Ahmad, B. & Fox, P. STEM Analysis of the Transient Oxidation of a Ni-20Cr Alloy at High Temperature. *Oxid Met* **52**, 113–138 (1999).
19. Douglass, D. L. The oxidation mechanism of dilute Ni-Cr alloys. *Corrosion Science* **8**, 665–678 (1968).

20. Chattopadhyay, B. & Wood, G. C. The Transient Oxidation of Fe-Cr and Ni-Cr Alloys. *J. Electrochem. Soc.* **117**, 1163–1171 (1970).
21. Lukaszew, R. A., Zhang, Z., Stoica, V. & Clarke, R. Annealing effects on (0 0 1) Ni films grown on MgO. *Applied Surface Science* **219**, 74–79 (2003).
22. Perry, S. S. & Merrill, P. B. Preparation and characterization of MgO(100) surfaces. *Surface Science* **383**, 268–276 (1997).
23. Wang, C.-M., Kaspar, T. C., Shutthanandan, V., Joly, A. G. & Kurtz, R. J. Structure of Cr film epitaxially grown on MgO(0 0 1). *Acta Materialia* **59**, 4274–4282 (2011).
24. McClimon, J. B., Monazami, E. & Reinke, P. Interaction of C60 with Tungsten: Modulation of Morphology and Electronic Structure on the Molecular Length Scale. *J. Phys. Chem. C* **118**, 24479–24489 (2014).
25. Ota, H., Sakai, K., Aoki, R., Ikemiya, N. & Hara, S. Superstructure observation on a MgO(100) surface. *Surface Science* **357**, 150–154 (1996).
26. Hata, K., Kimura, T., Ozawa, S. & Shigekawa, H. How to fabricate a defect free Si(001) surface. *Journal of Vacuum Science & Technology A* **18**, 1933–1936 (2000).
27. Ramalingam, G. & Reinke, P. Towards a Mn–Co surface alloy: Scanning Tunneling Microscopy (STM) study of Co adsorption on Si(100) and its interaction with Mn wires. *Surface Science* **620**, 1–8 (2014).
28. Schindelin, J., Rueden, C. T., Hiner, M. C. & Eliceiri, K. W. The ImageJ ecosystem: An open platform for biomedical image analysis. *Mol. Reprod. Dev.* **82**, 518–529 (2015).
29. Eastman, D. E. & Cashion, J. K. Photoemission Energy-Level Measurements of Chemisorbed CO and O on Ni. *Phys. Rev. Lett.* **27**, 1520–1523 (1971).

4. Growth of Ni and Ni-Cr Alloy Thin Films on MgO(001)

4.1. Introduction

Ni-Cr based superalloys have exceptional oxidation and corrosion resistance¹⁻⁶ and are currently used among other applications in nuclear power plants,⁵ gas turbines,⁷ and metallic dental implants.⁸ Oxidation resistance of these alloys depends strongly on the Cr concentration and it has been found that addition of <8 wt.% leads to an increase in oxidation rate while alloying with 10-20 wt.% Cr results in reduced oxidation rates due to the formation of a continuous chromium oxide layer protects the material from further degradation.⁹⁻¹¹ Despite the technological relevance, the initial reaction steps in the oxidation of the alloy are not well understood. A facile route for fabrication of high quality NiCr alloy thin films would open up a path for the atomic scale study of oxidation as a function of Cr composition and prevents the need for cost intensive fabrication and cleaning of single crystals of different compositions. Majority of the work to investigate oxidation of NiCr alloys has been performed on bulk polycrystalline samples^{10,12-15} where the effect of Cr concentration cannot be decoupled from other factors such as grain size, residual stresses and crystallographic orientations. In contrast, the use of smooth alloy thin films provides a direct route to study the initial stages of alloy oxidation as a function of Cr content with high spatial resolution.

The growth temperature and composition for the growth of smooth Ni-Cr alloy thin films should be such that we are operating in the solid solution regime. The phase diagram shows that Cr forms a substitutional solid solution with Ni but the solubility limit of Cr can only be extrapolated for $T < 500$ °C from current data.¹⁶ Experimental data exists only for

high temperatures and calculated phase diagrams differ in the Cr solubility limit as well as in predicting the presence of the Ni_2Cr intermediate compound. In addition, the lattice constant of the solid solution of Cr in Ni needs to be considered to determine the epitaxial constraints during growth. The constituent elements Ni and Cr have different crystal structures: Ni crystallizes in a face centered cubic (FCC) structure with lattice constant, $a_0=0.352$ nm while Cr crystallizes in the body centered cubic (BCC) structure with $a_0=0.288$ nm.¹⁷ The lattice mismatch between Ni(001) and MgO(001) at room temperature is $\approx 16\%$ while the mismatch between Cr(001) and MgO(001) is only 3.4%; in case of Cr, the unit cell is rotated by 45° such that the epitaxial relationship is (001)Cr||[(001)MgO, [110]Cr||[100]MgO. The change in lattice parameter due to Cr dissolution in Ni is negligible and increases by only 0.004 nm after alloying 40 wt.%Cr with Ni.^{18,19} Consequently, the growth of Ni-Cr alloy thin films should follow the characteristics of Ni thin film growth and any changes in the thin film structure can be attributed to chemical effects such as modified adsorption of atoms on MgO surface or change in surface mobility in the presence of Cr.

The growth of Ni thin films on MgO has been studied extensively and the film structure, in terms of surface morphology and terrace structure, was found to strongly depend on the growth parameters such as temperature and film thickness.²⁰⁻²⁴ Two dominant epitaxial orientation relationships are established: (001)Ni||[(001)MgO, [100]Ni||[100]MgO and $(1\bar{1}0)\text{Ni}||[(001)\text{MgO}$, $[11\bar{2}]\text{Ni}||[100]\text{MgO}$.^{21,23,24} The epitaxial relationship is influenced by the film thickness²⁵ and thinner films (25-40 nm), such as the ones used in our study, favor the (100) cube-on-cube orientation. The growth temperature also affects the crystallographic orientation of the Ni thin film and Ni(100) cube-on-cube orientation has been reported^{20,21} for deposition at 100 °C while the $(1\bar{1}0)\text{Ni}$ orientation is

found when films are grown at 350 °C.²³ Recently, a two-step process involving deposition at 100 °C and annealing at 300 °C was reported²⁰ to obtain smooth (100)-oriented films with well-defined terrace structure.

In this report, we demonstrate the growth of smooth $\text{Ni}_{1-x}\text{Cr}_x$ thin films ($0 \leq x \leq 35 \text{ wt.}\%$) with large terraces (up to 30 nm wide) on $\text{MgO}(001)$ substrates and discuss the critical aspects of the growth process. The quality of the films as expressed by the terrace width, surface morphology and roughness are characterized by scanning tunneling microscopy (STM) and atomic force microscopy (AFM). The NiCr alloy thin film growth depends sensitively on (i) surface structure of the MgO substrate (terrace sizes and step edge structure), (ii) growth temperature (100 °C and 400 °C) and (iii) Cr content in the alloy (0-35 wt.%).

4.2. Experimental Details

The experiments are performed in an Omicron Nanotechnology Variable Temperature Scanning Probe Microscopy (VT-SPM) system under ultrahigh vacuum (UHV) conditions. The base pressure is $<3 \times 10^{-10}$ mbar. Epi-polished $\text{MgO}(100)$ crystals (CrysTec GmbH) are used as substrates for thin film growth. Table I summarizes the substrate pre-treatments and growth conditions that are used in the current work. Based on the existing literature for metal film growth on MgO substrates,^{20,26–28} two different pre-treatment routes are used to prepare a smooth substrate surface for film growth: (T1) annealing at 600 °C in-situ (UHV conditions) for 2 hours immediately following an overnight anneal at 200 °C and (T2) two-step acid etch plus anneal route: the substrate is etched with 85% phosphoric acid for 30 seconds and annealed in air in a box furnace at 1200 °C for 5 hours

followed by a second 30 second etch and annealing in air at 1100 °C for 4 hours; this is followed by overnight anneal after introduction into the UHV chamber. The details of the substrate preparation process were provided in section 3.4.1. Ni (Alfa Aesar, 99.999% purity) and Cr (American Elements, 99.95% purity) are deposited by electron beam evaporation using a Mantis EV mini e-beam evaporator (QUAD-EV-C). The deposition rates of Ni and Cr are measured using a quartz crystal monitor and the deposition time is estimated to achieve a film thickness of 30 nm. The Ni flux is maintained between 0.30-0.35 nm/min and the Cr flux (0.01-0.14 nm/min) is adjusted to obtain the required composition of the alloy. Two growth conditions are used in this study: (G1) deposition at 100 °C followed by annealing at 300 °C for 2 hours, and (G2) deposition at 400 °C.

The as-grown thin films are characterized in situ by scanning tunneling microscopy. Imaging is performed at room temperature in constant current mode with W tips which are prepared by electrochemical etching. Empty and filled states images are recorded on the different films; low bias voltages ($V_b < 0.2$ V) and set-point currents greater than 0.5 nA resulted in good quality images. Surface morphology of the pre-treated MgO substrates are characterized ex-situ using atomic force microscopy (AFM) with an NT-MDT Solver Pro in tapping mode, using ETALON HA/NC tips with curvature radius less than 10 nm. The composition of the film is confirmed ex-situ by energy dispersive spectroscopy (EDS) performed in an FEI Quanta 650 scanning electron microscope (SEM). Film thickness estimates are confirmed by X-ray reflectometry (XRR) on films grown on T1-substrates while the rough film-substrate interface in the case of T2 films precluded reliable XRR measurement (see Figure 4-1 for MgO surface morphology). Time of flight secondary ion mass spectroscopy (ToF-SIMS) was performed on two randomly chosen films to check for

uniformity of alloy composition. ToF-SIMS measurements were performed on an ION-TOF (Gmbh) instrument at Surface Science Western (University of Western Ontario, Canada) and detailed information is provided in the Supplemental Information. STM and AFM images were analyzed with Gwyddion, an open source software for SPM data analysis.²⁹ A blue color scheme is chosen for all AFM images and an orange scheme is used for all STM images shown in this work.

Table 4-I. Sample Index showing the composition of thin films grown and the corresponding substrate pre-treatment and growth conditions.

	T1 Pre-treatment 600 °C UHV Anneal	T2 Pre-treatment H3PO4 etch + Air Annealing
G1 100 °C Growth + 300 °C Anneal	Ni, Ni-13Cr, Ni-23Cr	Ni
G2 400 °C Growth	Ni	Ni, Ni-5Cr, Ni-13Cr, Ni-14Cr, Ni-33Cr

4.3. Results

4.3.1. Effect of MgO Pre-Treatment

The AFM images of the MgO surface after T1 and T2 pre-treatment are shown in Figure 4-1(a,b). The MgO surface after T1 pre-treatment is smooth with an average RMS roughness of 0.18 ± 0.04 nm but no terrace structure is observed. The T2 pre-treatment yields a terrace structure with well-defined step-edges. The average RMS roughness of T2 substrates is 2.07 ± 0.47 nm. The higher roughness results from the residual features left behind by the etching of Ca spires (shown in Figure 3-6(c)) and the stacked terraces that result from high temperature annealing. The higher temperature annealing in the T2 pre-treatment results in wide terraces (50-100 nm) and the step edges are predominantly

oriented along the $\langle 110 \rangle$ direction. The T2 pre-treated substrates retain their terrace structure for at least 3 weeks when stored in a vacuum dessicator and yield good quality thin films.

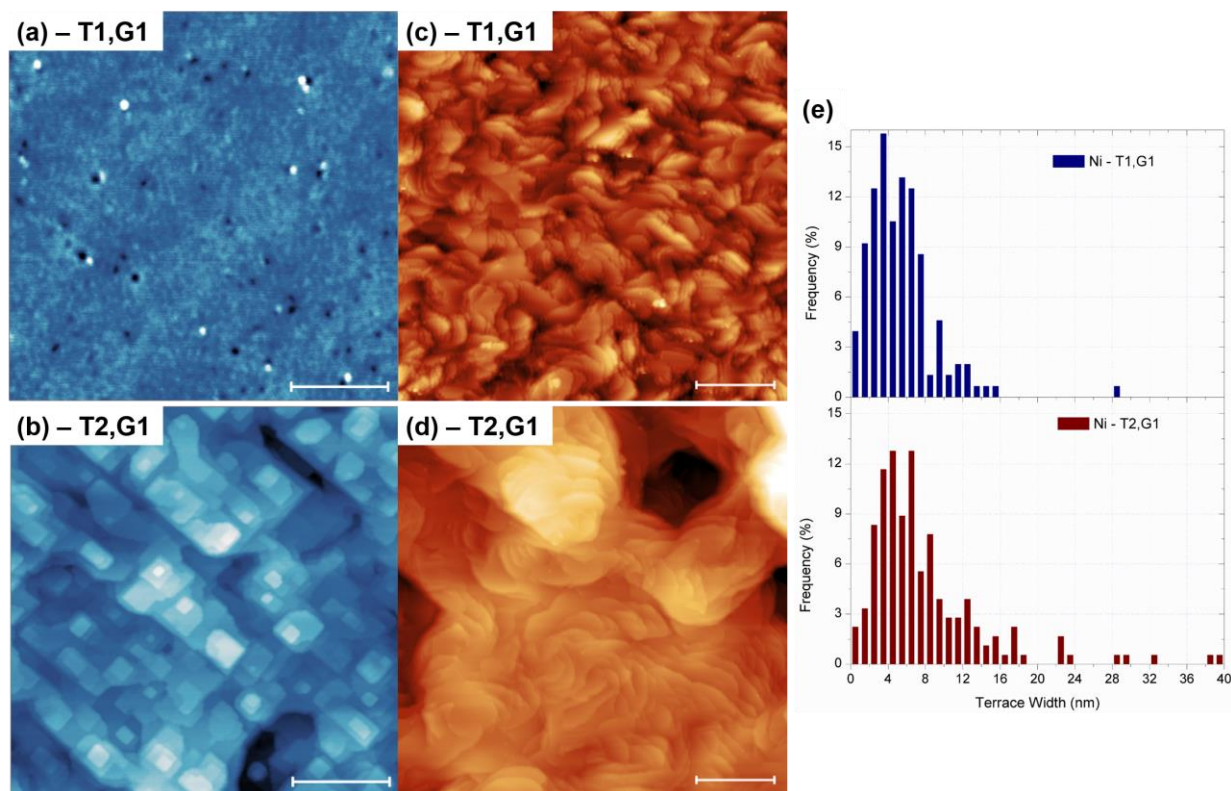


Figure 4-1. AFM images of MgO substrates after (a) T1 and (b) T2 pre-treatments (scale bar is 500 nm). STM images of Ni thin film grown on (c) T1 and (d) T2 substrates using the G1 growth recipe (scale bar is 50 nm). False color scale in AFM images is in nm.

STM images of the Ni thin films grown using G1 conditions on T1 and T2 substrates are included in Figure 4-1(c,d). The films show well-defined terraces on both the substrates. The average terrace width, measured along a line perpendicular to the step edges, is 5.26 ± 3.6 nm and 7.85 ± 6.3 nm on T1 and T2 substrates respectively. The large spread in the terrace width on T2 substrates is due to a few instances of very wide terraces (>25 nm) and the terrace width distribution is shown in Figure 4-1(e). The terrace

boundaries in Figure 4-1(d) are rounded and very few straight step edges are present. There is a long-range roughness associated with the etching-induced inhomogeneity for films on T2 substrates including the depression seen in Figure 4-1(d). Despite the similar terrace widths and step heights for Ni thin films grown on T1 and T2 substrates, the two surfaces look distinctly different. The terrace density is significantly lower on the T2 substrates and the terraces of films on T2 substrates are longer (measured parallel to the step edge). For identical terrace widths, long terraces observed on Ni films grown on T2 substrates results in a greater aspect ratio of the terraces when compared to films on T1 substrates. The lack of a texture on the T1 substrates results in explosive nucleation of Ni clusters while the nucleation density and consequently the terrace density is lower on crystalline T2 substrates. Therefore, the T2-MgO substrates that suppress the nucleation density during initial stages of film growth and yield thin films with long and wide terraces are recommended for good quality thin film growth.

4.3.2. Effect of Growth Temperature

AFM and STM images of Ni thin films grown using G1 and G2 conditions on T2 substrates are shown in Figure 4-2. The Ni thin film deposited at 100 °C (step 1 of G1 growth method) is rough with small islands and lacks the well-defined terrace structure (Figure 4-2(a)). The rms surface roughness of this surface is 0.37 ± 0.05 nm and the morphology is consistent with literature.²⁰ Subsequent annealing at 300 °C for 2 hours (step 2 of G1 method) leads to a smoother film (Figure 4-2(b)) and was discussed in detail in the previous section with reference to Figure 4-1(d,e). We grew Ni thin films (30-60 nm)

using the G2 conditions but did not achieve tunneling contact for STM imaging since the films are still discontinuous and below the percolation threshold for conduction.

Ex-situ AFM measurements of Ni films shown in Figure 4-2(c,d) illustrate the differences in the long-range surface morphology of G1 and G2 depositions. As expected from STM observations, the G1-Ni films are smooth with rms roughness of 2.7 ± 0.4 nm similar to a T2-treated MgO surface and the surface features are 3-8 nm in height. On the other hand, the G2-Ni film surface, shown in Figure 4-2(d), features an island-type morphology which is favored at higher temperatures. The high Ni/MgO interfacial energy (due to the 16% lattice mismatch which results in an incoherent interface) and increased surface mobility at 400 °C promotes island growth and leads to poor wetting to minimize contact area. The rms roughness of this surface is 9.3 ± 0.9 nm and the islands heights are in the 30-50 nm range with some islands exceeding 80 nm. The surface shown in Figure 4-2(d) is not sufficiently conductive to be measured with STM.

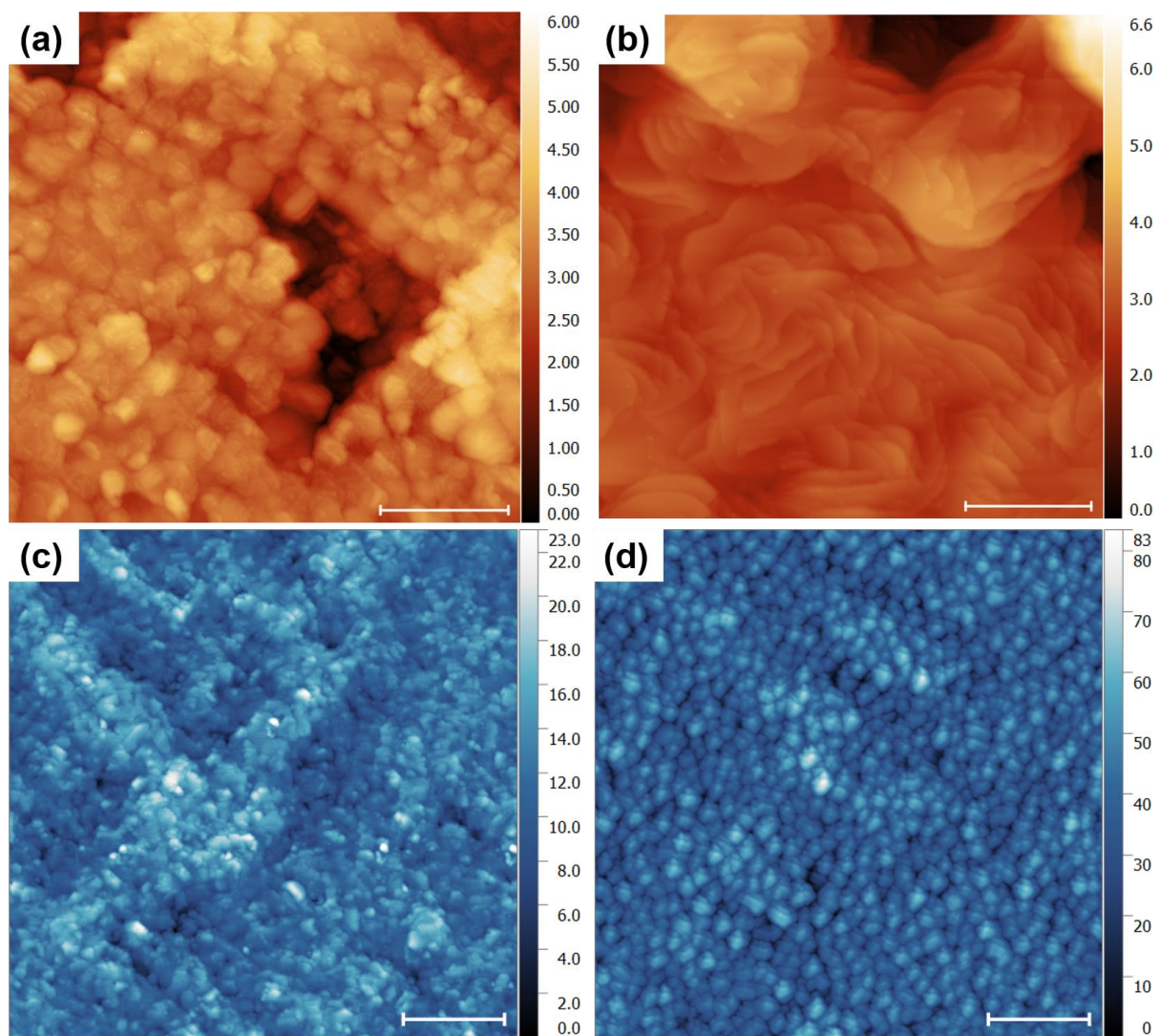


Figure 4-2. STM and AFM images show the effect of growth temperature on the Ni thin film morphology. STM images after (a) deposition at 100 °C (step 1 of the G1) and (b) post-deposition annealing at 300 °C for 2 hours (step 2 of G1) – same deposition as shown in Figure 1(d); scale bar is 50 nm. Ex-situ AFM images of Ni film grown using (c) G1 and (d) G2 growth conditions; scale bar is 1 μm . Color scale is in nm.

STM images of alloy thin films grown using G1 and G2 conditions are shown in Figure 4-3. The G2-type growth of the Ni-13Cr alloy yields a surface with crystalline terraces as shown in Figure 4-3(a). However, the alloy surface is interspersed with small 3D structures and these are likely intermediate compounds in the Ni-Cr system such as Ni_2Cr . The terrace sizes (shown in a histogram in Figure 4-3(c)) are consequently small due to the presence of

these 3D structures and have an average width of only 4.78 nm with a spread of 2.62 nm. Figure 4-3(b) shows the Ni-13Cr film grown using G2 conditions: in contrast to pure Ni thin films, the G2 growth condition yields continuous thin films in the alloy which are sufficiently conducting to be characterized with STM. The average terrace width is 11.57 ± 8.86 nm; the large width of the distribution is due to the numerous narrow terraces owing to the high density of step edges at the perimeter of the terraces. 40% of the terraces are less than 8 nm wide while the remaining 60% of the terraces are 10-30 nm wide. The terraces in alloy thin films are significantly larger than those obtained in Ni films and the combination of (T2,G2) is ideal for growth of good quality alloy thin films. At higher temperatures, we operate in the solid solution region of the Ni-Cr phase diagram thereby preventing the formation of intermediate compounds. Higher surface mobility due to the higher deposition temperature explains the smoothness of alloy films grown in G2 conditions. However, the contrast between Ni-Cr alloy films and the Ni films using the G2 growth route and the wider terraces obtained in alloy thin film warrants a deeper study of the effect of Cr on the growth behavior.

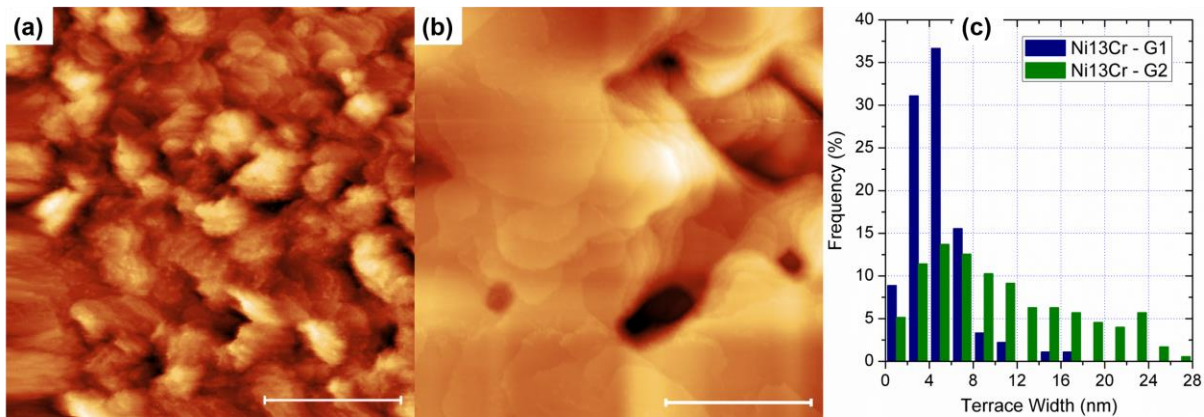


Figure 4-3. STM image of Ni13Cr alloy thin film showing the effect of growth temperature on surface morphology: (a) (G1,T1) conditions and (b) (G2,T2) conditions. Scale bar is 50 nm. (c) Terrace width distribution of Ni-13Cr thin film grown using G1 and G2 conditions.

4.3.3. Effect of Cr Alloying

In this section, we discuss the impact of increasing Cr concentration on the film terrace structure and roughness. For the same film thickness of ≈ 30 nm, Ni-Cr alloy thin films grown using G2 conditions on T2 substrates are continuous and electrically conductive and the full complement of STM and AFM images is available. The addition of just 5 wt.% of Cr (lowest in this study) is sufficient to alter the growth and yields continuous films amenable for STM characterization as shown in Figure 4-4(a). The derivative image (current image) is shown in this case due to extreme height variations. The film is very rough and is characterized by the coalescence of large islands. These islands have a flat top with well-defined terraces and a high density of step-edges at the island perimeters. With increasing Cr concentration, the films progressively smoothen as shown in Figure 4-4(b,c). This smoothening is represented in the variation of rms roughness of the films with increasing Cr concentration: Ni-5Cr, Ni-14Cr, and Ni-33Cr have a roughness of 3.63 ± 0.75 , 0.86 ± 0.04 , and 0.29 ± 0.13 nm respectively. The island in Ni-5Cr image shown in Figure 4-4(a) is ≈ 11 nm and the overall island height decreases with increasing Cr content with islands only 6 nm and 2 nm in case of Ni-14Cr (Figure 4-4(b)) and Ni-33Cr (Figure 4-4(c)) respectively. The terrace structure also changes with increasing Cr concentration and straighter step edges are observed indicating a change in step edge energetics with increasing Cr content.

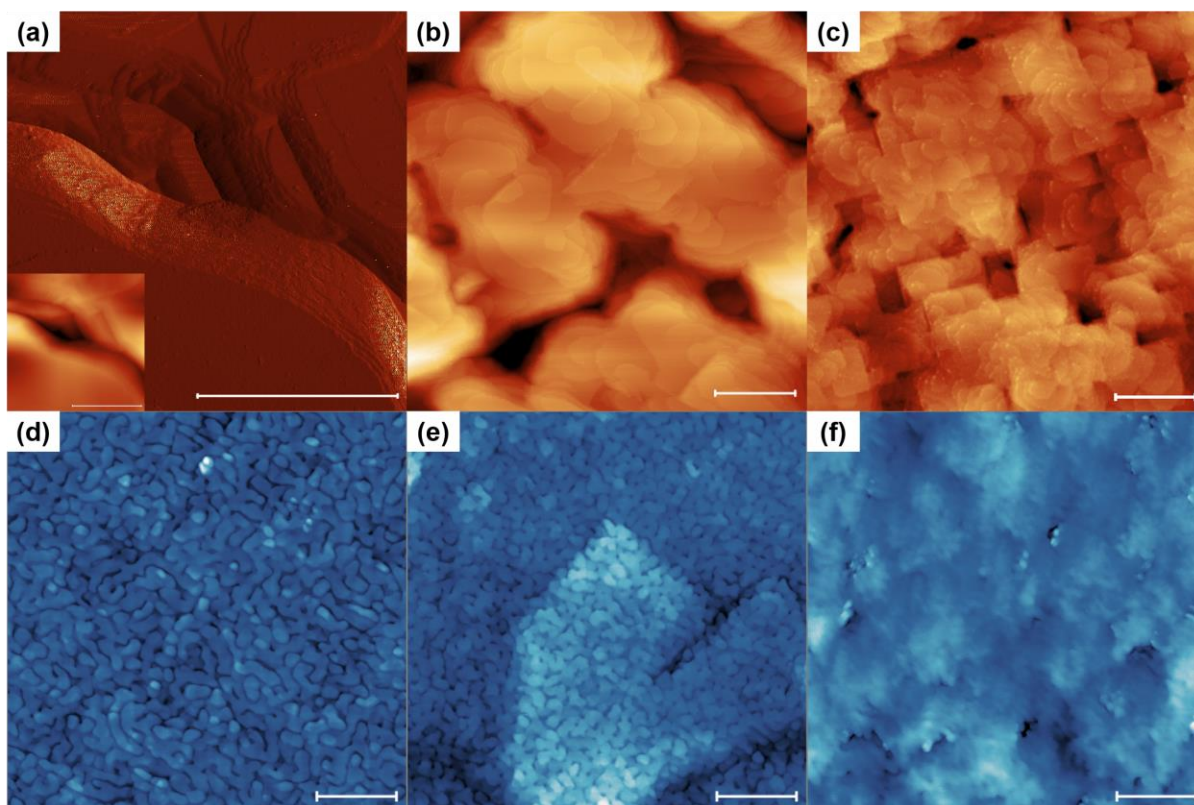


Figure 4-4. STM and AFM images of alloy thin films showing the effect of Cr addition on surface morphology: (a,d) Ni-5Cr, (b,e) Ni-14Cr and (c,f) Ni-33Cr films grown on T2 substrates using G2 growth recipe. Scale in STM and AFM images is 50 nm and 1 μm respectively. The derivative STM image (current image) is shown in (a) due to large height variations in the image; the inset shows the topographic image.

This terrace structure of Ni-33Cr is closer to a Cr thin film grown on MgO shown in Figure 4-5. After deposition at room temperature (with a Cr flux of 0.29 nm/min), the surface is rough (Figure 4-5(a)) with no evident terrace structure except for the faint imprint of the underlying MgO substrate. After annealing at 550 $^{\circ}\text{C}$, the film smoothens and has well-defined terraces (Figure 4-5(b)). The Cr film has terraces with predominantly straight step edges indicative of good epitaxial matching with the MgO surface (Figure 4-1(b)). The epitaxial relationship for the Cr/MgO(001) system is $(001)\text{Cr}|| (001)\text{MgO}$, $\langle 110 \rangle \text{Cr} || \langle 100 \rangle \text{MgO}$. High resolution images of the surface are shown in Figure 4-5(c,d)

and shows some circular step edges that are not resolved in the large area image shown in Figure 4-5(b). The atomic rows in Figure 4-5(c) which are along the $\langle 110 \rangle$ directions on the Cr(001) plane are oriented along the MgO $\langle 100 \rangle$ corresponding to the $\langle 110 \rangle_{\text{Cr}} || \langle 100 \rangle_{\text{MgO}}$ epitaxial matching that is expected in this system. The small segments in Figure 4-5(d) which present a different atomic structure are likely due to a trace adsorbate-induced reconstruction –adsorbate-induced reconstructions have been discussed in literature³⁰⁻³² but none of these match the structures observed here.

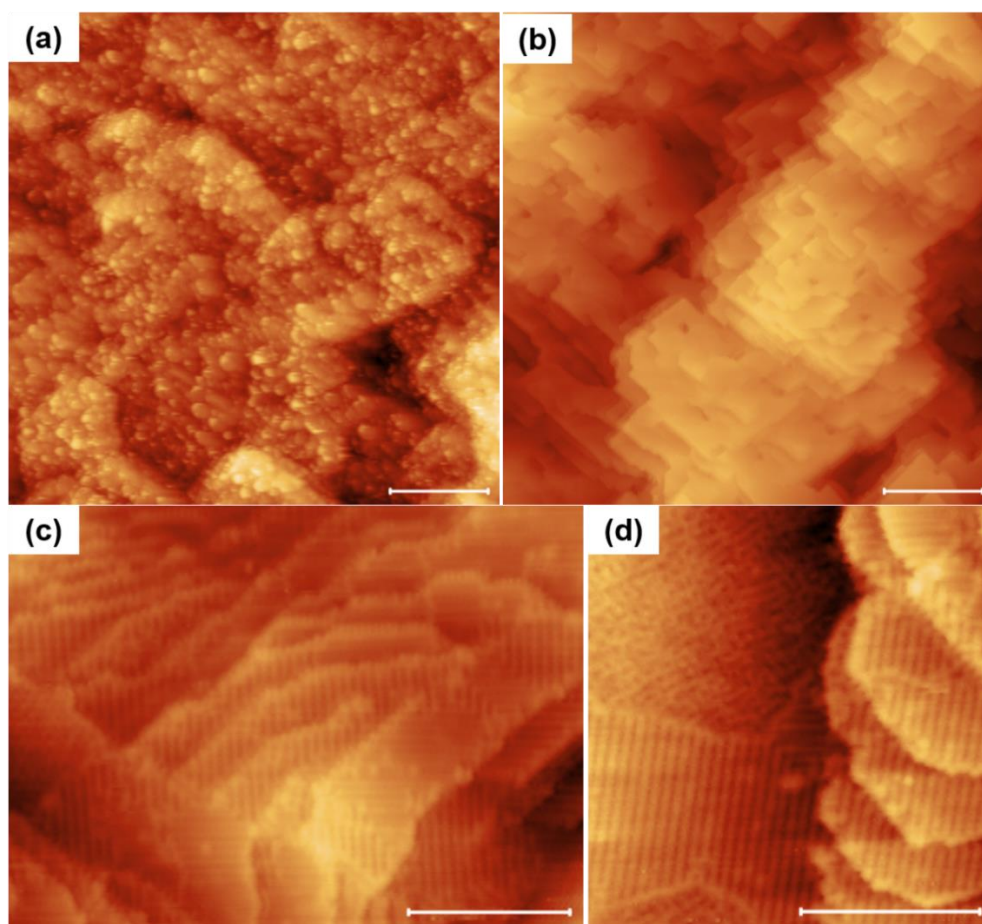


Figure 4-5. Large-area STM images of the Cr thin film grown on MgO(001): (a) as-deposited at room temperature, and (b) post-deposition anneal at 550 °C for 2 hours. Scale bar is 100 nm. High resolution images of the surface after 550 °C anneal showing (a) the atomic rows of the Cr film along $\langle 110 \rangle$, and (b) small pockets of trace adsorbate-induced reconstruction on an otherwise clean surface. Scale bar is 10 nm in (c) and (d).

It should be noted that the distribution of Cr throughout the alloy film is uniform as seen in the ToF-SIMS results obtained from a Ni₁₃Cr film (Figure 4-6). We see that the alloy composition is uniform throughout the film. Cr and Ni ion yields ratios are identical throughout the film and begin to drop at the same depth indicating no compositional segregation in the film. Since the ion yields of both elements vary differently as a function of their chemical environment, we cannot make quantitative conclusions based on ion yields. However, it is clear that Ni and Cr ion yields start to drop at the same depth (≈ 27 nm) and follow the same trend and plateau at ≈ 37 nm – this confirms, within the resolution of the instrument, that there is no segregation at the interface. Therefore, the changes in film growth with Cr additions are not due to preferential wetting of MgO by Cr atoms.

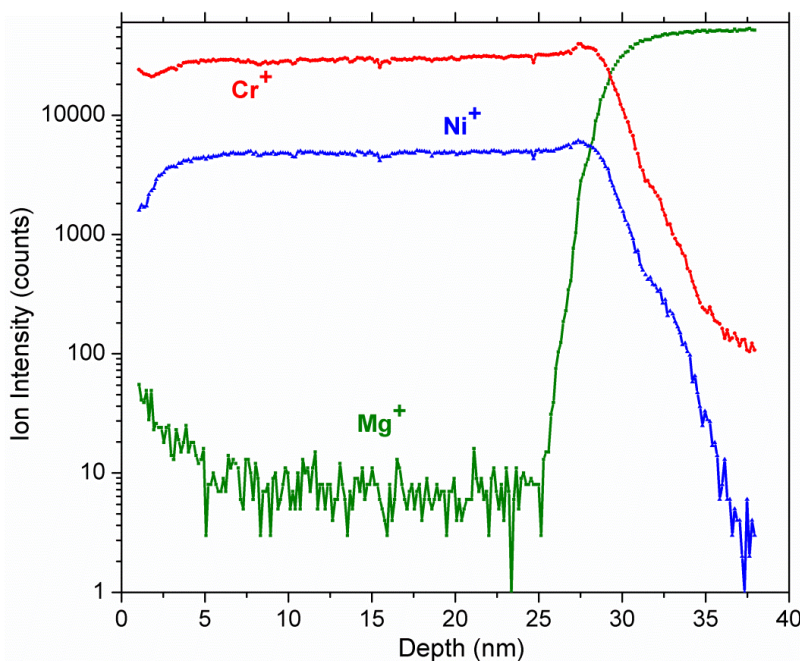


Figure 4-6. ToF-SIMS data of the Ni₁₃Cr sample grown on T2-MgO indicating uniform film composition and no segregation at the film-substrate interface.

AFM images of the Ni-5Cr, Ni-14Cr, and Ni-33Cr alloy films are shown in Figure 4-4(d-f). Consistent with the observations in STM, roughness of the film decreases with increasing Cr concentration. In addition, the island stacks prevalent in lower Cr content alloys are almost absent in the Ni-33Cr alloy. The variation of island stack heights measured from AFM images as a function of Cr concentration is shown in Figure 4-7. The height of an island stacks is measured from AFM images except for Ni-33Cr film where the island height is obtained from STM image. The alloy films are markedly different from Ni film (shown in Figure 4-2(d)) with the former characterized by wider but continuous islands while the latter consists of smaller but discontinuous islands. The average width of the island stacks in Ni-5Cr and Ni-14Cr films is nearly identical measured as 119.6 ± 24.47 nm and 114.24 ± 18.33 nm respectively. Ni islands are smaller with an average width of 104.34 ± 16.31 nm. The average island stack height decreases with increasing Cr content in the alloy: the addition of only 5wt.% Cr to the matrix results in a 70% reduction in the island height and the decrease continues to the point where individual islands are barely distinguished in the AFM images of the Ni-33Cr film. From these findings, we can conclude that the addition of Cr to the Ni matrix changes the initial wetting of the MgO and the subsequent film growth. The reduced height of the islands with increasing Cr content also suggests that interlayer diffusion is improved. An important kinetic factor that is likely affected by the Cr addition is the Ehrlich-Schwoebel (E-S) barrier.³³⁻³⁵ With increasing Cr content of the alloy, the E-S barrier decreases which results in decay of large islands as atoms can diffuse across step edges and leads to an overall flattening of islands as seen in the images in Figure 4-4 and the plot in Figure 4-7.

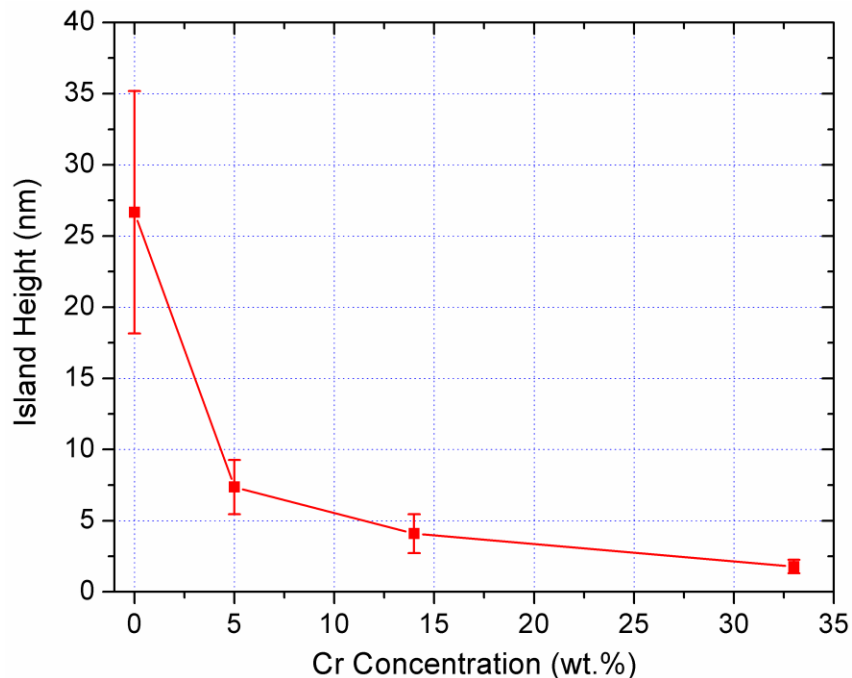


Figure 4-7. Variation of island heights in alloy thin films as a function of Cr concentration. The island heights are measured from AFM images except for the Ni-33Cr sample where STM images are used as the individual islands are not distinguished in AFM images.

4.4. Discussion

The growth of smooth Ni and NiCr thin films on MgO(001) was demonstrated and we will now discuss the important factors that affect the initial nucleation and growth process which manifests itself as a change in the terrace widths and/or surface morphology of the films.

The preparation of the MgO surface has a significant impact on the initial nucleation density of islands and affects the surface structure of the films as shown in Figure 4-1. The terraces of Ni film grown on T2 substrates are longer compared to films grown on T1 substrates and consequently have a greater aspect ratio (length/width ratio). The T1-MgO surface promotes greater nucleation density, which leads to the smaller terrace/island

sizes observed. This is a common observation on “glassy” substrates which are relatively smooth but possess chemical disorder and nanoscale inhomogeneities facilitating heterogeneous nucleation. The T2 surface which shows very well-defined crystalline ordering and the cube-type terrace structure typical for MgO promotes the formation of terraces in the metal overlayers. The T2 preparation favors a smaller nuclei density and thus larger crystallites, which can be concluded from the comparison of Figures 4-1(c,d). High temperature deposition (G2) leads to de-wetting of the Ni thin film and is independent of the MgO substrate pre-treatment. A discontinuous thin film even on the glassy T1-substrate suggests that the de-wetting is a consequence of the high interfacial energy between film and substrate. As a consequence of the de-wetting, the electrical conduction is reduced and thus contact is insufficient for STM measurements.

The surface morphology also exhibits distinct differences in terrace shape and spatial arrangement when comparing G1 and G2 growth modes, and an even larger variability as a function of Cr-concentration. A helical or screw-like arrangement of the terraces is seen in Ni-depositions using T2-G1 and T2-G2 and in most alloy thin films, but not in the low-T first step of T2-G1 (Figure 4-2(a)). The helical screw-like pattern has its origin in screw dislocations that are propagated during film growth. Possible sources of dislocation include inheritance from the substrate due to the T2 etch and anneal process, incoherent meeting of growth fronts and at the interface during growth to relieve mismatch strain.³⁶⁻⁴⁰ The terrace width is controlled by the pitch of the dislocation and remains fairly constant for all experiments discussed here. The Ni/NiCr islands grow outwards from the dislocation core lengthening and widening the terrace as the process continues. The length of the terrace on the other hand increases with distance from the dislocation core and has been observed in

other systems where screw-dislocation mediated film growth prevails.^{36,37,41} A higher growth temperature such as the 400 °C used in G2 method will lead to a widening to the terrace farther from the core as seen in the terrace width distribution in Figure 4-3(c) which shows a greater terrace width for alloy films grown at higher temperatures. The long-range helical arrangement of the terraces is mostly retained and is identical for all alloy experiments. The large misfit at the (001)Ni||(001)MgO interface can lead to recrystallization and local reorientation of the Ni crystallites in order to relieve the strain energy. However, such a recrystallization is only reported for growth temperatures (400 °C for G2) for a critical film thicknesses exceeding 50 nm which is outside the range of our experiments.²⁵ A slight reduction in the interfacial misfit with Cr alloying¹⁸ is expected to further increase the critical film thickness and recrystallization is not expected to have a significant impact on the alloy growth. The strong impact of Cr concentration on the film morphology is, therefore, attributable to the atomistic processes of growth and the interfacial chemistry rather than considerations of epitaxy as observed in the growth of $\text{Cr}_x\text{V}_{1-x}$ thin films on MgO(001).⁴²

It has been shown that Ni strongly interacts with the oxygen ions on the MgO surface and preferentially forms a covalent polar bond at the anionic sites while Cr only has a weak interaction on anionic sites of MgO surface.^{43–45} In any given alloy deposition experiment, the anionic adsorption sites are expected to be occupied by Ni. In this scenario, we posit that the weakly interacting Cr atoms adsorb on the nearby cationic site (occupying up to $\approx 14\%$ of the sites in Ni-14Cr). The presence of Cr on this site will statistically hinder the Ni occupation on anionic sites and increase the Ni-Ni distance towards equilibrium lattice spacing locally reducing strain and thereby leading to local stability. These local chemical

changes on the surface due to the presence of Cr are suggested as a model to explain the improved wetting of the MgO substrate during the initial stages of growth of alloy thin films which can consequently lead to smoother films.

4.5. Conclusions

We have demonstrated the growth of smooth Ni(001) and Ni-Cr(001) alloy thin films with wide, well-defined terraces on MgO(001). High temperature deposition at 400 °C on acid-treated substrates is recommended for obtaining the best quality Ni-Cr alloy thin films. The growth of thin films in this system is mediated by screw dislocation at the film-substrate interface which leads to the characteristic helical pattern of the terraces. Increasing Cr concentration in the alloy leads to a decrease in Ehrlich-Schwoebel barrier as manifested by progressively smoother films with large terraces. The drastic reduction in surface roughness and changes in film growth mechanism with Cr alloying are mainly driven by changes in the interfacial chemistry. The study of NiCr system is uniquely suited to further our understanding of thin film growth. The near constant lattice mismatch between NiCr-MgO up to 35wt% Cr enables us to decouple the impact of interfacial reactions, and local energy barriers such as the Ehrlich Schwoebel barrier, and the role of the strain field mitigated by lattice mismatch. In addition, such a method for the growth of thin films of Ni-Cr alloys, which are recognized for their exceptional corrosion resistance, opens up a new pathway for the study of reactivity of these alloys as a function of alloy composition.

References

1. Calvarin, G., Molins, R. & Huntz, A. M. Oxidation Mechanism of Ni—20Cr Foils and Its Relation to the Oxide-Scale Microstructure. *Oxid. Met.* **53**, 25–48 (2000).
2. Pollock, T. M. & Tin, S. Nickel-Based Superalloys for Advanced Turbine Engines: Chemistry, Microstructure and Properties. *J. Propuls. Power* **22**, 361–374 (2006).
3. Li, M. H. *et al.* Oxidation Behavior of a Single-Crystal Ni-Base Superalloy in Air. I: At 800 and 900°C. *Oxid. Met.* **59**, 591–605 (2003).
4. Jeng, S.-P., Holloway, P. H. & Batich, C. D. Surface passivation of Ni/Cr alloy at room temperature. *Surf. Sci.* **227**, 278–290 (1990).
5. Jambon, F., Marchetti, L., Jomard, F. & Chêne, J. Mechanism of hydrogen absorption during the exposure of alloy 600-like single-crystals to PWR primary simulated media. *J. Nucl. Mater.* **414**, 386–392 (2011).
6. Wood, G. C. & Chattopadhyay, B. Transient oxidation of Ni-base alloys. *Corros. Sci.* **10**, 471–480 (1970).
7. Viswanathan, R. High Temperature Corrosion of Some Gas Turbine Alloys. *Corrosion* **24**, 359–368 (1968).
8. de De Micheli, S. M. & Riesgo, O. Electrochemical study of corrosion in NiCr dental alloys. *Biomaterials* **3**, 209–212 (1982).
9. Tribbeck, T. D., Linnett, J. W. & Dickens, P. G. Oxidation of metals and alloys. Part 1.—Oxidation of nickel containing small amounts of chromium. *Trans. Faraday Soc.* **65**, 890–895 (1969).
10. Douglass, D. L. The oxidation mechanism of dilute Ni-Cr alloys. *Corros. Sci.* **8**, 665–678 (1968).
11. Essuman, E. *et al.* Protective and non-protective scale formation of NiCr alloys in water vapour containing high- and low-pO₂ gases. *Corros. Sci.* **50**, 1753–1760 (2008).
12. Hoflund, G. B. & Epling, W. S. Oxidation study of a polycrystalline Ni/Cr alloy I: room-temperature exposure to O₂. *Thin Solid Films* **307**, 126–132 (1997).
13. Hoflund, G. B. & Epling, W. S. Oxidation Study of a Polycrystalline Ni/Cr Alloy II. *Chem. Mater.* **10**, 50–58 (1998).
14. Ahmad, B. & Fox, P. STEM Analysis of the Transient Oxidation of a Ni-20Cr Alloy at High Temperature. *Oxid. Met.* **52**, 113–138 (1999).
15. Chattopadhyay, B. & Wood, G. C. The Transient Oxidation of Fe-Cr and Ni-Cr Alloys. *J. Electrochem. Soc.* **117**, 1163–1171 (1970).
16. Chan, K. S., Pan, Y.-M. & Lee, Y.-D. Computation of Ni-Cr phase diagram via a combined first-principles quantum mechanical and CALPHAD approach. *Metall. Mater. Trans. A* **37**, 2039–2050 (2005).
17. Hermann, K. in *Crystallography and Surface Structure* 265–266 (Wiley-VCH Verlag GmbH & Co. KGaA, 2011).
18. Chen, J. K., Farkas, D. & Reynolds, W. T. Atomistic simulation of an f.c.c./b.c.c. interface in Ni₃Cr alloys. *Acta Mater.* **45**, 4415–4421 (1997).
19. Karmazin, L. Lattice parameter studies of structure changes of Ni-Cr alloys in the region of Ni₂Cr. *Mater. Sci. Eng.* **54**, 247–256 (1982).
20. Lukaszew, R. A., Zhang, Z., Stoica, V. & Clarke, R. Annealing effects on (0 0 1) Ni films grown on MgO. *Appl. Surf. Sci.* **219**, 74–79 (2003).

21. McCaffrey, J. P., Svedberg, E. B., Phillips, J. R. & Madsen, L. D. Epitaxial variations of Ni films grown on MgO(0 0 1). *J. Cryst. Growth* **200**, 498–504 (1999).
22. Kumar, P., Krishna, M. G. & Bhattacharya, A. K. Effect of microstructural evolution on magnetic properties of Ni thin films. *Bull. Mater. Sci.* **32**, 263–270 (2009).
23. Takayanagi, K., Yagi, K. & Honjo, G. Roles of lattice fitting in epitaxy. *Thin Solid Films* **48**, 137–152 (1978).
24. Svedberg, E. B., Sandström, P., Sundgren, J.-E., Greene, J. E. & Madsen, L. D. Epitaxial growth of Ni on MgO(002)1×1: surface interaction vs. multidomain strain relief. *Surf. Sci.* **429**, 206–216 (1999).
25. Raatz, G. & Woltersdorf, J. Structure of metal deposits on ceramic materials studied in the Ni/MgO system. *Phys. Status Solidi A* **113**, 131–141 (1989).
26. Perry, S. S. & Merrill, P. B. Preparation and characterization of MgO(100) surfaces. *Surf. Sci.* **383**, 268–276 (1997).
27. Wang, C.-M., Kaspar, T. C., Shutthanandan, V., Joly, A. G. & Kurtz, R. J. Structure of Cr film epitaxially grown on MgO(0 0 1). *Acta Mater.* **59**, 4274–4282 (2011).
28. McClimon, J. B., Monazami, E. & Reinke, P. Interaction of C60 with Tungsten: Modulation of Morphology and Electronic Structure on the Molecular Length Scale. *J. Phys. Chem. C* **118**, 24479–24489 (2014).
29. Nečas, D. & Klapetek, P. Gwyddion: an open-source software for SPM data analysis. *Cent. Eur. J. Phys.* **10**, 181–188 (2012).
30. Gewinner, G., Peruchetti, J. C. & Jaéglé, A. Ordered oxygen overlayers on Cr(100) observed by leed and photoemission. *Surf. Sci.* **122**, 383–400 (1982).
31. Oka, H., Nakai, A. & Sueoka, K. Carbon-Induced Superstructure on Cr(001) Thin-Film Surfaces. *Jpn. J. Appl. Phys.* **46**, 5602–5606 (2007).
32. Schmid, M., Pinczolics, M., Hebenstreit, W. & Varga, P. Segregation of impurities on Cr(100) studied by AES and STM. *Surf. Sci.* **377**, 1023–1027 (1997).
33. Ehrlich, G. & Hudda, F. G. Atomic View of Surface Self-Diffusion: Tungsten on Tungsten. *J. Chem. Phys.* **44**, 1039–1049 (1966).
34. Schwoebel, R. L. & Shipsey, E. J. Step Motion on Crystal Surfaces. *J. Appl. Phys.* **37**, 3682–3686 (1966).
35. Michely, T. & Krug, J. *Islands, Mounds and Atoms*. **42**, (Springer Berlin Heidelberg, 2004).
36. Schlom, D. G. *et al.* Screw dislocation mediated growth of sputtered and laser-ablated YBa₂Cu₃O_{7-δ} films. *Z. Für Phys. B Condens. Matter* **86**, 163–175 (1991).
37. Morin, S. A. & Jin, S. Screw Dislocation-Driven Epitaxial Solution Growth of ZnO Nanowires Seeded by Dislocations in GaN Substrates. *Nano Lett.* **10**, 3459–3463 (2010).
38. Baronnet, A. Sur les origines des dislocations vis et des spirales de croissance dans les micas. *J. Cryst. Growth* **19**, 193–198 (1973).
39. Romanov, A. E., Pompe, W., Mathis, S., Beltz, G. E. & Speck, J. S. Threading dislocation reduction in strained layers. *J. Appl. Phys.* **85**, 182–192 (1999).
40. Bauer, M., Baudenbacher, F. & Kinder, H. Strain relaxation and formation of screw dislocations in YBCO films on MgO substrates. *Phys. C Supercond.* **246**, 113–118 (1995).
41. Eibl, O. & Roas, B. Microstructure of YBa₂Cu₃O_{7-x} thin films deposited by laser evaporation. *J. Mater. Res.* **5**, 2620–2632 (1990).

42. Kaspar, T. C. *et al.* Defect structure of epitaxial $\text{Cr}_x\text{V}_{1-x}$ thin films on $\text{MgO}(001)$. *Thin Solid Films* **550**, 1–9 (2014).
43. Neyman, K. M., Inntam, C., Nasluzov, V. A., Kosarev, R. & Rösch, N. Adsorption of d-metal atoms on the regular $\text{MgO}(001)$ surface: Density functional study of cluster models embedded in an elastic polarizable environment. *Appl. Phys. A* **78**, 823–828 (2004).
44. Matveev, A. V., Neyman, K. M., Yudanov, I. V. & Rösch, N. Adsorption of transition metal atoms on oxygen vacancies and regular sites of the $\text{MgO}(001)$ surface. *Surf. Sci.* **426**, 123–139 (1999).
45. Yudanov, I., Pacchioni, G., Neyman, K. & Rösch, N. Systematic Density Functional Study of the Adsorption of Transition Metal Atoms on the $\text{MgO}(001)$ Surface. *J. Phys. Chem. B* **101**, 2786–2792 (1997).

5. Atomic and Electronic Structure Changes during Oxidation of Ni(001)

Understanding the effects of oxygen adsorption on the atomic and electronic structure of metal surfaces is vital to improving our fundamental understanding of various processes such as oxidation, catalysis, and corrosion. In the context of this dissertation, the oxidation of Ni is studied under the same conditions as Ni-Cr alloys discussed in Chapter 6. Ni(001) is subjected to increasing oxygen exposures to understand the interplay between the chemisorbed phases and oxide formation at 300 °C. In addition, oxidation is performed at room temperature and at 450 °C to evaluate the temperature dependence of oxidation.

5.1. Introduction

The interaction of Ni with oxygen has been studied extensively, due to its prevalence in catalyst systems, using photoelectron spectroscopy (PES), Auger electron spectroscopy (AES), ion scattering spectroscopy (ISS), low energy electron diffraction (LEED), and scanning probe microscopy (SPM).¹⁻¹³ Oxide formation on Ni(001) surface after oxygen exposure is preceded by p(2×2) and c(2×2) chemisorbed structures (Figure 2-2). The stability of the two chemisorbed phases depends on the oxidation temperature and the partial pressure of oxygen.^{4,8,14} At room temperature, p(2×2)-O/Ni(001) is detected at low oxygen exposures (<2 L) and readily converts to c(2×2) structure with continued oxygen exposure. Full coverage of c(2×2) at room temperature is detected at ≈40 L where NiO formation is initiated. In contrast, oxide formation at 100 °C requires at least 120 L before the first nuclei are formed.^{4,8} Similar observations of oxide formation at room temperature and chemisorption structures at higher temperatures were made by Baumer et al.¹⁴

During oxidation at 100 °C, the $c(2\times 2)$ formation initiates restructuring of step edges (shown in Figure 2-3) into mutually perpendicular edge segments.⁸ The suppressed oxide nucleation at higher temperatures was explained on the basis of step edge restructuring whereby oxide nucleation is restricted to the corners of intersecting edges.^{8,15,16} Annealing the Ni surface after oxidation at room temperature at 600 K or greater in UHV results in massive surface reorganization to form oxide crystallites on an otherwise metallic $c(2\times 2)$ surface.⁴ The transformation of the room temperature oxidation products into the $c(2\times 2)$ phase suggests that it is more stable at higher temperatures than the oxides at least in UHV conditions (low pressures). This stability, in conjunction with suppressed oxide nucleation, explains the greater amounts of oxygen required to initiate oxide nucleation on Ni(001) at elevated temperatures.

In this chapter, the evolution of the atomic and electronic structure of the Ni surface during oxidation at 300 °C is presented. The oxidation conditions of the Ni-Cr alloys are replicated so that the results can be directly compared with the alloy oxidation results discussed in Chapter 6. The spatial variation of the LDOS is captured in the STS maps and the tunneling spectrum of the metal surface is contrasted with that of the chemisorbed phase and the oxide. We demonstrate that the $c(2\times 2)$ -O/Ni(001) phase has a characteristic signature in the tunneling spectra and it is highly stable at the temperatures studied. We also oxidize Ni at room temperature and determine the stability of the oxidation products during post-oxidation annealing. The gaps in literature on the initial stages of oxidation of Ni are addressed and future experiments are suggested to address further questions that have come up from the current work.

5.2. Methods

Materials The experiments are performed in an Omicron Nanotechnology Variable Temperature SPM system under ultrahigh vacuum (UHV) conditions with base pressure of $<3 \times 10^{-10}$ mbar. Ni thin films were fabricated by electron-beam evaporation (Mantis Deposition Ltd.) on pre-treated MgO(001) substrates (CrysTec GmbH) using the growth recipe outlined in Chapter 4. Oxidation is performed by backfilling the UHV chamber with O₂ (99.98%, Matheson Tri-gas Inc.) to the desired partial pressure. The coverage of oxygen is expressed in Langmuir (L) where 1 L (= 10^{-6} torr-s) corresponds to an exposure of 1×10^{-6} torr in 1 second.

Characterization The surface structure of the as-deposited and oxidized films is characterized in-situ by scanning tunneling microscopy and spectroscopy (STM/STS). Imaging and spectroscopy are performed with atomically sharp W-tips which were prepared by electrochemical etching with 1 M NaOH. The STM images, measured usually with a resolution of 512×512 pixels, were analyzed using WSxM¹⁷ and Gwyddion.¹⁸ STS maps were analyzed as outlined in section 3.5.2. The ideal conditions for imaging on metallic Ni are low bias voltage (<0.15 V) and high feedback current (>0.5 nA) while best resolution for oxides is achieved at 2 V or higher with a feedback current of 0.1 nA. This makes it impossible to image both regions of the same surface simultaneously with good resolution. Tunneling spectra are recorded between 2 and -2 V or 3 and -3 V at a set-point current of 0.1 nA. Since the voltages are much higher than the ideal conditions for imaging on metal surfaces, recording STS maps on the metal Ni films proved to be difficult due to the strong tip-sample interaction at high voltages as discussed below:

We observed that the oxidized surfaces are prone to sudden changes midway through the imaging due to strong interactions of the tip with the oxygen chemisorbed surface. One such example is shown in the STM image after 30 L oxidation in Figure 5-1(a) where the lower portion has nano-scale features on the surface and the upper portion appears smooth; the corresponding $(dI/dV)/(I/V+\epsilon)$ map is shown in Figure 5-1(b). The region where the tip change occurs is clearly visible. In the bottom portion, we are able to clearly identify the step edges while the spectra in the upper region are noisy. The averaged STS curve before and after the tip change is shown in Figure 5-1(c) and the trend of the spectra is similar in both cases. However, the spectral noise from the upper region is higher and the $(dI/dV)/(I/V+\epsilon)$ curve from the region that appears featureless has numerous kinks with a greater overall error bar. Therefore, the STS spectra can be used to differentiate the metal surface from the oxide and/or chemisorbed species while quantitative measures might be rendered difficult.

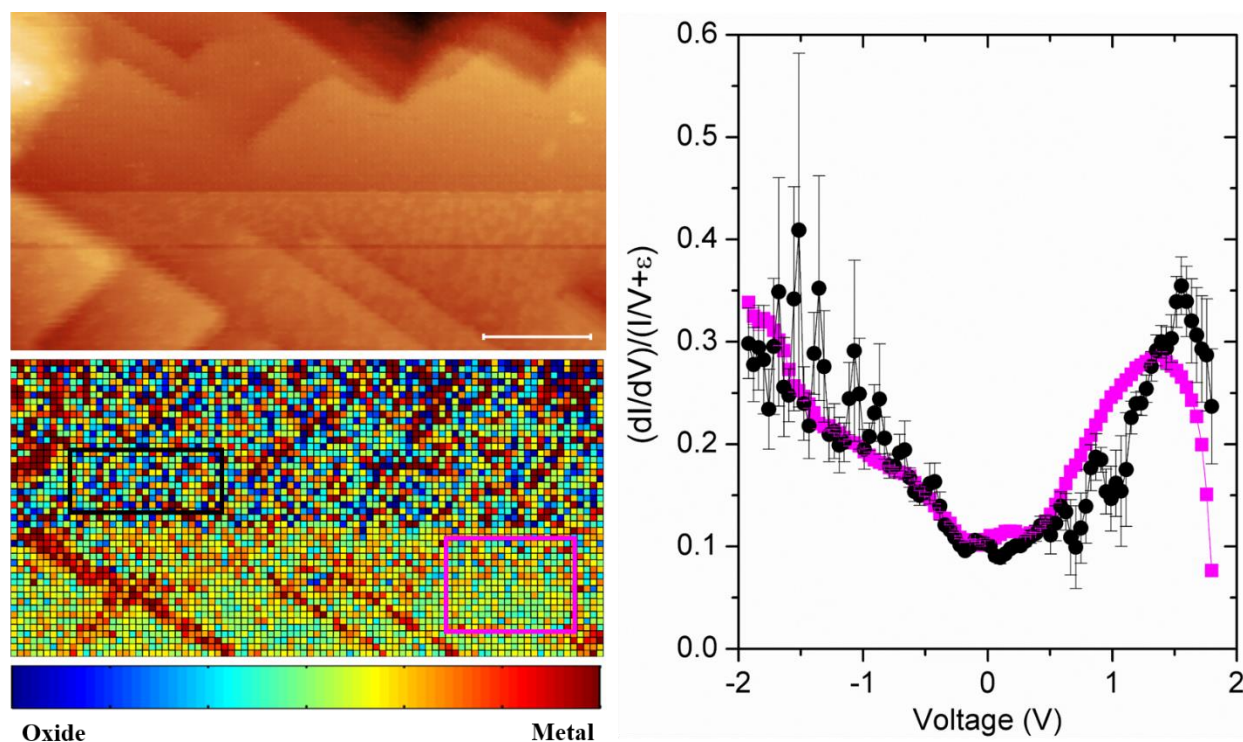


Figure 5-1. Variation of tip character during grid spectroscopy: the region when nanoscale features are imaged corresponds to good quality spectra (pink curve) while the featureless region in the upper portion of the image corresponds to noisy spectra (black curve).

In Figure 5-2, the difference in tunneling contrast most likely due to a switch in the tip termination (change from W tip to an O-termination) is shown after 2 L oxidation: depending on the tip termination, the step edges either present a high (Figure 5-2(b)) or low density of states (Figure 5-2(d)). This variation in tunneling contrast is only observed while measuring the surface after 2 L and 7 L oxidation and not observed either on pristine metal or after 30 L oxidation. Averaged STS spectra from the terrace region and step edges are shown before and after the tip change: regions at the edge of a step has a higher LDOS due to electron tunneling from the side (i.e., the step) and is observed in the first case while the contrast is reversed in the case of O-termination and the regions adjacent to a step edge appear less conductive (lower LDOS).

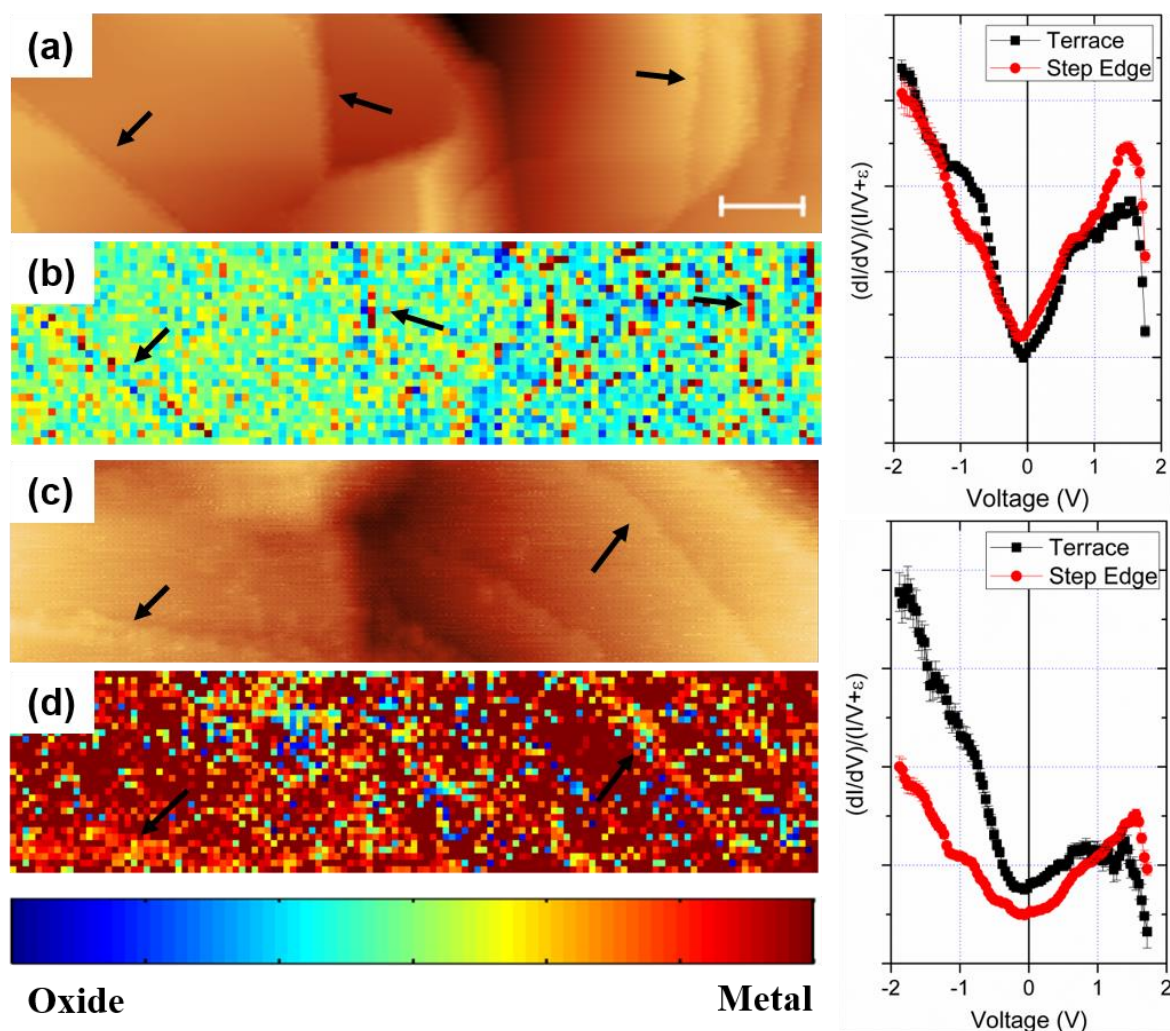


Figure 5-2. Contrast changes in the conductance maps due to changes in tip termination: (a,b) W-terminated tip when regions near the step edge appear more conductive, (c,d) likely O-termination at the tip resulting in contrast reversal.

5.3. Results and Discussion

5.3.1. Ni Oxidation at 300 °C

5.3.1.1. Topography Changes during 0-180 L Oxidation

The evolution of the surface during oxidation is captured in the STM images shown in Figure 5-3. The as-deposited Ni surface shown in Figure 5-3(a) is characterized by well-defined, circular terraces as discussed in Chapter 4. After the first 2 L oxidation step (at

2×10^{-9} mbar), no changes are observed on the surface as seen in Figure 5-3(b). The terrace widths are similar to the metallic surface and the step edge structure is also unchanged. After the second 5 L oxidation (total of 7 L) at 5×10^{-9} mbar, there are still no observable changes to the step edge structure but the terrace width decreases with oxygen exposure and multiple instances of step bunching as shown in Figure 5-3(c) are observed. Under these conditions, a combination of $p(2 \times 2)$ and $c(2 \times 2)$ O-chemisorbed phase is expected although this could not be unambiguously confirmed with atomic resolution in this experiment. No large scale reorientation of step-edges reminiscent of the $c(2 \times 2)$ O-chemisorbed phase on Ni(100) is observed at these exposures which confirms that a complete $c(2 \times 2)$ O-layer has not formed.⁸ An additional 23 L oxidation at 2×10^{-8} mbar (total of 30 L), however, results in significant surface reorganization and the circular step edges transform to straight edges with mutually perpendicular segments indicating the formation of the $c(2 \times 2)$ phase.⁸ The step edges are oriented along the $\langle 100 \rangle$ directions on the surface. The heavily step-bunched surface and the step-edge reorientation after oxidation even at a low temperature of 300 °C is indicative of a massive atomic flow initiated by the presence of oxygen atoms. The surface is characterized by large isolated terraces (≈ 50 nm wide) which are surrounded by step bunched terraces. Some pyramidal structures are observed on the surface which result when the steps propagating in the four different $\langle 100 \rangle$ directions intersect on the surface. The delayed transformation of the metallic surface into a fully chemisorbed $c(2 \times 2)$ phase is not surprising as the sticking coefficient of oxygen on Ni(001) drops from close to unity to ≈ 0.1 after the first Langmuir of oxygen.⁶ Under these conditions, the minimum amount of oxygen required for the formation of a monolayer of $c(2 \times 2)$ -O/Ni(001) at 300 °C is between 7 and 30 L. With an

additional 50 L oxidation at 5×10^{-8} mbar (total: 80 L), no new features are observed. The pyramidal features on the surface are elongated after 80 L oxidation due to additional step flow. Similarly, additional 100 L oxidation (total of 180 L) did not change the long-range surface morphology in terms of the terrace and step edge structure.

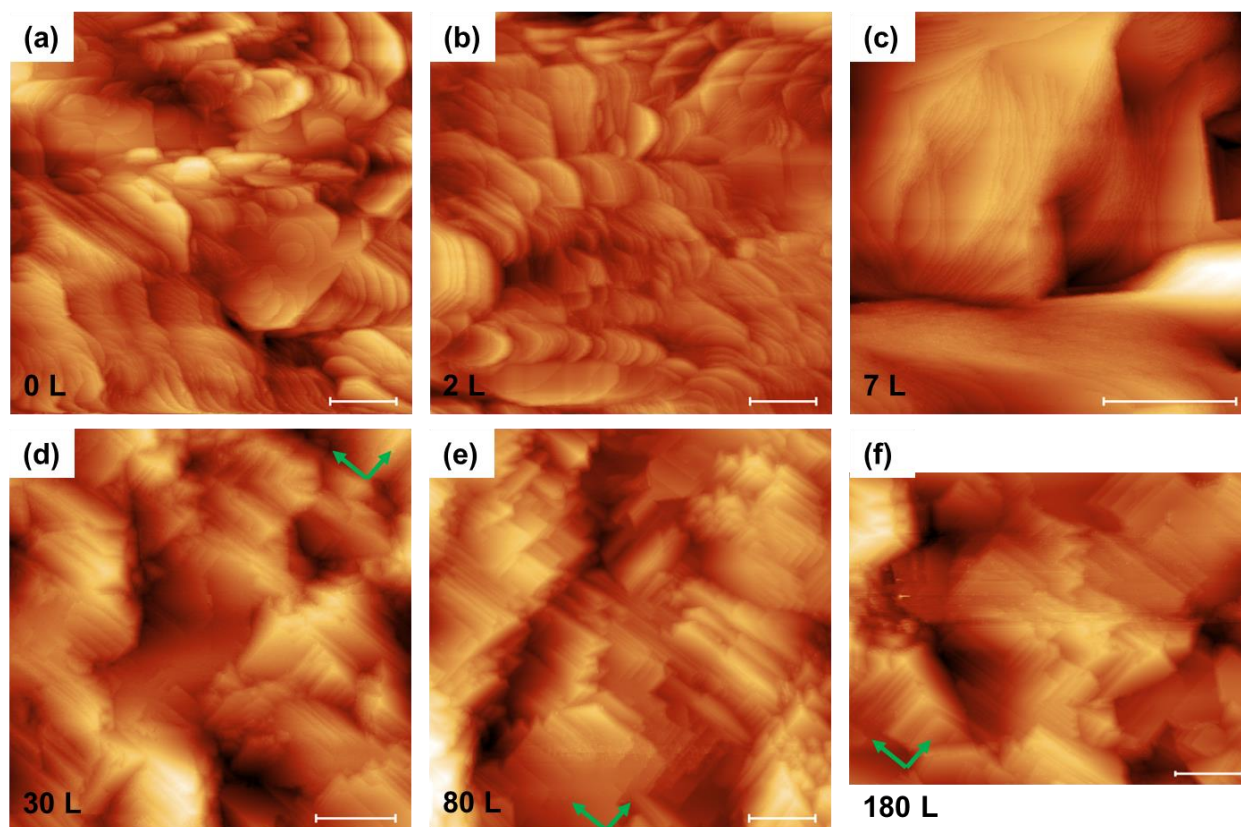


Figure 5-3. Sequence of STM images of the Ni surface showing the changes on the surface during oxidation at 300 °C: (a) as-deposited film, (b) 2 L, (c) 7 L, (d) 30 L, and (e) 80 L. The arrows indicate the $\langle 100 \rangle$ direction. Scale bar is 50 nm in all images.

Our main interest in this work was to capture the oxide evolution on the surface and the focus was, therefore, on STS measurements rather than achieving atomic resolution which is quite challenging on metal surfaces. The two measurements are often mutually exclusive with a blunt tip is preferable for spectroscopy to avoid frequent changes at the apex of the tip during voltage cycling. In contrast, atomic resolution requires an atomically

sharp tip so that maximum spatial resolution is achieved. Images of the facets of the pyramidal structures after 30 L and 80 L oxidation are shown in Figure 5-4. From these images, it can be seen that the pyramidal structures are step-bunched structures composed of isolated stacked terraces formed due to the $c(2\times 2)$ reconstruction-induced motion of step edges and eventual intersection. The inset in Figure 5-4(a) shows a high resolution image of a small pyramid structure where stacked edges are visible in the bottom face while right facet presents a different reconstruction. Based on the different step edge orientations surrounding the marked island, it is reasonable to assume that the observed reconstruction is a consequence of termination of different step edges. Figure 5-4(b,c) shows STM images after 80 L oxidation; the height variations does not allow for good contrast in the topography image (b) and the current image (c) is shown for clarity. Nanoscale islands are resolved on the surface after 80 L oxidation; however, they do not present a bandgap and were not observed after an additional 100 L oxidation. Another feature that is seen in these images is that left side of these stacked structures is resolved while the other side appears featureless; the same contrast difference is observed in the backward image. It is possible that the facet on the right side of these pyramidal structures in Figure 5-4(b,c) contains step edge segments oriented along the scanning direction.

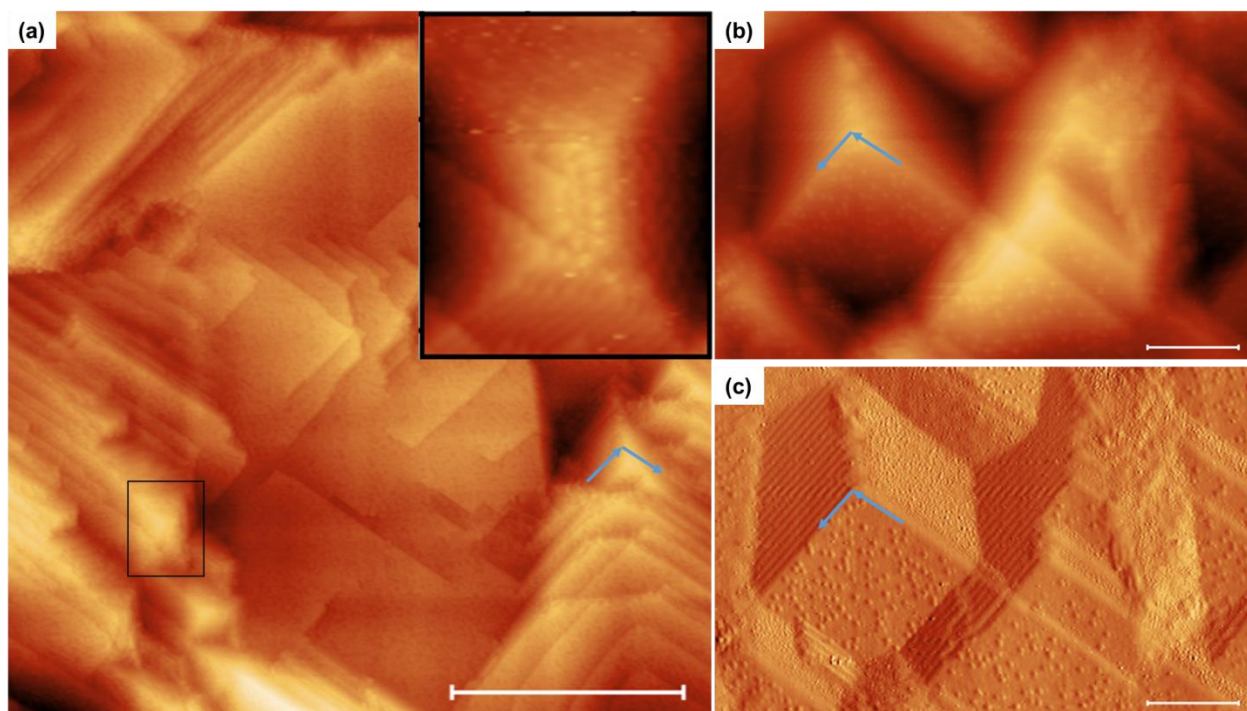


Figure 5-4. High resolution images of the stacked pyramid structures observed on the Ni(001) surfaces after (a) 30 L and (b,c) 80 L oxidation. Derivative image of (b) is shown in (c) for better contrast. Scale bar is 50 nm in (a) and 20 nm in (b,c). Blue arrows are pointers marking the orientation of the step edges.

5.3.1.2. Variation of LDOS with Oxidation

Tunneling spectra recorded after different stages of oxidation are shown in Figure 5-5(a). On Ni(001) surface, the STS curves presents a characteristic metal spectrum with a high density of states at Fermi level and a relatively featureless density of states (DOS). After the initial 2 L oxidation, the conductance curve remains unchanged and retains the characteristics of the metal surface. This is consistent with the unchanged topography discussed in the previous section. The electronic structure changes after 7 L oxidation and the density of states is reduced near the Fermi level consistent with literature.^{3,9} The minimum in the tunneling spectrum is shifted to 0.2 eV. The changes in the $(dI/dV)/(I/V)$ curves after oxidation is most striking after 30 L oxidation when a complete $c(2\times 2)$ -O

structure is presumably formed on the surface. Compared to the spectra after 7 L oxidation, the density of states near the Fermi level is further decreased after the formation of the $c(2\times 2)$ -O layer in the 30 L spectrum. In addition to the lowered LDOS, a small kink is observed at E_F and we find that this is characteristic of the chemisorbed surface. This feature persists even after additional 150 L oxidation (total=180 L) as seen in Figure 5-5(a) although it is weaker in comparison to 30 L spectrum. The decrease in the LDOS at E_F with continued oxidation after the formation of a complete $c(2\times 2)$ layer is negligible which suggests that the chemisorbed phase is stable under the conditions we have explored. The $c(2\times 2)$ structure is composed of O atoms occupying the four-fold hollow site on the Ni(001) surface^{19,20} and is at a height of 0.8 Å above the topmost Ni layer. We suggest that (i) the O-adsorbate layer reduces the tunneling efficiency by screening the underlying metal surface and leads to the reduced density of states with increasing oxidation or (ii) bond formation (i.e., electron transfer) during chemisorption reduces the LDOS.

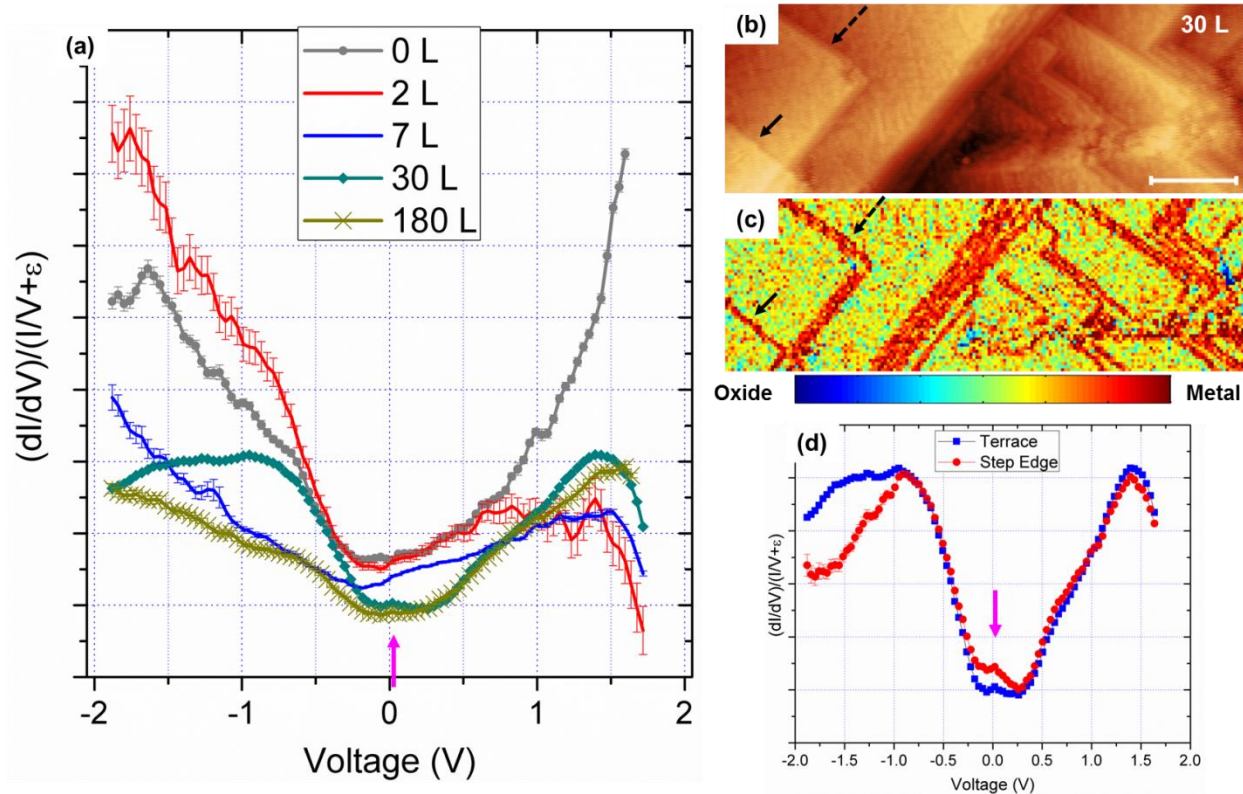


Figure 5-5. (a) Scanning tunneling spectroscopy curves after 0, 2, 7, 30 and 180 L oxidation at 300 °C, (b) STM image section of $c(2 \times 2)$ -O/Ni surface (scale is 10 nm), (c) corresponding $(dI/dV)/(I/V)$ map showing the difference in electronic structure on terrace and at step edge. The map is sliced at -0.1 V where contrast between terrace and step edge is maximum. Single and double steps are marked with solid and dotted arrows respectively. (d) Averaged STS curves from the surface and from the step edges after 30 L oxidation. Pink arrows point to the distinct signature of $c(2 \times 2)$ layer.

An STM image section and corresponding spectroscopy map after 30 L oxidation are shown in Figure 5-5(b,c). Averaged spectroscopy curves from the terrace and step edge region is shown in Figure 5-5(d). It is clear from the grid STS at -0.1 eV that the step edges have a higher density of states compared to the terrace and this difference is clear in the spectroscopy curves. While a higher density of states adjacent to the step edge is expected on any given surface due to additional tunneling contribution, the surface after 30 L oxidation is unique as all step edges including single and double steps are clearly identified compared to the initial metallic surface or after 2 or 7 L oxidation when only a few tall step

edges are distinguished in the STS maps. The maps on the 2 L oxidation were shown in Figure 5-2 where only some of the step edges are identified and finer features are not as well resolved as in the map shown in Figure 5-5. The conductance map after 80 L oxidation (not shown here) is similar to ones recorded after 30 L oxidation with all the step edges clearly distinguished.

5.3.2. Effect of Temperature on Ni Oxidation

5.3.2.1. Room Temperature Oxidation (200 L)

Figure 5-6(a) shows the Ni surface after 200 L oxidation at room temperature and the surface morphology is significantly different compared to a Ni surface oxidized at 300 °C (Figure 5-3). When Ni is oxidized at room temperature, the surface is characterized by the presence of small granular oxide particles with no evidence of the c-(2×2) O-chemisorbed structure and is consistent with data by Baumer et al.¹⁴ In contrast, no oxide structures are observed even after 180 L oxidation at 300 °C and is consistent with the delayed onset of oxide nucleation on Ni(001) with increasing temperatures.^{5,8,14} The overall terrace structure of the Ni surface is visible but the sharp step edges are replaced by smoother and more rounded edges. The epitaxial orientation of the oxide on Ni(001) at low temperatures is expected to be the NiO(111).^{1,4,8,14} It has been observed that the oxide thickness at low temperatures is only 2-3 layers in height and oxide growth stops after 1 nm at low temperatures. The granular oxides observed here are 0.3-0.6 nm in height after 200 L oxidation at 300 K and this suggests further oxidation at room temperature would result in vertical growth of the oxides.

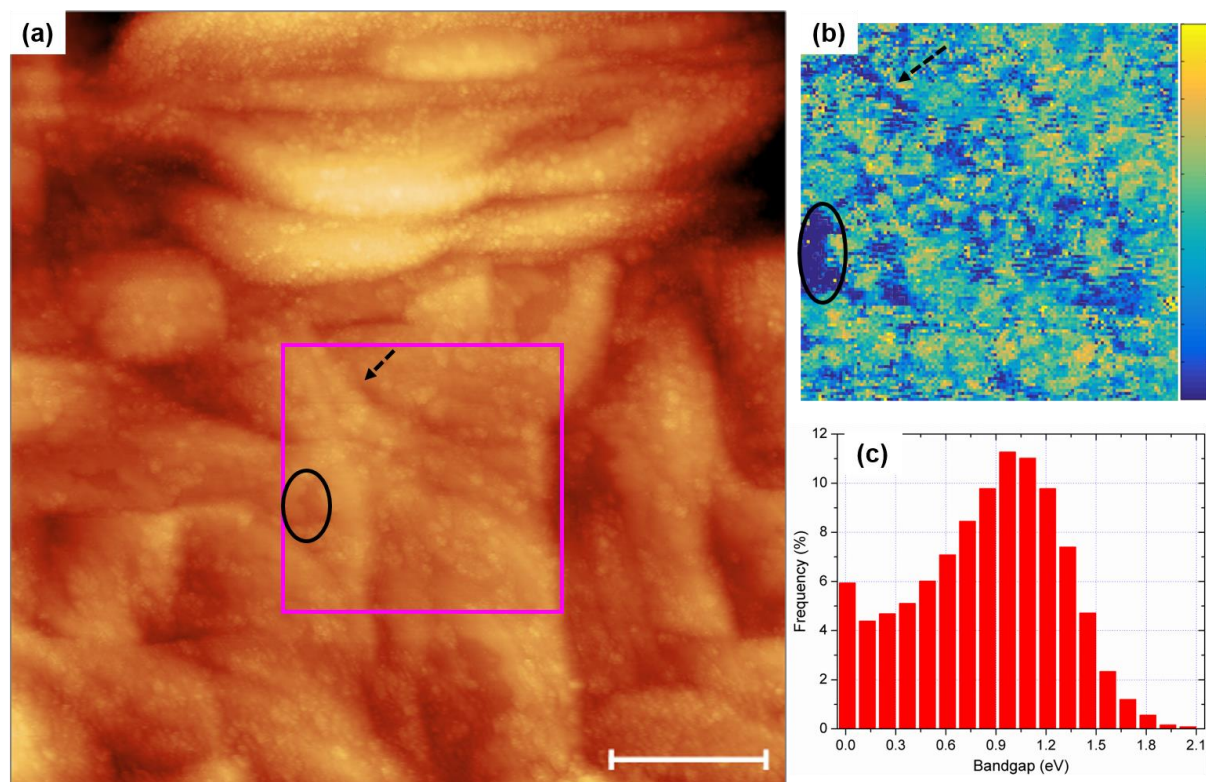


Figure 5-6. STM and STS data of a Ni surface after 200 L oxidation (in 1×10^{-7} mbar of O_2) at room temperature: (a) STM image of the surface showing the presence of small oxide particles; the imaging conditions are 2 V, 0.1 nA and scale bar is 50 nm, (b) bandgap map measured in the area marked by the pink square in (a); the ellipse and arrow in the image correspond to the same regions in the bandgap map; the color scale is from 0 to 2 eV, (c) distribution of bandgap on the surface populated from the bandgap map.

The bandgap map, measured on the marked region in the STM image, is shown in Figure 5-6(b) along with distribution of the bandgap values from the same area. A different color scale is chosen for the bandgap map to avoid confusion with the conductance maps shown earlier and the dark blue regions are metallic (zero gap) while yellow regions corresponds to regions with larger bandgap. The bandgap maps and STS spectra confirm that these small granules are oxide particles due to the presence of a bandgap. The bandgap histogram of the map area (Figure 5-6(c)) shows a broad distribution with an average gap value of 1.0 eV. The average STS spectra from the metallic and oxide regions (not shown

here) present typical spectra characteristic of metal and oxide. The characteristic kink at E_F exhibited by the $c(2\times 2)$ phase as shown in Figure 5-5 is not observed on the small exposed areas that are not covered with oxides. The yellow regions on the map which correspond to a large gap are always measured only at the apex of the oxide particles indicating that the measured bandgap is dependent on the height of the oxide. This suppression of the bandgap of the overlayer by the underlying metal surface has been described previously in literature and has its origin in the screening of the metal.²¹ In a perfect oxide, full bandgap is reached after 3-4 unit cells and the oxides observed are well below this limit.

5.3.2.2. Post-Oxidation Annealing at 450 °C

When the 200 L oxidized surface presented in section 5.3.2.1 is annealed at 450 °C for 40 minutes, massive surface reorganization leads to the formation of large, isolated nickel oxide structures on an otherwise $c(2\times 2)$ O-chemisorbed surface. The changes to the surface after annealing at 450 °C for 40 minutes are shown in Figure 5-7. The separation of a low temperature oxidized Ni surface into metallic and oxide regions after annealing in vacuum has been observed by Wang et al.⁴ and we now have quantitative information on the oxide coverage after this transformation. The STM topography image (4 V, 0.1 A) in Figure 5-7(a) shows the typical step-edge structure that is the fingerprint of the $c(2\times 2)$ -O chemisorbed structure interspersed with large oxide islands. The oxides do not have a clear, faceted shape and are 15-30 nm in size (lateral dimensions) and tend to nucleate at the corners of intersecting step edges. LEED studies have shown that NiO(111) transforms during annealing to yield NiO(001).^{5,14,22,23} Due to the $\approx 16\%$ lattice mismatch between

NiO(001) and Ni(001), it is not surprising that the oxide islands observed after the short annealing do not present a well-faceted structure and present an amorphous structure.

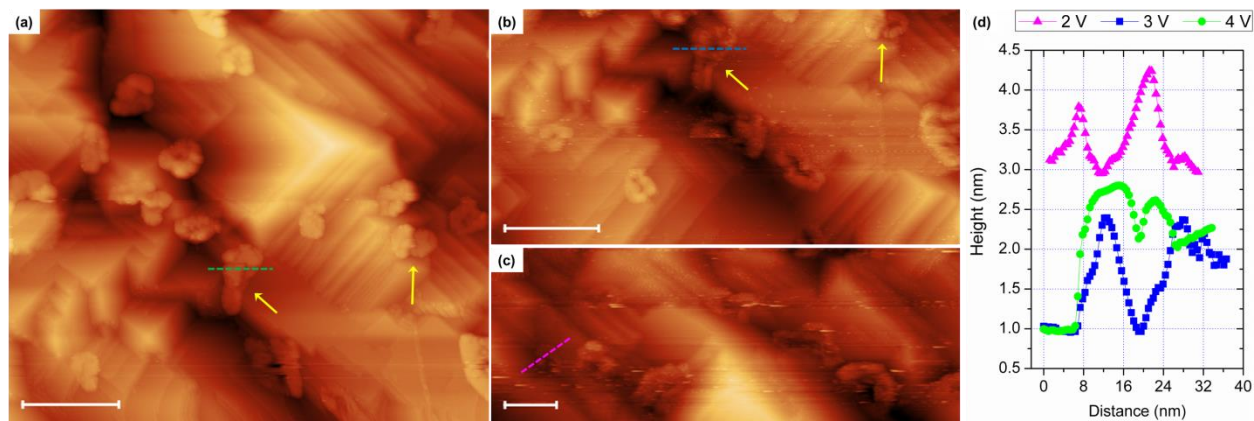


Figure 5-7. Scanning tunneling microscopy images of the Ni(001) surface after 200 L oxidation at room temperature and 450 °C anneal recorded at (a) 4 V, 0.1 nA, (b) 3 V, 0.1 nA, and (c) 2V, 0.1 nA; scale bar is 50 nm in all images. (d) Height profiles of oxide islands as a function of bias voltage. The arrows in (a) and (b) point to the same oxide islands and the 2V image in (c) is from a different region on the sample.

STM image in Figure 5-7(b) is recorded at 3 V, 0.1 nA and is a small section of the area imaged in Figure 5-7(a) and the arrows in both the images point to the same oxides. The oxide structure imaged at 3 V differs from the 4 V image due to the presence of a hole-like region in the middle of all the oxide structures. In addition to the crater in the center of the oxide island, the apparent height of the same island is slightly lower when imaged at 3 V in comparison to 4 V. The STM image recorded at 2 V, 0.1 nA presented in Figure 5-7(c) is from a different region on the sample. Increased streaking whilst imaging is evident from the image but the presence of craters at the center of most oxide islands is still discernible. It should be noted that the streaks are usually present in and around the oxide but rarely on the chemisorbed regions. Height profiles measured across oxide islands as a function of bias voltage is shown in Figure 5-7(d); the oxide island profiled is marked with dashed

lines in the STM images (Figure 5-7(a-c)). The same oxide island is compared at 3 V and 4 V and the curves are translated so that left terrace level is identical. On average, the apparent heights of oxides decreases and the craters increase in depth when the bias voltage is increased. The presence of an apparent crater in the center of the oxide suggests that the oxide is sufficiently thick to completely screen the underlying metal. This creates a scenario where no states are available for tunneling at lower bias voltages in the thickest regions of the oxide and these regions, which are at the center of the oxide structure, consequently appear like a crater (dark contrast) in STM images. The increasing crater depths measured with decreasing bias voltage support our theory that this voltage-dependent contrast is a consequence of the oxide electronic structure (large bandgap).

Electronic structure information of the surface is presented in Figure 5-8 with an STM image of the surface with its corresponding bandgap map and separated STS curves from the oxide (marked with black arrows) and O-chemisorbed region. The bandgap map clearly illuminates the two oxide structures on the surface, which have a nonzero bandgap, on an otherwise metallic surface with a $c(2\times 2)$ reconstruction; the O-chemisorbed region does not present a gap as shown earlier in Figure 5-5. The $(dI/dV)/(I/V)$ curve averaged from the two oxide structure captured in the bandgap map is shown in Figure 5-8(c) and has the typical curve of an oxide surface with no density of states in the gap region. The oxide structures present an average gap value of 0.9 ± 0.2 eV. The STS curve of the chemisorbed surface retains the characteristic kink at the Fermi level as shown earlier in Figure 5-5(a,d). The identical bandgap of the oxides obtained after annealing and the room temperature oxide layer is an interesting observation as the high temperature oxide islands are approximately 2 nm high (10 times as large as the granular oxides in Figure 5-6).

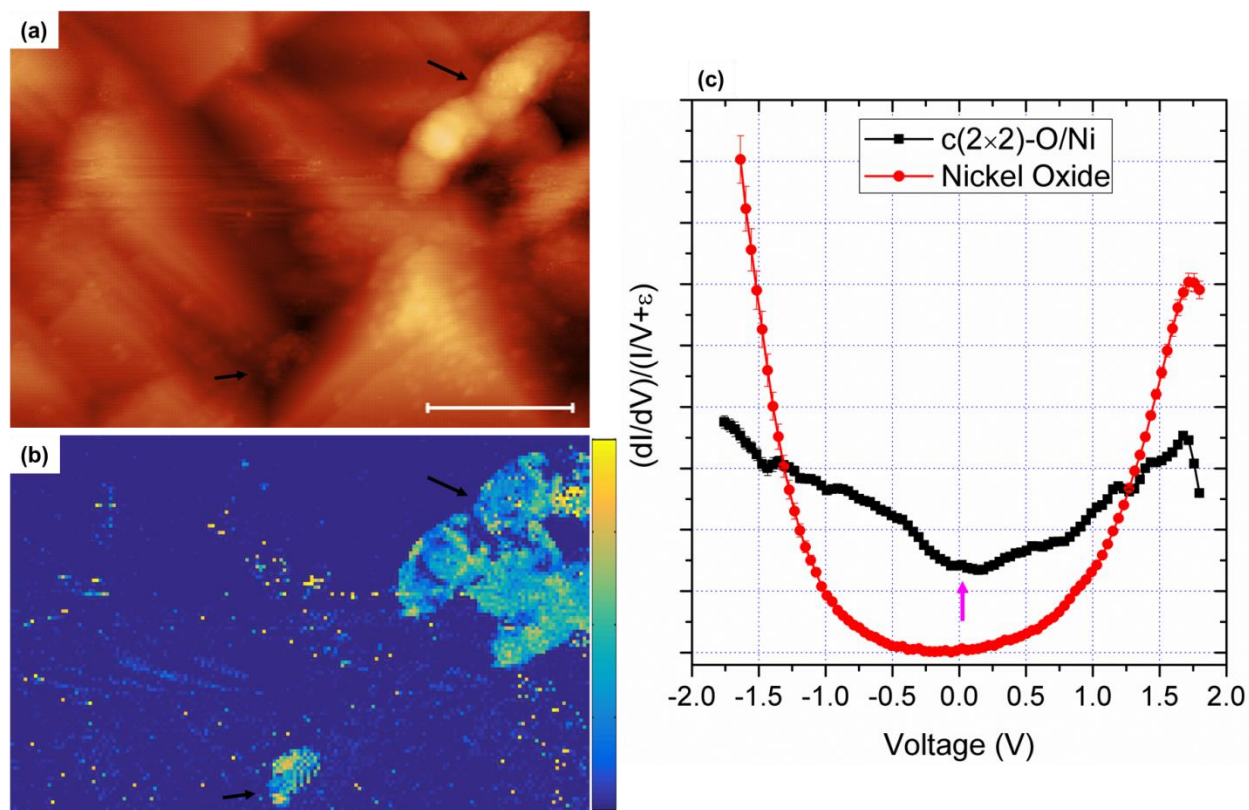


Figure 5-8. (a) STM image of the Ni(001) surface after 200 L oxidation at room temperature and 450 °C anneal; scale bar is 25 nm, (b) bandgap map of the image shown in (a); color scale is 0 to 2 eV, and (c) STS curves recorded from the chemisorbed surface and nickel oxide structures.

5.4. Summary

The different structures observed after the oxidation of Ni(001) is summarized in Table I. The oxidation temperature has a strong influence over the oxidation products that are observed with room temperature (RT) oxidation resulting in nucleation of small oxide particles while the same oxidation at 300 °C results in a $c(2 \times 2)$ chemisorbed structure. The $c(2 \times 2)$ reconstruction presents a characteristic signature in the tunneling spectra and can be used to differentiate it from the metal or the $p(2 \times 2)$. A complete $c(2 \times 2)$ layer is observed after 30 L oxidation at 300 °C and is accompanied by massive step edge restructuring into mutually perpendicular straight edge segments. Step edge motion during

oxidation at 300 °C results in residual pyramid structures on the surface when moving edges intersect (step bunching). Sustained oxidation does not form oxides but more pyramidal structures are observed due to the step edge motion.

Table 5-I. Various structures observed after each oxidation step on Ni(001)

Oxidation Parameters	Structures observed	Bandgap (eV)
≤ 7 L at 300 °C	p(2×2) – no step edge restructuring	0
$7 \leq X \leq 30$ L at 300 °C	c(2×2) – straight step edges No curved steps	0
$30 \leq X \leq 180$ L at 300 °C	c(2×2) – continued step motion forms step bunched structures	0
200 L at room temperature	Full oxide coverage; 0.3-0.6 nm in height and 2-5 nm wide	1.1
200 L at RT + 450 °C anneal	Small oxide islands convert into large oxides on a c(2×2) surface	0.9

The nickel oxide layer formed at room temperature after 200 L oxidation transforms to a c(2×2) surface after annealing at 450 °C with new oxide structures present at the corners of intersecting step edges. The oxide islands are different from the RT-oxide and are 15-30 nm in size with a height of 1-2 nm. In addition, imaging at different bias voltages changes the contrast of these oxides with a recess appearing in the center of the oxide when imaged at low voltages.

5.5. Future Work

1. The conversion of RT-oxides into a c(2×2) phase suggests that a stability regime can be defined: high temperature favors the presence of chemisorbed structure while low temperature oxidation facilitates rapid oxide formation. The low temperature oxides

convert into a chemisorbed structure upon annealing in UHV and the transformation is irreversible. In addition, it has been observed that the $c(2\times 2)$ is stable at lower pressures while high pressure increases the oxygen uptake and results in oxide nucleation. More experiments are required to determine the stability regime of the $c(2\times 2)$ phase.

2. The effect of pressure on the stability of the $c(2\times 2)$ chemisorbed structure needs to be investigated to fully predict the oxide products that can be expected during oxidation. For the same oxidation amount (in Langmuir) and temperature, the partial pressure of O_2 can be systematically varied and its effect on the formation of $c(2\times 2)$ -O can be determined.

3. The stability of $c(2\times 2)$ and suppressed NiO formation has consequences for our understanding of Ni-Cr alloy oxidation. A direct comparison of the oxide products on Ni and NiCr will provide insight on whether the presence of Cr induces Ni oxidation and eventual formation of NiO on the surface. The results of Cr addition on the oxidation products at 300 °C are discussed in Chapter 6 and it should be extended to oxidation at room temperature and higher temperatures (>500 °C).

4. DFT simulations of the oxygen-induced $c(2\times 2)$ and $p(2\times 2)$ structures on Ni(001) need to be performed to obtain information of the local density of states. The effect of oxygen adsorption on the local electronic structure of Ni might help explain the stability of the $c(2\times 2)$ phase or conversely, the reduced reactivity of Ni due to the O-adsorbate layer.

References

1. Holloway, P. H. & Hudson, J. B. Kinetics of the reaction of oxygen with clean nickel single crystal surfaces. *Surface Science* **43**, 123–140 (1974).
2. Holloway, P. H. Chemisorption and oxide formation on metals: Oxygen–nickel reaction. *Journal of Vacuum Science & Technology* **18**, 653–659 (1981).
3. Eastman, D. E. & Cashion, J. K. Photoemission Energy-Level Measurements of Chemisorbed CO and O on Ni. *Phys. Rev. Lett.* **27**, 1520–1523 (1971).
4. Wang, W.-D., Wu, N. J. & Thiel, P. A. Structural steps to oxidation of Ni(100). *The Journal of Chemical Physics* **92**, 2025–2035 (1990).
5. Wang, W.-D., Wu, N. J., Thiel, P. A. & Tringides, M. C. Epitaxial growth in a strained system: Ni(100)-O(7×7). *Surface Science* **282**, 229–236 (1993).
6. Stuckless, J. T. *et al.* Oxygen chemisorption and oxide film growth on Ni{100}, {110}, and {111}: Sticking probabilities and microcalorimetric adsorption heats. *The Journal of Chemical Physics* **106**, 2012–2030 (1997).
7. Kopatzki, E. & Behm, R. J. STM imaging and local order of oxygen adlayers on Ni(100). *Surface Science* **245**, 255–262 (1991).
8. Kopatzki, E. & Behm, R. J. Step Faceting: Origin of the Temperature Dependent Induction Period in Ni(100) Oxidation. *Phys. Rev. Lett.* **74**, 1399–1402 (1995).
9. Liebsch, A. Electronic structure of c (2×2) oxygen chemisorbed on Ni (001). *Physical Review B* **17**, 1653 (1978).
10. Brundle, C. R. & Carley, A. F. Oxygen adsorption on nickel surfaces: Detection of different species by x-ray photoelectron spectroscopy. *Chemical Physics Letters* **31**, 423–427 (1975).
11. Mac Rae, A. U. Adsorption of oxygen on the {111}, {100} and {110} surfaces of clean nickel. *Surface Science* **1**, 319–348 (1964).
12. Hopster, H. & Brundle, C. R. Use of SIMS for studies of adsorption on well-defined metal surfaces (1) Combined XPS/LEED/SIMS studies of O₂, CO, H₂O, and H₂ on Ni (100). *Journal of Vacuum Science & Technology* **16**, 548–551 (1979).
13. Vattuone, L., Yeo, Y. Y. & King, D. A. Adatom bond energies and lateral interaction energies from calorimetry: NO, O₂, and N₂ adsorption on Ni{100}. *The Journal of Chemical Physics* **104**, 8096–8102 (1996).
14. Bäumer, M. *et al.* The structure of thin NiO(100) films grown on Ni(100) as determined by low-energy-electron diffraction and scanning tunneling microscopy. *Surface Science* **253**, 116–128 (1991).
15. Coulman, D. J., Wintterlin, J., Behm, R. J. & Ertl, G. Novel mechanism for the formation of chemisorption phases: The (2×1)O-Cu(110) “added row” reconstruction. *Phys. Rev. Lett.* **64**, 1761–1764 (1990).
16. Li, L., Liu, Q., Li, J., Saidi, W. A. & Zhou, G. Kinetic Barriers of the Phase Transition in the Oxygen Chemisorbed Cu(110)-(2×1)-O as a Function of Oxygen Coverage. *J. Phys. Chem. C* **118**, 20858–20866 (2014).
17. Horcas, I. *et al.* WSXM: A software for scanning probe microscopy and a tool for nanotechnology. *Review of Scientific Instruments* **78**, 13705 (2007).

18. Nečas, D. & Klapetek, P. Gwyddion: an open-source software for SPM data analysis. *Central European Journal of Physics* **10**, 181–188 (2012).
19. Caputi, L. S., Jiang, S. L., Amoddeo, A. & Tucci, R. Oxygen-nickel bond length in Ni(111)-p(2×2)O determined by electron-energy-loss fine-structure spectroscopy. *Phys. Rev. B* **41**, 8513–8515 (1990).
20. Stöhr, J., Jaeger, R. & Kendelewicz, T. Structure of p(2×2) and c(2×2) Oxygen on Ni(100): A Surface Extended-X-Ray Absorption Fine-Structure Study. *Phys. Rev. Lett.* **49**, 142–146 (1982).
21. Schintke, S. *et al.* Insulator at the Ultrathin Limit: MgO on Ag(001). *Phys. Rev. Lett.* **87**, 276801 (2001).
22. Saiki, R., Kaduwela, A., Osterwalder, J., Fadley, C. & Brundle, C. Observation and characterization of a strained lateral superlattice in the oxidation of Ni(001). *Phys. Rev. B* **40**, 1586–1592 (1989).
23. Hickman, J. W. & Gulberansen, E. A. An electron diffraction study of oxide films formed on alloys of iron, cobalt, nickel and chromium at high temperatures. *Trans Am Inst Min Metall Eng* **171**, 344–70 (1947).

6. Nano- and Meso-scale Insights into the Evolution of Atomic and Electronic Structure during Oxidation of Ni-Cr Alloys

6.1. Introduction

NiCr-based superalloys are ubiquitous in applications such as turbine blades and steam reactors that require a combination of good mechanical strength and exceptional oxidation/corrosion resistance.¹⁻⁹ In general, elements such as Cr or Al, in case of NiAl-based alloys, are used as alloying elements due to their increased reactivity with oxygen that promotes the formation of a passive oxide layer to protect the metallic component from further degradation. However, the high temperature oxidation resistance of Ni_{1-x}Cr_x alloys depends strongly on composition:^{6,10-12} improvements in oxidation resistance are observed only in alloys containing more than 10 wt.% Cr with dilute alloys (<8 wt.% Cr) oxidizing faster than pure Ni. Commercial Ni-Cr based superalloys contain 18-25 wt.% Cr and greater amounts of Cr deliver negligible improvements in oxidation resistance that do not justify the trade-offs in mechanical properties that accompany greater additions of Cr. The oxidation of various Ni-Cr alloys has been studied extensively to understand the evolution of oxide microstructure^{6,7,10,13-21} and to ascertain if the alloy will withstand the service conditions of desired applications. However, most of the work was formed on polycrystalline materials that were subjected to varying heat treatment and consequently different starting surfaces. This hindered direct comparison of the oxide microstructures observed during transient oxidation as the initial oxidation stages are more sensitive to grain sizes, orientations and dislocation densities.

Improved sensitivity of surface science techniques such as photoelectron-, Auger electron-, and ion scattering- spectroscopy revived the interest in the oxidation of Ni-Cr

and other passivating alloys.^{5,22-30} It has been observed^{7,22,24} that Cr is preferentially oxidized during the initial oxygen exposure at room temperature (in UHV) and sustained oxidation results in a bilayer oxide structure with chromium oxide at the top and a mixture of nickel oxide and metallic Cr at the oxide/metal interface (bottom). This oxide structure during the initial stages of oxidation contrasts with the picture of an internal chromium oxide in thick scales ($>10\text{ }\mu\text{m}$) observed during ambient pressure oxidation: the internal Cr_2O_3 is located at the oxide/metal interface and passivates the metal below. Annealing the room temperature oxidized alloy surface at $500\text{ }^\circ\text{C}$ in UHV facilitates diffusion of Cr from the bulk with a concomitant reduction of NiO to form Cr_2O_3 .^{23,25} Annealing the oxidized surfaces at temperatures above $600\text{ }^\circ\text{C}$ results in oxygen dissolution in the bulk and metallic surface with some remnant Cr_2O_3 is reclaimed.²⁵

Current literature on Ni and NiCr oxidation suggests a strong effect of pressure on the oxidation products that are formed. Luo et al.²⁹ observed that only NiO was formed on Ni10Cr alloy after $\approx 300\text{ L}$ oxidation at $450\text{ }^\circ\text{C}$. The formation of NiO at $450\text{ }^\circ\text{C}$ diverges, at first glance, from reports on Ni(001) oxidation where oxide formation was not observed at high temperatures for comparable O_2 exposures.³¹⁻³³ However, the oxygen pressures used in the various references are different: Luo et al.²⁹ used O_2 pressures of $3\times 10^{-6}\text{ mbar}$ while Wang et al.³¹ used lower pressures of $1\times 10^{-8} - 1\times 10^{-7}\text{ mbar}$ of O_2 . Therefore, higher p_{O_2} likely favors the formation of NiO independent of temperature while the $c(2\times 2)$ chemisorbed structure is stable at low temperatures and pressures. In this work, oxidation is performed at $300\text{ }^\circ\text{C}$ with O_2 pressures less than $1\times 10^{-7}\text{ mbar}$ and no NiO formation is expected. Ni oxidation experiments in Chapter 5 confirm that oxidation at $300\text{ }^\circ\text{C}$ is

dominated by the $c(2\times 2)$ reconstruction and NiO formation only occurs at low temperatures or with oxygen exposures in excess of 200 L. The current status of literature on initial stages of oxidation is shown in Figure 6-1.

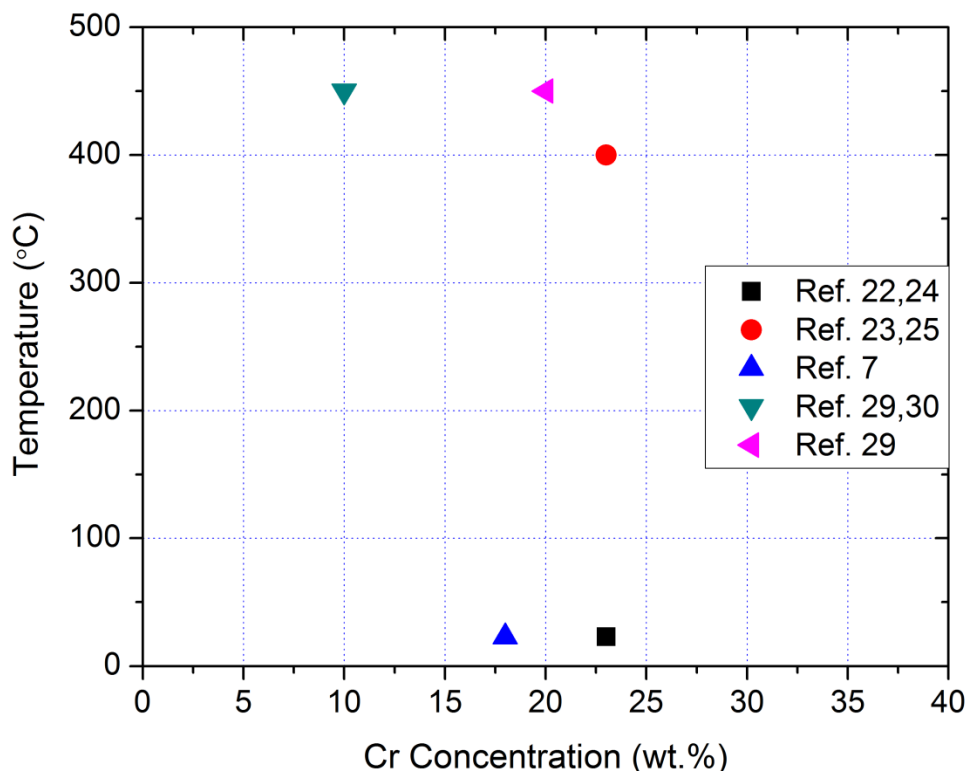


Figure 6-1. Current status of the literature on the initial stages of oxidation of Ni-Cr alloys. The plot does not include the partial pressure of oxygen used in the study which is another parameter that affects the oxidation products.

Oxidation studies of Ni-Cr alloys until now have been performed by spectroscopic methods and no surface microscopy techniques have been used to investigate the oxide nucleation sites, the initial stages of oxidation or the structure of the oxides. In addition, the effect of alloy composition (%Cr in this case) on the initial stages of oxidation has not been systematically investigated. The current work serves to bridge the current gap in literature and the key questions that motivate the work outlined in this chapter are:

- ◆ How does the amount of Cr in the alloy affect the initial nucleation of the oxides?
- ◆ Does Cr solely act as a getter for oxygen or does it promote Ni to react with oxygen?
- ◆ Does the Cr content in the alloy affect the electronic structure of the oxide?

In this chapter, we provide nanoscale insights into the initial stage of oxidation of $\text{Ni}_{1-x}\text{Cr}_x$ alloys at 300 °C as a function of alloy composition. Changes in the surface structure are characterized by scanning tunneling microscopy and oxide nucleation is discussed as a function of composition. Scanning tunneling spectroscopy maps provide spatially-resolved electronic structure information and the evolution of bandgap on the surface with increasing oxidation is discussed. The changes in the bandgap of the oxide are correlated with the height of the oxide³⁴ and information on the mechanism of oxide growth is obtained. This work establishes an experimental framework to understand the evolution of atomic and electronic structure of passivating alloys during controlled exposure to technically relevant reactive gases such as oxygen, steam or carbon dioxide.

6.2. Methods

Materials The experiments are performed in an Omicron Nanotechnology Variable Temperature SPM system under ultrahigh vacuum (UHV) conditions with base pressure of 3×10^{-10} mbar or better. Ni-Cr alloy thin films were fabricated by electron-beam evaporation (Mantis Deposition Ltd.) of Ni and Cr on pre-treated MgO(001) substrates (CrysTec GmbH). The details of film growth are discussed in Chapter 4. The coverage of oxygen is expressed in Langmuir (L) where 1 L (= 10^{-6} torr-s) corresponds to an exposure of 1×10^{-6} torr in 1 s.

Characterization The surface structure of the as-deposited and oxidized thin films is characterized in-situ by scanning tunneling microscopy and spectroscopy (STM/STS). Imaging and spectroscopy are performed with atomically sharp W-tips which were prepared by electrochemical etching with 1 M NaOH. The composition of the alloy film is confirmed ex-situ by energy dispersive spectroscopy (EDS). The STM images were analyzed using WSxM³⁵ and Gwyddion³⁶ using procedures described in section 3.5.1. Images are recorded at 2.0 V and feedback current of 0.1 nA unless otherwise specified.

6.3. Results

The alloy compositions and oxidation amounts investigated in this study are shown in Figure 6-2. We investigated the effect of chromium on the initial stages of oxidation by studying alloys containing 5 wt.% (low), 14 wt.% (nominal) and 33 wt.% (high) of Cr. The Ni-14Cr alloy contains the minimum amount of Cr necessary to form a passivating oxide layer while the other two alloys capture oxidation reaction at the extreme ends of the composition spectrum. The oxygen exposure required for the oxide to cover >75% of the alloy surface is sketched in the plot to show the strong effect of Cr on the oxidation response of the alloy. The formation of a thick, continuous oxide layer is not pursued as we are interested in the initial stages of oxidation where the atomic and electronic structure can be characterized using STM and STS.

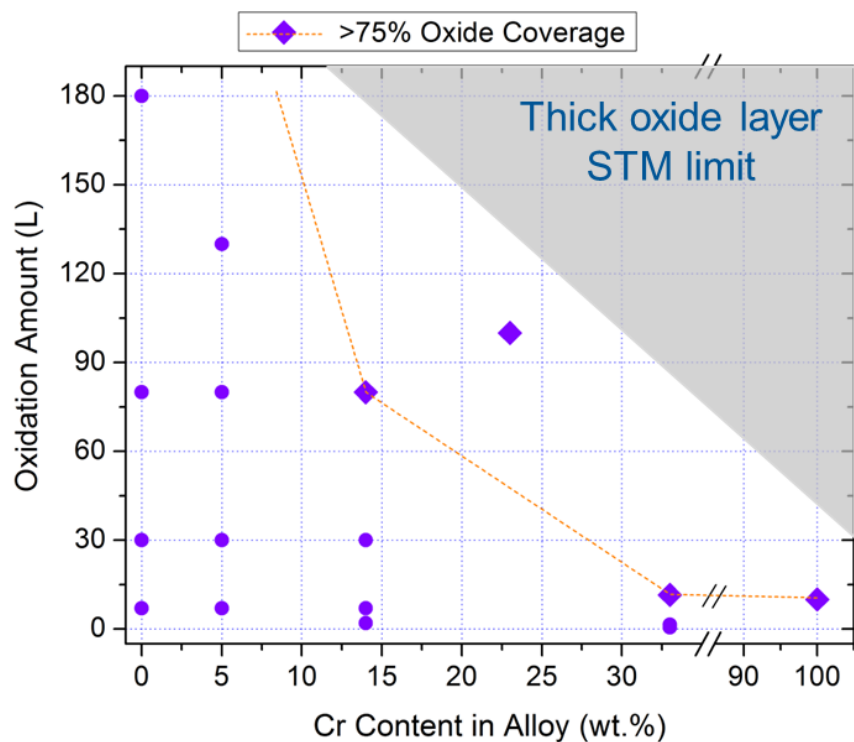


Figure 6-2. Plot of alloy composition and oxygen exposures used in this study. The minimum amount of oxygen required for >75% oxide coverage during oxidation at 300 °C is marked. Pure Cr was oxidized at 200 °C to avoid formation of a thick oxide layer that cannot be measured with STM.

6.3.1. Oxidation of Low-Cr Alloy: Ni5Cr

6.3.1.1. Topography Evolution

STM images of the Ni-5Cr alloy surface after different amounts of oxidation are shown in Figure 6-3. In contrast to pure Ni (Figure 6-3), exposure to just 7 L of O₂ at 300 °C leads to the formation of discrete oxide nuclei on the surface. The formation of oxide structures on the surface shows that the addition of even a small amount of a more reactive element markedly changes the behavior of the alloy. The oxide coverage of $16.79 \pm 0.96\%$ exceeds the surface concentration of Cr in the alloy and suggests that diffusion of Cr from the subsurface layers assists to form the thermodynamically stable chromium oxide on the surface. The average height of the oxide nuclei is 0.16 ± 0.1 nm. At these low oxygen exposures, the oxides are distributed uniformly on the surface with no clear preference for

step edges as opposed to the flat terraces (53% of the oxides are at the edges). An additional 23 L oxidation (total of 30 L) results in a two-fold increase in oxide surface coverage with $21.59 \pm 4.9\%$ of the surface covered with an oxide. At this point, we begin to observe nucleation of the oxides at the step edges and all additional oxides are nucleated exclusively at the step edges (coverage on terrace does not change after additional 23 L oxidation). With continued oxidation to 80 and 130 L, oxide coverage increases as seen from the topography images (Figure 6-3(c,d)) and the oxides densely populate the step edges.

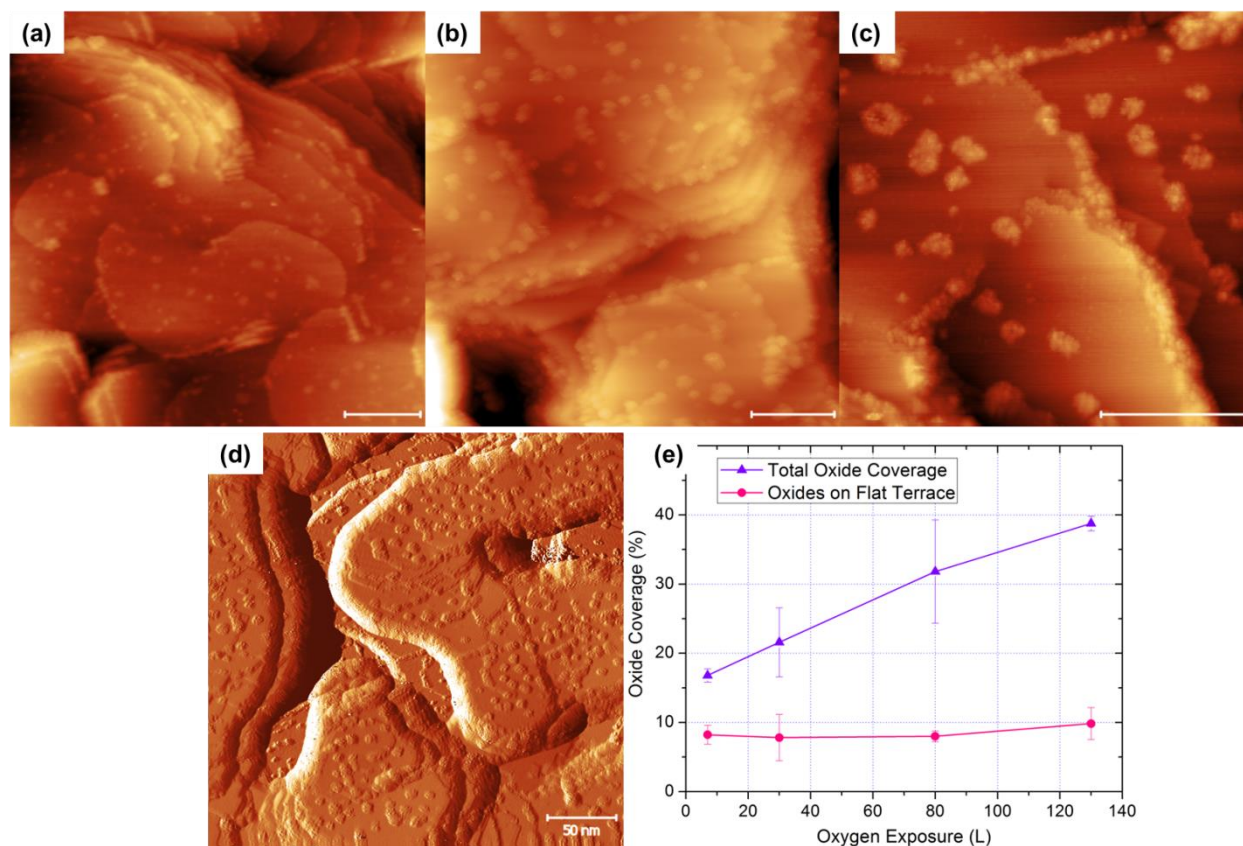


Figure 6-3. STM images of Ni-5Cr surface with different amounts of oxygen exposure: (a) 7 L, (b) 30 L, (c) 80 L, and (d) 130 L. Scale bar in (a-c) is 25 nm and is 50 nm in (d). The derivative image is shown in (d) due to large height variations. All images are recorded at 2 V and 0.1 nA. (e) Oxide coverage evolution during oxidation.

The total oxide surface coverage and the coverage only on the flat terrace regions (away from step edges) are summarized in Figure 6-3(e). Full oxide coverage is not reached in these low-Cr alloys and only 45% surface coverage is attained even after 130 L oxidation. The oxide coverage increases with increasing oxygen exposure but the increase occurs exclusively at the step edges: 51% of oxides on the surface are present at the step edges after 7 L and it increases to 63.8% and 74.2% after 30 and 80 L oxidation. In an alloy where oxidation is limited by the supply of Cr, we can see that the oxidation preferentially occurs at the step edges where the barrier for nucleation is lower due to the presence of dangling bonds. It will be shown later in case of Ni-14Cr alloy that the barrier for nucleation on the terrace is not prohibitive and the preference for oxidation at the step edges in Ni-5Cr is, in fact, a manifestation of a preferred diffusion path for Cr from the bulk to the step edges on the surface (and a resultant paucity of Cr on the flat terrace).

The variation of oxide height and projected area during oxidation of Ni-5Cr is shown in Figure 6-4 along with the oxide number density on the surface. The slow oxygen uptake and absence of continuous oxide layer on the surface allow us to capture the evolution of the oxide sizes up to 130 L without errors that coalescence lends to size distributions. The average height of the oxide nuclei after 7 L oxidation is 0.16 ± 0.1 nm indicating that they are only 2-3 monolayers high. With an additional 23 L oxygen exposure, the oxide height increases to 0.32 ± 0.17 nm (equivalent to Y monolayers) indicating that vertical growth occurs and the barrier for upward diffusion of atoms (inverse Ehrlich-Schwoebel) is not excessive and thermal energy at 300 °C is sufficient to overcome this activation barrier. In addition, the area covered by oxide islands also increases as seen in the area distribution after 7 and 30 L oxidation. Between 30 and 80 L, the oxides continue to grow vertically as

seen in the height histogram and the average height is 0.47 ± 0.2 nm. At this stage, the mean oxide area remains unchanged with some minor changes in the area histogram. Sustained oxidation (total of 130 L) is characterized by lateral growth of the oxide with minimal changes in the oxide height and suggests a change in the oxidation mechanism. Therefore, there exists a threshold oxide height beyond which vertical growth becomes untenable and lateral growth dominates. The oxide island density decreases with increasing oxidation and this suggests that there is significant oxide coalescence on the surface. This is surprising since the number density on Ni-5Cr after 30 L is lower than for the Ni-14Cr alloy which will be discussed in section 6.3.2. Coalescence is observed mostly at the step edges and the change in oxide structure is clearly illustrated in Figure 6-3(b,c). An oxide island is unlikely to migrate to the step edges as an ensemble and smaller oxide islands on the terrace will likely dissolve as a larger oxide grows at its expense (ripening). Since the oxide coverage consistently increases during oxidation, the drop in island density can be explained by ripening and is controlled by the coalescence of the islands located at the step edges.

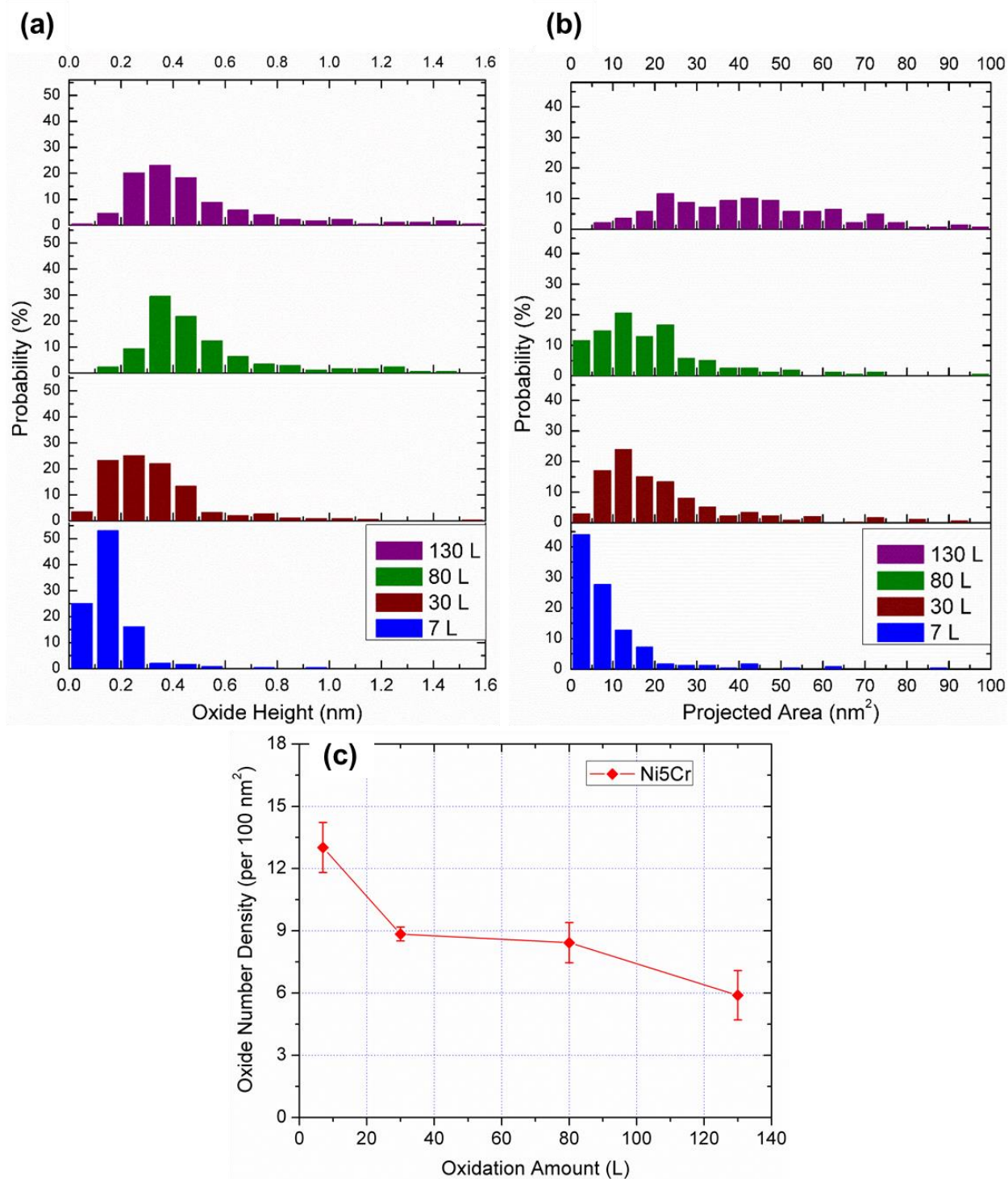


Figure 6-4. Evolution of (a) oxide height, (b) oxide area and (c) number density (per 100 nm²) during oxidation of Ni-5Cr alloy at 300 °C.

6.3.1.2. Characterization of Electronic Structure

The combination of STM images and bandgap maps from the same image area captures the changes in the both the atomic/nanoscale structure as well as the electronic structure of the surface and is one of the major strengths of the current work. An STM image after 30 L oxidation is shown in Figure 6-5(a) along with the corresponding bandgap map in Figure 6-5(b). There is excellent one-to-one correlation between the STM image and the map: the oxide structures in the topography image appear as regions with a nonzero bandgap in the map while the alloy surface retains its metallic character (no gap). The average bandgap of the oxides in Figure 6-5(b) is 0.5 ± 0.2 eV. The spectrum from the metallic region in between the oxide islands does not exhibit the characteristic kink at the Fermi level which is observed on a $c(2 \times 2)$ -O/Ni surface (Figure 5-5) indicating that a random distribution of Cr on the surface hinders the formation of the ordered $c(2 \times 2)$ -O phase on the alloy surface. A histogram of the bandgap values after 7-130 L (in Figure 6-5(c)) captures the evolution of the electronic structure of the surface with increasing oxidation. The relative proportion of the surface with metallic character decreases from 7 to 130 L in agreement with increase in coverage (Figure 6-3(e)). An interesting observation is that the oxides after 7 L oxidation do not present a bandgap even though distinct oxide islands are resolved in the topography image. However, after 30 L oxidation, the oxides grow and they present an average gap of 0.6 ± 0.2 eV. The bandgap, however, does not increase appreciably with sustained oxidation (small increase in gap is within error bar) despite the structural evolution of the oxide that was discussed in the previous section. We will revisit this observation in section 6.4 when we compare the results of different alloys and postulate models to explain our results.

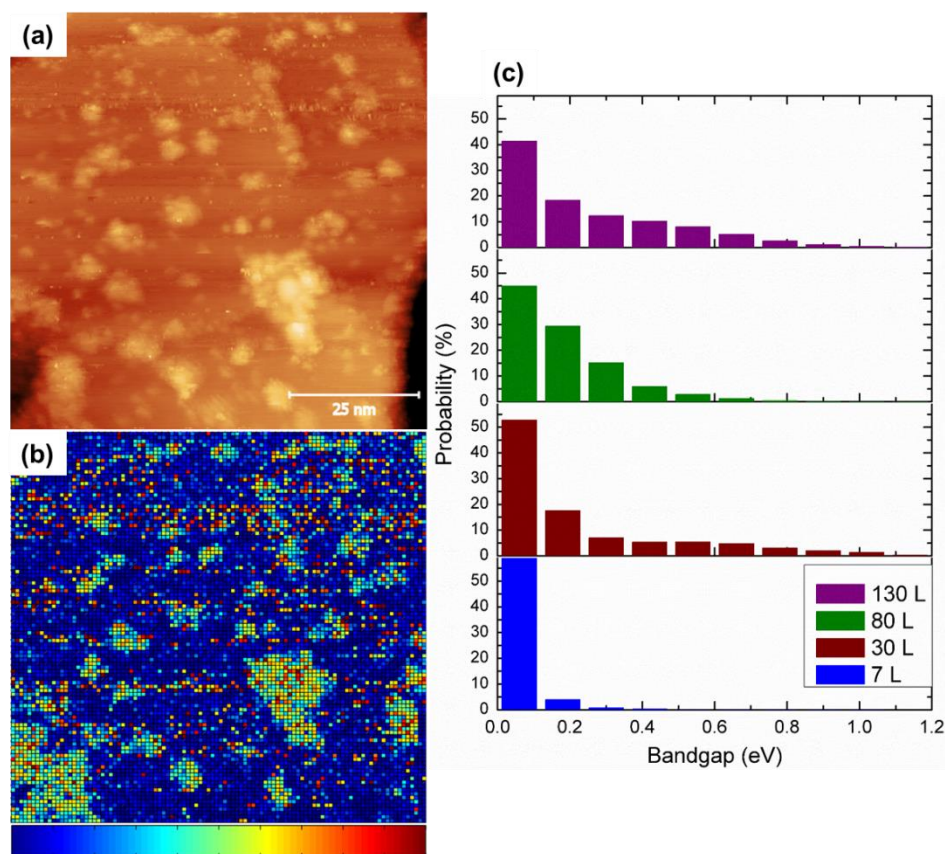


Figure 6-5. Scanning tunneling spectroscopy data during Ni-5Cr oxidation: (a) topography image after 30 L, (b) corresponding bandgap map; color scale is 0 eV (blue) to 1 eV (red), and (c) Bandgap distribution as a function of oxidation progression.

6.3.2. Oxidation of a Nominal NiCr alloy – Ni-14Cr

6.3.2.1. Topography Evolution

Changes in the surface structure of Ni-14Cr after 30 and 80 L oxidation are shown in Figure 6-6. After 7 L oxidation, oxides are nucleated on the surface and the oxide coverage is $16 \pm 4.6\%$. The oxide coverage observed is similar to the coverage on Ni-5Cr after 7 L. However, oxidation behavior sharply deviates after the 23 L (total of 30 L) oxidation step. The oxide coverage increases to $44.6 \pm 3.8\%$ and is the same as the final coverage observed on the Ni-5Cr after 130 L oxidation. This increase in oxide coverage is accompanied by an increase in the oxide number density suggesting that new oxide islands are nucleated. The

oxides have an average height of 0.47 ± 0.19 nm. The final 50 L oxidation (total of 80 L) results in almost complete oxide coverage on the surface as seen in Figure 6-6(c,d). $78 \pm 3.4\%$ of the surface is covered with oxide and the average area of oxides increases from 12.2 ± 6.2 nm² after 30 L to 30.0 ± 11.2 nm². The average oxide height does not increase but the small oxide islands such as the ones marked in Figure 6-6(d) begin to coalesce. At this stage, the oxide island density is sufficiently high so that the inter-oxide distance is smaller than the diffusion length of oxygen atoms on the surface. Therefore, the oxidation reaction mechanism switches to a regime where lateral growth of oxide is more favorable compared to nucleation of a new oxide island. This mechanism was proposed for Ni oxidation^{37,38} and it should hold true for the current case of Ni-Cr oxidation if Cr-diffusion to the surface is sufficiently high. Our results suggest that it would not be valid for Ni-5Cr where oxide growth plateaus after 80 L but would hold true for Ni-14Cr and other high-Cr alloys.

In addition to the smaller structures that nucleate and grow from 7-80 L oxidation, larger oxide structures that are 2-4 nm high are seen after 80 L oxidation (Figure 6-6(c)). Compared to the smaller oxides which have a projected area of 50-150 nm², the new oxide structures are massive with an area of at least 1000 nm² and are exclusively found at sites of extensive step bunching. These structures are not observed on Ni-5Cr even after 130 L while they are also seen on Ni-10Cr-6Mo after 130 L (Chapter 7). The common link between the Ni-14Cr surface after 80 L oxidation and the Ni-10Cr-6Mo surface after 130 L is the $>75\%$ oxide coverage: the presence of a near-continuous oxide layer on the surface appears to correlate with the formation of these large oxide islands. Based on the results of Ni oxidation, we can conclude that these oxides are most likely not NiO which do not form under these conditions. The large oxide islands also do not show bias voltage-dependent

contrast in the images and are different compared to NiO/Ni(001) shown in Figure 5-7. Since a sudden rapid growth of new chromia islands is unlikely, these large oxides could be a new species such as mixed oxides (spinel structures). Complementary XPS experiments are necessary so that the various oxides that form on the surface can be unambiguously identified in the absence of atomic resolution in SPM experiments.

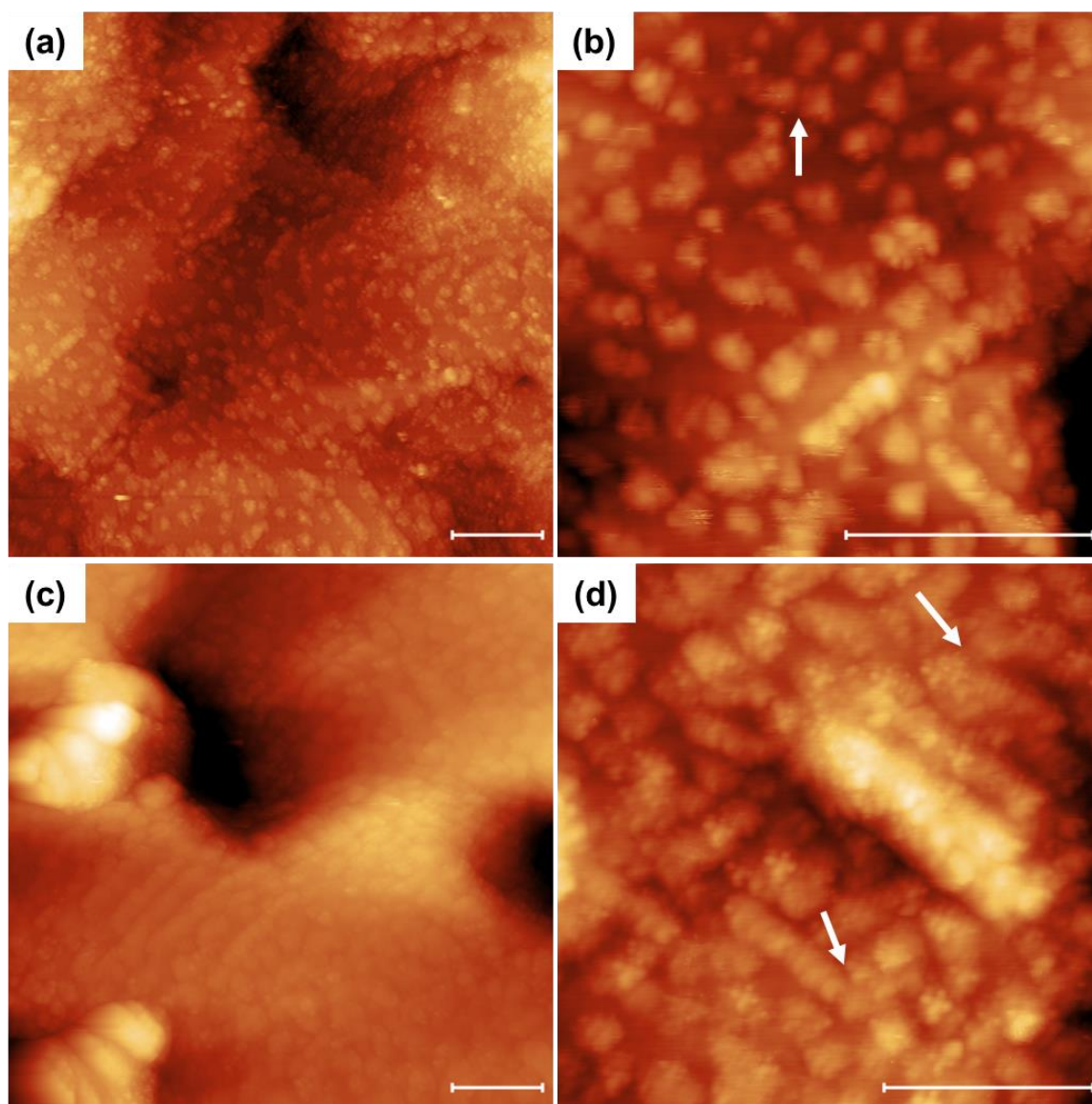


Figure 6-6. STM images of Ni-14Cr alloy after (a,b) 30 L and (c,d) 80 L oxidation at 300 °C. Scale bar is 25 nm. White arrows point to opposing oxide growth interfaces that have coalesced. Large oxides having a different surface structure compared to the flatter oxides are seen in (c).

6.3.2.2. Characterization of Electronic Structure

The combination of STM and STS images from the same area captures the changes in both the atomic/nanoscale structure as well as the electronic structure of the surface and is one of the major strengths of the current work. In Figure 6-7, bandgap map of the Ni-14Cr surface after 30 L oxidation is shown along with the STM image on which it was measured. The average bandgap of the oxides is 1.2 ± 0.1 eV and is greater than the gap measured on the Ni-5Cr alloy. Spectra from the metallic region do not carry the signature of the $c(2 \times 2)$ -O/Ni phase which is consistent with the absence of step edge reconstruction that accompanies the chemisorbed phase. Some of the oxides that are marked with white arrows have lower bandgap compared to the other islands around it and merit further analysis. Due to the one-to-one correlation between the topography image and the bandgap map, we can determine the relation between the oxide height (or area/volume) and the bandgap. The height of one such low bandgap oxide (dotted white arrow) is 0.26 nm and it has a bandgap of 0.79 ± 0.1 eV. In contrast, an oxide such as the one marked with a pink arrow is 0.66 nm in height and expressed a gap of 1.2 ± 0.1 eV. In this way, newly nucleated oxides can be differentiated from the oxides that have undergone sufficient growth to present a larger height and consequently a larger bandgap. The oxide bandgap is plotted as a function of oxide height in Figure 6-7(c) and we see that the bandgap increases with increasing height in the 30 L dataset while the 80 L data shows a small increase with height. This plot reinforces the fact that the evolution of electronic structure of the oxide is concurrent with the structural evolution observed in the STM images.

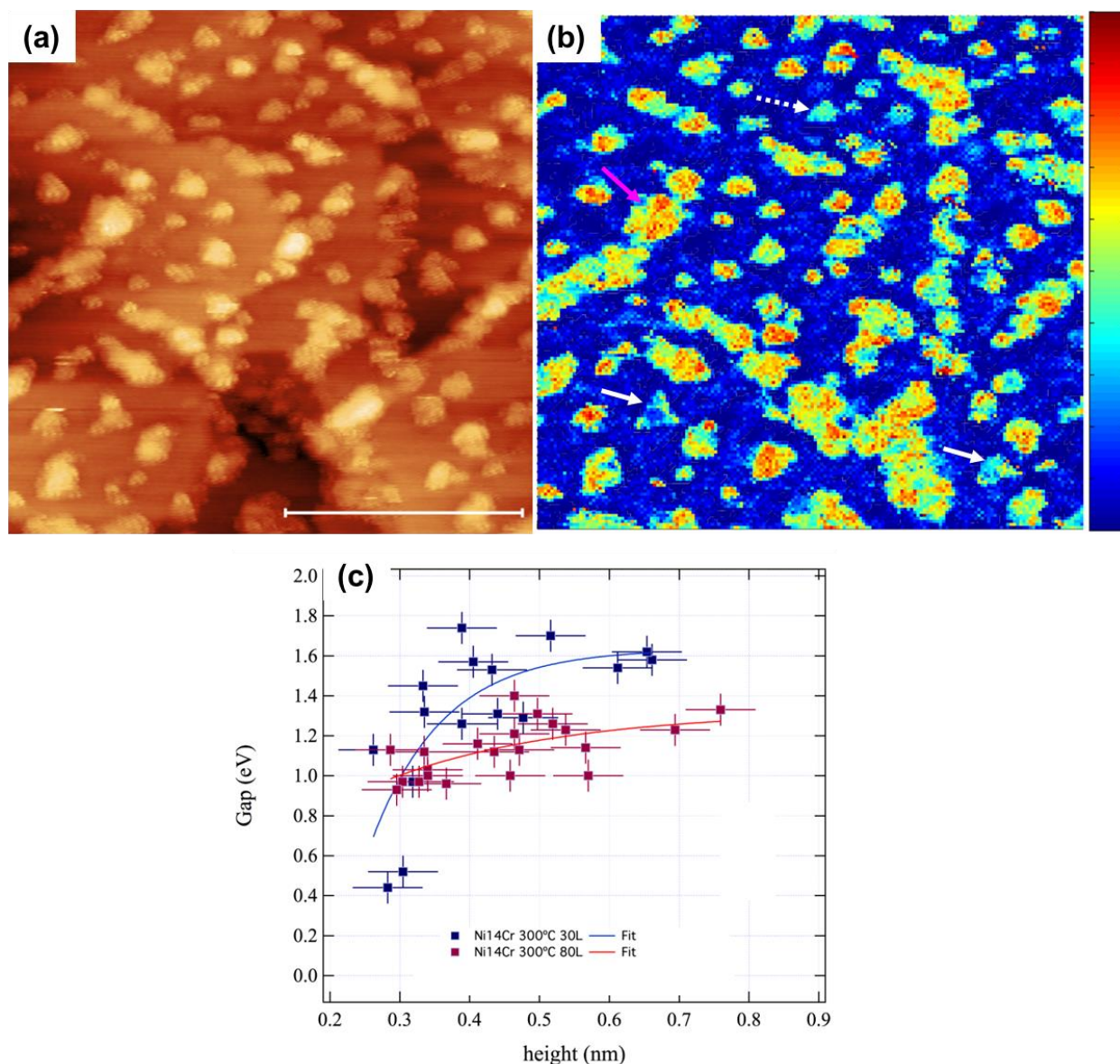


Figure 6-7. STS data recorded on Ni-14Cr alloy after 30 L oxidation at 300 °C showing (a) the STM topography image with the corresponding (b) bandgap map. The scale bar in STM image is 25 nm and the color scale in the bandgap map is 0 eV (blue) to 2 eV (red). (c) The variation of oxide gap as a function of oxide dimensions is shown on the oxides after 30 and 80 L. The arrows in (b) indicate oxides of different height exhibiting different bandgap.

The bandgap distribution of the surface after different stages of oxidation is shown in Figure 6-8. As expected, we see that metallic contribution in the histograms decreases with sustained oxidation. There is a maximum in the bandgap distribution at ≈ 1.2 eV and the peak height increases from 30 to 80 L. This peak corresponds to the average gap of the

oxides and does not capture the salient height-dependent information discussed earlier. Note that the 7 L distribution shows a predominantly metallic surface despite the presence of oxide nuclei that are clearly resolved in an STM image (this was also seen on the Ni-5Cr alloy). Therefore, there is a minimum oxide height that needs to be crossed before an oxide island on a metal surface expresses a bandgap and behaves like a typical semiconductor. This interpretation is aided by the observation of suppressed bandgap in case of the smaller oxide islands (white arrows in Figure 6-7(b)) compared to the mature oxide islands (pink arrow). The height dependence of the bandgap and the reasons for a suppressed bandgap on smaller oxide islands requires an understanding of the tunneling phenomenon. An ultrathin oxide (less than 4 unit cells)³⁴ on a metal always presents a lower gap than the bulk value due to insufficient screening of metal electrons. Beyond this, the reasons for variation of bandgap with the height of the oxide are: (i) oxides that form at low temperature (300 °C) have defect states which can tunnel electrons and reduce the gap measured by tunneling spectroscopy, and (ii) other tunneling effects such as effect of bias voltage (tip-oxide distance). The two effects cannot be de-convoluted without modeling the double tunnel barrier (vacuum gap and oxide) and XPS experiments that provide bonding information (valence state of Cr and/or Ni).

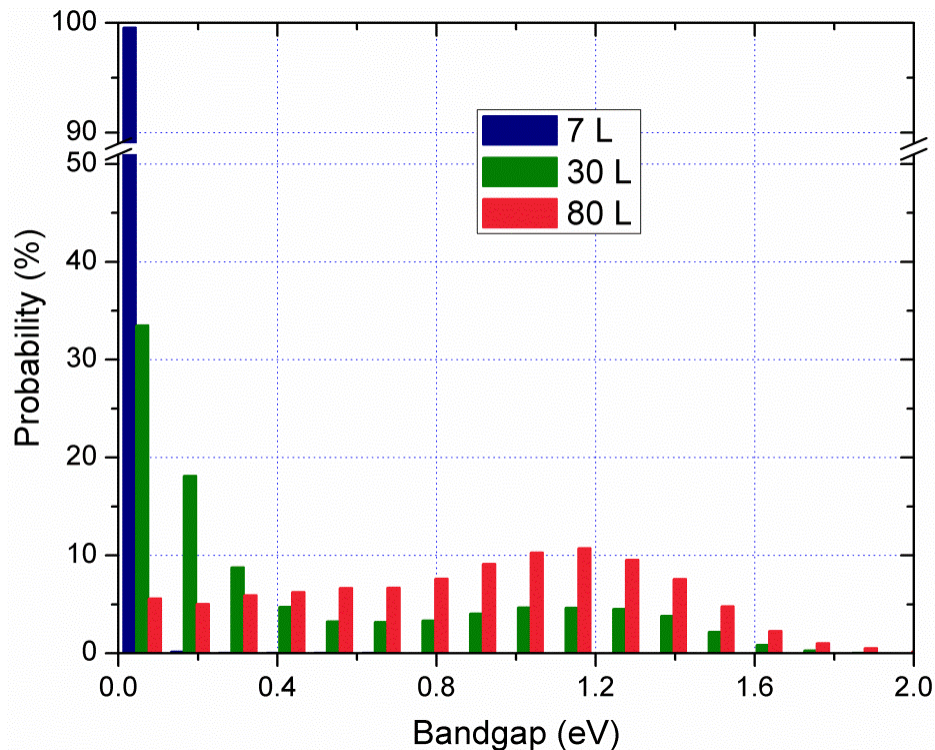


Figure 6-8. Bandgap distribution of Ni-14Cr surface after 7, 30 and 80 L oxidation at 300 °C.

6.3.3. Oxidation of High-Cr Alloys

STM image and corresponding bandgap map of Ni-33Cr alloy surface after 11.5 L oxidation at 300 °C is shown in Figure 6-9. Lower oxygen exposures are conservatively chosen so as to prevent the formation of a thick oxide layer that would impede STM/STS characterization. The STM images during the initial 0.5 and 1.5 L oxidation on Ni-33Cr show small isolated oxide structures that are consistent with previous STM images and oxides are nucleated at such low oxygen doses due to the higher Cr content. The surface coverage of oxide drastically increases after an additional 10 L (total of 11.5 L): compared to Ni-14Cr alloy which shows >75% coverage after only 80 L, the Ni-33Cr surface is almost fully covered with oxide with $\approx 1/8^{\text{th}}$ of that oxygen dose. The apparent height of the oxide structures on the Ni-33Cr alloy is only 0.27 ± 0.1 nm and is likely due to low oxygen dose.

However, it is might be possible that a continuous oxide layer is already established below the structures that are imaged and we are underestimating the real oxide height. Bandgap map recorded on the oxidized surfaces is shown in Figure 6-9(b). The gap value can be used to ascertain if the measured oxide height is the true value or if there is evidence of bandgap suppression by the underlying oxide layer. The average oxide gap is 0.6 ± 0.1 eV and the reduced gap supports the notion that the oxide height is the true height.

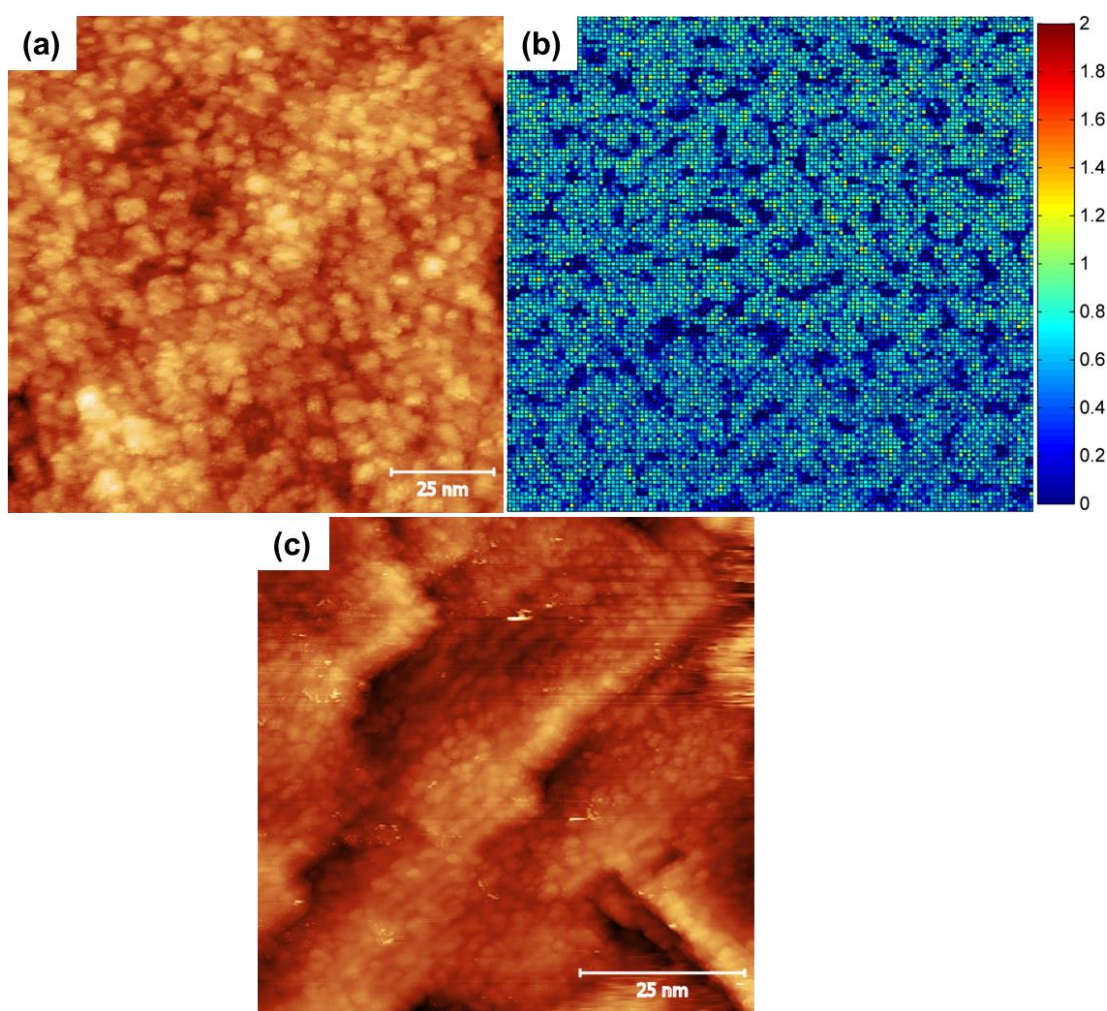


Figure 6-9. (a) STM image of Ni-33Cr thin film after 11.5 L oxidation at 300 °C with over 75% oxide coverage, (b) corresponding bandgap map indicating an average gap of 0.6 eV, and (c) Cr thin film after 10 L oxidation at 200 °C presenting a near-continuous oxide layer.

A pure Cr film was also grown to evaluate the oxidation process on this highly reactive metal surface. Figure 6-9(c) shows the STM image of the Cr surface after 10 L oxidation at 200 °C. A lower oxidation temperature was chosen to avoid the formation of a thick oxide film. Over 85% of the surface is covered with oxides after just 10 L despite the lower temperature. A combination of densely packed oxides and poor image quality does not allow for an accurate determination of oxide height: some features were as small as 0.1 nm while others were 0.4 nm in height. Due to near-continuous oxide layer on Ni-33Cr and Cr surfaces, individual oxide islands could not be measured and no statistics are provided.

6.4. Discussion

A visual summary of the oxidation results on different Ni-Cr alloys is provided by the oxide coverage plot shown in Figure 6-10. It is clear from this plot that the Cr content in the alloy plays a strong role on the initial oxide layer that is formed on the alloy. No oxide structures are formed on pure Ni after 180 L oxidation at 300 °C while the alloying of just 5 wt.% of Cr results in the nucleation and growth of oxide islands on the surface after oxygen exposure. The alloy composition determines if a continuous oxide layer will be established: the oxide coverage saturates at $\approx 50\%$ after 130 L on a Ni-5Cr alloy while a near-continuous oxide layer is achieved on Ni-33Cr after only 11.5 L. However, the nucleation and growth of the oxides and hence the structure of the oxide layer is also controlled by the Cr content in the alloy. An oxide layer that results from the coalescence of numerous small oxide islands will not afford good passivation compared to an oxide layer that is formed with fewer grain boundaries. Therefore, an alloy design protocol with a “more Cr is better for oxidation resistance” assumption is not the best approach and there exists an optimum amount of Cr

at which the nucleation density is low enough and the lateral oxide growth rate is fast enough to establish a passive oxide layer.

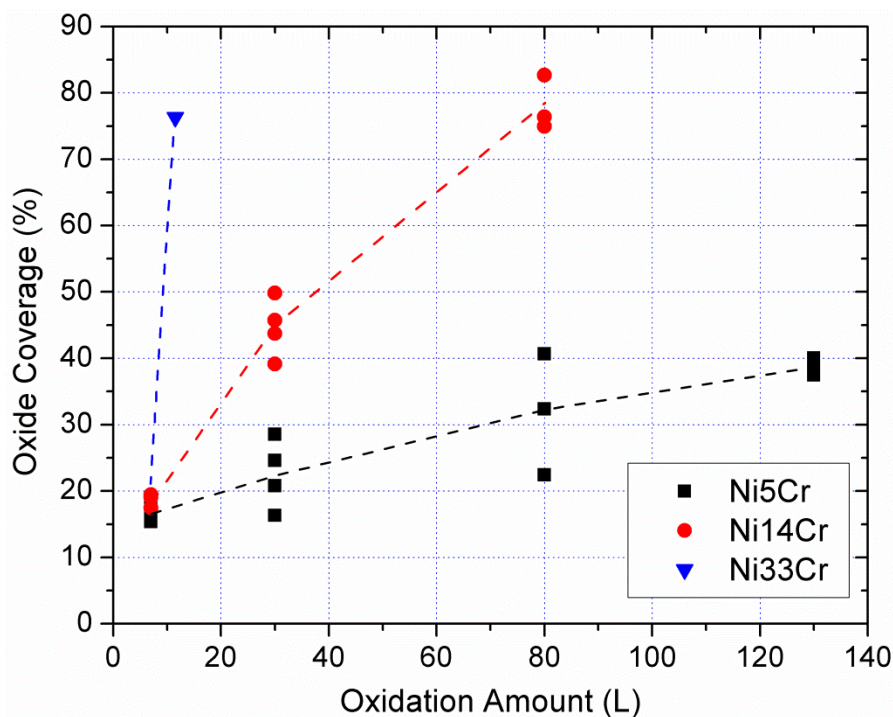


Figure 6-10. The variation of oxide surface coverage is shown as a function of oxygen exposure for the three Ni-Cr alloys that are studied in this work.

In general, oxides nucleate on both the flat terrace and edges when Cr supply is not the limiting factor. This is the case on Ni-14Cr and Ni-33Cr alloys and also on Ni-5Cr after 7 and 30 L oxidation. However, the formation of oxides after 30 L oxidation on the low-Cr alloy results in a depletion of Cr in the subsurface regions. This depletion affects the response of the alloy to continued oxidation as evidenced by the slower rate of increase in the oxide coverage. The STM images show that the oxidation reaction in this regime is dominated by ripening and preferential nucleation of oxides at the step edges. The oxide island density decreases with oxidation on Ni-5Cr due to a combination of ripening (large oxides grow at the expense of smaller ones) and fewer nucleation events. Nucleation is a

statistical process and if enough Cr atoms are not available to grow a subcritical nucleus, these oxides will dissolve. However, the nucleation barrier is lower at step edges and a subcritical nucleus has a higher likelihood that it survives. This combined with the possibility of an easier diffusion path for Cr from subsurface regions to the step edge suggests that nucleation is more at the step edges. This step-edge decoration is not unique to the Ni-5Cr and the STM images after oxidation of Ni-14Cr (Figure 6-6) show that the step edges are decorated with oxides which coexist with oxide islands on the terraces.

In the oxygen exposure regime investigated here, the diffusion of Cr from the bulk to the surface appears to be the rate-limiting step and this rate-limiting effect is prominent in the low-Cr Ni-5Cr alloy. Diffusion constants for Cr in Ni exist only for high temperatures³⁹⁻⁴¹ and extrapolation of diffusion constants yield unrealistically high diffusion lengths for Cr (20-40 nm). Theoretical calculations, on the other hand, show that the diffusion length is extremely small (≈ 0.03 nm) at 300 °C.⁴² These numbers are clearly incompatible and the significant difference means that we cannot provide quantitative backing for our hypothesis at this stage. However, comparison of these observations with the reference Ni oxidation experiments at 300 °C suggest there is appreciable Cr diffusion that drives the nucleation and eventual growth of oxides even after multiple oxidation steps in case of high-Cr alloys.

Based on the current results and our understanding of the atomistic processes during the initial stages of the oxidation reaction, we propose a basic reaction model shown in Figure 6-11 that captures the evolution of the surface before an oxide is nucleated at the atomic scale. When oxygen is introduced into the chamber, the oxygen molecules dissociate

and adsorb on the surface atoms to yield a chemisorbed surface. Based on Ni oxidation literature, the initial chemisorbed structure is likely a $p(2\times 2)$ -O/NiCr(001) which converts to a $c(2\times 2)$ with continued oxidation. Due to the multivalent nature of Cr atoms, they can leach oxygen from nearby Ni atoms and form CrO_x units on the surface. In an oxygen atmosphere, the exposed Ni atoms are instantaneously covered by chemisorbed oxygen. Concurrently, due to the high reactivity of Cr with oxygen, a large driving force (chemical potential gradient) exists for the diffusion from the bulk to the surface. When a diffusing subsurface Cr atom meets a CrO_x unit on the surface, it can bond with the CrO_x fragments to form a Cr_2O_3 unit on the surface. Under favorable conditions when several such events occur in the vicinity, chromium oxide is nucleated on the surface. In our experiments, the first image of the surface that is obtained is when the sub-critical CrO_x oxide cluster has grown beyond the critical size to result in the nucleation of oxides on the surface.

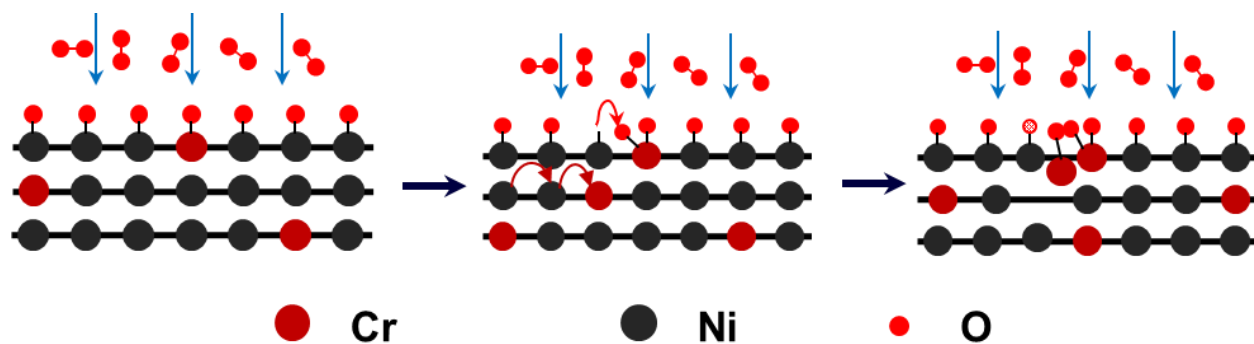


Figure 6-11. Schematic reaction model during the very initial stages of oxidation of Ni-Cr alloys.

6.5. Future Directions

It should be noted that even with sufficient supply of Cr atoms, we cannot confirm with certainty that the oxides are pure Cr_2O_3 and not mixed spinel oxides. Since we do not know the effect of Cr incorporation on the local electronic structure of the surrounding Ni atoms, our confidence in the model is tempered despite the reference Ni oxidation data. If the Cr alloying were to increase the reactivity of Ni with oxygen, then it would be reasonable to expect mixed oxides. The disordered nature of the oxides that form at 300 °C does not allow for atomic resolution and this uncertainty cannot be resolved at this point. However, UHV-XPS experiments that replicate the oxidation conditions can definitively identify the type of oxide that is formed on the surface.

Annealing of the samples at 300 °C in UHV after oxidation will need to be performed to determine if larger oxide islands ripen and grow at the expense of smaller islands. Ripening can occur when the sample is heated from room temperature to 300 °C for a subsequent oxidation step and can alter the size distributions. Since the statistics on the oxide sizes are input for ongoing phase field modeling (Peter Voorhees, at Northwestern University) to describe initial stages of oxidation, a control experiment becomes necessary.

The current work was performed at relatively low temperatures and the current findings need to be extended to oxidation studies at temperatures closer to the service temperatures (600-1000 °C) of these alloys. Unlike oxidation at 300 °C in UHV conditions, NiO formation is “switched on” at temperatures in excess of 600 °C and the interplay between chromium and nickel oxides can be studied. Higher oxidation temperatures will result in crystalline oxides which can be atomically resolved for chemical identification.

Post-oxidation annealing of the NiO-containing oxide layers at ≈ 500 °C will initiate solid-state reaction between NiO and Cr (to form Cr_2O_3). The evolution of the oxide atomic and electronic structure during this solid-solid reaction will be quite valuable. In addition, the interface between NiO and Cr_2O_3 are also likely to react due to their solubility and the formation of mixed oxides could possibly be visualized.

Mo is frequently added to the NiCr alloy system to improve the mechanical properties of the alloy. However, the effect of Mo addition on the oxidation response is not well understood and both beneficial^{43,44} and deleterious effects⁴⁵⁻⁴⁷ were observed depending on the temperature. A good understanding of the oxidation on Ni-Cr alloy surfaces is necessary to extend the work to ternary alloys in this materials system. On the basis of the current work, the effect of Mo addition on the initial nucleation of the oxide, oxide growth with sustained oxidation and changes in electronic structure can be identified.

References

1. de De Micheli, S. M. & Riesgo, O. Electrochemical study of corrosion in NiCr dental alloys. *Biomaterials* **3**, 209–212 (1982).
2. Bocher, F., Huang, R. & Scully, J. R. Prediction of Critical Crevice Potentials for Ni-Cr-Mo Alloys in Simulated Crevice Solutions as a Function of Molybdenum Content. *Corrosion* **66**, 55002–55002–15 (2010).
3. Marchetti, L., Miserque, F., Perrin, S. & Pijolat, M. XPS study of Ni-base alloys oxide films formed in primary conditions of pressurized water reactor. *Surf. Interface Anal.* **47**, 632–642 (2015).
4. Li, M. H. *et al.* Oxidation Behavior of a Single-Crystal Ni-Base Superalloy in Air. I: At 800 and 900°C. *Oxidation of Metals* **59**, 591–605 (2003).
5. Essuman, E. *et al.* Protective and non-protective scale formation of NiCr alloys in water vapour containing high- and low-pO₂ gases. *Corrosion Science* **50**, 1753–1760 (2008).
6. Wood, G. C., Hodgkiess, T. & Whittle, D. P. A comparison of the scaling behaviour of pure iron-chromium and nickel-chromium alloys in oxygen. *Corrosion Science* **6**, 129–147 (1966).
7. Steffen, J. & Hofmann, S. Oxidation of NiCr and NiCrFe alloys at room temperature. *Surf. Interface Anal.* **11**, 617–626 (1988).
8. Pollock, T. M. & Tin, S. Nickel-Based Superalloys for Advanced Turbine Engines: Chemistry, Microstructure and Properties. *Journal of Propulsion and Power* **22**, 361–374 (2006).
9. Viswanathan, R. High Temperature Corrosion of Some Gas Turbine Alloys. *Corrosion* **24**, 359–368 (1968).
10. Wood, G. C. & Hodgkiess, T. Mechanism of Oxidation of Dilute Nickel–Chromium Alloys. *Nature* **211**, 1358–1361 (1966).
11. Hindam, H. & Whittle, D. P. Microstructure, adhesion and growth kinetics of protective scales on metals and alloys. *Oxid Met* **18**, 245–284 (1982).
12. Calvarin, G., Molins, R. & Huntz, A. M. Oxidation Mechanism of Ni—20Cr Foils and Its Relation to the Oxide-Scale Microstructure. *Oxidation of Metals* **53**, 25–48 (2000).
13. Douglass, D. L. The oxidation mechanism of dilute Ni-Cr alloys. *Corrosion Science* **8**, 665–678 (1968).
14. Ecer, G. M. & Meier, G. H. Oxidation of high-chromium Ni-Cr alloys. *Oxid Met* **13**, 119–158 (1979).
15. Atkinson, A. Transport processes during the growth of oxide films at elevated temperature. *Rev. Mod. Phys.* **57**, 437–470 (1985).
16. Wallwork, G. R. The oxidation of alloys. *Rep. Prog. Phys.* **39**, 401 (1976).
17. Hickman, J. W. & Gulbransen, E. A. An electron diffraction study of oxide films formed on nickel-chromium alloys. *Trans. Am. Inst. Min. Metall. Pet. Eng* **180**, 519–546 (1949).
18. Gulbransen, E. A. & McMillan, W. R. Oxide Film on Nickel-Chromium Alloys - Crystal Structure Studies. *Ind. Eng. Chem.* **45**, 1734–1744 (1953).
19. Lund, C. H. & Wagner, H. J. *Oxidation of nickel and cobalt-base superalloys*. (DTIC Document, 1965).
20. Tribbeck, T. D., Linnett, J. W. & Dickens, P. G. Oxidation of metals and alloys. Part 1.—Oxidation of nickel containing small amounts of chromium. *Trans. Faraday Soc.* **65**, 890–895 (1969).

21. Chattopadhyay, B. & Wood, G. C. The Transient Oxidation of Fe-Cr and Ni-Cr Alloys. *J. Electrochem. Soc.* **117**, 1163–1171 (1970).
22. Jeng, S.-P., Holloway, P. H. & Batich, C. D. Surface passivation of Ni/Cr alloy at room temperature. *Surface Science* **227**, 278–290 (1990).
23. Jeng, S.-P., Holloway, P. H., Asbury, D. A. & Hoflund, G. B. Changes induced at Ni/Cr alloy surfaces by annealing and oxygen exposure. *Surface Science* **235**, 175–185 (1990).
24. Hoflund, G. B. & Epling, W. S. Oxidation study of a polycrystalline Ni/Cr alloy I: room-temperature exposure to O₂. *Thin Solid Films* **307**, 126–132 (1997).
25. Hoflund, G. B. & Epling, W. S. Oxidation Study of a Polycrystalline Ni/Cr Alloy II. *Chem. Mater.* **10**, 50–58 (1998).
26. Jussila, P., Lahtonen, K., Lampimäki, M., Hirsimäki, M. & Valden, M. Influence of minor alloying elements on the initial stages of oxidation of austenitic stainless steel materials. *Surf. Interface Anal.* **40**, 1149–1156 (2008).
27. Biesinger, M. C. *et al.* Resolving surface chemical states in XPS analysis of first row transition metals, oxides and hydroxides: Cr, Mn, Fe, Co and Ni. *Applied Surface Science* **257**, 2717–2730 (2011).
28. Mazenc, A., Galtayries, A., Seyeux, A., Marcus, P. & Leclercq, S. ToF-SIMS study of the behavior of thermally oxidized films formed on nickel-based 690 alloy in high-temperature water. *Surf. Interface Anal.* **45**, 583–586 (2013).
29. Luo, L. *et al.* In-situ transmission electron microscopy study of surface oxidation for Ni–10Cr and Ni–20Cr alloys. *Scripta Materialia* **114**, 129–132 (2016).
30. Luo, L. *et al.* In situ atomic scale visualization of surface kinetics driven dynamics of oxide growth on a Ni–Cr surface. *Chem. Commun.* **52**, 3300–3303 (2016).
31. Wang, W.-D., Wu, N. J. & Thiel, P. A. Structural steps to oxidation of Ni(100). *The Journal of Chemical Physics* **92**, 2025–2035 (1990).
32. Kopatzki, E. & Behm, R. J. Step Faceting: Origin of the Temperature Dependent Induction Period in Ni(100) Oxidation. *Phys. Rev. Lett.* **74**, 1399–1402 (1995).
33. Bäumer, M. *et al.* The structure of thin NiO(100) films grown on Ni(100) as determined by low-energy-electron diffraction and scanning tunneling microscopy. *Surface Science* **253**, 116–128 (1991).
34. Schintke, S. *et al.* Insulator at the Ultrathin Limit: MgO on Ag(001). *Phys. Rev. Lett.* **87**, 276801 (2001).
35. Horcas, I. *et al.* WSXM: A software for scanning probe microscopy and a tool for nanotechnology. *Review of Scientific Instruments* **78**, 13705 (2007).
36. Nečas, D. & Klapetek, P. Gwyddion: an open-source software for SPM data analysis. *Central European Journal of Physics* **10**, 181–188 (2012).
37. Holloway, P. H. & Hudson, J. B. Kinetics of the reaction of oxygen with clean nickel single crystal surfaces. *Surface Science* **43**, 123–140 (1974).
38. Holloway, P. H. Chemisorption and oxide formation on metals: Oxygen–nickel reaction. *Journal of Vacuum Science & Technology* **18**, 653–659 (1981).
39. Askill, J. Tracer diffusion in the chromium–nickel system. *phys. stat. sol. (a)* **8**, 587–596 (1971).
40. Murarka, S. P., Anand, M. S. & Agarwala, R. P. Diffusion of Chromium in Nickel. *Journal of Applied Physics* **35**, 1339–1341 (1964).

41. Chen, T.-F., Iijima, Y., Hirano, K. & Yamauchi, K. Diffusion of chromium in Nickel-Base Ni-Cr-Fe Alloys. *Journal of Nuclear Materials* **169**, 285–290 (1989).
42. Voorhees, P. W. *Personal communication*
43. Mathieu, H. J. & Landolt, D. An investigation of thin oxide films thermally grown in situ on Fe-24Cr and Fe-24Cr-11Mo by auger electron spectroscopy and X-ray photoelectron spectroscopy. *Corrosion Science* **26**, 547–559 (1986).
44. Montemor, M. F., Simões, A. m. p., Ferreira, M. G. S. & Belo, M. D. C. The role of Mo in the chemical composition and semiconductive behaviour of oxide films formed on stainless steels. *Corrosion Science* **41**, 17–34 (1999).
45. Kofstad, P. *High Temperature Corrosion*. (Elsevier Applied Science, 1988).
46. Hussain, N., Shahid, K. A., Khan, I. H. & Rahman, S. Oxidation of high-temperature alloys (superalloys) at elevated temperatures in air: I. *Oxid Met* **41**, 251–269 (1994).
47. Khalid, F. A., Hussain, N. & Shahid, K. A. Microstructure and morphology of high temperature oxidation in superalloys. *Materials Science and Engineering: A* **265**, 87–94 (1999).

7. Oxidation of Ni-Cr-Mo Alloys: Probing the Effect of Mo Addition

7.1. Introduction

Ni-Cr-Mo alloys are important technical alloys used in high temperature components as well as aqueous environments due to the combination of excellent high temperature strength and corrosion resistance.¹⁻⁹ Mo is frequently added to corrosion-resistant Ni-superalloys as it drastically improves the resistance to localized corrosion.^{2,3,10} In high temperature alloys, molybdenum is added to enhance high temperature strength by solid solution hardening.⁶ However, Mo forms volatile oxides which can rupture the passive chromium oxide that is formed in these alloys.^{7,8,11} This spallation at temperatures greater than 600 °C severely degrades the operational lifetime of components.

However, there is some uncertainty in the effect of Mo addition when alloys are oxidized at temperatures below 500 °C. Greeff et al¹² observed no influence of Mo on the oxidation of Fe9Cr1Mo steel after 1000 L oxidation at 157-758 °C. However, Mathieu and Landolt¹³ observed at 384 °C that the oxidation rate of Fe-24Cr-11Mo alloy is lower than the corresponding alloy with Mo. It was observed that Mo accumulates at the oxide/metal interface in hexavalent and metallic state and this barrier layer slows down the oxidation rate. Montemor et al.¹⁴ also observed the presence of Mo at the interface and in the internal chromium oxide layer on stainless steels oxidized at 250-450 °C.

We aim to address this gap in understanding by studying the changes in atomic and electronic structure of the NiCrMo alloy surface during oxidation. The effect of Mo on the initial oxide nucleation is evaluated by comparing the structure of the oxide islands on the Mo-containing ternary alloy with the oxides on Ni-Cr. The presence of Mo in the barrier

oxide layer^{13,14} has important consequences in the development of the Mott potential.^{15,16} The electronic structure of the oxides formed on Ni-Cr-Mo is characterized by scanning tunneling spectroscopy and the role of Mo in causing changes in LDOS or oxide bandgap, the type of oxide (p- or n-type), and Fermi level position can be unequivocally identified.

7.2. Methods

The approach is closely related to the NiCr alloy oxidation experiments. In addition to the co-evaporation of Ni and Cr from the quad e-beam evaporator, we evaporate Mo from a mini e-beam evaporator. Ni, Cr and Mo deposition rates are chosen so that a Ni-10Cr-6Mo alloy thin film is grown. This alloy is expected to oxidize slower than Ni-14Cr and will allow us to oxidize the sample for greater than 80 L to observe any changes on the oxide structure due to Mo addition. Oxidation is performed at 300 °C by backfilling the UHV chamber with O₂ (99.98%, Matheson Tri-gas Inc.). The coverage of oxygen is expressed in Langmuir (L) where 1 L = 10⁻⁶ torr-s. The rest of the experimental and analysis details are the same as Chapter 5 and 6.

7.3. Results and Discussion

7.3.1. Topography Evolution (0-130 L Oxidation)

STM images of the alloy surface during oxidation at 300 °C are shown in Figure 7-1 along with the oxide coverage plot that quantifies the structural changes during the oxidation reaction. The surface of the ternary alloy is identical to the Ni-Cr alloy surfaces discussed in previous chapters and presents flat terraces with well-defined step-edges. After the first 7 L oxygen exposure, oxide islands are nucleated both at the step edges as well as on the flat terraces as seen in Figure 7-1(b). The surface coverage of the oxides is

26.8±4.7% and is similar to the initial oxide coverage observed on the other Ni-Cr alloys (Figure 7-6 in section 7.4). The initial oxide nuclei are remarkably circular and aggregate to form either one-dimensional chains (black arrows) or ordered square lattices (white arrows) oriented along the <110> directions. Imaging is performed with high bias voltage (2 V) in order to image the oxides and the metal surface is not well-resolved (voltage-dependent imaging is discussed in section 7.3.2.1). Additional 23 L oxidation (total: 30 L) results in an increase in the oxide coverage (Figure 7-1(f)) without changes in the oxide island density. Sustained oxidation (80 and 130 L) results in an increase in oxide coverage with a final coverage of $\approx 75\%$ after 130 L. The oxides begin to coalesce at these oxygen exposures and island density cannot be reliably calculated. Oxidation in excess of 80 L results in decoration of step edges with oxide islands and no metallic segments are visible at the edges. In addition to the small and shallow islands (<1 nm high), larger oxide structures are observed after 80 L oxidation. Three such islands are captured in Figure 7-1(d) and are 23-25 nm wide with heights of 1.8-2.0 nm. The inset in Figure 7-1(e) shows a large oxide island also observed after the final 130 L oxidation step and is structurally similar to the large oxides observed on Ni-14Cr after 80 L oxidation. We have not ascertained the exact nature of these oxides but we posit, based on the hindrance to the formation of NiO under these conditions, that they are likely mixed oxides consisting of Cr, Ni and Mo oxides. It is possible that mixed oxides are formed even in the earlier stages of oxidation but they dissolve or convert to chromia as a result of the solid state reaction between Cr and NiO/MoO_x albeit pockets of mixed oxides can still be retained in the absence of complete transformation at 300 °C.

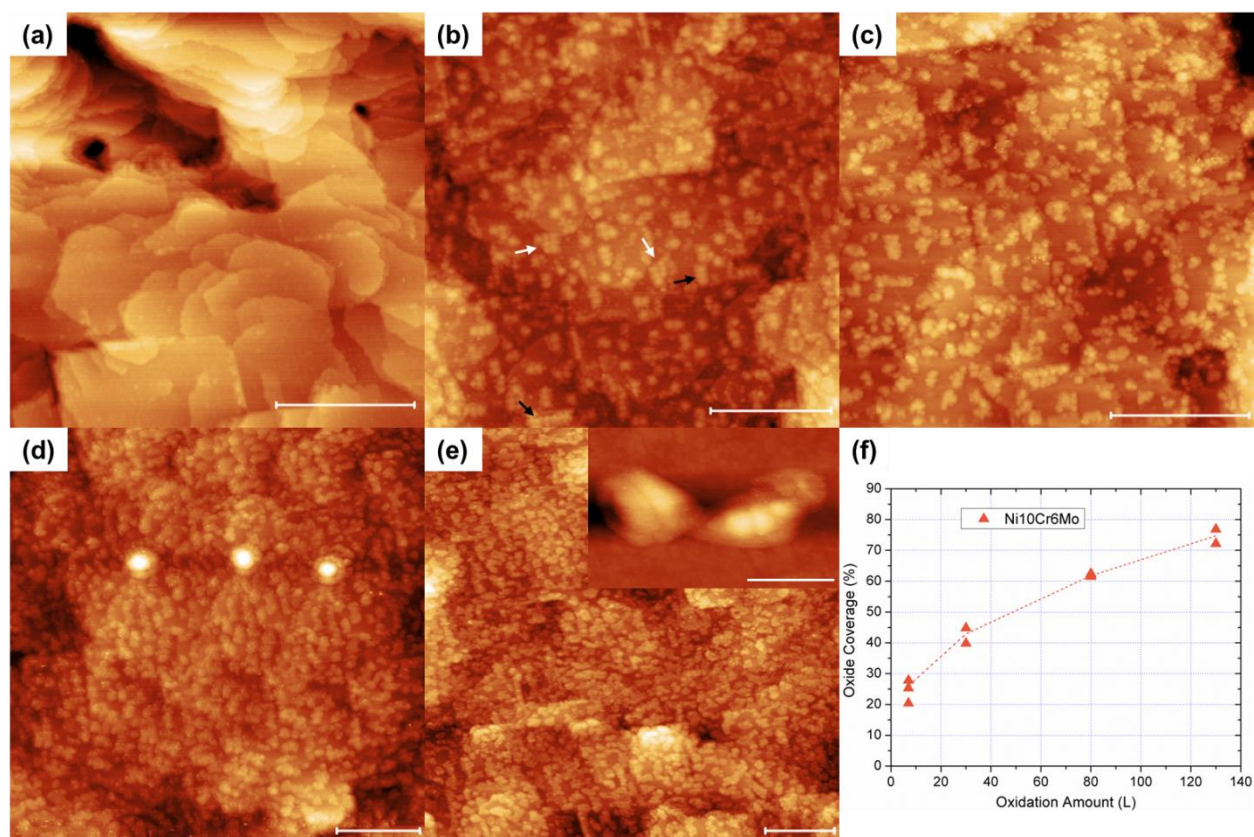


Figure 7-1. STM images of Ni-10Cr-6Mo surface after (a) 0 L, (b) 7 L, (c) 30 L, (d) 80 L, and (e) 130 L oxidation recorded at 2 V, 0.1 nA. Inset in (e) shows a large oxide structure observed after 50 nm. Scale bar is 50 nm in all images. Black and white arrows in (b) point to oxide islands that assemble into 1D chains and lattices respectively (f) Plot of oxide coverage as a function of oxygen exposure captures the surface evolution and shows a parabolic trend.

The average height of oxide islands does not change appreciably with oxidation with only a small change from 0.36 ± 0.12 nm after 7 L to 0.43 ± 0.16 nm after 30 L. The average size, however, only conveys half the information and a distribution of oxide dimensions (Figure 7-2) provides more insight into the development of the oxide during oxidation. The height distribution suggests that the smaller oxide islands still persist even after 80 L oxidation and some taller islands are also present on the surface. The height of each oxide is plotted against its area in Figure 7-2(b) and it shows that the maximum height attained by an oxide is approximately 0.8 ± 0.1 nm and is independent of the area of the oxide. During

oxidation, an oxide island that reaches this critical height, h_c , will continue to grow laterally with minimal vertical growth. This suggests that the activation barrier for uphill diffusion, which is necessary for the vertical growth, is not crossed at 300 °C when the oxide height is great than h_c . There is an increasingly number of oxides with area greater than 150 nm² after 80 and 130 L as seen in Figure 7-2(b). From the STM images, we can see that oxide islands show a high degree of coalescence. Increased stitching of the oxides eventually leads to formation of a continuous oxide layer albeit with a high density of boundaries which will facilitate faster cation diffusion from the alloy for continued oxide formation at the gas/metal interface. If this structure of the oxide layer with a large network of boundaries is retained, sustained oxidation will likely result in rapid growth of the oxide film and the underlying metal is not protected.

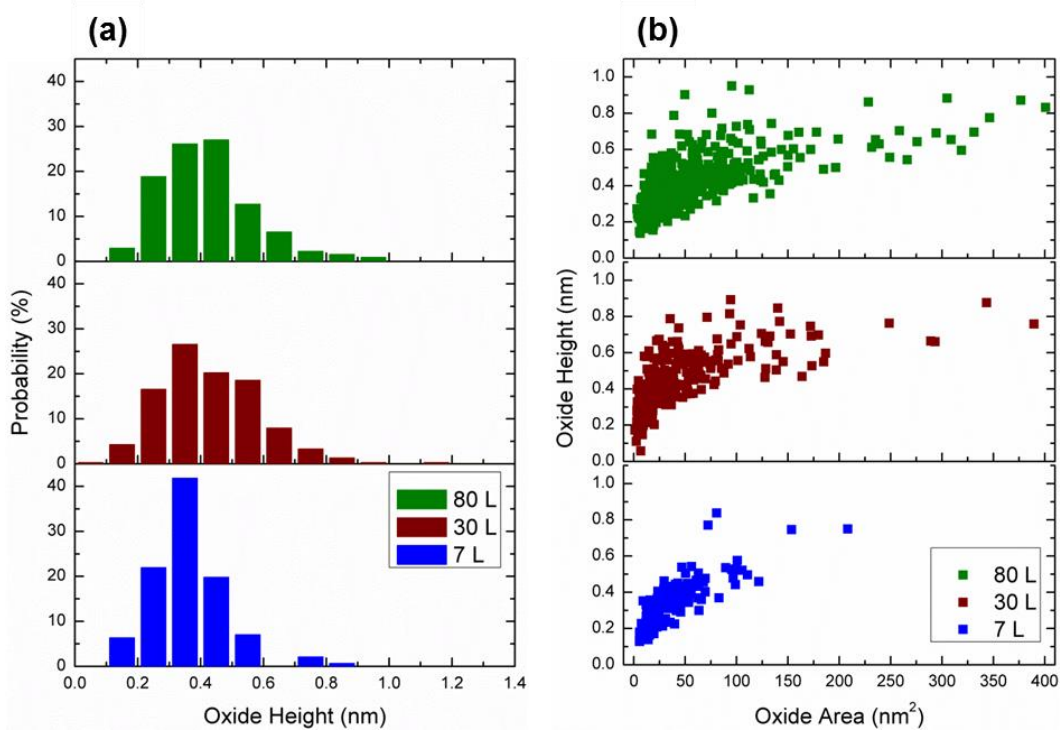


Figure 7-2. (a) Oxide height distributions after 7-80 L oxidation, (b) Correlated area versus height indicating the existence of a critical height above which vertical growth does not occur. The oxide dimensions are obtained from images recorded at 2.0 V.

7.3.2. Evolution of Electronic Structure

7.3.2.1. Bias Voltage Dependent Imaging

STM images contain both topography as well as electronic structure information and images are often recorded at different bias voltages (V_b). Bias-dependent images that are recorded after 7 L oxidation are shown in Figure 7-3. When imaged at 0.15 V (Figure 7-3(a)), the oxide islands are sharply resolved and are perfectly circular in shape. When imaged at 2 V, the oxide islands are not perfectly circular and also appear larger in size. The regions around the circular oxide nuclei appear disordered. The average size of the oxide islands imaged at 0.15 V is 3.48 ± 0.45 nm while the apparent size increases to 4.74 ± 0.61 nm when imaged at 2 V. It should be noted that 0.15 V is the voltage typically used to image the starting metal surface and 2 V is used for imaging the surface during the oxidation experiment. A sequence of higher resolution images recorded at 0.15, 1 and 2 V is shown in Figure 7-3(c-e). When thin oxides on metallic surface are imaged at low bias voltages, it is also possible to either tunnel entirely through the oxide and image the metal/oxide interface¹⁷ or to tunnel into defect states in the oxide. The former case can be excluded here since we are able to see the islands in Figure 7-3. The oxide height distribution obtained from over 150 islands is shown in Figure 7-4 when the oxides are imaged at 0.15 V and 2.0 V. The oxide islands appear higher when imaged at a higher bias voltage and the height distribution peaks at ≈ 0.25 nm and ≈ 0.4 nm respectively for 0.15 V and 2.0 V.

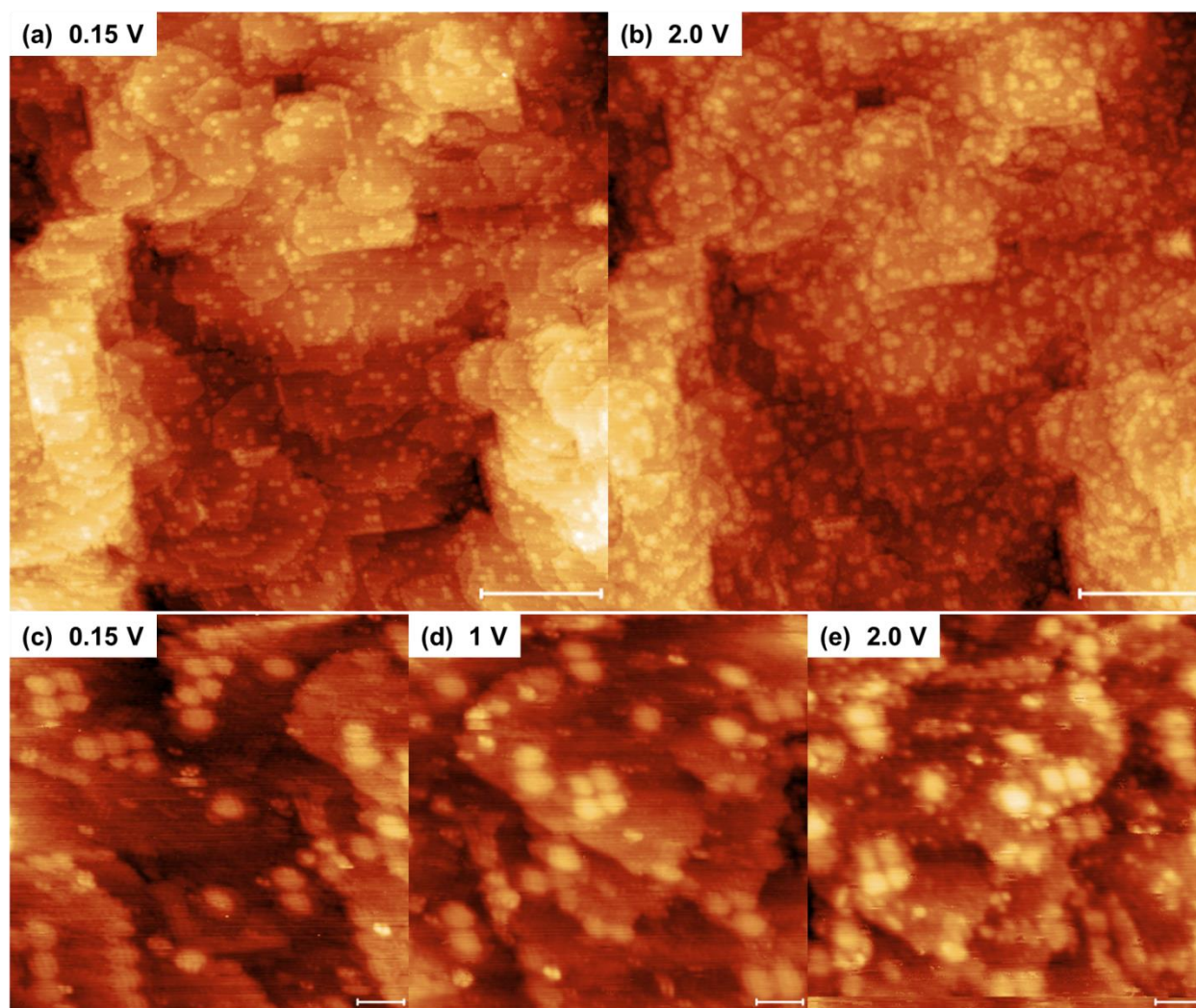


Figure 7-3. STM images of Ni-10Cr-6Mo surface after 7 L oxidation at 300 C recorded at different bias voltages: (a) 0.15 V, (b) 2.0 V, (c) 0.15 V, (d) 1.0 V and (e) 2.0 V. Feedback current is constant at 0.1 nA. Scale bar is 50 nm in (a,b) and 5 nm in (c-e).

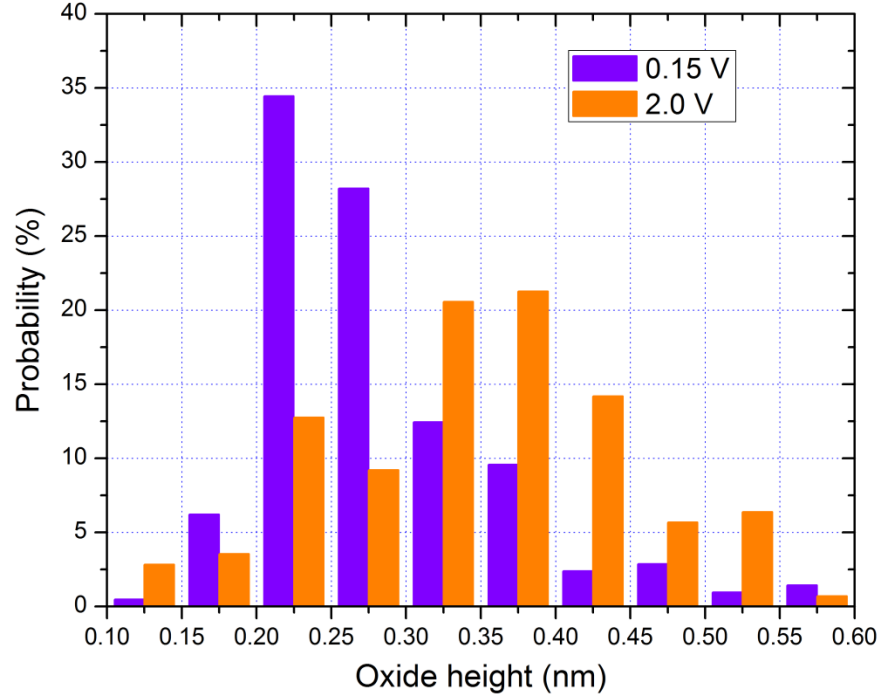


Figure 7-4. Oxide height distribution as a function of bias voltage. Feedback current is 0.1 nA.

The case when electrons tunnel through the oxide is shown in its extreme case in Figure 7-5 where a 30 L oxidized area is imaged at 2 V and 0.15 V. Some of the oxides (black arrow) that are clearly imaged at $V_b=2$ V become transparent when imaged at $V_b=0.15$ V. A representative line scan recorded across an oxide island in 2 V image and at the corresponding location on the 0.15 V image is shown in Figure 7-5(c). In addition, there are also some oxides that appear only as faint streaks (white arrow) in the low bias image or as flatter islands (red arrow). The height of the oxides marked with arrows that appear transparent, as faint streaks or as flatter islands, as measured from the 2V image, are 0.26, 0.38 and 0.49 nm respectively. Depending on the height of the oxide, electrons either tunnel entirely through the oxide so that we cannot detect it on the surface or partially into the oxide so that we image atomic layers below the oxide surface. The contributions of

electrons from the oxide to the tunneling current depend therefore on (i) oxide thickness, (ii) bias voltage, and (iii) tip-sample distance.

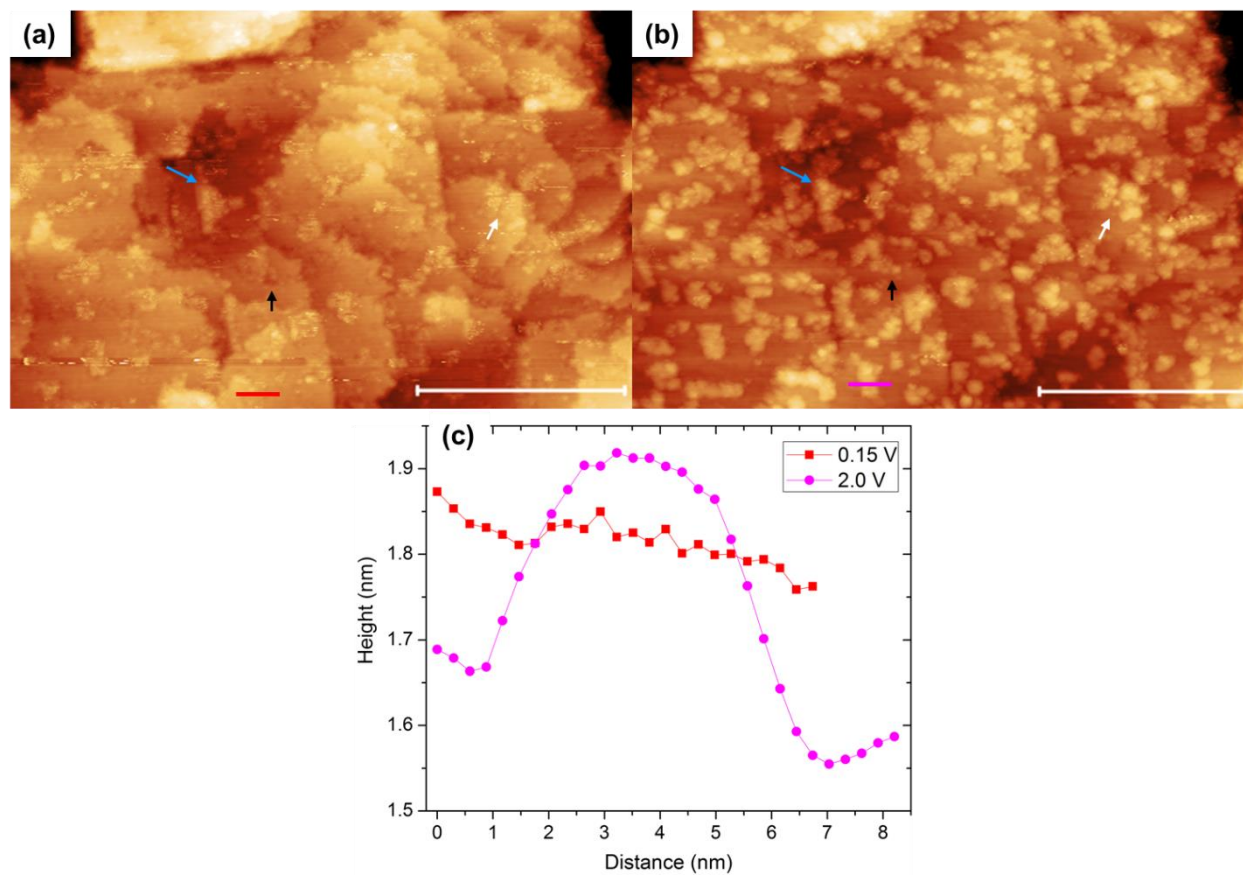


Figure 7-5. STM image of 30 L oxidized Ni-10Cr-6Mo surface recorded at (a) 0.15 V and (b) 2.0 V illustrating the different contrast mechanisms; scale bar is 50 nm. Oxides in (a) which completely disappear, appear as streaks or appear as flatter islands are marked by black, white and blue arrows respectively. (c) Representative height profile across the oxide marked with pink and red lines in both images quantifies the contrast variation observed as a function of bias voltage.

7.3.2.2. Bandgap Evolution

Scanning tunneling spectroscopy is performed after each oxidation step to quantify the spatial variation of the electronic structure during oxidation. One such bandgap map acquired on a 30 L oxidized surface is shown in Figure 7-6(b) with the corresponding topography image in Figure 7-6(a). The oxide structures present an average bandgap of

0.50±0.1 eV and the rest of the surface appears metallic and is not oxidized. Averaged STS spectra obtained on the oxide and metal regions marked in the topography image is shown in Figure 7-6(c). We see that the metal has a high density of states near the Fermi level (E_F) while the oxide has a low density of states around E_F . The oxide is p-type in nature as deduced from the E_F position of -0.12 eV (below the intrinsic level). The bandgap distribution after different amounts of oxidation is shown in Figure 7-6(d). This plot, similar to the coverage plot, captures the evolution of the alloy surface during oxidation: a predominantly metallic surface ($\approx 60\%$) after 30 L oxidation is increasingly covered with oxides with only 20% of the surface appearing metallic after 130 L oxidation. The mean oxide bandgap after 30 L oxidation is ≈ 0.4 eV and it increases slightly to ≈ 0.6 eV after 130 L. The change in the mean value is just outside the measurement error but the gap distribution clearly shows that the oxide gap maximum shifts to higher values. It is clear, therefore, that the electronic structure of the oxide evolves as the oxide grows laterally during oxidation (negligible change in oxide height).

The evolution of the oxide bandgap as a function of the oxide dimensions after various oxidation amounts is shown in Figure 7-7. Data from Ni-14Cr, the binary alloy with similar Cr content, is also added for comparison. The average gap of the oxide on Ni-10Cr-6Mo does not change appreciably with oxide island height. This is in contrast to the results from the Ni-14Cr oxidation where the oxide presents a larger gap while a variation of bandgap with the oxide height is also observed (discussed in section 6.3.2).

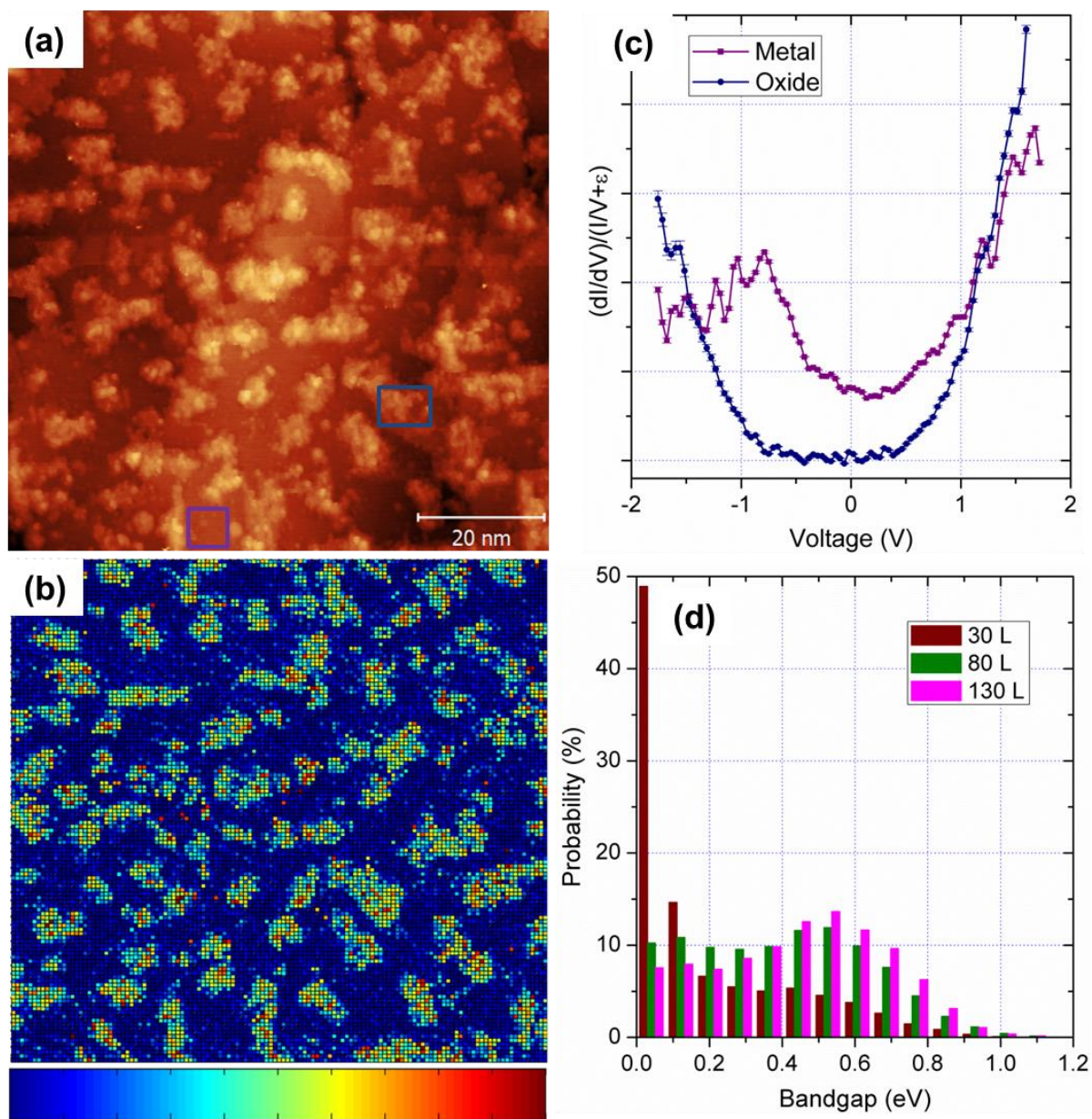


Figure 7-6. Scanning tunneling spectroscopy data from Ni-10Cr-6Mo surface: (a,b) topography image after 30 L oxidation with corresponding bandgap map; color scale of map is 0-1 eV, (c) STS spectra obtained from oxide and metal region marked in (a), (d) Bandgap distribution on the surface after 30, 80 and 130 L oxidation of alloy.

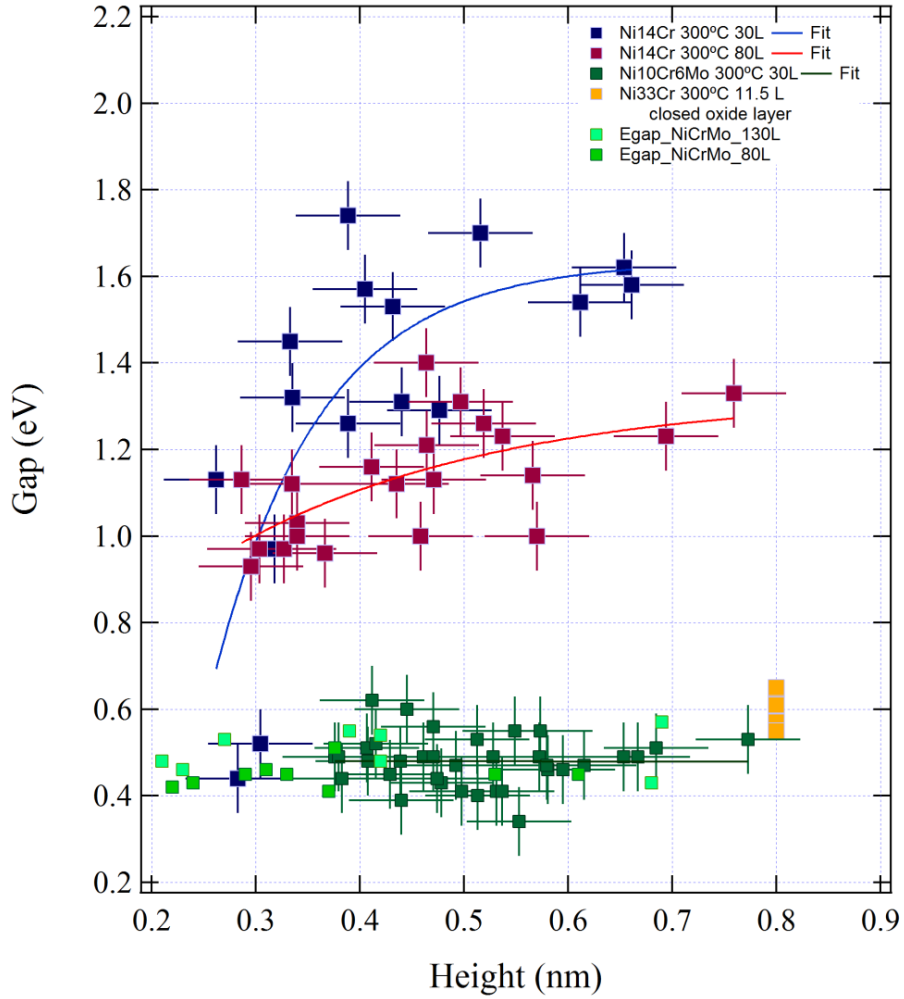


Figure 7-7. Variation of oxide bandgap as a function of height for Ni-10Cr-6Mo and Ni-14Cr alloys.

7.4. Summary

We have shown that smooth thin films of ternary Ni-Cr-Mo alloys with well-defined terraces and step-edges can be grown using the growth recipe established for binary alloys. This is an important result since the role of Mo in the film growth process was unknown prior to this work. The initial nucleation behavior is altered by the addition of Mo and circular oxide structures are observed on the terrace and at step edges. These oxides self-assemble on the surface and one possible driving force for this ordering is the strain

between the oxide and metal interface. After the initial nucleation, the surface evolution, expressed as total oxide coverage, is similar to Ni-Cr alloys. Once the oxides are nucleated, the evolution of the oxide is controlled by the Cr concentration and the trend is seen clearly in Figure 7-8. The oxide growth rate of Ni-10Cr-6Mo alloy is intermediate between Ni-5Cr and Ni-14Cr alloys: >75% oxide coverage is achieved on the ternary alloy (10 wt.% Cr) after 130 L oxidation while it is reached after just 80 L on Ni-14Cr. Compared to the Ni-14Cr alloy, the striking differences in the electronic structure of the oxides on Ni-10Cr-6Mo is the lower gap value as well as the relative independence of the bandgap on the oxide structure (height or area). This independence of oxide gap on the height was discussed in section 7.3.2.2 and expressed clearly in Figure 7-6.

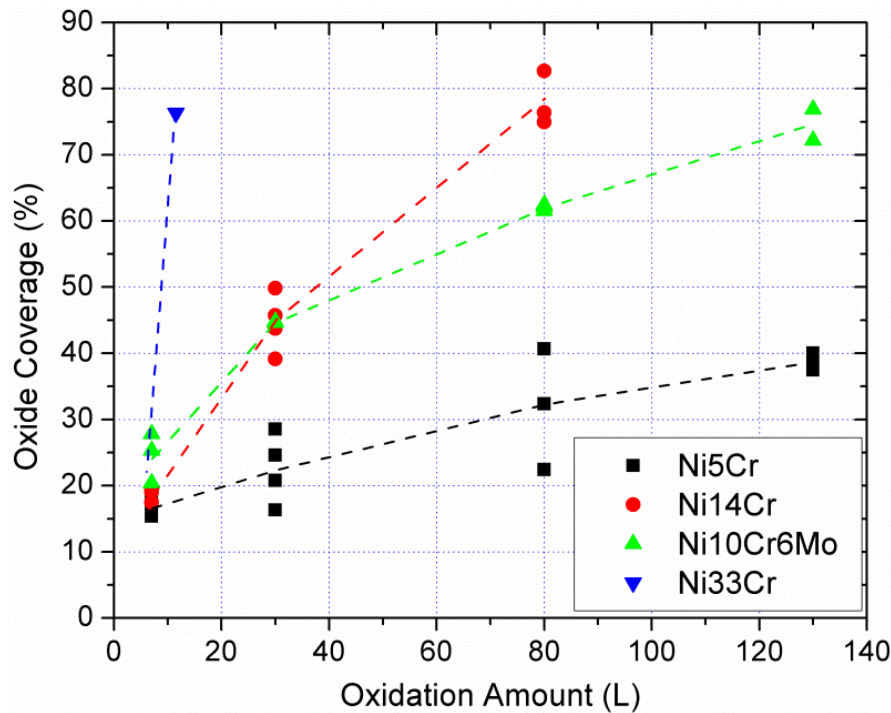


Figure 7-8. Variation of oxide coverage on Ni-Cr and Ni-Cr-Mo alloys during oxidation at 300 °C.

7.5. Future Work

Based on this first dataset, it is clear that molybdenum alters the nucleation of the oxides during the first oxygen exposure (7 L) and also affects the electronic structure of the oxide. Contrary to expectation that oxidation response is solely dictated by the amount of Cr in the alloy, we see that the addition of a third alloying element such as Mo (or W) distinctly affects the initial stages of oxidation of the alloy on the atomic length-scale. These changes are not captured by the nano-/micro-scale oxidation models that currently exist in literature. Future experiments will study alloys containing different amounts of Mo and are necessary to unravel the role of Mo addition on the nucleation and growth of oxides.

The presence of hexavalent Mo in the chromium oxide lattice, as observed by Montemor et al.¹⁴ on thicker oxide films, could be one of the possible explanations for the reduced bandgap observed on the ternary alloys and experiments on alloys with different amounts of Mo will allow us to ascertain the effect of Mo content on the bandgap and Fermi level position.

We have a good understanding of the Ni-Cr alloy oxidation which allows for targeted experiments in the future. For example, a sub-monolayer of Mo could be deposited on a NiCr surface and subsequently oxidized for 7 L: characterization of the oxides formed will shed more light on the role of Mo since we will operate in a regime where oxidation reaction is not limited by the diffusion of Mo to the surface.

References

1. Hayes, J. R., Gray, J. J., Szmodis, A. W. & Orme, C. A. Influence of Chromium and Molybdenum on the Corrosion of Nickel-Based Alloys. *Corrosion* **62**, 491–500 (2006).
2. Lloyd, A. C., Noël, J. J., McIntyre, S. & Shoesmith, D. W. Cr, Mo and W alloying additions in Ni and their effect on passivity. *Electrochimica Acta* **49**, 3015–3027 (2004).
3. Bocher, F., Huang, R. & Scully, J. R. Prediction of Critical Crevice Potentials for Ni-Cr-Mo Alloys in Simulated Crevice Solutions as a Function of Molybdenum Content. *Corrosion* **66**, 55002–55002–15 (2010).
4. Chen, L. J. *et al.* High Temperature Low-Cycle Fatigue Behavior of HAYNES 230 Superalloy. *Superalloys 2000* 573–581 (2000).
5. Gorman, D. M. *et al.* Microstructural Analysis of IN617 and IN625 Oxidised in the Presence of Steam for use in Ultra-Supercritical Power Plant. *Oxid Met* **79**, 553–566 (2013).
6. Liu, C. T., Ma, J. & Sun, X. F. Oxidation behavior of a single-crystal Ni-base superalloy between 900 and 1000 °C in air. *Journal of Alloys and Compounds* **491**, 522–526 (2010).
7. Hussain, N., Shahid, K. A., Khan, I. H. & Rahman, S. Oxidation of high-temperature alloys (superalloys) at elevated temperatures in air: I. *Oxid Met* **41**, 251–269 (1994).
8. Khalid, F. A., Hussain, N. & Shahid, K. A. Microstructure and morphology of high temperature oxidation in superalloys. *Materials Science and Engineering: A* **265**, 87–94 (1999).
9. Yun, D. W., Seo, S. M., Jeong, H. W., Kim, I. S. & Yoo, Y. S. Modelling high temperature oxidation behaviour of Ni–Cr–W–Mo alloys with Bayesian neural network. *Journal of Alloys and Compounds* **587**, 105–112 (2014).
10. Mishra, A. k. & Shoesmith, D. w. Effect of Alloying Elements on Crevice Corrosion Inhibition of Nickel-Chromium-Molybdenum-Tungsten Alloys Under Aggressive Conditions: An Electrochemical Study. *Corrosion* **70**, 721–730 (2014).
11. Kofstad, P. *High Temperature Corrosion*. (Elsevier Applied Science, 1988).
12. Greeff, A. P., Louw, C. W. & Swart, H. C. The oxidation of industrial FeCrMo steel. *Corrosion Science* **42**, 1725–1740 (2000).
13. Mathieu, H. J. & Landolt, D. An investigation of thin oxide films thermally grown in situ on Fe-24Cr and Fe-24Cr-11Mo by auger electron spectroscopy and X-ray photoelectron spectroscopy. *Corrosion Science* **26**, 547–559 (1986).
14. Montemor, M. F., Simões, A. m. p., Ferreira, M. G. S. & Belo, M. D. C. The role of Mo in the chemical composition and semiconductive behaviour of oxide films formed on stainless steels. *Corrosion Science* **41**, 17–34 (1999).
15. Mott, N. F. The theory of the formation of protective oxide films on metals.—III. *Trans. Faraday Soc.* **43**, 429–434 (1947).
16. Cabrera, N. & Mott, N. F. Theory of the oxidation of metals. *Rep. Prog. Phys.* **12**, 163 (1949).
17. Maurice, V., Despert, G., Zanna, S., Bacos, M.-P. & Marcus, P. Self-assembling of atomic vacancies at an oxide/intermetallic alloy interface. *Nat Mater* **3**, 687–691 (2004).

8. Ambient Pressure Photoelectron Spectroscopy Study of Oxidation of NiCr Alloys

Ambient pressure x-ray photoelectron spectroscopy (AP-XPS) was performed on Ni-Cr and Ni-Cr-Mo polycrystalline alloys at the National Synchrotron Light Source II (NSLS-II) at Brookhaven National Laboratory under the supervision of the beamline scientist Dr. Iradwikanari Waluyo. The experiments were performed with the help of Dr. Valentina Angelici Avincola who is a postdoctoral researcher in Prof. Opila's group at UVA. This work was carried out in August, 2016 and analysis of the data has not been finalized. This chapter is focused on information that is obtained from the data acquired at BNL. The oxidation and annealing protocols used in the experiment are outlined with special emphasis on the cleaning procedure to remove the native oxide layer on the alloy. Results of Ni-5Cr oxidation are then qualitatively discussed using raw Ni and Cr spectra. The pending work that needs to be completed in order to publish our findings is laid out in the end of the chapter. This work will be continued in Spring of 2017 and synchrotron beam time has been awarded to our group.

8.1. Motivation

We aim to study the initial stages in the oxidation of Ni-Cr and Ni-Cr-Mo alloys with near-ambient pressure photoelectron spectroscopy (PES) up to 1 torr. We aim to understand the different processes (gas-solid interaction and solid-state reactions) during the initial stages of oxidation of Ni-Cr and Ni-Cr-Mo alloys. A fundamental grasp of the oxidation reaction is critical to improve and predict adhesion, lifetime and protective function of the passive oxide layer. The experiments at ambient pressure are complementary to the STM work performed in UHV conditions. These experiments will

deliver a detailed view of compositional changes in the alloy, the detailed bonding environment in the oxide layer and at the oxide/alloy interface, and capture the complex gas-solid and solid-solid reaction sequences involved in formation of the passivating oxide layer. We will study the transformation of the alloy surface to oxide as a function of Cr concentration (5-30 wt.%), temperature (473 to 673 K), and oxygen partial pressure from 0.01-1.0 mbar.

8.2. Merits of our Approach

- The chemical shifts during oxidation provide valuable insight on the oxides that form during the initial stages of oxidation and enable us to determine the type of oxide species (valence state of metal), presence of mixed oxides as well as compositional gradients in the alloy.
- Experiments performed at near-ambient pressures allow us to address the role of the “pressure gap” on oxidation reaction kinetics¹ and provide the bridge between model experiments in UHV and real-life scenarios.
- Tunable photon energies at the beamline enables us to probe different depths of the sample i.e., we can probe only the near-surface oxide layer or through entire oxide layer right up to the oxide/metal interface if the oxide thickness is of the order of the inelastic mean free path.

8.3. Methods

Materials Four alloys were used to perform this experiment: Ni-5Cr, Ni15Cr, Ni30Cr and Ni15Cr6Mo. The alloys have been cast, and cold worked to achieve a grain size significantly smaller than the beam diameter by the research group of John Perepezko

(UW-Madison). The samples are recrystallized after cold-working by annealing at 895 °C for 1 hour. All samples are cut in rectangles with length of 11-13 mm, width of 6-9 mm and a thickness of 2 mm or lower to meet the requirements of the experimental setup at BNL. The cold worked samples are polished at UVA to reduce the surface roughness. Before introduction into the chamber, the sample is scratched lightly with a 1200 grit emery paper to remove as much of the native oxide as possible.

Characterization The samples were analyzed using a Kratos AXIS Ultra X-ray photoelectron spectrometer. High resolution spectra of Ni2p and Cr2p were recorded continuously during oxidation with pass energy of 10 eV and a time resolution of 2-3 minutes depending on the scan window. The binding energy windows used for Ni2p and Cr2p are 880-840 eV and 595-565 eV respectively. The primary photon energy used in this work is 1120 eV and was chosen so that Ni2p electrons have sufficient kinetic energy ($\approx 1120 - 880 = 240$ eV). The photon energies were varied and energies of 750, 850, 1020, 1120, and 1395 eV were used. Some photon energy choices were motivated by the need to maintain constant photoelectron kinetic energy: at 850 eV, KE of Cr2p electrons have the same KE as Ni2p electrons when measured at 1120 eV.

8.4. Results

8.4.1. Sample Cleaning Strategies

The experimental protocol followed in the PES-oxidation experiment on Ni-5Cr alloy is shown in Figure 8-1. Experiments on other alloys are similar and involve at least two oxidation steps starting at 200 °C followed by one or more post-oxidation annealing steps in UHV. XPS spectra on the as-introduced sample show the presence of nickel and

chromium oxides along with their hydroxides.²⁻⁹ Before the initial stages of oxidation of the alloy can be studied, the sample surface must be stripped of the native oxide layer. The first strategy which was tried in order to achieve a clean surface was reductive annealing in a hydrogen pressure of 1 torr at 300 °C. This annealing removed all traces of the nickel oxides and hydroxides but the chromium oxide was not removed from the surface even after 2 hours. The second approach was more successful and involved annealing of the sample in UHV at an elevated temperature of 1073 K. This removed all traces of Ni oxide/hydroxide as well as significantly reducing the amount of chromium oxide. In the case of Ni-5Cr, an almost metallic surface (<5% oxide) was reclaimed while larger amounts were present on the alloys with greater Cr content even after annealing for 2 hours or more.

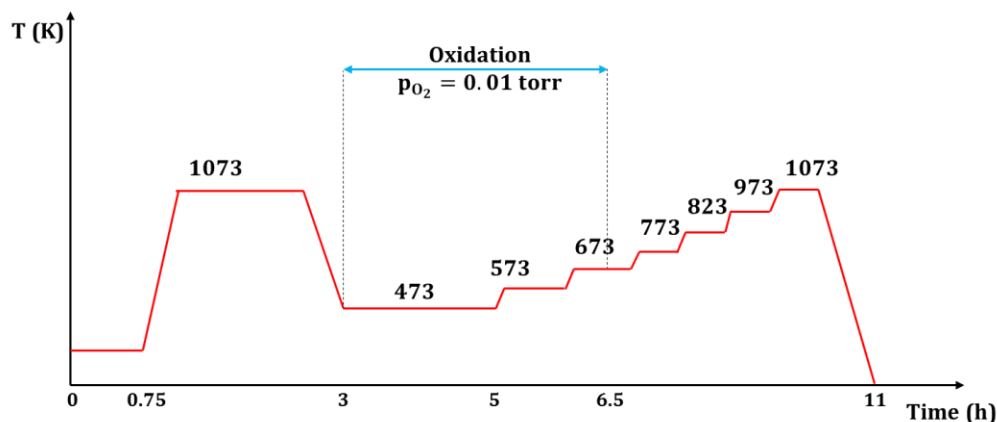


Figure 8-1. Experimental protocol followed in the PES-oxidation experiments on the Ni-5Cr alloy. The base pressure of the chamber is $<1.5 \times 10^{-8}$ torr.

8.4.2. Ni-5Cr Oxidation

High resolution Ni2p spectra at various stages of the Ni-5Cr oxidation experiment are shown in Figure 8-2. Since curve fitting is not complete, the results are discussed

qualitatively and we can only speculate on future insights once quantitative data have been extracted. The spectra in Figure 8-2 are representative ones at the end of each step in the protocol outlined earlier; about 15-25 intermediate spectra have been recorded in each step. High resolution Ni2p (and Cr2p) spectra are recorded every 2 minutes and the evolution of the surface during each of the oxidation and annealing steps can be tracked. Therefore, we obtain information on (i) rate of reduction of native oxides during initial high temperature UHV annealing, (ii) rate of formation of oxides, (iii) the different types of oxides (for example, Ni²⁺ or Ni³⁺), and (iv) the solid state reaction and reduction of thermally formed oxides during post-oxidation annealing.

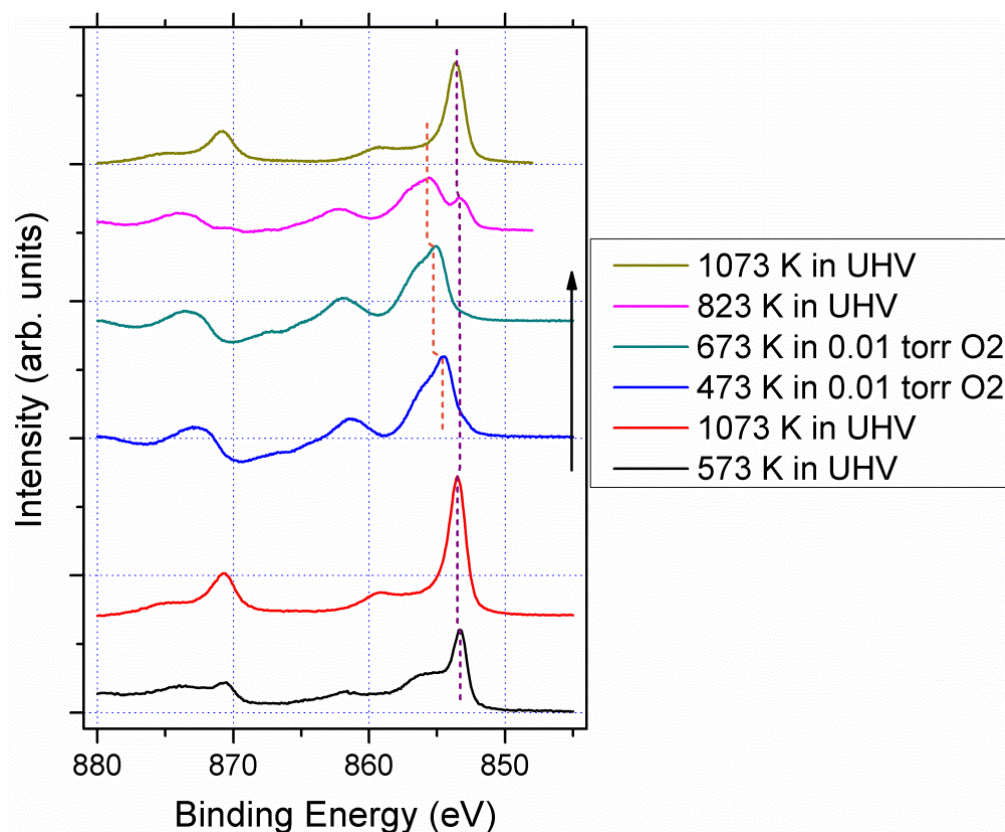


Figure 8-2. High resolution Ni 2p spectra at various stages of Ni-5Cr oxidation recorded using a photon energy of 1120 eV. The purple and orange dotted lines correspond to the Ni-metal and NiO positions respectively.^{2,3}

The peaks corresponding to Ni^0 (metal) and Ni^{2+} (NiO) in Figure 8-2 are marked on the Ni2p peak (≈ 853 eV) by purple and orange dotted lines respectively. The trace oxide and hydroxide on the as-introduced sample are removed after the 1073 K anneal. When the alloy is oxidized, the metal contribution is suppressed almost instantaneously and indicates fast rates of formation of NiO. This is in contrast to the lack of NiO formation in our UHV-STM experiments at 300 °C and other literature.¹⁰⁻¹² However, as mentioned in Chapter 6 and based on the Ni and NiCr oxidation literature, that NiO formation depends strongly on the oxygen pressure. The shape of the Ni2p peak after 473 K oxidation suggests there is a small contribution from the Ni metal at lower binding energy (right of the peak). When the thermally oxidized sample is annealed in UHV, NiO reduces and the Ni-metal contribution increases again. After the post-oxidation anneal at 1073 K, NiO is completely reduced to Ni^0 metal. Whether this is due to the reducing nature of UHV ambient or due to a solid-state reaction between metallic Cr atoms and the NiO at the metal/oxide interface still remains open but can be answered by tracking the variation of the Cr/Ni ratio during annealing.

The ability to tune photon energies is a major advantage of synchrotron-based XPS instruments and Cr2p spectra recorded at different photon energies during oxidation at 473 K are shown in Figure 8-3. The peaks at ≈ 576 and 585 eV (Cr $2p^{3/2}$ and $2p^{1/2}$) corresponds to Cr^{3+} in Cr_2O_3 and metallic Cr is not detected at this stage. However, we see a prominent shoulder at higher binding energies (≈ 580 eV) in spectra recorded at lower photon energies (850 and 750 eV). Based on literature, this peak is likely due to Cr^{4+} ions in CrO_2 . Note that at $E_{\text{ph}}=850$ eV, Cr2p photoelectrons have the same kinetic energy as Ni2p electrons from an 1120 eV beam: this means that we are probing similar depths and these spectra can be directly compared.

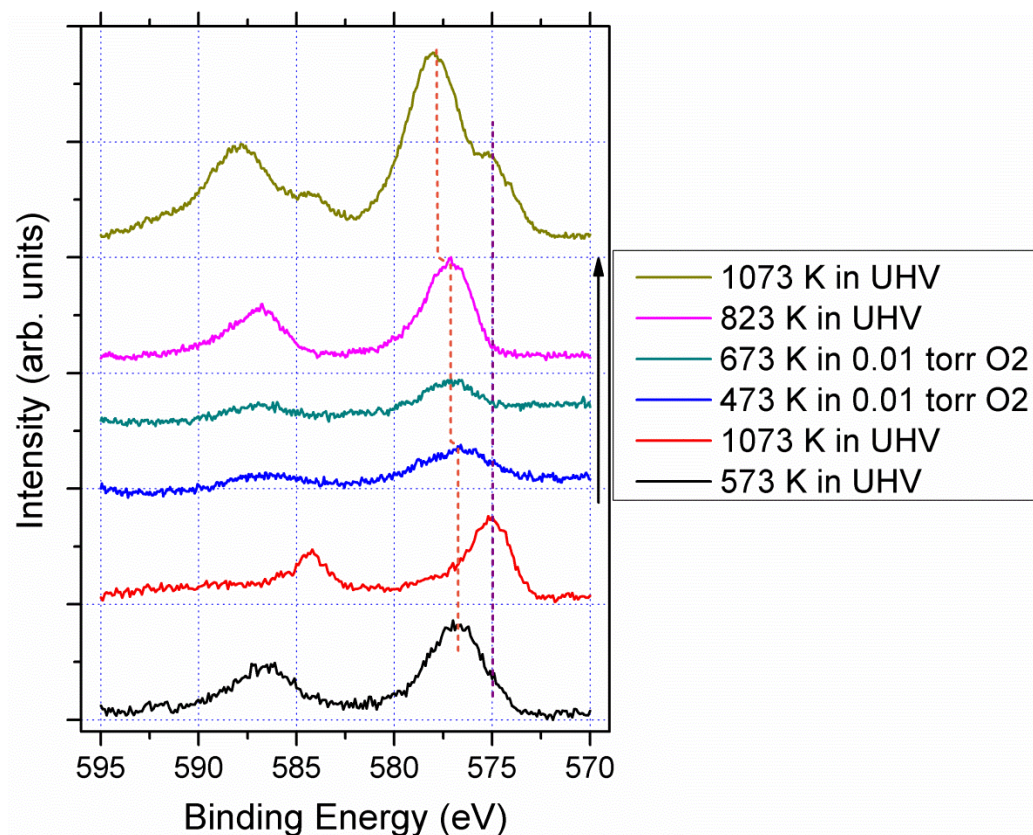


Figure 8-3. High resolution Cr2p spectra on a thermally oxidized Ni-5Cr alloy as a function of incident photon energy for the 473 K oxidation step. The purple and orange dotted lines correspond to the Cr-metal and Cr₂O₃ positions respectively.^{4,5,13,14}

8.5. Summary and Future Work

The types of information that is obtained by the experiments performed at BNL and the insights provided into the oxidation process are highlighted in this chapter. In the absence of quantitative results at this moment, it is qualitatively shown that the oxidation rate is rapid at near-ambient conditions and does not allow us to capture the evolution of the metal surface during the initial stages of oxidation. Instead, we are able to capture the evolution of oxide surface after a complete layer has been established.

The next steps in this project are to complete peak fitting for all four samples and obtain data on the relative proportion of different oxide species during oxidation and

compositional variation on the alloy surface during oxidation and post-oxidation annealing in UHV. The different oxide species that are formed as a function of alloy composition will be studied. In addition, the effect of Mo addition on the oxidation products will be assessed by comparing the results of Ni₁₅Cr and Ni₁₅Cr₆Mo oxidation.

References

1. Ertl, G. *Reactions at Solid Surfaces*. (John Wiley & Sons, 2010).
2. Biesinger, M. C. *et al.* Resolving surface chemical states in XPS analysis of first row transition metals, oxides and hydroxides: Cr, Mn, Fe, Co and Ni. *Applied Surface Science* **257**, 2717–2730 (2011).
3. Grosvenor, A. P., Biesinger, M. C., Smart, R. S. C. & McIntyre, N. S. New interpretations of XPS spectra of nickel metal and oxides. *Surface Science* **600**, 1771–1779 (2006).
4. Marchetti, L., Miserque, F., Perrin, S. & Pijolat, M. XPS study of Ni-base alloys oxide films formed in primary conditions of pressurized water reactor. *Surf. Interface Anal.* **47**, 632–642 (2015).
5. Biesinger, M. C., Brown, C., Mycroft, J. R., Davidson, R. D. & McIntyre, N. S. X-ray photoelectron spectroscopy studies of chromium compounds. *Surf. Interface Anal.* **36**, 1550–1563 (2004).
6. Allen, G. C., Tucker, P. M. & Wild, R. K. X-ray photoelectron/Auger electron spectroscopic study of the initial oxidation of chromium metal. *J. Chem. Soc., Faraday Trans. 2* **74**, 1126–1140 (1978).
7. Baltrusaitis, J. *et al.* Generalized molybdenum oxide surface chemical state XPS determination via informed amorphous sample model. *Applied Surface Science* **326**, 151–161 (2015).
8. Minni, E. & Werfel, F. Oxygen interaction with Mo(100) studied by XPS, AES and EELS. *Surf. Interface Anal.* **12**, 385–390 (1988).
9. Słoczyński, J. *et al.* Oxidative Dehydrogenation of Propane on $\text{Ni}_x\text{Mg}_{1-x}\text{Al}_2\text{O}_4$ and NiCr_2O_4 Spinels. *Journal of Catalysis* **187**, 410–418 (1999).
10. Wang, W.-D., Wu, N. J. & Thiel, P. A. Structural steps to oxidation of Ni(100). *The Journal of Chemical Physics* **92**, 2025–2035 (1990).
11. Kopatzki, E. & Behm, R. J. Step Faceting: Origin of the Temperature Dependent Induction Period in Ni(100) Oxidation. *Phys. Rev. Lett.* **74**, 1399–1402 (1995).
12. Kopatzki, E. & Behm, R. J. STM imaging and local order of oxygen adlayers on Ni(100). *Surface Science* **245**, 255–262 (1991).
13. Salvi, A. M., Castle, J. E., Watts, J. F. & Desimoni, E. Peak fitting of the chromium 2p XPS spectrum. *Applied Surface Science* **90**, 333–341 (1995).
14. Jussila, P., Lahtonen, K., Lampimäki, M., Hirsimäki, M. & Valden, M. Influence of minor alloying elements on the initial stages of oxidation of austenitic stainless steel materials. *Surf. Interface Anal.* **40**, 1149–1156 (2008).

9. AFM Characterization of Electrochemically Oxidized Ni-Cr and Ni-Cr-Mo Alloys

An important component of the current MURI project is to understand the oxide structures that are formed when Ni-Cr and Ni-Cr-Mo alloys are electrochemically oxidized in chloride and sulfate solutions. Ni-Cr-Mo alloys are important in applications where the alloy interacts with corrosive media such as saline water. In this work, the real-life interaction of the alloy with chloride (or sulfate) solutions is simulated in the laboratory by suitable choice of potentials and solution concentrations. The surface structure of the alloy before and after electrochemical passivation is characterized by atomic force microscopy. Since this is an ongoing project, the data shown here are not finalized and a number of experiments are either underway or planned for the future. The motivation and the information that is pursued in each experiment cycle are listed below:

1. **Details on the growth of passive oxide:** The development of the passive oxide film is studied by characterizing the surface morphology after different oxidation times. It is vital to understand how the oxide layer forms so that we may be able to model the growth of passive oxides in the Ni-Cr system as well as other passivating alloys. The current AFM work in combination with TEM (MURI team) and electrochemistry data provides insight into the growth of passive oxide layer.
2. **Effect of Mo on the oxide structure** – The addition of Mo drastically improves the resistance to localized corrosion of Ni-Cr alloys. The role of Mo during oxide nucleation may be determined by the passivation mechanism of alloys containing low and high Mo content using the approach described in #1.

3. **Effect of grain orientation on oxide structure** – The role of the grain orientation on the type of oxide structure as well as the differences in oxide thickness and oxide breakdown is studied. This information is invaluable for applications where the polycrystalline alloy is used: pit initiation, repassivation and crevice corrosion as a function of grain orientation can allow for better prediction of component lifetimes before catastrophic failure. The grains of interest are isolated by photolithography and oxide structures are imaged by AFM.

9.2. Methods

Ultrathin oxide films (1-3 nm) are grown on bulk alloys samples in both chloride and sulfate solutions by Kateryna Gusieva and Katie Lutton from the John Scully research group. The solutions of interest are: 0.1 M NaCl and 0.1 M H₂SO₄ adjusted to pH 4. Bulk polycrystalline samples, obtained from Perepezko research group in UW Madison, are arc melted, cold rolled and subsequently heat-treated for recrystallization. These samples are then polished to a mirror finish before electrochemical experiments are started. The native oxide on the surface is first potentiostatically reduced at -1.3 V_{sce} and then grown at +0.2 V in the de-aerated cell. Electrochemical impedance spectra are recorded at the end of the potentiostatic hold to calculate the overall oxide film thickness. These oxide films are subsequently characterized by AFM with an NT-MDT Solver Pro in tapping mode, using ETALON HA/NC tips with curvature radius less than 10 nm.

In order to study electrochemistry on single grains, the alloys are heat-treated so that the grain sizes of at least 500 μ m are obtained. EBSD maps are collected from the samples to obtain orientation information of the grains. In order to be able to identify the grain

during photolithography masking, the alloy is electrochemically etched in 5 M HCl (at 5 V) to make the grain boundaries visible in an optical microscope. The etched sample is spin-coated with a photoresist to expose the grains of interest. These isolated grains can then be electrochemically passivated while the masked region, due to the nonconductive nature of the photoresist, cannot be passivated. The exposed grains are imaged before and after oxidation with the AFM and changes in the surface structure after oxidation are correlated to the crystallographic orientation and electrochemical response of the grain.

9.3. Results

9.3.1. Chloride versus Sulfate Oxidation

The variation of surface roughness of the Ni₂₂Cr alloy after oxidation is shown in Figure 9-1 and representative AFM images are shown in Figure 9-2. The polished alloy surface is rough and the large structures are polishing residue that is not removed even after ultrasonic cleaning. The evolution of the surface structure with oxidation depends strongly on the oxidizing solution as seen in Figure 9-1(a). Oxidation in sulfate results in a steady decrease of the roughness. In contrast, oxidation in chloride solution causes an initial increase in the surface roughness followed by sharp drop after 1000 s exposure. The region when the roughness decreases in the Cl⁻ media corresponds to the regime when oxide growth and thickening is expected. Representative AFM images before oxidation, after 10⁴ s oxidation in chloride and 5000 s in sulfate solution are shown in Figure 9-2. The polished surface is rough and some polishing residue still present. The chloride oxidation presents uniform nanoscale features that are not observed on the unoxidized or the reduced surface. The surface roughness measured after 10⁴ s is lower than the actual

thickness of the oxide (2-3 nm) due to the coalescence of the oxides that nucleated on the surface during oxidation. The alloy surface after oxidation in sulfate presents similar nanoscale features that are observed on samples oxidized in chloride.

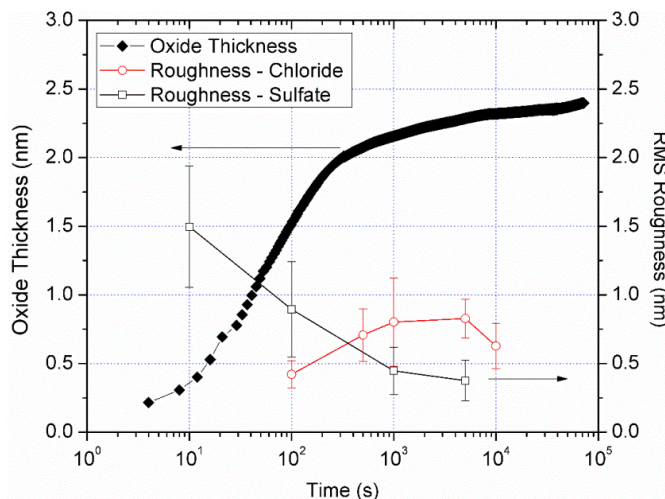


Figure 9-1. The evolution of the Ni22Cr surface during oxidation in chloride and sulfate solution is shown along with the variation of oxide film thickness measured by impedance spectroscopy.

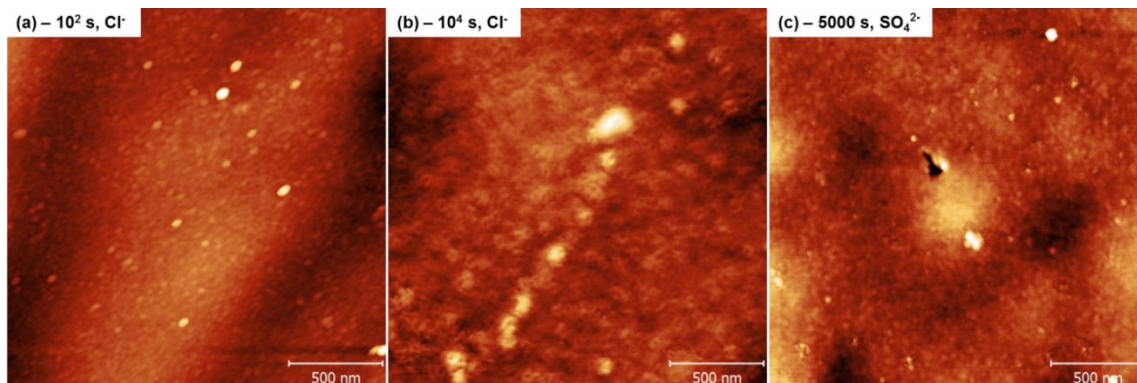


Figure 9-2. AFM images of Ni22Cr sample after electrochemical corrosion at pH=4 for (a) 100 s in Cl^- , (b) 10⁴ s in Cl^- , and (c) 5000 s in SO_4^{2-} .

9.4. Future Work

The morphological changes on the Ni22Cr surface after electrochemical corrosion for different times in chloride and sulfate solutions has been studied. The sample preparation (polishing), sample handling (to maintain integrity of the surface), pre- and post-oxidation

cleaning, and imaging parameters have been optimized. This work will be extended to Mo-containing alloy to determine the effect of Mo on the growth of the oxide layer. We are currently using the RMS roughness to track the evolution of the surface and while this quantity captures the morphological changes, more information can be obtained from the height distribution of the features and calculating the variance of the height data.

Single grain electrochemistry has been performed on Ni11Cr and images have been recorded before and after corrosion (100 s in Cl^-). However, image analysis is currently underway and the data have not been finalized. An example of an etched grain before and after oxidation is shown in Figure 9-3 and there are visible changes in the surface structure after oxidation. The oxide layer presents a surface structure that is suggestive of large-scale coalescence of individual oxide islands that nucleate and grow during oxidation. Strategies to quantify the surface structures on different grains will be devised. Similar experiments will be performed on high-Cr binary alloy as well as a Mo-containing ternary alloy.

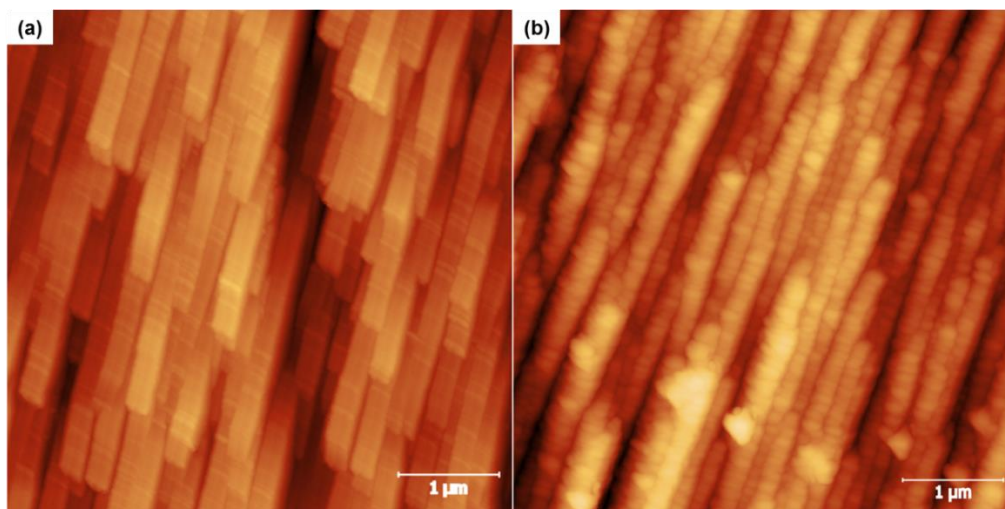


Figure 9-3. AFM images of {514} grain on Ni11Cr alloy (a) before and (b) after electrochemical oxidation in chloride solution.

10. Concluding Remarks

In the course of this work, we set out to study the initial stages of oxidation of Ni-Cr alloys with the goal of determining the effects of Cr alloying on the reactivity of the binary alloy. This would serve as the basis for probing the effect of other minor alloying additions, such as Mo in NiCr-based superalloys. Towards that goal, we establish a processing route to fabricate smooth Ni-Cr alloy thin films with well-defined terraces which can now serve as the testbed for studying chemical reactions on alloy surfaces. The ability to easily tune the composition of the thin film and to replicate identical starting alloy surfaces makes these films an ideal template for oxidation studies as a function of Cr concentration.

During oxidation at 300 °C, pure Ni does not form an oxide while the addition of just 5 wt.% of Cr alters the reactivity and initiates the nucleation of oxides on the surface. With increasing Cr content in the alloy, the oxide coverage increases rapidly for the same oxygen exposure with oxides forming at the step edges and on the flat terrace. In the case of Ni-5Cr, the growth mode changes after 30 L oxidation when Cr is depleted from the near-surface region: in this regime, no new oxides are nucleated and the existing oxides either grow laterally due to reaction with the gaseous oxygen or ripen at the expense of a nearby smaller oxide island. High-Cr alloys form a near-continuous network of oxides after just 11.5 L oxidation. Since the nucleation density is also high on these alloys, the oxide layer that forms is expected to be highly defective. The addition of Mo to the matrix alters the initial nucleation of the oxide and an ordered layer of oxides is formed. Subsequent oxidation results in the surface evolution similar to the binary alloys where Cr-diffusion and oxidation dominates.

On both Ni-Cr and Ni-Cr-Mo alloys, oxides will initially nucleate and grow vertically to a critical height beyond which sustained oxidation will only result in lateral growth until a complete oxide layer is achieved. The oxide density on the surface, which is a function of Cr content, determines when the oxidation reaction transitions to a lateral growth regime. On the atomic level, oxygen atoms are initially chemisorbed on all the sites on the surface. Owing to its multivalent nature, Cr can leach oxygen atoms from nearby Ni atoms to form CrO_x units on the surface. When Cr atoms diffusing on the surface or in the subsurface layer meets a CrO_x unit, the first nucleus of chromium oxide is formed if the barrier for nucleation is overcome.

The evolution of the electronic structure of the alloy surface during oxidation is also studied. We show that the $c(2\times 2)\text{-O/Ni}(001)$ chemisorbed structure introduces a characteristic signature in the local density of states of the surface which allows us to identify the chemisorbed phase on alloy surfaces during oxidation. During alloy oxidation, the bandgap of the oxides depend on alloy composition (Cr content) and oxide thickness. In addition, analyzing the Fermi energy of the oxides suggests that there is no band-bending and a potential across the oxide is not yet developed under our experimental conditions. Mo addition alters the electronic structure of the oxide and the oxides present a bandgap that is relatively independent of the oxide height. A lower bandgap is also observed, compared to the binary NiCr alloys, which is likely a consequence of Mo incorporation in the chromium sesquioxide.

Such a detailed study focused on the fundamental processes during the initial stages of oxidation has not been undertaken previously in the technically relevant Ni-Cr alloy

system. Information obtained from this study will serve as input for theoretical models that describe the nucleation and growth of oxides on the alloys. Insight into the effects of Cr and Mo alloying on the nanoscale structure of the alloy surface and the oxides that grow on the alloy surface opens up the opportunity to identify newer alloying additions that offer superior oxidation resistance. The observation of a defective oxide layer on the Ni-33Cr, for example, is an important finding with practical consequences in alloy design: we propose that, in addition to the minimum Cr necessary to form a continuous oxide layer, there exists a maximum Cr concentration above which the oxide layer is too defective, due to explosive nucleation, to adequately protect the underlying metal. Electronic structure information allows us to determine the oxide thickness corresponding to a potential across the oxide layer which determines when the oxide follows the Cabrera-Mott oxide film growth kinetics. The effect of alloying additions on the onset of the Mott potential and its magnitude can be evaluated and the incorporation of minor alloying additions in the oxide lattice can be deduced from this data.

The current work to understand the fundamental effects of Cr and Mo alloying on the initial stages of oxidation of Ni-Cr and Ni-Cr-Mo alloys on the nanoscale is the first of its kind in this materials system. Therefore, there is tremendous opportunity for fundamental science research that has implications for the alloy design of the technologically relevant NiCr-based superalloys. For example, the current work was performed at relatively low temperatures and the current findings need to be extended to oxidation studies at temperatures closer to the service temperatures (600-1000 °C) of these alloys. Unlike oxidation at 300 °C in UHV conditions, NiO formation is “switched on” at temperatures in excess of 600 °C and the interplay between chromium and nickel oxides can be studied.

Higher oxidation temperatures will result in crystalline oxides which can be atomically resolved for chemical identification.

The first dataset of ternary Ni-Cr-Mo alloy oxidation demonstrated the strong effect of Mo on the initial oxide nucleation and the electronic structure of the oxide. More work is required to understand how the Mo content affects the oxidation response in terms of Mo incorporation in the oxide lattice as well as formation of molybdenum oxides. The low temperature used in this work, which is below the sublimation point of volatile MoO_3 , is ideal to determine if Mo-oxides are formed. This can be taken further by annealing the oxides products and observing the effect of oxide sublimation, if any, on the structural integrity of the oxide layer at the nanoscale.

Although our analysis of oxide island morphology and electronic structure on the alloys and comparison with the reference experiments of pure Ni strongly indicates the formation of pure Cr_2O_3 , we cannot state unambiguously, in the absence of atomic resolution, that the oxides are pure chromia. DFT simulations to understand the changes in the local electronic structure of the Ni atoms due to the incorporation of Cr during alloying can provide some evidence of whether the presence of chromium catalyzes Ni atoms to react with oxygen and participate in oxide nucleation process. This work will be initiated in our group in collaboration with DFT research groups in the MURI project.

UHV-XPS experiments that replicate the oxidation conditions in this work will close the loop and unambiguously identify the type of oxides that are formed on the surface. XPS experiments on the ternary alloys will also provide confirmation of Mo-incorporation in the oxide, if any, and will complement our interpretation of STM data. This work is slated to

commence in the next year when our group acquires the UHV-XPS instrument. This work complements both the UHV-STM experiments and the near-ambient pressure XPS (AP-XPS) experiments. Quantitative analysis of data obtained in the first experiment cycle (Fall-2016) will be performed and will form the basis for next set of oxidation experiments.

This dissertation work establishes a framework to study the initial stages of oxidation of binary alloys with a focus on identifying the role of alloying elements on the atomic and electronic structure of the oxides. With the addition of complementary XPS experiments, this approach will allow us to evaluate both structural effects on the surface by microscopy and chemical effects by spectroscopy. This experimental methodology can be extended to other Ni-X alloys where alloying addition, X, has varying reactivity with oxygen compared to Ni as determined from the Ellingham diagram. The changes in the initial stages of oxidation of different alloys can then be effectively linked to the thermodynamic driving force and kinetic aspects for oxide formation and predictive models could be established.

PART – II

11. Co Adsorption on Si(100) and its Interaction with Mn Wires

11.1. Introduction

The search for magnetic semiconductors ideal for application in spintronics has been ongoing in the past decade with the discovery of ferromagnetism in p-type, Mn-doped III-V and II-VI compound semiconductors¹⁻⁴ enabling the study of magnetic phenomena as a function of carrier and spin densities. Dilute magnetic semiconductors (DMSs), in which ferromagnetism results from an interaction between electrons in the semiconductor and the magnetic moments of the dopant atoms via an exchange bias, has evolved into an important branch of materials with prediction of high- T_c DMSs in the pioneering work by Dietl et al.⁵ Ferromagnetism in delta-doped Mn-GaAs was reported by Nazmul et al.⁶ which triggered a search for similar properties in delta-doped Si and Ge. High temperature ferromagnetism in delta-doped Group-IV semiconductors has not yet been realized and ferromagnetic manganese silicides and germanides are the successes in Group-IV based systems⁷⁻¹³. One of the major issues in the field of DMSs is in explaining the origin of ferromagnetism with secondary phase precipitates and dopant clustering responsible for the observed magnetism in many cases. A thorough understanding of the initial stages of adsorption of magnetic dopants on the substrate and its bonding structure would greatly help in the explanation of observed magnetism. The understanding of the adsorption behavior and its control will also help to tailor new materials systems with enhanced properties.

A number of theoretical investigations on the adsorption of transition metals on Si(100) have been performed¹⁴⁻²². Among the various transition metals which have been

experimentally studied, only Mn self-assembles into wires on a Si(100)-2×1 surface and has been extensively investigated^{23–27}. The Mn wires have been observed first in 2008,²³ and since then been presented by several groups, but the details of Mn wire bonding to the Si(100)-2×1 surface is still discussed^{24,27–29}. A number of theoretical and experimental studies of Co on Si(100) exist on the adsorption of Co on the 2×1 reconstructed surface at room temperature and the initial growth structure of silicide films at elevated temperatures.^{19,20,30–35} The silicide growth is of interest for their application as interconnects. Several theoretical studies predict that it is energetically favorable for Co atoms to diffuse subsurface into the symmetric under-dimer site (U_D site). A general observation for the adsorption of most transition metal atoms on the Si-surface is the creation of a large number of defects even with very low ad-atom concentrations. The most prominent signature of this effect is the appearance of so-called dimer vacancy lines at elevated temperature, which form due to agglomeration of dimer vacancies. The formation of the dimer vacancies in the presence of transition metals has been described in detail for Ti, where the dimer vacancies are understood to form through the ejection of a surface dimer by the Co-atom after it moved into a subsurface position.²¹ The sub-surface atom then continues to diffuse and can therefore contribute to the formation of a relatively large number of defects. This mechanism is thought to also apply to other transition metals such as Co. The defect creation also has consequences for co-deposition of other metals with Co as the defects can significantly alter the adsorption behavior of metals. Despite a number of theoretical studies on the energetically favorable adsorption sites for Co, the pathway for the subsurface diffusion remains unclear. Scheuch and coworkers³³ reported that the deposition of Co at room temperature leads to a local 2×n reconstruction but a detailed

study of the initial adsorption structure was not possible due to experimental limitations. Choi et al.³⁴ recently studied initial stages of Co adsorption at room temperature using a combination of STM and DFT and report that the preferred adsorption site is the symmetric sub-surface U_D site.

In the present study we investigate the interaction of Co with the Si(100) surface, and then expand our work to study possible synergistic effects of the co-adsorption of Co and Mn with the goal to achieve magnetism with higher Curie temperatures than can be reached with Co or Mn on their own. The combination of Mn and Co with Si is at the same time presented in the half-metallic Heusler alloys Co_2MnSi and $CoMn_2Si$, where the Co-rich Co_2MnSi Heusler alloy has a Curie temperature of 985 K,³⁶ and the Mn-rich alloy is ferrimagnetic with a critical temperature of 578 K. Magnetism in the Mn-rich Mn_2CoZ ($Z=Al, Si, Ge, Sn$) Heusler alloys is extremely sensitive to the Mn-Mn, Co-Co, and Co-Mn interatomic distances, which have a bearing on the exchange interactions between various atoms.³⁷ The ability to create selected structures or surface alloys where the Mn-Co, Mn-Mn and Co-Co distance can be adjusted might allow for an improved understanding of the complex magnetic interactions. A good understanding of the adsorption of Mn and Co on a Si(001) surface is therefore essential. While the former has been extensively studied, this article attempts to address the still-debated room temperature adsorption behavior of Co on Si(100)- 2×1 .

In this paper, we observe the initial stages of adsorption of Co on Si(100) at room temperature and show that there is a greater preference for Co to occupy the asymmetric U_H or U_L subsurface site underneath the higher or lower Si atom of the buckled surface

dimer. The deposition of Co results in defect creation due to the ejection of the surface Si atoms by the diffusing subsurface Co atoms. With an understanding of the Co adsorption on pristine Si(100), we continue with the observation of adsorption behavior of Co on a Si surface with Mn wires to study the competing interactions of Co with the Mn wires and Si surface. We also perform a co-deposition experiment of Mn and Co on Si(100) and report that while Co continues create a substantial number of defects, the Mn-Co interaction dominates in the vicinity of the Mn wires.

11.2. Experimental Section

All experiments were performed in an Omicron Nanotechnology Variable Temperature SPM system under ultrahigh vacuum (UHV) conditions. The base pressure was 1.5×10^{-10} mbar or better. The Si(100) samples were B-doped with resistivity between 0.065-0.074 $\Omega \cdot \text{cm}$. The sample was annealed overnight at 550 $^{\circ}\text{C}$ and then flashed repeatedly to 1250-1300 $^{\circ}\text{C}$ to obtain the 2×1 reconstruction, similar to the procedure outlined Hata et al.³⁸ The defect concentration (missing dimers and missing atoms) on the Si(100)-(2×1) reconstruction was 4% or less prior to Mn deposition. Figure 11-1(a) is representative of a typical surface obtained prior to Mn and Co deposition. Co (GoodFellow, >99.99% purity) and Mn (Kurt Lesker, 99.99% purity) were deposited by electron beam evaporation using a Mantis Mini e-beam evaporator (QUAD-EV-C). The deposition rates were adjusted using a quartz crystal monitor (QCM). All deposition experiments were performed at room temperature and the Co and Mn deposition rates used were $\approx 1.4 \times 10^{-3}$ ML/s and 6.6×10^{-3} ML/s respectively. The exact coverage was determined by analysis of the STM images.

Imaging was done at room temperature in constant current mode with W tips prepared by electrochemical etching. All images were taken at sample bias of +1.5 V (empty states) and -1.5 V (filled states) and a feedback current of 0.03 nA. Gwyddion,³⁹ WSxM,⁴⁰ and ImageJ⁴¹ software packages were used for image analysis. The defect concentration, Co, and Mn coverage were obtained by extracting a mask from the STM image based on height thresholds that can be set in WSxM and Gwyddion. This binary mask was fed into ImageJ and the projected area gives the coverage of any structure investigated. Mn wire refers to a 1D structure that is one atom thick and is three atoms or longer,²³ and the "defect concentration" corresponds to the fraction of the surface occupied by defects whereas 100% is 1 ML. The error indicated in the data is the standard deviation calculated for each individual data set.

11.3. Results and Discussion

11.3.1. Co on Si(100)-2×1

Figure 11-1(a) shows the pristine Si(100) surface with the 2×1 reconstruction and a defect concentration of $1.98 \pm 0.5\%$. The majority of the defects are missing atoms (C-type defects) which appear as protrusions in an empty states image and as a depression in the filled states image.⁴²⁻⁴⁴ The deposition of only 0.054 ± 0.005 ML of Co leads to a degradation of the surface quality, which is expressed as a significant increase in the defect concentration as seen in Figure 11-1(b). The defect concentration as calculated by image analysis is $10.43 \pm 0.9\%$ and this represents a five-fold increase in the number of defects. The increase in the defect concentration illustrated in Figure 11-1(c) was consistently observed across all our experiments and is nearly independent of the Co-concentration.

The average defect concentration before deposition of Co is $3.40 \pm 0.81\%$ and it increases by 8.4% to $11.82 \pm 1.27\%$ after Co-deposition. Compared to the predominantly C-type defects before Co-deposition, the A-type defects (missing dimer), and double dimer vacancies (B-type or 2-DVs) defects dominate after Co-deposition. A-type and B-type defects are indicated in Figure 11-1(b) by circular and square markings, respectively. There are also defect structures such as the 1+2 DVs (1- and 2-DVs separated by a dimer) which are not discussed separately. Line scans across the A-type and a B-type defect marked in Figure 11-1(b) is shown in Figure 11-2(a). The apparent increase in depth of the B-type defects can be attributed to the fact that the double dimer is larger and the tip can probe the entire depth of the vacancy. The depths of A-type and B-type defects before and after Co deposition are summarized in Figure 11-2(b), which shows that the depths are not altered by Co deposition. These data were collected from several samples using different tips, which accounts for the width of the depth distribution. This result is significant in terms of eliminating the DV site as the preferred adsorption site as will be discussed later.

Such a degradation of the Si surface quality has not been observed during room temperature deposition of Mn but is characteristic of most transition metal depositions on Si-surfaces, including Co deposition on (100) surfaces of Si and Ge,^{34,45,46} and Ni deposition on Si(100).⁴⁷ The addition of only traces of transition metals such as Ni, Fe, Co or Ti and subsequent annealing or flashing of the Si substrate initiates the formation of an extended (2x1) reconstruction with DVLs (dimer vacancy lines). The DVLs, which define this reconstruction, can only be formed at temperatures exceeding about 500° C when the dimer vacancies (DV) are sufficiently mobile. At lower temperatures the vacancies are

created by the interaction of the transition metal with the surface, but they remain stationary and thus a defect-rich surface is formed as can be seen in Figure 11-1(b).

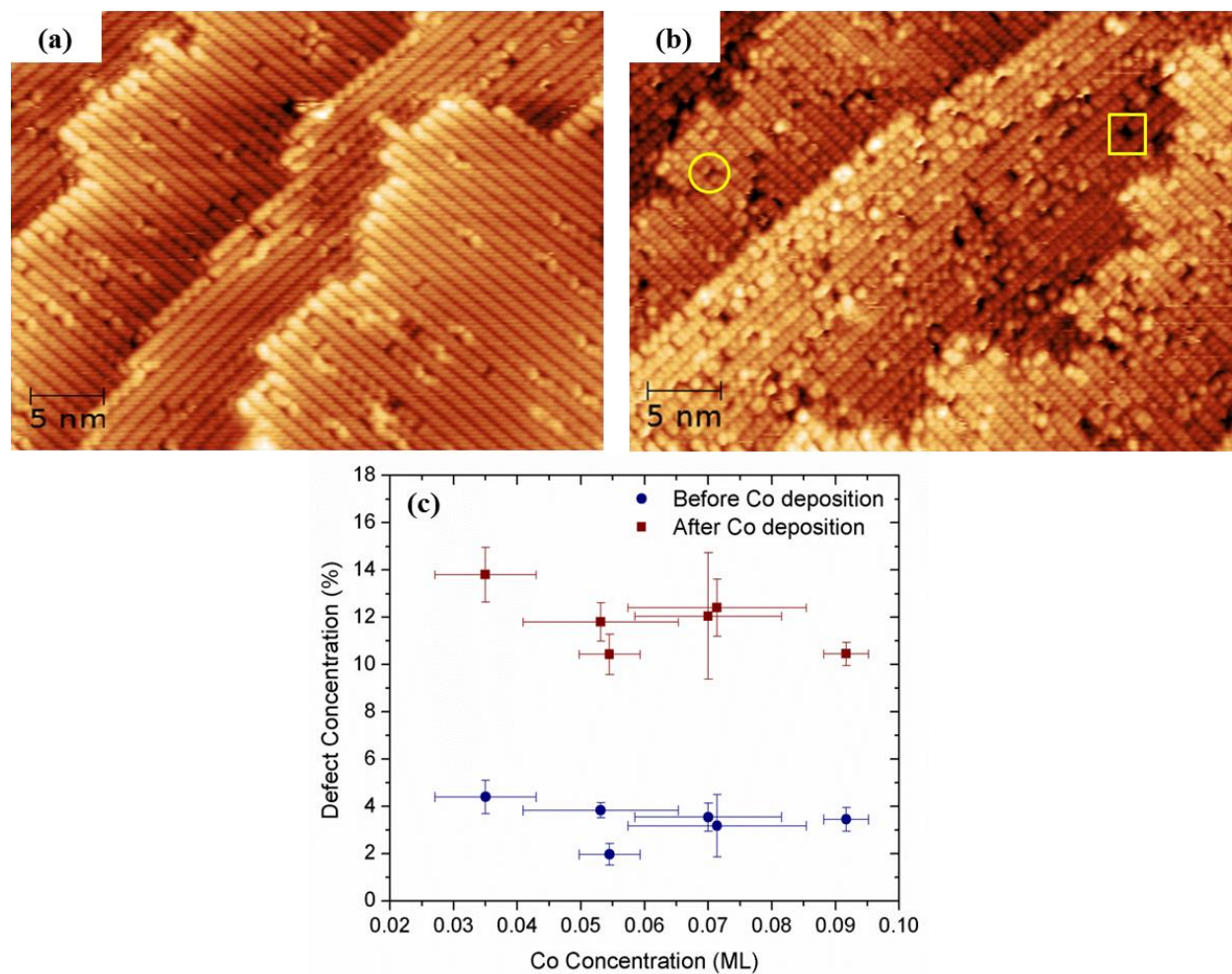


Figure 11-1. STM images (-1.5 V, 0.03 nA) of (a) pristine Si(100)-2×1 surface, and (b) Si surface after deposition of 0.054 ML of Co. The circle and square in (b) mark an A-type defect (single missing dimer) and a B-type defect (two adjacent dimers missing). (C) summarizes the overall defect concentration in % of surface occupied by defects as a function of Co-concentration.

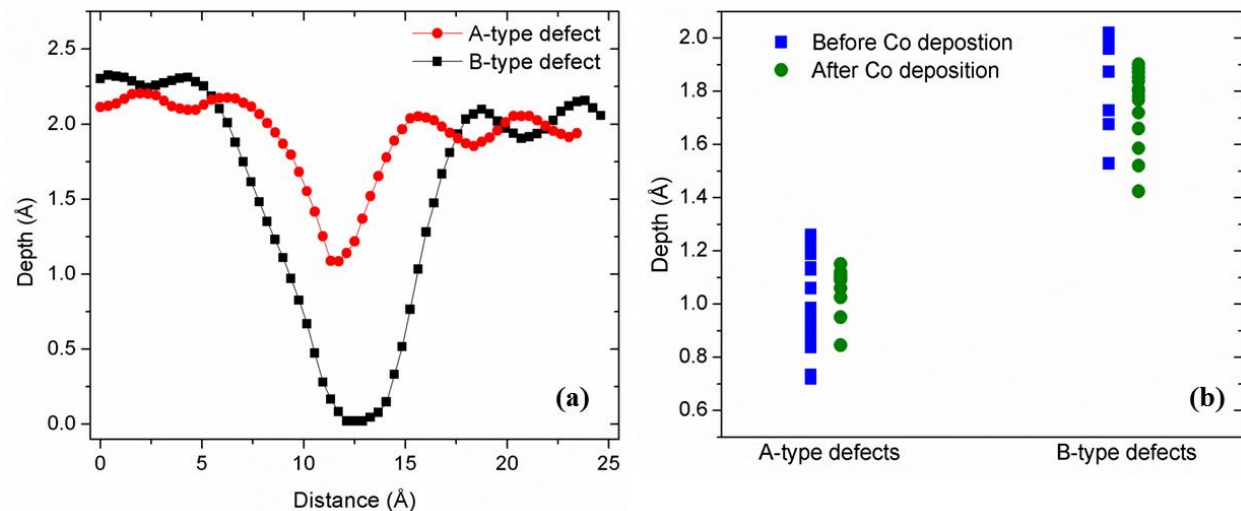


Figure 11-2. (a) Line scans across an A-type and a B-type defect on a pristine Si surface are shown. (b) shows the depth distribution of A-type and B-type defects before and after Co deposition.

The creation of the defects is attributed to the ejection of Si atoms from the surface due to the strain induced by the diffusing, subsurface Co atom similar to the defect creation by Ni in Si(100);^{22,47,48} it is generally assumed without explicit confirmation in all instances that the mechanisms of defect creation are similar across these elements. The ejection of surface Si atoms can take place via the ejection of the Si dimer as a whole or by the breaking down of the dimer and subsequent ejection of individual Si atoms. The resultant Si-ad-atoms are highly mobile at room temperature and annihilate with other defects or at the step edges; Si-ad-dimers, on the other hand, are still stationary at room temperature, but agglomerate into islands once they become mobile. No indication for ad-dimer island formation or the presence of ad-dimers in the vicinity of dimer vacancies is seen in our images after Co-deposition. This is consistent with the theory of ejection of highly mobile Si-ad-atoms, which cannot be imaged, rather than stationary ad-dimers during the formation of A and B-type defects.

Figure 11-1(c) summarizes the defect concentrations before and after Co deposition and illustrates that the increase in the concentration of defects (single and double dimer vacancies) is with about 8% independent of the amount of Co for coverages between 0.03 to 0.1 ML. Therefore, on average, each Co atom produces fewer defects at higher coverage, albeit there is currently no obvious and satisfactory model to explain a drop in defect production per se. On the other hand, rather than assuming a decrease in the production rate of defects, the defect concentration can be depressed by an increased rate of defect recombination with Si-adatoms or dimers driven by an increased Si-ad-atom or dimer concentration on the surface.

The constant defect concentration, independent of Co-coverage, can be understood as an equilibrium reaction between the defects created by the deposited Co atoms, and defect annihilation by Si atoms, which diffuse on the surface. One way to illustrate the competition between defect creation and annihilation is to assume, for the sake of our argument, that every Co-atom creates the same number of defects and consequently Si-ad-atoms, which are now mobile on the Si-surface. Increasing the number of Co-atoms then increases initially the number of defects, which are now separated by a smaller mean distance - the Si-ad-atoms are now more likely to encounter and recombine with a defect as they move across the surface. This leads overall to higher recombination rates and can explain the constant defect concentration observed in the range of 0.03 to 0.1 ML Co-coverage.

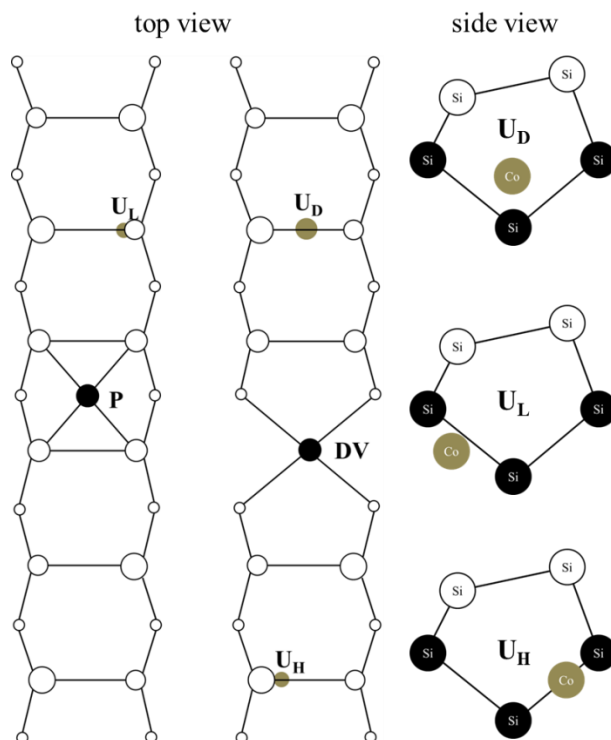


Figure 11-3. Ball and stick model of the adsorption sites of Co on the Si(100)-2x1 surface reconstruction. The adsorption sites are named as following: Surface site: P – Symmetric Pedestal Site; Subsurface sites: U_D – Under dimer site, U_H – Site under high site of Si-surface dimer, U_L – Site under low site of Si-surface dimer, DV – Dimer vacancy site. The ball and stick model of adsorption sites and the site nomenclature were adapted from Refs.^{19,20}.

The Co atoms are seen as protrusions (bright features), which are most likely the Si-atoms sitting above the sub-surface Co, in Figure 11-1(b) which are attributed to Co atoms incorporated in symmetric or asymmetric subsurface adsorption sites based on a recent combined STM and DFT study of Co adsorption on Si(100)-2x1.³⁴ The interpretation of a few adsorption sites on Si(100) and the side views of the three important subsurface interstitial sites (U_D , U_H , and U_L) are shown in Figure 11-3; this was adapted from Figure 1 in Ref.^{19,20} Other theoretical studies on the adsorption of Co on Si(100)-2x1 also report subsurface incorporation to be energetically more favorable than the surface adsorption,^{19,20} and several adsorption sites have been studied. The symmetric U_D site is

the energetically favorable adsorption site for Co, followed by the two asymmetric sites: U_H and U_L . The U_H site is assigned in Figure 11-3 to the Co atom sitting beneath the higher Si-dimer atom, and U_L site is for the Co sitting beneath the lower Si-dimer atom. It should be noted that there is a discrepancy in the literature about the relaxed geometry of Co atom adsorbed in the U_H site^{19,20} and the relative stability of the two asymmetric subsurface sites is still discussed. The relaxed geometry obtained by Choi et al.³⁴ for a Co atom adsorbed at the U_H site is similar to the preceding work by Peng et al.²⁰ and they agree that U_H is the most stable asymmetric subsurface adsorption site.

A high resolution image of a Si terrace after Co deposition is shown in Figure 11-4 where the symmetric and asymmetric adsorption sites can be recognized. The Co atoms adsorbed at U_H/U_L sites and U_D sites are marked with circles and squares in the figure. Bright protrusions which are symmetric about the center of the dimer and extend across the Si dimer row are attributed to subsurface Co atoms adsorbed at the U_D site. Protrusions that are asymmetric and do not extend across the entire dimer row are attributed to U_H or U_L sites. It should be noted that it is not possible to make a distinction between the two asymmetric sites based on STM images. In these asymmetric sites, the Si atom directly above a Co atom is pinned resulting in only the higher Si atom in the dimer being visible in the STM image (seen in Figure 11-4). A Si dimer flips rapidly between the two buckled orientations even at room temperature, and dimers otherwise imaged using STM images show therefore an average between the two buckling orientations.^{49,50} If, however, one dimer is pinned in a specific orientation such as in an asymmetric Co-adsorption site, the adjacent dimers can also be pinned, and this modified local reconstruction extends for a

small distance along the dimer row. This pinning effect is not observed in the vicinity of Co atoms adsorbed in U_D sites.

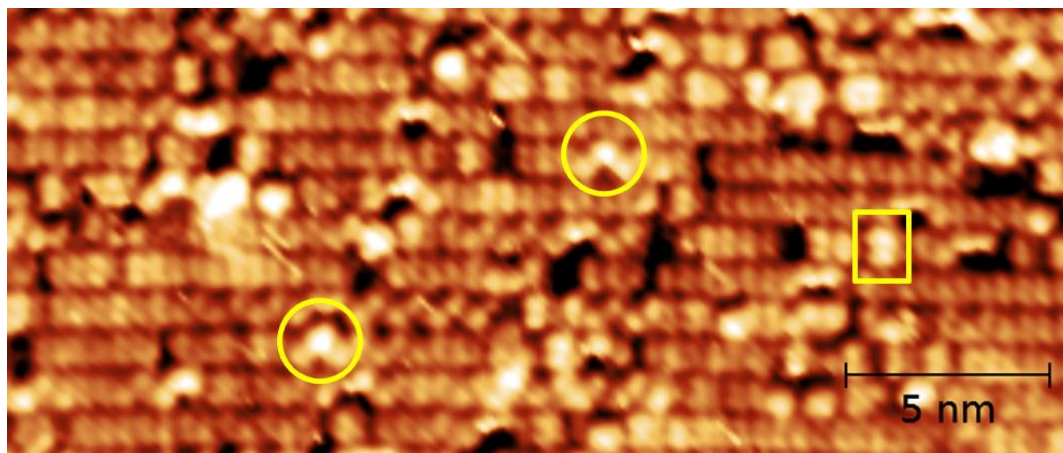


Figure 11-4. Higher resolution STM image (-1.5 V, 0.03 nA) of an individual Si terrace after Co deposition. The circles in the image indicate Co occupying the asymmetric U_H/U_L site and the square indicates Co adsorbed at symmetric U_D site.

In all our experiments we observe the asymmetric as well as the symmetric Co-adsorption sites irrespective of the amount of Co deposited. The distribution of Co adsorbed in the symmetric and asymmetric subsurface sites is shown in Figure 11-5 and it illustrates that Co preferentially occupies the asymmetric U_H and/or U_L sites despite calculations predicting the symmetric U_D site as being the thermodynamically most stable site. Bright features, which extend beyond the width of the Si dimer row are termed clusters, and cannot be assigned a specific bonding site. These are not included in the present analysis and amount to less than 20% in all cases. Irrespective of the amount of Co deposited, it is seen that there is a greater preference for Co to occupy the asymmetric U_H/U_L site with about 72 % of the deposited Co at these sites. That only 28 % of the Co atoms are adsorbed in the U_D sites is a clear departure from a previous STM study of the initial stages of Co adsorption,³⁴ albeit the amount of Co in this study was with 0.04 ML

even lower than in the present study except for one of our samples. Even if all clusters are attributed to U_D sites as the primary nucleus site for a cluster formation, the preference for occupation of the asymmetric subsurface sites still persists with an estimated 62% of Co atoms occupying these sites. The difference in the occupancy of Co atoms between our work and Choi et al.³⁴ is surprising because the Si surface preparation, the Co deposition method, and the base pressures of our system are similar as far as we can judge from the experimental description in Ref.³⁵ The origin of this discrepancy might lie in the quality of the surface as defined by the concentration and distribution of different defects prior to Co-deposition; Choi et al.³⁴ did not include an analysis of the pre-deposition Si-surface but from the comparison of both our studies and Meyerheim et al.,⁵¹ knowledge of the initial Si(100) surface might be more important than expected, especially in the low Co-coverage regime.

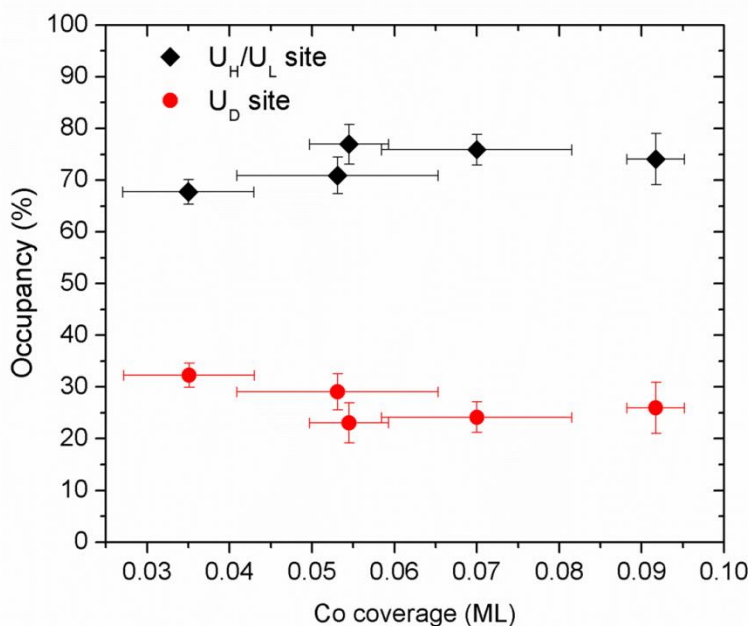


Figure 11-5. Percentage of Co in UD and UH/UL sites as a function of Co coverage.

Assuming that the stability of the adsorption sites is reflected correctly in the DFT calculations, the preference for the asymmetric sites has to be kinetic in origin, and linked to an easier diffusion path, which promotes the asymmetric over the symmetric sites at room temperature. In addition, the analysis of the profile of the A- and B-type defects summarized in Figure 11-2 strongly indicates that Co-atoms are not bonded in the dimer-vacancy sites - the depth of the dimer vacancies remains unaffected by the presence of Co. These data include several depositions, and different tips which accounts for the breadth of the distribution. This observation indicates that after ejection of Si-atoms and formation of a defect site, the Co-atoms rapidly leaves the vacancy and diffuses to a more favorable sub-surface bonding site. The bonding site at the bottom of a vacancy has not been included in any of the DFT calculations, but should be taken into account in future assessment of Co-bonding on Si.

A comparison of diffusion pathways of Co-ad-atoms into the symmetric and asymmetric sub-surface sites following the predictions from a recent DFT study might help to understand the discrepancy between site-stability and occupation observed in our work.²⁰ According to the calculated activation energies by Peng et al.,²⁰ the diffusion into the intermediate subsurface site - the under-pedestal site (U_P), directly underneath the pedestal site (see Figure 11-3) - carries a small activation barrier and is thus unlikely to be the rate-limiting step, but likely to be the first step for Co to move sub-surface. Therefore, we concentrate on the diffusion pathways from the U_P site to the three stable interstitial sites to explain the preferential occupation of the asymmetric sites. While the U_D site is the energetically stable subsurface site, its population might be inhibited by the relatively high activation energies of 0.61 eV for motion from the intermediate U_P site $U_P \rightarrow U_D$, and 0.48 eV

for motion from the asymmetric site $U_L \rightarrow U_D$. However, the activation energy for $U_H \rightarrow U_D$ is only 0.02 eV and therefore, any Co atom in the asymmetric U_H site is expected to relax instantaneously to the symmetric U_D site. The diffusion paths /energy barriers from the surface or the U_P site into the asymmetric sites remain an open question and have been suggested to require several consecutive steps. Therefore, on the basis of numbers given in Peng et al.,²⁰ we speculate that the occupied asymmetric adsorption sites observed in Figures 11-1(b) and 11-4 are Co atoms adsorbed in the U_L bonding site and conclude that this preferential occupation is due to kinetic limitation imposed on the occupancy of the U_D site.

11.3.2. Sequential deposition of Mn and Co

Figure 11-6(a) is an empty states STM image showing self-assembled Mn wires on the 2×1 reconstructed surface of Si(100).²³⁻²⁶ The Mn coverage on the surface is 0.23 ± 0.02 ML. This image illustrates the high quality of Mn wires prior to Co deposition. The wire length is defined from the STM images as the number of units in a given wire, where a unit is defined as the dimensions of a Si dimer along the direction of the Mn wire. The structure marked in the inset in Figure 11-6(a) corresponds to a wire, which is 6 units long.

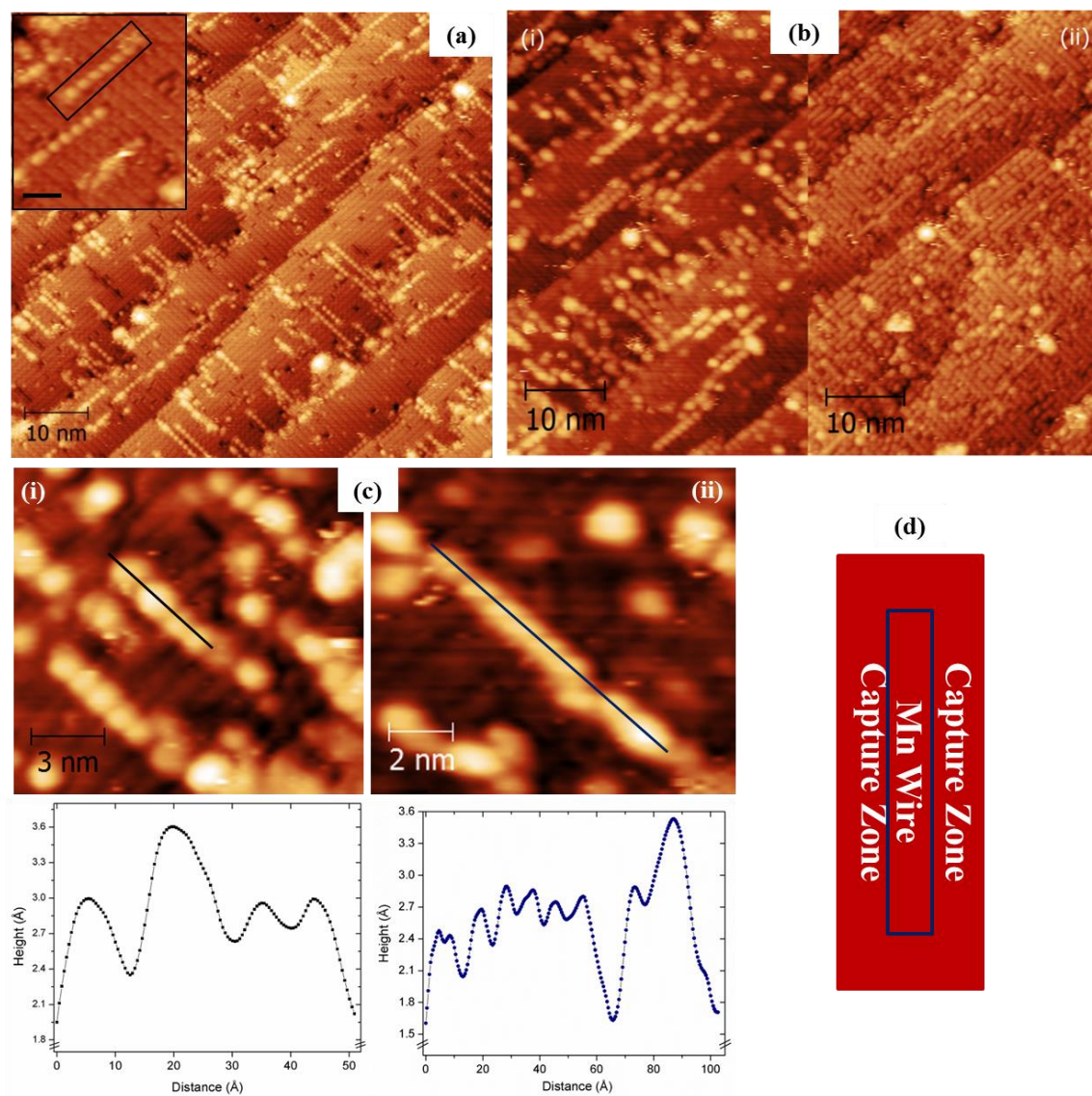


Figure 11-6. STM images after (a) deposition of 0.23 ML of Mn, and (b) deposition of 0.06 ML of Co on the same surface; (i) and (ii) in part-(b) are empty and filled states image of the same area. Part (c) shows image segments illustrating a kink (i) and protrusion (ii) along a Mn wire with corresponding line scans. The inset in (a) shows a representative wire-structure (scale bar is 3 nm). Empty and filled states images are recorded at +1.5 V and -1.5 V at feedback current of 0.03 nA.

Figure 11-6(b) shows the same sample imaged after the deposition of 0.056 ± 0.01 ML of Co. The Mn wire quality is severely degraded and the number of clusters and structures that consist of only one or two units has increased substantially. Since the Mn wires are best imaged in positive sample bias (empty states), the images after Co deposition were

also acquired under the same conditions and is shown in the left half of Figure 11-6(b). However, the surface defects created by Co as discussed in section 11-3.1 cannot be imaged well under these conditions. Therefore, a filled state image of the same area is shown on the right half of Figure 11-6(b) for comparison - the defect structures are now clearly visible. The observation of typical defect structures for Co deposition on Si indicates that the defect-creation through the interaction between Co and Si proceeds in the same manner as on the bare Si surface. On the other hand, the quality of the Mn wires degrades substantially, both with respect to the wire length and homogeneity. The latter is illustrated in Figure 11-6(c) which shows representative wires with a kink along the length of the wire and a protrusion on the wire. The corresponding line scans show an abrupt absence of Mn atom along the wire (kink) and an increased height of 0.63 \AA from the surface of the wire (protrusion). These protrusions on the wire generally have a height of $0.5\text{-}0.8 \text{ \AA}$ measured from the surface of the wire. This was not seen prior to Co deposition except at wire-ends where Mn clusters are often present.^{23,26} We interpret the protrusions on the wires as Co atoms adsorbed on the wire or Co-atoms inserted between Mn and Si - the exact bonding configuration cannot be identified at present. The kinks, on the other hand, might be due to introduction of defects from the Co-atom subsurface diffusion in a mechanism similar to the creation of Si-surface defects, albeit the large number of bonds involved in this rearrangement process makes it somewhat counterintuitive. These questions will be addressed in a future DFT calculation and additional experimentation.

The wire length distribution before and after Co deposition is shown in Figure 11-7. The Co deposition leads to the appearance of a large number of Mn dimers and these are included in the distribution. Before the deposition of Co, the most probable wire length is 4

units and the distribution is characterized by a long tail with a considerable number of longer wires. After deposition of Co, however, the distribution is dominated by Mn dimers and ultrashort wires (3 units long) and decays much more rapidly; the number of longer wires is significantly reduced. This process is clearly induced by the presence of Co, which is correlated with the appearance of numerous kinks along the wires and slight offsets between short wires are readily apparent, which visually appear like breaking of longer wires with a consequent loss of continuity. The greater number of ultrashort wires combined with the decrease in the number of longer wires, and the faster decay of the distribution leads us to the conclusion that the interaction of the Co adatoms with Mn wires locally modifies the bonding between of the Mn wires to the Si-surface.

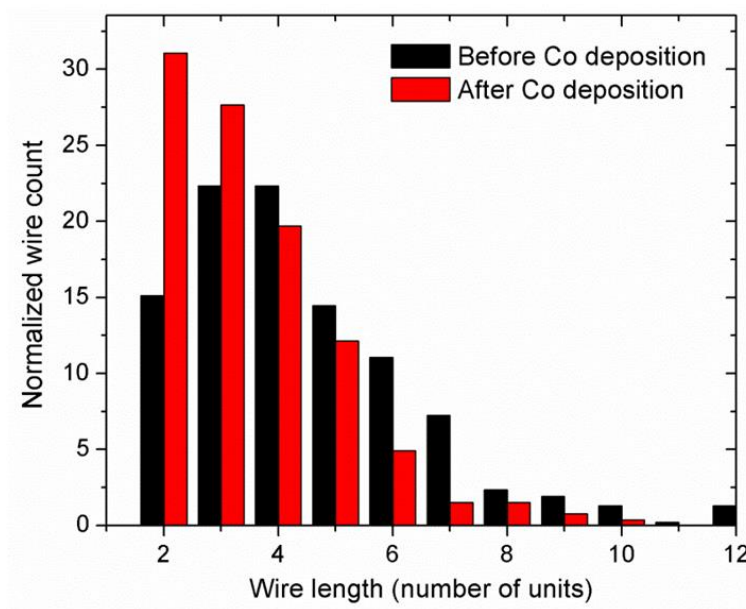


Figure 11-7. Wire length distribution before and after Co deposition which indicates a greater number of Mn dimers and ultrashort wires after the deposition of Co.

In order to quantify the Co distribution on the surface, we defined a so-called capture zone (see Figure 11-6(d)): a region around a Mn wire with a width corresponding to the

diameter of approximate a Co-atom and the total width of the capture zone is 3.9 nm. All Co-atoms within this capture zone will therefore touch the Mn wire and are within bond-range. One implicit assumption for this analysis is the assignment of protrusions at the Mn wires to Co-atoms - this was discussed in detail in conjunction with Figure 6 in the previous paragraph. The Mn wires and Co-ad-atoms can be distinguished in empty and filled state images: the apparent height of the Mn wires is reduced in the filled state images²⁴ (see Figure 11-6(b)) while the appearance of Co remains unchanged. This knowledge is used to separate the Co atoms from Mn wires and C-type defects⁴²⁻⁴⁴ by careful comparison of several filled and empty states images of the same area. The data included in Table I were collected from two experiments S1, and S2, at different positions on the sample.

The comparison of the area density of Co-atoms in the capture zone with the density of Co atoms on the free surface is summarized in Table I. For the experiment shown in Figure 11-6 (S1 in the table), the capture zone area has a width of 3.9 nm and occupies 44 ± 1 % of the surface area. The width of the capture zone is defined by the space occupied by a Co-atom adsorption site in contact with the Mn wire and is 3.9 nm based on diameter of the Mn and Co atoms as measured from STM images. The Co-atom density is on average $8.4 \times 10^4 \mu\text{m}^2$ in the capture zone, and only $3.4 \times 10^4 \mu\text{m}^2$ on the free surface, illustrating the preference of Co to stay close to a Mn wire. The Mn wire likely acts as an obstacle to Co-diffusion, and the stability of the Co-site close to wire is stabilized by the Co-Mn bonding or by the modulation of the local strain field in the Si(100) surface around the wire. The preference for Co and Mn to occupy adjacent surface sites can be understood as the early stages of alloying. Co atoms farther away from the Mn wire expended their thermal energy

available for diffusion before they could attach to a Mn wire and stay at bonding positions equivalent to those on the free surface for Co-only deposition.

Table 11-I. Summary of Mn and Co coverage for sequential deposition experiments, capture zone area as percent of total surface area [definition of capture zone CZ is given in Figure 3], and density of Co-atoms in the CZ and on the free surface - not touching any Mn wire. The last column gives the ratio of Co-atoms in the CZ compared to the FS.

Sample	Mn ($\times 10^{-2}$ ML)	+ Co ($\times 10^{-2}$ ML)	Capture Zone CZ (% of surface area)	Co _{CZ} - density of Co in CZ (atoms/ μm^2)	Co _{FS} - density of Co atoms on free surface (atoms/ μm^2)	R=Co _{CZ} /Co _{FS}
S1	23.3	6.0	44.4 %	1.09×10^5	3.2×10^4	3.4
S1	21.1	7.4	59.1 %	1.25×10^5	6.3×10^4	2
S2	27.7	4.4	43.2 %	6.1×10^5	1.6×10^4	3.9
S2	28.5	4.2	54.7 %	4.03×10^5	2.1×10^4	2

11.3.3. Co-deposition of Co and Mn:

The sequential deposition experiments described in section 11.3.2 leads us to investigate the co-deposition of both reactants, where both reactants are mobile, to explore the feasibility of forming ordered surface-alloy structures. In the co-deposition experiment, ≈ 0.3 ML of Mn and ≈ 0.06 ML of Co were deposited on a Si(100)- 2×1 surface; this is comparable to the element concentrations used in sequential deposition. The empty states and filled state images are shown in Figures 11-8(a) and (b), and surprisingly the formation of Mn wire structures can still be observed. The presence of wires is particularly astonishing in light of the high defect concentration initiated by the interaction of Co atoms with the Si surface. The defect structure on the Si surface, as seen in Figure 11-8(b), is equivalent to those observed on Si with Co (Figure 11-1), or at the end of the sequential deposition sequence. This supports our previous model that a Co atom initially adsorbed on Si relaxes into a subsurface site, initiates the formation of defects, and continues

diffusing independently unless it encounters a Mn wire at which point the Co atom relaxes into a position close to the wire. However, this process happens at the same time as the growth of the Mn wires. A previous study from our group demonstrated the detrimental impact of surface defects on Mn wire formation but those surfaces were dominated by C-type defects, while Co atoms create predominantly A- and B-type defects as shown in section 11.3.1. The type of defect therefore appears to be critical and A- and B-type defects are not as detrimental to Mn wire growth as the highly reactive C-type defects.

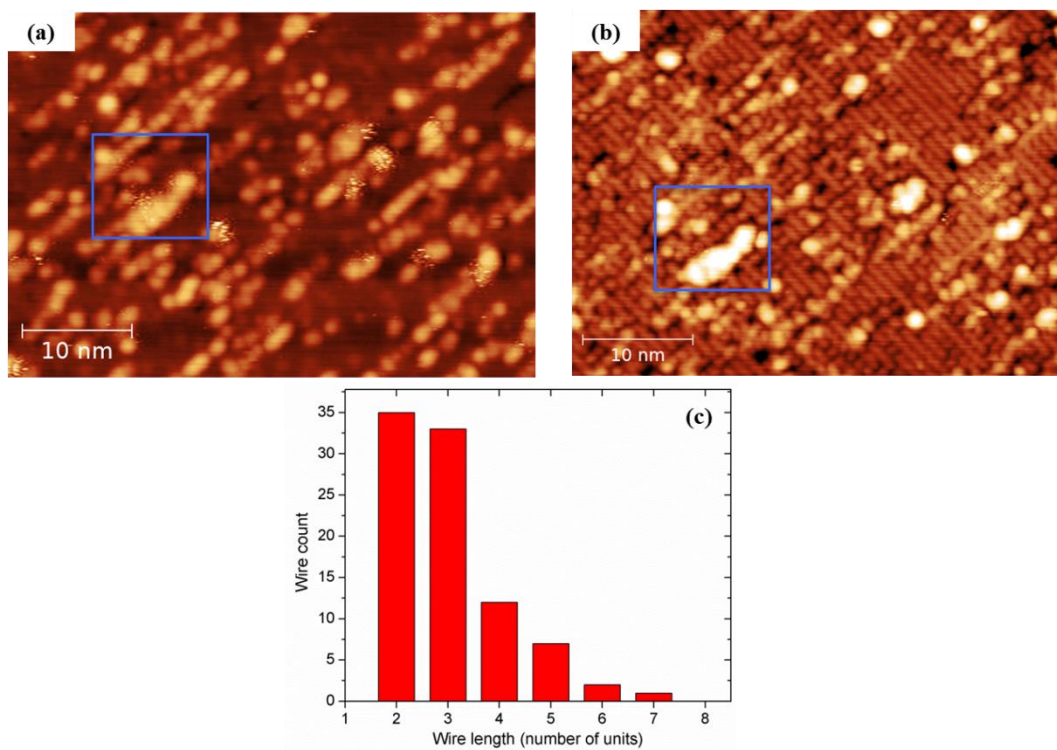


Figure 11-8. STM images of the Si surface after co-deposition of 0.3 ML of Mn and 0.06 ML of Co - the blue squares marks identical image segments offset by a slight drift between the images: (a) empty states image recorded at +1.5 V, 0.03 nA, (b) filled states image recorded at -1.5 V, 0.03 nA; (c) shows the wire length distribution for the same experiment.

We can qualitatively conclude based on the continued self-assembly of Mn atoms during the co-deposition of Mn and Co that the drive to form surface-bonded Mn wires is

stronger than the impact of Mn-Co interaction on surface structure formation. If the Mn-Co interaction were dominant, the surface would likely be populated by Mn-Co clusters with only very few wires. The wire length distribution is shown in Figure 11-8(c) and it is quite similar to the distribution obtained for sequential deposition experiments, albeit the percentage of clusters is larger (as seen in Figures 11-7(b) and 11-8(a)). The Mn wire distribution is dominated by Mn dimers and ultrashort wires that are 3 units long. The limitation of wire growth might be attributed to two factors: (a) the defects created by Co atoms, and (b) clusters induced by Mn-Co interaction, or Co atoms attaching at the end of Mn wires. About 75% of Co atoms and small clusters of undefined composition (0.045 ML Co was deposited) are positioned alongside the Mn wires, which was earlier defined as the capture zone. This indicates a preference for surface clustering of Co and presumably Mn, albeit the driving force for Mn wire formation is still sufficient to lead to significant wire formation. More co-deposition experiments are necessary to fully understand the interaction between Mn and Co and, in the future, to correlate the magnetic signature with the specific bonding environment for both atoms. This also defines the direction of our future work.

11.4. Conclusions

To conclude, we report preferential incorporation of Co into the asymmetric, subsurface U_H/U_L (70% of Co atoms) site compared to a much lower occupancy of the symmetric under-dimer U_D site, which is predicted to be the thermodynamically stable site. We propose that there is a kinetic limitation for Co incorporation into the theoretically more stable under-dimer site. The dimer-vacancy sites, which are created by the

interaction of the Co atoms with the Si-surface, is not a preferred site for Co adsorption based on statistics of defects depth before and after Co deposition. A signature for subsurface diffusion of Co is the ejection of surface Si atoms resulting in a highly defective surface post-deposition and this was observed in all our experiments. A statistical analysis of the defect and Co atom concentrations indicates that surface defect concentrations are determined by the equilibrium between defect creation and annihilation.

In the sequential deposition of Mn and then Co, we consistently observe that the Mn wires become more disordered, and are characterized by protrusions on top and the side of the wires and kinks along the length of the wire, which disrupt their continuity. This is expressed in the wire length distribution, which shows a greater number of Mn dimers and ultrashort wires (3 units long). The majority of the Co atoms are adsorbed in the vicinity of the Mn wire, which suggests that the Mn wires provide preferred adsorption sites and might indicate that Mn-Co interaction dominates the Co-Si interaction near the wires. In the co-deposition of Mn and Co the self-assembly of Mn wires is surprisingly still observed despite the defect creation that accompanies the deposition and subsequent diffusion of Co in Si. The increasing number of clusters in this process and preponderance of protrusions at the Mn wires can be understood as the early stages of alloying. The sequential or co-deposition of Mn and Co can be used to control the bonding environment of the respective elements, with a stronger mixing of Co and Mn in the co-deposition sequence owing to both reactants being mobile. Knowledge of the specific bonding environment will allow us to connect the Mn-Co distribution, with the magnetic signature in future experiments, and develop an in-depth understanding of the exchange coupling in this system.

References

- ¹ H. Ohno, A. Shen, F. Matsukura, A. Oiwa, A. Endo, S. Katsumoto, et al., Applied Physics Letters. **69** (1996) 363–365.
- ² H. Ohno, H. Munekata, T. Penney, S. von Molnár, L.L. Chang, Phys. Rev. Lett. **68** (1992) 2664–2667.
- ³ A. Haury, A. Wasiela, A. Arnoult, J. Cibert, S. Tatarenko, T. Dietl, et al., Phys. Rev. Lett. **79** (1997) 511–514.
- ⁴ H. Hori, S. Sonoda, T. Sasaki, Y. Yamamoto, S. Shimizu, K. Suga, et al., Physica B: Condensed Matter. **324** (2002) 142–150.
- ⁵ T. Dietl, H. Ohno, F. Matsukura, J. Cibert, D. Ferrand, Science. **287** (2000) 1019–1022.
- ⁶ A.M. Nazmul, T. Amemiya, Y. Shuto, S. Sugahara, M. Tanaka, Phys. Rev. Lett. **95** (2005) 017201.
- ⁷ Y.D. Park, A.T. Hanbicki, S.C. Erwin, C.S. Hellberg, J.M. Sullivan, J.E. Mattson, et al., Science. **295** (2002) 651–654.
- ⁸ L. Vinokurova, V. Ivanov, E. Kulatov, A. Vlasov, Journal of Magnetism and Magnetic Materials. **90–91** (1990) 121–125.
- ⁹ H.J. Liu, J.H.G. Owen, K. Miki, C. Renner, M Journal of Physics: Condensed Matter. **23** (2011) 172001.
- ¹⁰ S. Picozzi, A. Continenza, A. Freeman, Physical Review B. **70** (2004).
- ¹¹ G. Profeta, S. Picozzi, A. Continenza, R. Podloucky, Physical Review B. **70** (2004).
- ¹² P. Kratzer, S.J. Hashemifar, H. Wu, M. Hortamani, M. Scheffler, Journal of Applied Physics. **101** (2007) 081725.
- ¹³ H. Wu, P. Kratzer, M. Scheffler, Physical Review B. **72** (2005).
- ¹⁴ E.R. Weber, Applied Physics A Solids and Surfaces. **30** (1983) 1–22.
- ¹⁵ M. Hortamani, H. Wu, P. Kratzer, M. Scheffler, Phys. Rev. B. **74** (2006) 205305.
- ¹⁶ M.R. Krause, A.J. Stollenwerk, J. Reed, V.P. LaBella, M. Hortamani, P. Kratzer, et al., Phys. Rev. B. **75** (2007) 205326–5.
- ¹⁷ G.M. Dalpian, A.J.R. da Silva, A. Fazzio, Surface Science. **566–568** (2004) 688–692.
- ¹⁸ C.-Y. Niu, J.-T. Wang, Solid State Communications. **152** (2012) 127–131.
- ¹⁹ A.P. Horsfield, S.D. Kenny, H. Fujitani, Phys. Rev. B. **64** (2001) 245332.
- ²⁰ G.W. Peng, A.C.H. Huan, E.S. Tok, Y.P. Feng, Phys. Rev. B. **74** (2006) 195335.
- ²¹ B.D. Yu, Y. Miyamoto, O. Sugino, T. Sasaki, T. Ohno, Phys. Rev. B. **58** (1998) 3549–3552.
- ²² S. Higai, T. Ohno, Applied Surface Science. **166** (2000) 149–153.
- ²³ H. Liu, P. Reinke, Surf. Sci. **602** (2008) 986–992.
- ²⁴ C.A. Nolph, H. Liu, P. Reinke, Surface Science. **605** (2011) L29–L32.
- ²⁵ C.A. Nolph, K.R. Simov, H. Liu, P. Reinke, J. Phys. Chem. C. **114** (2010) 19727–19733.
- ²⁶ K.R. Simov, C.A. Nolph, P. Reinke, J. Phys. Chem. C. **116** (2012) 1670–1678.
- ²⁷ A. Fuhrer, F.J. Rueß, N. Moll, A. Curioni, D. Widmer, Phys. Rev. Lett. **109** (2012) 146102.
- ²⁸ A.M.P. Sena, D.R. Bowler, J. Phys.: Condens. Matter. **23** (2011) 305003.

- ²⁹ J.H.G. Owen, K. Miki, D.R. Bowler, *Journal of Materials Science*. **41** (2006) 4568–4603.
- ³⁰ S.P. Dash, D. Goll, H.D. Carstanjen, *Applied Physics Letters*. **90** (2007) 132109.
- ³¹ W.S. Cho, J.Y. Kim, N.G. Park, I.W. Lyo, K. Jeong, S.S. Kim, et al., *Surface Science*. **453** (2000) L309–L314.
- ³² G. Rangelov, P. Augustin, J. Stober, T. Fauster, *Phys. Rev. B*. **49** (1994) 7535–7542.
- ³³ V. Scheuch, B. Voigtländer, H.P. Bonzel, *Surface Science*. **372** (1997) 71–82.
- ³⁴ J. Choi, Y. Kim, D.K. Lim, D.H. Kim, S. Kim, *The Journal of Physical Chemistry C*. **115** (2011) 15467–15470.
- ³⁵ S.H. Brongersma, M.R. Castell, D.D. Perovic, M. Zinke-Allmang, *Phys. Rev. Lett.* **80** (1998) 3795–3798.
- ³⁶ P.J. Webster, *Journal of Physics and Chemistry of Solids*. **32** (1971) 1221–1231.
- ³⁷ M. Meinert, J.-M. Schmalhorst, G. Reiss, *J. Phys.: Condens. Matter*. **23** (2011) 116005.
- ³⁸ K. Hata, T. Kimura, S. Ozawa, H. Shigekawa, *J. Vac. Sci. Technol. A*. **18** (2000) 1933–1936.
- ³⁹ D. Nečas, P. Klapetek, *Central European Journal of Physics*. **10** (2012) 181–188.
- ⁴⁰ I. Horcas, R. Fernandez, J.M. Gómez-Rodríguez, J. Colchero, J. Gómez-Herrero, A.M. Baro, *Rev. Sci. Instrum.* **78** (2007) 013705–013705.
- ⁴¹ M.D. Abramoff, P.J. Magelhaes, S.J. Ram, *Biophotonics International*. **11** (2004) 36–42.
- ⁴² R.J. Hamers, U.K. Kohler, *J. Vac. Sci. Technol. A*. **7** (1989) 2854–2859.
- ⁴³ M. Nishizawa, T. Yasuda, S. Yamasaki, K. Miki, M. Shinohara, N. Kamakura, et al., *Phys. Rev. B*. **65** (2002) 161302.
- ⁴⁴ S.-Y. Yu, H. Kim, J.-Y. Koo, *Phys. Rev. Lett.* **100** (2008) 036107.
- ⁴⁵ J. Choi, D. Lim, Y. Kim, D. Kim, S. Kim, *Physical Review B*. **82** (2010).
- ⁴⁶ H.J.W. Zandvliet, A. van Houselt, P.E. Hegeman, *Surface Science*. **605** (2011) 1129–1132.
- ⁴⁷ M. Yoshimura, I. Ono, K. Ueda, *Applied Surface Science*. **130–132** (1998) 276–281.
- ⁴⁸ S. Higai, T. Ohno, *Phys. Rev. B*. **65** (2002) 165309.
- ⁴⁹ R.M. Tromp, R.J. Hamers, J.E. Demuth, *Phys. Rev. Lett.* **55** (1985) 1303–1306.
- ⁵⁰ J. Dąbrowski, M. Scheffler, *Applied Surface Science*. **56–58** (1992) 15–19.
- ⁵¹ H.L. Meyerheim, U. Döbler, A. Puschmann, *Phys. Rev. B*. **44** (1991) 5738–5744.

12. 3D Nanostructures on Ge/Si(100) Wetting Layers: Hillocks and Pre-Quantum Dots

12.1. Introduction

The quantum effects in strain-induced Ge quantum dots (QDs) result in novel properties that make them candidates for use in photonic and electronic devices and solid-state quantum computing.¹⁻⁵ Ge deposition on Si(001) has been studied extensively and QD growth occurs from an initially flat Ge wetting layer (WL) which roughens as its thickness increases during continued deposition. Once the WL reaches a critical thickness, which corresponds to a critical strain energy, the formation of pyramidal quantum dots is observed and these transform, with continued Ge deposition, into large domes and superdomes.⁴⁻⁸ The synthesis of ordered 2D and 3D arrays of Ge QDs has been achieved through the use pre-patterned and vicinal substrates where kinetic step bunching can induce an array of nano-patterns,⁹ or seeding of nucleation centers by intentional introduction of impurities on a growth surface.¹⁰

The advances in understanding and manipulation of Ge QD nucleation and growth are contrasted by only few studies which investigate WLs with sub-critical thickness. Zhang et al.¹¹ recently demonstrated that monolithic Ge-nanowires can be synthesized by annealing of Ge-WLs with sub-critical thicknesses and their work renewed our interest in this growth regime. The metastable Ge WL was deposited at 560 °C and transformed into monolithic Ge wires upon annealing at a slightly lower temperature of 550 °C.¹¹ The monolithic nanowires, are {105}-faceted and only 2-3 unit cells in height,^{11,12} and formed in a very narrow parameter space defined by the annealing time, temperature and WL thickness. Prolonged annealing leads to bunched wire structures.¹³ Zhang et al.^{14,15} also showed that

the Ge wires could be used as templates to grow other novel Ge nanostructures such as dumbbells, dashes and dot-chains. These studies reignited the discussion about the equilibrium shapes of {105}-faceted Ge islands (pyramids, huts and wires).¹² Daruka et al.¹² re-examined the energetic contributions to the thermodynamic treatment of WL, wire and QD formation, and includes a new assessment of the excess surface energy (ESE) in which edge energies constitute a driving force for shape selection.

These observations have prompted us to widen the parameter space and study the response to annealing of WLs of variable thicknesses as a pathway to the formation of a wider range of nanostructures. Our work extends over a relatively large parameter space defined by the WL thickness (1.2 to 3.5 ML) and annealing temperature range (450 °C to 600 °C) to capture specifically the impact of WL thickness and consequently strain energy on roughening and relaxation of the WL into nanostructures. We have investigated wetting layers in the thickness range of 1.2-3.5 ML, which is below the critical WL thickness required to nucleate QDs at the growth temperatures used in this work.¹⁶

12.2. Experimental section

The experiments were performed in an Omicron Nanotechnology Variable Temperature SPM system under ultrahigh vacuum (UHV) conditions. The base pressure was $\leq 3 \times 10^{-10}$ mbar and the Si(100) samples were B-doped with resistivity between 0.01-0.02 Ω -cm. The sample was annealed overnight at 450 °C and thermally cleaned by flashing repeatedly to 1200-1300 °C to obtain a clean 2×1 reconstruction.^{17,18} Ge (GoodFellow, 99.99% purity) was deposited from a Veeco effusion cell at a rate of 0.25 ML/min. Imaging was performed at room temperature in constant current mode with W tips prepared by

electrochemical etching. Empty and filled states are imaged with a bias voltage of + 1.5 V and -1.5 V and a tunneling current of 0.03 nA. The temperature calibration procedure has been described by Nolph et al.¹⁹ and the error in our temperature measurement is +/- 25 °C on account of the small sample size (5×1 mm²) which prohibits reliable pyrometer measurements. Images were analyzed with Gwyddion, an open-source software for SPM data analysis.²⁰

12.3. Results

Ge layers, with a thickness of 1.6 ML to 3.5 ML, were deposited at temperatures from 540-550 °C and subsequently annealed below the growth temperature for varying durations. Additionally, a 1.2 ML thick WL was deposited at 360 °C and annealed in multiple steps in the temperature range of 360-540 °C. The entire parameter space explored in this study is pictorially represented in a 3D plot of anneal temperature, annealing time and WL thickness in Figure 12-1. The samples are labeled by the initial WL thickness before annealing and is represented as S[WL-thickness]. A reference QD growth sample, S_{ref} , (3.8 ML at 470 °C) is used to calibrate the sample temperature and deposition rates and showed the characteristic hut-shaped QDs expected for a WL thickness exceeding the critical thickness for QD nucleation. Two distinct 3D structures are obtained when subcritical Ge wetting layers are annealed: (i) hillocks, shown in Figures 12-2(c,d), with a wedding-cake type structure composed of stacked Ge(100) layers with narrow terraces, and (ii) pre-quantum dots (p-QDs), shown in Figure 12-3, which are {105}-faceted structures rotated by 45° compared to hillocks and similar to the conventional growth quantum dots.^{5,16,21} The pre-quantum dots are so named because we are operating in a

regime below the critical thickness required to nucleate quantum dots yet they already exhibit the $\{105\}$ facet. In S[3.5], the terrace structure of the initial Si surface is reminiscent of a 4-6° miscut wafer and the corresponding p-QDs obtained in this experiment are triangular in shape consistent with triangular QDs observed by Persichetti et al.²² on miscut Si wafers.

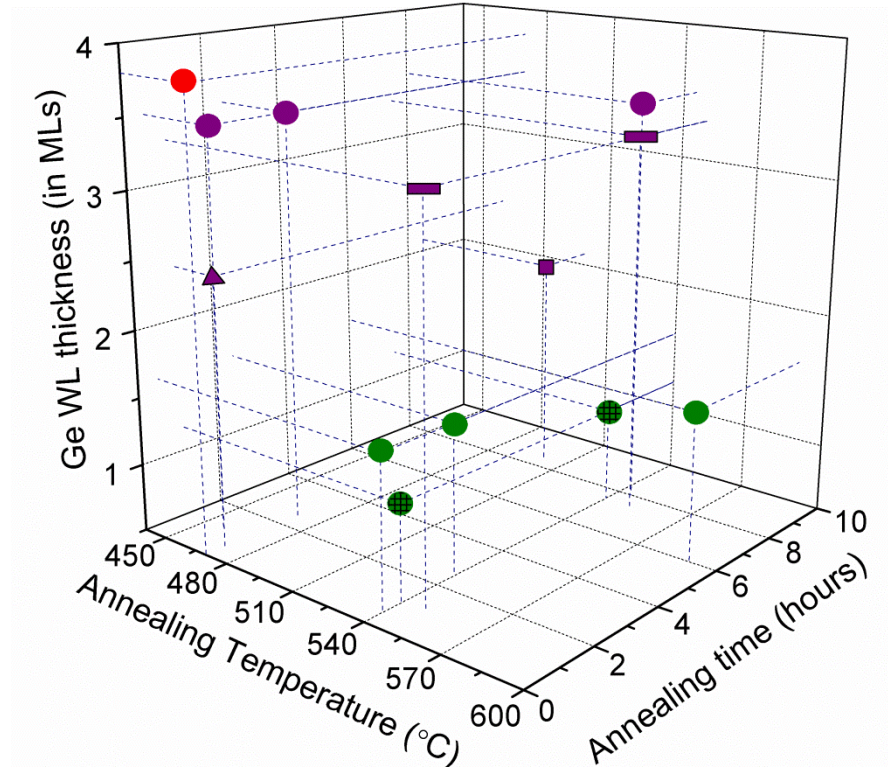


Figure 12-1. (a) 3D parameter space map of all the samples prepared in the current work. The parameters that yield hillocks and p-QDs (pre-quantum dots) are color coded as green and violet respectively. The red circle in (a) is the reference QD sample. Each symbol in the map represents a sequential annealing experiment and is summarized in Table I.

Table 12-I. Sample index with corresponding wetting layer growth temperature and annealing temperatures used in this work.

Sample Index	Growth Temperature (°C)	Annealing Temperature (in °C) and Time	Structures Formed
S[1.2]	360	405 (1h), 460 (0.75h), 540 (1h + 6.5h)	Hillocks
S[1.6]	540	540 (0.5h + 2.5h), 590 (6h), 650 (2h)	Hillocks
S[2.1]	550	500 (8.75h)	p-QDs
S[2.4]	400	470 (1h)	p-QDs
S[3.3]	570	540 (1h + 7h), 525 (1.5h)	p-QDs
S[3.5]	475	470 (0.5h + 2h), 545 (8h)	p-QDs
S _{ref}	470	-	Normal QDs

The evolution of sample S[1.2], which was deposited at a low temperature of 360 °C, during sequential annealing from 400 °C to 540 °C is shown in Figure 12-2. The first layer of Ge completely wets the Si(100) surface owing to its low surface energy.^{23,24} However, the Ge deposition at low temperatures results in a rough WL surface with many small islands 2-3 MLs in height due to kinetic barriers to diffusion as shown in inset in Figure 12-2(a). Annealing for 1 hour at 405 °C does not significantly modify the surface morphology (as seen in Figure 12-2(a)) indicative of a lack of long-range atomic diffusion which precludes the formation of a smooth layer. Dimer vacancy lines (DVLs), which are dimer vacancies running across the width of a terrace leading to a 2xn reconstruction, are not yet observed and vacancies are not yet mobile at these low temperatures. Annealing S[1.2] at 460 °C for one hour leads to significant reorganization of the surface and results in a smoother terrace structure (Figure 12-2(b)) which is consistent with the WL structure seen during QD

deposition.^{25,26} The DVLs run across the entire width of a terrace resulting in the equilibrium 2x8 reconstruction for this system.

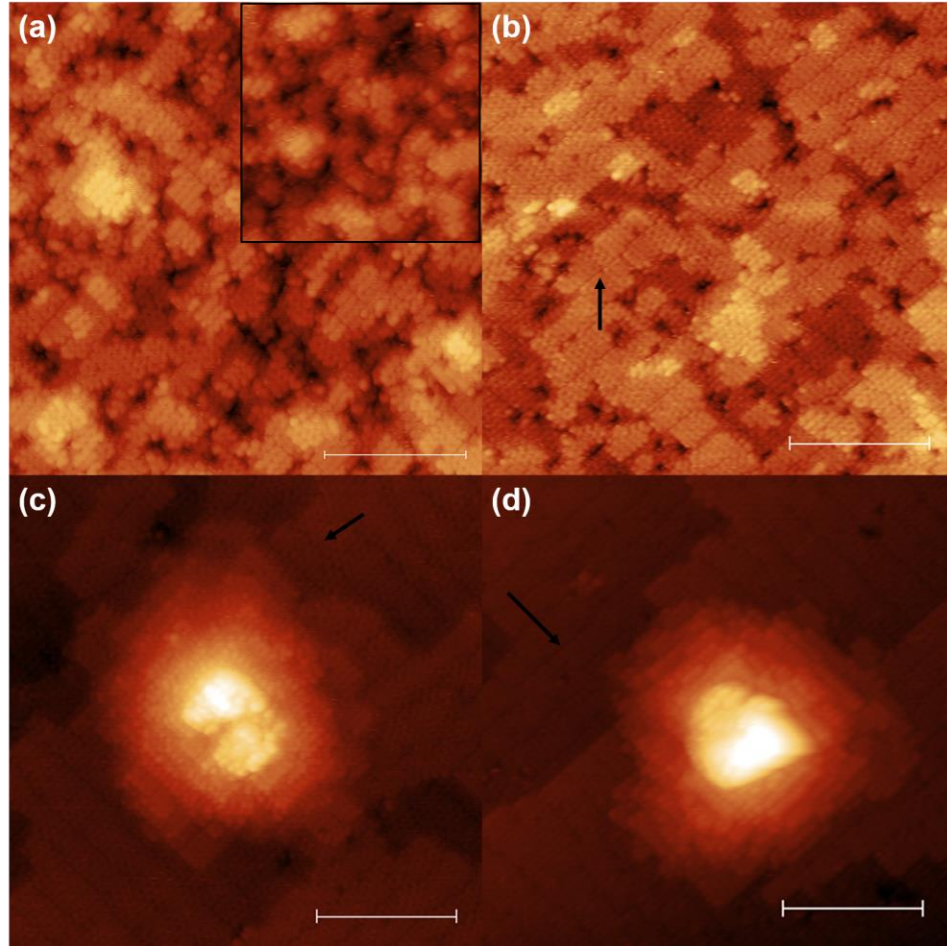


Figure 12-2. Evolution of S[1.2] when annealed at (a) 405 °C for 1 hour and the inset shows the as deposited surface (at 360 °C) with the same magnification, (b) 460 °C for 45 minutes, (c) 540 °C for 1 hour, and (d) 540 °C for 7.5 hours. Scale bar is 15 nm. Black arrows in (b), (c) and (d) point to DVLs on the surface.

Continued annealing of S[1.2] at 540 °C for 1 hour results in the formation of hillock structures which have not been observed previously in the Ge/Si system. Hillocks are characterized by a “wedding-cake type” stacked structure made up of Ge(100) terrace segments as seen in Figure 12-2(c,d). The hillock captured in Figure 12-2(c,d) are 1.4 and 3.4 nm high after cumulative anneal times of 1 and 7.5 hours and they make angles of

6.67±0.86° and 6.25±0.86° with the (100) plane (measured along <110>). This corresponds to an average terminating plane defined by the (001) step edges which is parallel to the $\{\bar{1}112\}$ plane. Annealing sample S[1.6] at temperatures and times indicated in Figure 12-1 and Table 12-I yielded hillocks with identical crystallographic orientation but larger in size. The edge configuration in hillocks is determined by the goal to minimize the step length and the terrace width is controlled by a balance between the step formation energy and the repulsive interactions between the steps^{27,28} which leads to local emergence of the stacking parallel to the $\{\bar{1}112\}$ plane. The corresponding facet is assigned based on the angle between two adjacent steps²⁹ and if the step edge configuration is uniform, the overall angle the hillocks make with the (100) plane can be used. Based on the angle of 6.25±0.86° which the S[1.2] hillocks make with the surface, the hillock terminating plane facet can be assigned a Miller index of $\{\bar{1}112\}$.

Ge WLs with thickness greater than 2.0 ML evolve differently during annealing and form pre-quantum dots (p-QDs) which are characterized by the presence of {105} facets. The data points in purple in Figure 12-1 correspond to those samples which yield p-QDs. The transformation of the flat wetting layer into the faceted p-QDs as observed in the sample S[3.3] is shown in Figure 12-3 and representative of all sample where p-QDs are observed. The starting wetting layer surface shown in Figure 12-3(a) corresponds to the MxN reconstruction described in literature.^{6,30,31} When annealed at 540 °C for 1 hour, small structures are nucleated on the surface some of which are partially {105}-faceted as seen in Figure 12-3(b). Prolonged annealing (+6 h at 540 °C) results in an increased number of fully faceted p-QDs (Figure 12-3(c)). The facet angle of 11.54±0.58° with the (100) surface

confirms the {105} facet as known in Ge QDs. Note that not all the structures are faceted after extended annealing and a few partially-faceted and unfaceted structures are still present on the surface. High resolution images of the p-QDs and conventional QDs are presented in Figure 12-4. All 3D nanostructures have an amorphous mound at the apex similar to the observations of Sanduijav et al.³² when the Ge/Si(100) samples were annealed between sequential Ge deposition cycles. They attributed these structures to growth defects resulting from extended storage of sample in ultrahigh vacuum (UHV) but we observe them in the annealing of freshly deposited samples. The discussion of amorphous apex structures is continued later once all datasets have been presented.

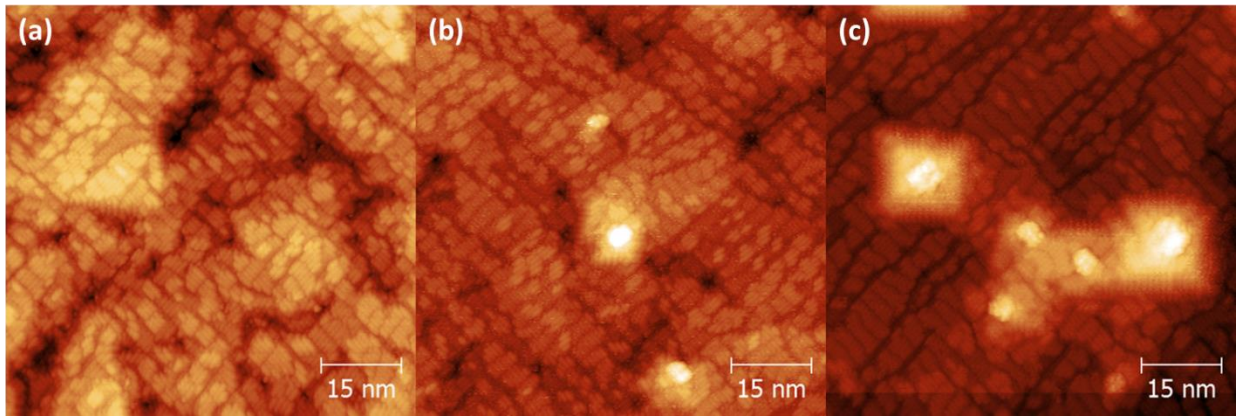


Figure 12-3. Evolution of 3.3 ML thick Ge wetting layer: (a) as deposited at 570 °C and after annealing at 540 °C for (b) 1 hour and (c) 7 hours. Partially and fully formed {105} facets on p-QDs are seen in (b) and (c).

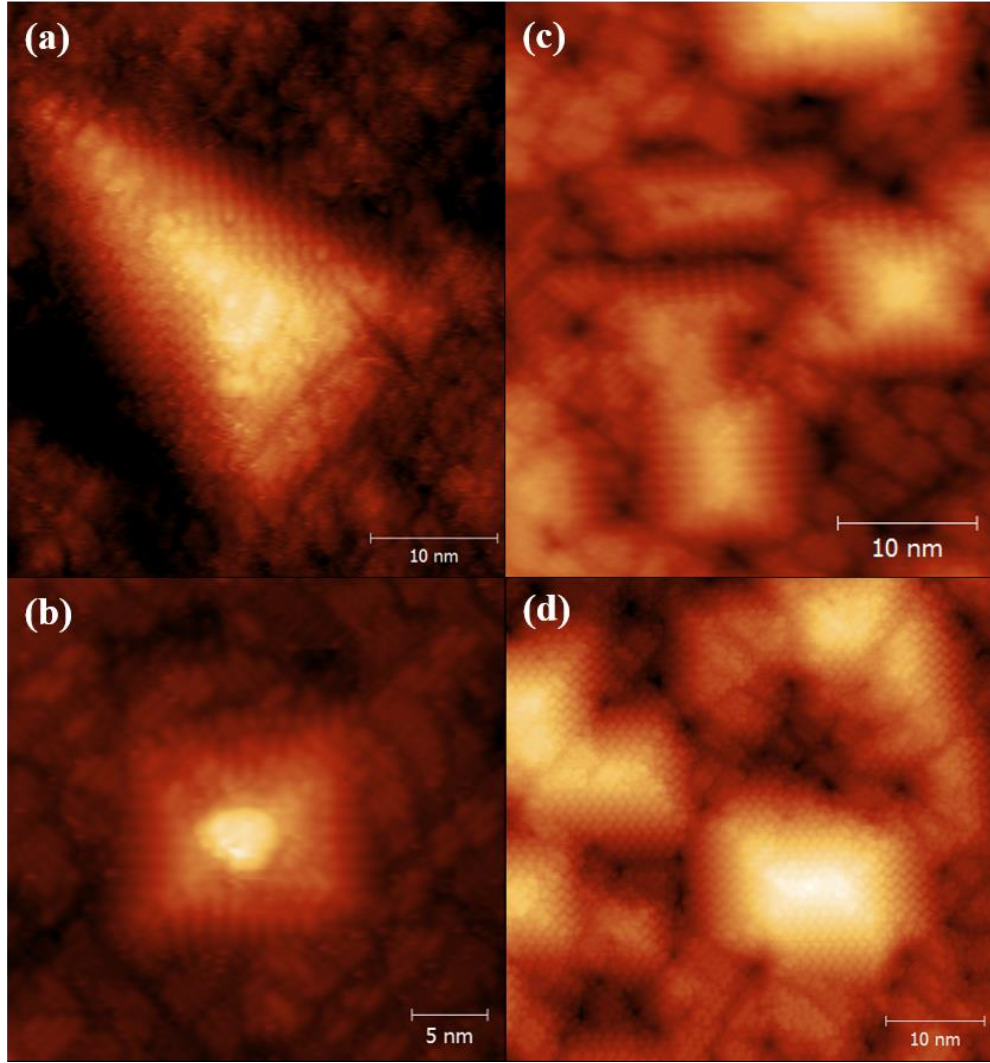


Figure 12-4. High resolution STM images of pre-quantum dots (p-QDs) and conventional quantum dots: (a) and (b) show images of p-QD from S[3.5], filled states, and S[3.3], empty states. (c) and (d) show empty and filled states images of conventional QDs from S_{ref} . The reconstructed $\{105\}$ surface is clearly visible and consistent with literature.⁴⁻⁶ Empty states images were recorded at +2.0 V, 0.1 nA and the filled states images were recorded at -2.0 V, 0.1 nA.

One of the key parameters distinguishing hillocks and p-QDs is the angle made by the islands with the Ge(001) surface and this is expressed in Figure 12-5(a) as a function of the initial WL thickness. The hillocks make an average angle of $6.25 \pm 0.86^\circ$ with the surface (measured along $\langle 110 \rangle$) while the p-QDs across all experiments make an average angle of $11.18 \pm 0.61^\circ$ (measured along $\langle 100 \rangle$) in agreement with a $\{105\}$ facet. Another striking

observation is that the p-QDs are bounded by $\langle 100 \rangle$ directions, similar to conventional Ge huts and pyramids,^{16,26,33} while the hillocks are rotated by 45° and are bounded by $\langle 110 \rangle$ directions (for reference, dimer rows and DVLs are oriented along $\langle 110 \rangle$). The difference in orientation between hillocks and pre-quantum dots is clearly illustrated by STM images of structures from S[1.2] and S[3.3] (Figures 12-2 and 12-3) as well as in the insets in Figure 12-5(a). Poor imaging encountered during measurement of samples S[1.6] and S[2.4] precluded sufficiently precise measurements of facet angles.

Figures 12-5 and 12-6 illustrate the transition between the two types of nanostructures - hillocks and p-QDs. We observe in Figure 12-5(a) that hillocks only form at low coverages and that crossover from hillock formation to p-QDs occurs at a WL thickness between 1.6 ML and 2.1 ML, which can be related to the increased strain energy. The lower temperature limit for nanostructure formation is 460°C , where only transformations of the WL surface structure are observed. In addition, the first layer of Ge is conserved owing to its exceptional stability compared to the bare on Si(100)- 2×1 surface.²⁴ We can now construct a stability diagram as shown in Figure 12-5(b) which predicts the type of structure that will be obtained for any given pair of WL thickness and annealing temperature ($[\text{WL}, T_{\text{anneal}}]$). For example, a combination of [3 ML, 425°C] will result in reorganization of the WL with no 3D nanostructures while [3 ML, 500°C] will yield {105}-faceted p-QDs. The initial WL thickness is the key variable that controls the type of nanostructure.

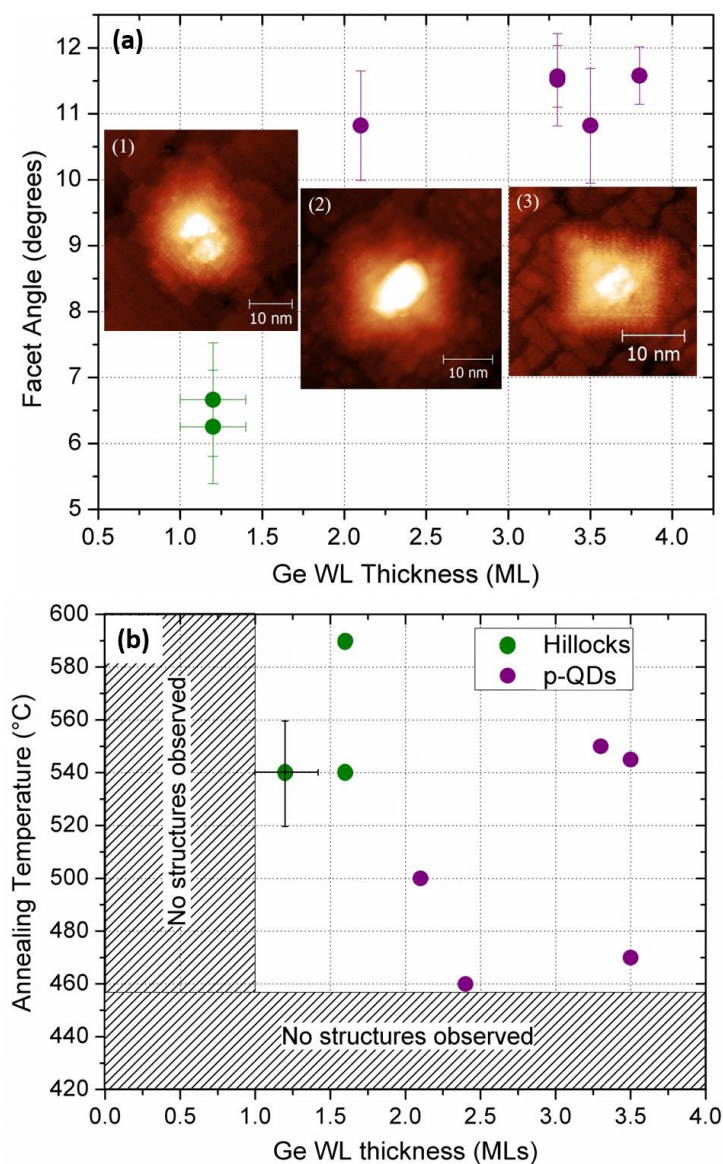


Figure 12-5. (a) Distribution of facet angles as a function of WL thickness with representative STM images of the structures obtained from S[1.2] (inset-1), S[2.1] (inset-2) and S[3.3] (inset-3). (b) WL thickness-annealing temperature map showing the minimum WL thickness and temperature required to nucleate hillocks and p-QDs. The error in our measurements is indicated for the data point corresponding to S[1.2].

The morphology of hillocks and p-QDs are summarized in Figure 12-6, which shows volume, and lateral dimensions as a function of WL thickness. Hillocks have a considerably larger volume compared to the p-QDs and the island number density follows the reverse trend where the number density of p-QDs is significantly higher than that of hillocks. The

hillocks obtained after annealing S[1.2] at 540 °C for 1 hour have an average volume of $515 \pm 51 \text{ nm}^3$ ($\approx 2.27 \times 10^4$ atoms) and a density of 66 hillocks per μm^2 . Prolonged annealing (540 °C for an additional 6.5 hours) increased in the density to 96 hillocks per μm^2 with an average volume of $655 \pm 75 \text{ nm}^3$ ($\approx 2.89 \times 10^4$ atoms). For sample S[3.3] discussed earlier (Figure 12-3), the p-QDs have an average volume of 43.13 nm^3 (≈ 1903 atoms) with an island density of 637 p-QDs per μm^2 after annealing at 540 °C for 1 hour and it increases to 133.73 nm^3 (≈ 5900 atoms) and 925 p-QDs per μm^2 after the subsequent 6 hour anneal. The absence of the steeper facets such as $\{113\}$ and $\{15\ 3\ 23\}$ that populate Ge domes even after prolonged annealing indicates that the misfit strain energy in the system is insufficient to compensate the energy cost for the formation of these facets while new islands with $\{105\}$ facets are continually added as evidenced by the increase in p-QD density. S[2.1] shows an unusually low number density compared to other p-QDs which is likely due to the WL thickness being just above the crossover thickness and the insufficient driving force for the nucleation of more p-QDs. The presence of the crossover is a strong indication that the formation of hillocks and p-QDs follow fundamentally different mechanisms.

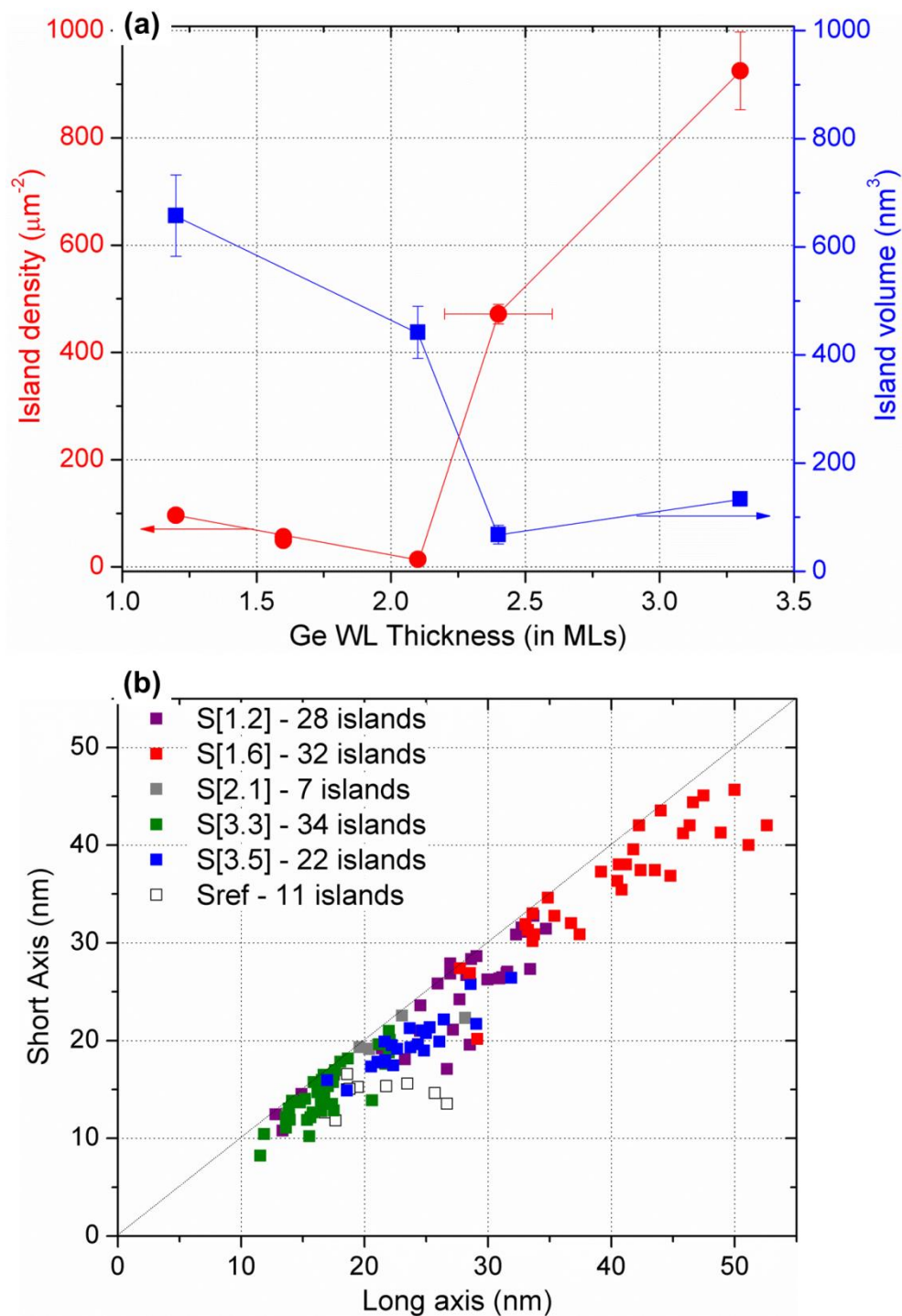


Figure 12-6. (a) Island volume and number density of hillocks and p-QDs as a function of Ge WL thickness. (b) Scatter plot of lateral dimensions of all hillocks, p-QDs, and the reference QD sample. The number in parenthesis refers to the wetting layer thickness.

The lateral dimensions of all the islands, including reference quantum dots from S_{ref} , are expressed in Figure 12-6(b). This plot shows clearly that the faceted p-QDs, on average, have smaller in-plane dimensions (length and width) compared to hillocks: for example, p-QDs from sample S[3.3] have final lateral dimensions of 16.5 and 16.0 nm (with standard deviation of 2.2 and 2.6 nm respectively) while the dimensions of hillocks obtained in sample S[1.6] are more than twice as large with 40.3 and 36.7 nm (standard deviation of 4.3 and 4.1 nm respectively). Both groups prefer a nearly square profile, and some p-QDs present a very small base length of 10 nm, which is only very rarely observed in Stranski-Krastanov growth of QDs. Hillocks grow faster compared to p-QDs and the evolution of the structures when annealed is summarized in Figure 12-7. This figure shows a complete set of size distributions for hillocks (S[1.6]) and p-QDs (S[3.3]) visualizing the significantly slower growth of p-QDs. The slow growth rate of {105} facets³⁴ can be attributed to kinetic limitations in the nucleation of a new layer on the {105} facet. Figure 12-7 also confirms that the structures observed are not metastable fluctuations which dissolve beyond a threshold barrier and that they are, in fact, growing structures.

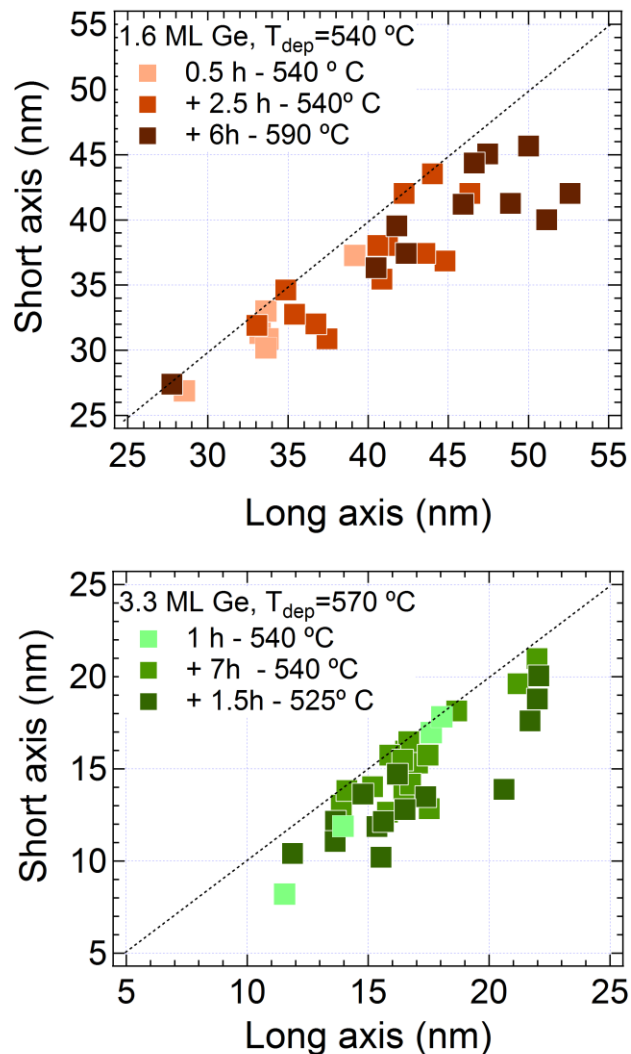


Figure 12-7. The evolution of (a) hillocks (from sample S[1.6]) and (b) p-QDs (from sample S[3.3]) with sequential annealing steps after Ge wetting layer deposition. The hillocks are, on average, larger than the corresponding p-QDs and also show increasing lateral dimension with multiple annealing steps. The size and shape distribution for all QDs are included in Figure 12-6.

Mass balance calculations were performed to determine the amount of Ge consumed in the formation of hillocks and p-QDs. Among all the samples prepared, only a fraction of the available Ge in the WL is consumed and the maximum amount of Ge consumed was 0.44 ML in case of S[1.6] at the end of the final annealing step. For example, in sample S[3.3], only 0.07 ± 0.03 ML of Ge was incorporated in the p-QDs after the first annealing step

(540 °C for 1 hour). After the subsequent anneal for 7 hours, an additional 0.26 ± 0.08 ML of Ge was consumed in the formation of p-QDs with 2.99 ± 0.08 ML of wetting layer remaining. In case of hillock formation in S[1.2], 0.07 ± 0.01 ML and 0.17 ± 0.02 ML of Ge are consumed after annealing for 1 hour and 6.5 hours, respectively, which is slightly lower than for S[3.3] using a similar annealing cycle. These results confirm that the formation of three-dimensional islands is not limited by the supply of Ge atoms. The first Ge-layer in contact with the Si-substrate is never consumed, which is consistent with existing literature²⁴ which shows that a monolayer of Ge on Si(001) has a lower surface energy than a bare silicon surface. A “wetting potential” has often been invoked to explain the stabilization of the wetting layer to thicknesses significantly in excess of 1 ML. However, our results could imply that this stabilization is largely kinetic in origin, rather than being due to a true energetic interaction.

12.4. Discussion

The fundamental aspects of Ge quantum dot growth on Si(100) have been studied intensely and while many aspects of QD growth are well-understood, the multiple factors controlling island shape remain open to discussion.^{4,12,16,26,30} The elongation of a pyramidal Ge QD into huts and wires has traditionally been attributed to kinetic factors but Daruka et al.¹² used basic thermodynamic parameters such as strain energy, surface energy, and edge energy to determine the stability of pyramidal, hut and wire structures under equilibrium conditions. In heteroepitaxial growth of faceted islands, the excess surface energy (ESE) is defined as the difference between the total surface energy of the system in the presence of islands and without islands (strained wetting layer).¹² By taking into account the edge and

kink energies and the surface energy of the strained {105} facet,³⁵ it has been shown that ESE is negative for conventional pyramidal and hut quantum dot structures as well as for elongated wire structures on a Ge WL surface,^{11,36} whose synthesis provided the initial motivation for our study. The delicate energy balance between surface energy and strain energy stored in the Ge-WL determines whether QDs or wires are formed assuming the temperature is sufficient to allow for the expression of the equilibrium structure. Earlier work by Tersoff et al.²¹ focused on the initial formation of QDs, and suggests a process where small, unfaceted mounds transform into faceted QDs based on several STM studies.^{4,5,16,37}

The formation of hillocks can be understood in the framework of the evolution of the Ge-WL surface as a function of temperature illustrated in Figure 12-2: the initial surface is rough on a very short length-scale and in response to annealing, the surface roughness decreases, the step edges thaw, and the dimer vacancies become mobile and condense in dimer vacancy lines. A further increase in the annealing temperature triggers the formation of hillocks with a roughly square footprint and wedding cake like structure. The sides of the square are always perpendicular to the direction of step bunching on Si and Ge(001) surfaces, which is the <110> direction, and their slope is at a near constant angle, which can be interpreted as the saturation angle representative of the stable configuration at this temperature. The hillock formation is observed below the roughening transition temperature^{38,39} where the free energy of step formation vanishes, and can be better described as localized step bunching. The inverse Ehrlich-Schwöbel barrier is sufficiently small to allow for an upward adatom flux thus destabilizing the terrace structure and leading to reduction in the local terrace width at the hillock but increasing the terrace size

in between hillocks. The magnitude of the inverse Ehrlich-Schwöbel barrier is likely influenced by the line tension and edge structure in the hillocks, and the compressive stress in the Ge-WL.⁴⁰ The wedding-cake type structure of hillocks is reminiscent of 3D structures that result from massive step bunching on the surface; considerable step motion is expected at the annealing temperatures used (>540 °C) and we propose this as a possible mechanism for the growth of hillocks. Prior work on the formation of QDs in a conventional growth process indicates that small surface mounds on the WL (pre-pyramids) initiate the formation of the {105} faceted QDs.⁵ We propose that the unfaceted and partially faceted islands in Figure 12-3(b) are identical to the mounds observed by Vailionis et al.⁵ and are precursors for both hillocks as well as p-QDs (as seen in the sequence in Figure 12-3).

The next question that arises from the current work is to determine the parameter(s) that controls the type of structure. The type of structure formed (hillock versus p-QDs) is dictated by the intricate balance between the various energies involved in the nucleation and growth process: (a) surface energy of the initial metastable WL and the final configuration with hillocks/p-QDs, (b) energy cost for formation of faceted p-QDs or step-edge creation in case of hillocks (dangling bonds at edges), and (c) release of misfit strain energy, an intrinsic function of WL thickness, which follows the formation of 3D islands. Under the conditions used here, the cross-over between hillock and p-QD formation is relatively abrupt and is tied to the WL thickness which is proportional to the magnitude of the strain energy stored in the WL. Figure 12-5 shows the abrupt transition between hillocks and p-QDs with a crossover thickness between 1.6 and 2.1 ML. We did not observe any direct transformations from hillocks to p-QD - either one or the other is formed and continues to grow in size during the continued annealing process. In this sense, our results

for annealing Ge wetting layers differ from those of Vailionis et al.⁵ and Tersoff et al.²¹ where a direct transition between the two shapes occurs during continuous deposition.

The formation of hillocks/p-QDs is likely initiated by surface or subsurface defects and adventitious impurities, which act as a sink for mobile Ge species on the surface.³⁹ Some intermixing is also expected in this system due to the annealing at these temperatures as has been observed by Zhang et al.¹¹ The amorphous structure at the apex of QDs has been observed previously by Vailionis et al.⁵ and Sanduijav et al.³² during the conventional fabrication of Ge QDs and in case of the latter, it was attributed to the presence of impurities. In our experiments, the amorphous apex structure is confined to the hillock/p-QD regime as shown in Figures 12-2 and 12-3 and is not present in the QDs grown in the reference experiment S_{ref} – this eliminates the Ge source as the origin of contamination. A control experiment where a Si(001)-(2×1) substrate was annealed at 600 °C for 2 hours did not show any surface structures like hillocks, step bunching or reconstructions, which are typically associated with carbon contamination.³⁹ While the presence of impurities can never be completely excluded, in light of the results presented here, we favor the development of an inherent surface instability as the origin of hillock and p-QD formation.

12.5. Conclusion

In conclusion, we have demonstrated the conversion of the metastable, sub-critical Ge wetting layers grown on a Si(001)-2×1 surface into two distinct types of 3D nanostructures by a post-growth annealing process. Hillocks have a wedding-cake type stacked structure while p-QDs are {105}-faceted structures similar to conventionally grown QDs. The WL

thickness (correlated with misfit strain energy) is the key parameter that controls the type of structure obtained and a stability map is developed which predicts the type of nanostructure which will emerge. The minimum annealing temperature for the nucleation of any nanostructure is 460 °C and the crossover WL thickness above which {105}-faceting is stable and p-QDs form is between 1.6 and 2.1 ML. These p-QDs can be exceptionally small and reach lateral dimensions down to 10 nm.

Our results demonstrate the possibility of obtaining quantum dots at WL thicknesses below the nominal equilibrium critical thickness used in current literature to demarcate the thickness where {105} faceted QDs emerge. This could suggest that the true equilibrium wetting layer thickness is significantly smaller, perhaps only a single monolayer of Ge. However, more work is needed to assess this. Indeed, if a growth experiment with very low Ge deposition rates were to be performed for example: 2 hours to deposit 3 ML of Ge at 550 °C (critical thickness at 550 °C is ≈ 4.5 ML according to the literature on growth experiments), it might yield fully-formed {105}-faceted QDs despite not crossing the critical thickness as it is currently defined. This would imply that the critical thickness for forming Ge QDs depends on the growth rate. It also indicates that the concept of critical thickness has to be expanded and include pathway along the transformation of 3D structures, including formation of hillocks or p-QDs described here.

References

1. Schmidt, O. G. *et al.* Laterally aligned Ge/Si islands: a new concept for faster field-effect transistors. *Materials Science and Engineering: B* **89**, 101–105 (2002).
2. Wang, K. L., Cha, D., Liu, J. & Chen, C. Ge/Si Self-Assembled Quantum Dots and Their Optoelectronic Device Applications. *Proceedings of the IEEE* **95**, 1866–1883 (2007).
3. Alkhatib, A. & Nayfeh, A. A Complete Physical Germanium-on-Silicon Quantum Dot Self-Assembly Process. *Sci. Rep.* **3**, (2013).
4. Sutter, P. & Lagally, M. G. Nucleationless Three-Dimensional Island Formation in Low-Misfit Heteroepitaxy. *Phys. Rev. Lett.* **84**, 4637–4640 (2000).
5. Vailionis, A. *et al.* Pathway for the Strain-Driven Two-Dimensional to Three-Dimensional Transition during Growth of Ge on Si(001). *Phys. Rev. Lett.* **85**, 3672–3675 (2000).
6. Aqua, J.-N., Berbezier, I., Favre, L., Frisch, T. & Ronda, A. Growth and self-organization of SiGe nanostructures. *Physics Reports* **522**, 59–189 (2013).
7. Wu, F., Chen, X., Zhang, Z. & Lagally, M. G. Reversal of Step Roughness on Ge-Covered Vicinal Si(001). *Phys. Rev. Lett.* **74**, 574–577 (1995).
8. Ross, F. M., Tromp, R. M. & Reuter, M. C. Transition States Between Pyramids and Domes During Ge/Si Island Growth. *Science* **286**, 1931–1934 (1999).
9. Men, F. K. *et al.* Self-Organized Nanoscale Pattern Formation on Vicinal Si(111) Surfaces via a Two-Stage Faceting Transition. *Phys. Rev. Lett.* **88**, 96105 (2002).
10. Schmidt, O. G., Schieker, S., Eberl, K., Kienzle, O. & Ernst, F. Carbon-induced germanium dots: Kinetically-limited islanding process prevents coherent vertical alignment. *Applied Physics Letters* **73**, 659–661 (1998).
11. Zhang, J. J. *et al.* Monolithic Growth of Ultrathin Ge Nanowires on Si(001). *Phys. Rev. Lett.* **109**, 85502 (2012).
12. Daruka, I., Grossauer, C., Springholz, G. & Tersoff, J. Equilibrium phase diagrams for the elongation of epitaxial quantum dots into hut-shaped clusters and quantum wires. *Phys. Rev. B* **89**, 235427 (2014).
13. Zhang, J. J. *et al.* Self-organized evolution of Ge/Si(001) into intersecting bundles of horizontal nanowires during annealing. *Applied Physics Letters* **103**, 83109 (2013).
14. Zhang, J. J. & Schmidt, O. G. Strain-induced self-assembly of Ge nanodashes, nanodumbbells, and dot chains on Si(001). *Applied Physics Letters* **103**, 143112 (2013).
15. Zhang, J., Brehm, M., Grydlik, M. & Schmidt, O. G. Evolution of epitaxial semiconductor nanodots and nanowires from supersaturated wetting layers. *Chem. Soc. Rev.* (2014). doi:10.1039/C4CS00077C
16. Mo, Y.-W., Savage, D. E., Swartzentruber, B. S. & Lagally, M. G. Kinetic pathway in Stranski-Krastanov growth of Ge on Si(001). *Phys. Rev. Lett.* **65**, 1020–1023 (1990).
17. Hata, K., Kimura, T., Ozawa, S. & Shigekawa, H. How to fabricate a defect free Si(001) surface. *Journal of Vacuum Science & Technology A* **18**, 1933–1936 (2000).
18. Ramalingam, G. & Reinke, P. Towards a Mn–Co surface alloy: Scanning Tunneling Microscopy (STM) study of Co adsorption on Si(100) and its interaction with Mn wires. *Surface Science* **620**, 1–8 (2014).

19. Nolph, C. A., Simov, K. R., Liu, H. & Reinke, P. Manganese Nanostructures on Si(100)(2 × 1) Surfaces: Temperature-Driven Transition from Wires to Silicides. *J. Phys. Chem. C* **114**, 19727–19733 (2010).
20. Nečas, D. & Klapetek, P. Gwyddion: an open-source software for SPM data analysis. *Central European Journal of Physics* **10**, 181–188 (2012).
21. Tersoff, J., Spencer, B. J., Rastelli, A. & von Känel, H. Barrierless Formation and Faceting of SiGe Islands on Si(001). *Phys. Rev. Lett.* **89**, 196104 (2002).
22. Persichetti, L., Sgarlata, A., Fanfoni, M. & Balzarotti, A. Shaping Ge Islands on Si(001) Surfaces with Misorientation Angle. *Phys. Rev. Lett.* **104**, 36104 (2010).
23. Stekolnikov, A. A., Furthmüller, J. & Bechstedt, F. Absolute surface energies of group-IV semiconductors: Dependence on orientation and reconstruction. *Phys. Rev. B* **65**, 115318 (2002).
24. Beck, M. J., van de Walle, A. & Asta, M. Surface energetics and structure of the Ge wetting layer on Si(100). *Phys. Rev. B* **70**, 205337 (2004).
25. Nolph, C. A., Kassim, J. K., Floro, J. A. & Reinke, P. Addition of Mn to Ge quantum dot surfaces—interaction with the Ge QD {105} facet and the Ge(001) wetting layer. *J. Phys.: Condens. Matter* **25**, 315801 (2013).
26. Sutter, P., Zahl, P. & Sutter, E. Continuous formation and faceting of SiGe islands on Si(100). *Applied Physics Letters* **82**, 3454–3456 (2003).
27. Shenoy, V. B. & Freund, L. B. A continuum description of the energetics and evolution of stepped surfaces in strained nanostructures. *Journal of the Mechanics and Physics of Solids* **50**, 1817–1841 (2002).
28. Shenoy, V. B., Ciobanu, C. V. & Freund, L. B. Strain induced stabilization of stepped Si and Ge surfaces near (001). *Applied Physics Letters* **81**, 364–366 (2002).
29. Lüth, H. *Solid surfaces, interfaces and thin films*. (Springer, 2010).
30. Voigtländer, B. Fundamental processes in Si/Si and Ge/Si epitaxy studied by scanning tunneling microscopy during growth. *Surface Science Reports* **43**, 127–254 (2001).
31. Goldfarb, I., Hayden, P. T., Owen, J. H. G. & Briggs, G. A. D. Nucleation of “Hut” Pits and Clusters during Gas-Source Molecular-Beam Epitaxy of Ge/Si(001) in In Situ Scanning Tunneling Microscopy. *Phys. Rev. Lett.* **78**, 3959–3962 (1997).
32. Sanduijav, B., Matei, D., Chen, G. & Springholz, G. Shape transitions and island nucleation for Si/Ge molecular beam epitaxy on stripe-patterned Si (001) substrate. *Physical Review B* **80**, (2009).
33. Kästner, M. & Voigtländer, B. Kinetically Self-Limiting Growth of Ge Islands on Si(001). *Phys. Rev. Lett.* **82**, 2745–2748 (1999).
34. McKay, M. R., Venables, J. A. & Drucker, J. Kinetically Suppressed Ostwald Ripening of Ge/Si(100) Hut Clusters. *Phys. Rev. Lett.* **101**, 216104 (2008).
35. Migas, D. B., Cereda, S., Montalenti, F. & Miglio, L. Electronic and elastic contributions in the enhanced stability of Ge(1 0 5) under compressive strain. *Surface Science* **556**, 121–128 (2004).
36. Shklyaev, O. E., Beck, M. J., Asta, M., Miksis, M. J. & Voorhees, P. W. Role of Strain-Dependent Surface Energies in Ge/Si(100) Island Formation. *Phys. Rev. Lett.* **94**, 176102 (2005).
37. Tromp, R. M., Ross, F. M. & Reuter, M. C. Instability-Driven SiGe Island Growth. *Phys. Rev. Lett.* **84**, 4641–4644 (2000).

38. Maxson, J. B. *et al.* Thermal Roughening of a Thin Film: A New Type of Roughening Transition. *Phys. Rev. Lett.* **85**, 2152–2155 (2000).
39. Gray, S. M., Johansson, M. K.-J. & Johansson, L. S. O. Nanoscale roughening of Si(001) by oxide desorption in ultrahigh vacuum. *Journal of Vacuum Science & Technology B* **14**, 1043–1047 (1996).
40. Liu, Z.-J. & Shen, Y. G. Roughening kinetics of thin films in the presence of both stress and Ehrlich–Schwobel barrier. *Applied Physics Letters* **83**, 5404–5406 (2003).